SAND2020-11692R

KomPass

Compaction of crushed Salt for the safe Containment

Supported by:

Federal Ministry for Economic Affairs and Energy

on the basis of a decision by the German Bundestag

U.S. DEPARTMENT OF ENERGY

National Nuclear Security Administration

GRS - 608

BGE TECHNOLOGY GmbH

Bundesanstalt für Geowissenschaften und Rohstoffe

Gesellschaft für Anlagen- und Reaktorsicherheit (GRS) gGmbH

Sandia National Laboratories

TU Clausthal

Institut für Gebirgsmechanik GmbH
Untersuchung·Prüfung·Beratung·Begutachtung

KOMPASS

Compaction of crushed salt for the safe containment

Oliver Czaikowski (GRS)
Larissa Friedenberg (GRS)
Klaus Wieczorek (GRS)
Nina Müller-Hoeppe (BGE-TEC)
Christian Lerch (BGE-TEC)
Ralf Eickemeier (BGR)
Ben Laurich (BGR)
Wenting Liu (BGR)
Dieter Stührenberg (BGR)
Kristoff Svensson (BGR)
Kornelia Zemke (BGR)
Christoph Lüdeling (IfG)
Till Popp (IfG)
James Bean (Sandia)
Melissa Mills (Sandia)
Benjamin Reedlunn (Sandia)
Uwe Düsterloh (TU Clausthal)
Svetlana Lerche (TU Clausthal)
Juan Zhao (TU Clausthal)

August 2020

Remark:

This work was conducted by the BGE Technology GmbH (BGE-TEC), the Federal Institute for Geosciences and Natural Resources (BGR), the Institut für Gebirgsmechanik GmbH, Leipzig (IfG), the Technical University of Clausthal (TUC), Sandia National Laboratories (Sandia) and the Gesellschaft für Anlagen- und Reaktorsicherheit gGmbH (GRS).

The authors are responsible for the content of this report.

GRS-608
ISBN 978-3-947685-94-3

Descriptor

Crushed salt compaction, Heat-emitting radioactive waste, Repository

Abstract

In Germany, rock salt formations are a possible host rock taken into account for the safe disposal of heat-emitting radioactive waste. With respect to crushed salt will be used in the repository for backfilling of open cavitied (using dry material) and for construction of long-term seals in the main access drifts (using wetted material). With time, the crushed salt will be compacted by the convergence of the host rock and reaches porosities comparable with the rock salts.

The compaction behaviour of crushed salt has been investigated within the last 40 years, however, its behaviour at low porosities and the resulting low permeabilities becomes relevant with the introduction of the approach of the containment providing rock zone. In the current state, the database and process understanding have some important gaps in knowledge referring the material behaviour, existing laboratory and numerical models, especially for the low porosity range.

The objective of this project was the development of methods and strategies for the reduction of deficits in the prediction of crushed salt compaction leading to an improvement of the prognosis quality. It includes the development of experimental methods for determining crushed salt properties in the range of low porosities, the enhancement of process understanding and the investigation and development of existing numerical models.

Kurzfassung

Steinsalzformationen werden in Deutschland für die Entsorgung hochradioaktiver wärmeproduzierender Abfälle als Wirtsgestein in Betracht gezogen. Dabei sollten in einem Endlagerbergwerk im Steinsalz, sowohl Resthohlräume mit (trockenem) Salzgrus versetzt als auch Langzeitdichtungen mit (angefeuchtetem) Salzgruß in den Hauptzugangsstrecken errichtet werden. Mit der Zeit wird der Salzgrus durch die Konvergenz der Grubenbaue infolge der Kriechfähigkeit des Salzgesteins kompaktiert.

Salzgrus als Versatzmaterial wurde in Deutschland zwar seit mehr als 40 Jahren untersucht, aber erst seit der Einführung des Konzepts des einschlusswirksamen Gebirgsbereichs (eWG) beim Langzeitsicherheitsnachweis ist sein Verhalten bei niedriger Porosität und der erwarteten niedrigen Permeabilität von sicherheitstechnischer Bedeutung. Es bestehen derzeit noch Defizite sowohl bei der experimentellen Datenbasis als auch bei der Entwicklung, Validierung und Verifizierung der numerischen Modelle, insbesondere im Bereich niedriger Porositäten.

Gesamtziel des Vorhabens ist die Methoden- und Strategieentwicklung, um die Defizite bei der Prognose der Kompaktion von Salzgrusversatz zu verringern und damit die Voraussetzungen für die Stärkung des Sicherheitsnachweises für ein Endlager im Steinsalz zu schaffen. Dies beinhaltet die Schaffung experimenteller Grundlagen für die Bestimmung von Salzgruseigenschaften im Bereich kleiner Porositäten, die Entwicklung des Prozessverständnisses und die Entwicklung modelltechnischer Strategien zur Ermöglichung einer belastbaren Prognose der Salzgruskompaktion im Hinblick auf den sicheren Einschluss.

Acknowledgement

The authors of BGE-TEC (FKZ 02E11708B), GRS (FKZ 02E11708A), IfG (FKZ 02E11708C) and TUC (FKZ 02E11708D) gratefully acknowledge the funding received by the Federal Ministry for Economic Affairs and Energy (BMWi), represented by the Project Management Agency Karlsruhe (PTKA).

The Sandia National Laboratory authors gratefully acknowledge funding from the U.S. Department of Energy. Sandia National Laboratories is a multimission laboratory managed and operated by National Technology & Engineering Solutions of Sandia, LLC, a wholly owned subsidiary of Honeywell International Inc., for the U.S. Department of Energy's National Nuclear Security Administration under contract DE-NA0003525. SAND2020-XXXX.

The project coordinator GRS is sincerely thankful for the good collaboration and fruitful discussions along the project lifetime with all project partners.

Table of Content

1 Introduction

Internationally, the most preferred solution for the safe disposal of heat-emitting radioactive waste is the storage in deep geological formations. Therefore, different types of host rock are considered which are in Europe: clay/claystone, crystalline rock and rock salt. With the new site selection law, entered into force as from 5th of July 2017, the German Federal Government started a new site selection process, considering all available host rocks for the disposal of radioactive waste. Especially in Germany, rock salt formations (flat-bedded salt and domal salt) are available for a possible repository and had been the objective of many research work during the last 40 years.

The German concept for a safe disposal is based on a multiple barrier system including the geological barrier, the sealing elements in shafts and drifts, backfilling of cavities and the waste packages. In particular, the access drifts and shafts must be backfilled and sealed for ensuring a safe containment of the radioactive waste. First, for a limited time period of 50,000 years the containment is ensured by the sealing elements which are composed of cementitious materials following the principle of diversity and redundancy. In the long-term, the safe containment of the radioactive waste is ensured by dry crushed salt used as backfill material for open cavities and wetted material as natural seals in the main access drifts. The crushed salt will be reconsolidated with time by the convergence of the surrounding host rock portions reaching a final state with the matrix properties comparable to the undisturbed host rock.

For a repository in rock salt crushed salt is the best solution for backfilling and sealing measures because of its favourable properties and its easy fabrication out of the excavated rock salt material. The rock salt possesses a special property, the creep behaviour, which leads to a backfill compaction with time by convergence of the openings. During the compaction, the crushed salts porosity is reduced from the initially relative high porosity of 30 – 40 % to a value which is comparable to the porosity of undisturbed rock salt (usually ≤ 1 %). In such low porosity ranges the technical impermeability is assumed.

The compaction behaviour of crushed salt is rather complex and involves several coupled thermo-hydro-mechanical processes /KRÖ 09/ /HAN 14/. It is influenced by internal properties, like mineralogy, grain size distribution and humidity as well as boundary conditions such as temperature, compaction rate or stress state. However, a quantitative understanding of the acting microstructural and THM-processes is still lacking.

For demonstration of long-term safety of the repository, numerical simulations with validated and verified numerical models describing the occurring processes are needed. The migration and release of radionuclides is strongly dependent on the compaction behaviour of crushed salt acting as the geotechnical long-term barrier, especially on the decrease of porosity and permeability in the seal elements, thus, the prediction of their evolutions is very important.

In the current state, the database and process understanding of the crushed salt reconsolidation have some important gaps in knowledge referring the material behaviour, existing laboratory data which mostly has been derived in oedometer test with loss of knowledge about the three-dimensional mechanical behaviour and referring the existing numerical models which still need to be verified and validated, especially in the range of low porosities /WIE 15/.

The objective of the project KOMPASS is the development of methods and strategies for the reduction of deficits in the prediction of crushed salt compaction leading to an improvement of the prognosis quality. It includes the development of experimental methods for determining crushed salt properties in the range of low porosities, the enhancement of process understanding and the investigation and development of existing numerical models.

First, the basics for the investigation of crushed salt compaction are outlined and its special properties are described. Further the function of crushed salt backfill in a repository is defined and some remarks on quality assurance are given (Section 2).

Section 3 outlines the importance of natural and technical analogues referred to the key uncertainty time scale for granular salt consolidation. The analogues are also referenced to the microstructural relevance of crushed salt and methods for the microstructural investigation of crushed salt material are described and first results are shown.

The experimental work is summarized in Section 4. In the beginning, a short overview of existing laboratory data is given and discussed. Since the compaction behaviour of crushed salt strongly depends on the material properties which differ for various rock salts, a synthetic material had to be chosen which is easily available and reproducible for experimental investigations during and also over the project phase. Therefore, a crushed salt from the Staßfurt-sequence in a bedded Zechstein salt formation was chosen and its microstructure investigated.

Most of the past experimental work was executed on crushed salt from domal formations. Since bedded salt is also considered as a possible host rock an oedometric characterization of present crushed salt material was done.

The loading history and its boundary conditions have an important influence on the structure and following on the consolidation behaviour of crushed salt. Thus, one focus of the project was on the development of pre-compaction methods which allow to produce crushed salt samples with a microstructure comparable to in-situ compacted material. Different methods were newly developed within the project and successfully executed.

Using the pre-compacted samples isostatic long-term compaction tests were executed in a Kármán triaxial cell. Additionally, two past experiments are described in this section which are chosen for a first numerical benchmarking.

Another focus of the project was to develop methods for the microstructural analysis of crushed salt material in different compaction states, since the grain and pore structure are strongly influencing the THM-coupled compaction behaviour. First results of microstructural investigations on pre-compacted and long-term compacted samples are shown in Section 4 and the methods are advanced so far that a verification is possible in future work.

Based on the results of Section 4, a proposal for an extended laboratory program for the systematic determination of the THM-coupled long-term behaviour of crushed salt was developed. The focus was on gaining a systematically structured database on the THM-coupled compaction behaviour by an isolated consideration of various processes and dependencies.

For a prediction of the long-term behaviour of a repository validated and verified numerical models are required. Existing crushed salt models are investigated, and differences are outlined in Section 5. For a deeper comparison the performances of the models are tested by a benchmark modelling of existing laboratory experiments.

Finally, the outcome of the project and future recommendations are described and outlined in Section 6.

2 Basics for the investigation of crushed salt compaction

2.1 The rock salt barrier - form of occurrence

Intact rock salt constitutes a tight barrier against gas and brine. Mining of underground openings results inherently in creation of an EDZ due to dilatant deformation in the cavity contour. The resulting permeability is significantly higher and ranges up to k = 10^{-15} m² to 10^{-14} m² (depending on the acting minimal stress) although the accompanied porosity increase is small, i. e. in the range of 0.1 –1 % (Fig. 2.1). The opening of pore space and the creation of pathways due to dilatant deformation is described as initial crack percolation process. If an interconnecting pore network is created the effect of further crack widening leads only to a moderate permeability increase despite a further porosity increase. Thus, the porosity/permeability ranges of dilatant salt and crushed salt aggregates overlaps. However, it's important to note that the reverse path of crack closure of the EDZ respectively crushed-salt consolidation is different to the dilatant-deformation path resulting in a hysteresis.

The efficiency of crack closure in the EDZ depends mainly on the site situation, e. g. if a dam as a stiff abutment is constructed, and the acting minimal stress increasing according to convergence. Such a crack sealing process can proceed within a time span of some months to a few years, or at most some decades (Fig. 2.2). It's worth to note that although the fissures are solely closed and not yet healed the damaged rock salt shows a permeability as low as intact rock salt if the fluid pressure criterion is met and constitutes a tight barrier. As well as in the case of intact rock salt the permeability of (slightly) damaged rock salt depends on the effective pore pressure if its barrier function is addressed i.e. in the case of fluid pressure (Fig. 2.3).

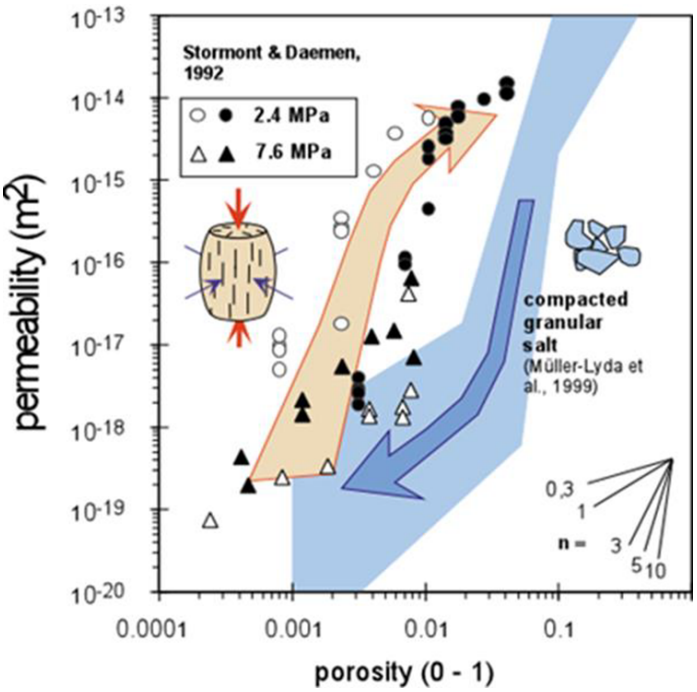

Fig. 2.1 Permeability – porosity relations of dilating rock and reconsolidating granular salt /HAN 14/

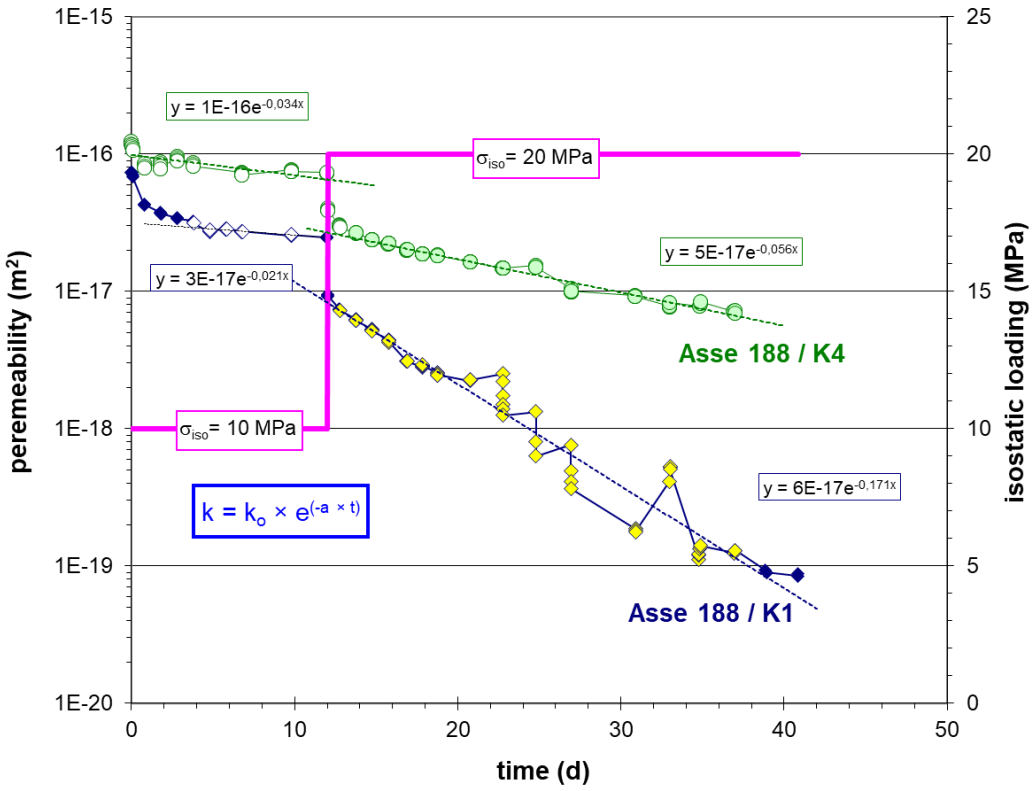

Fig. 2.2 Gas-permeability decrease of disturbed rock salt as function of time and effective stress /POP 07/

Crushed salt can be considered as a highly damaged rock salt barrier with high porosity. Experimental results show that it can be compacted to the same porosity range of 0.1 – 1.0 % typically for intact rock salt. If this low porosity range is reached highly compacted crushed salt's permeability shows the same magnitude order of $k < 10^{-20}$ m² as a re-consolidated EDZ (Fig. 2.2, Fig. 2.3).

Thus, the hypothesis is established that by the compaction of crushed salt a tight rock salt barrier may be re-established around a radioactive waste repository located inside a geological salt structure after a time span that depends on the convergence/stress state of the host rock´s location at one hand, the initial porosity of the crushed salt after emplacement and the backfill resistance against convergence and pressure build-up at the other hand. As a consequence, the conclusion is drawn that highly compacted crushed salt depends on functional relationships similar to slightly damaged rock salt and finally intact rock salt. This state of transition is of main interest when considering the re-establishment of the rock barrier by compaction of crushed salt.

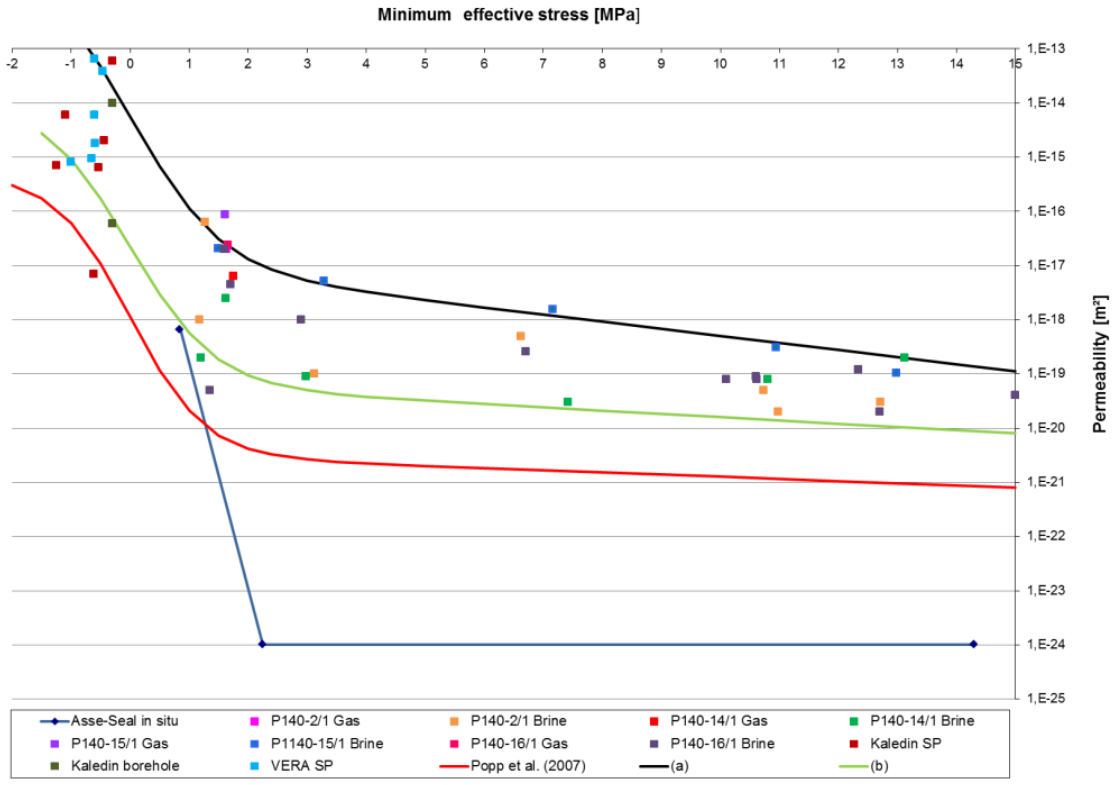

Fig. 2.3 Permeability to gas and brine of EDZ and contact zones as function of minimum effective stress /MUE 14/

2.2 Functions of crushed salt backfill

Although the barrier function of crushed salt is mainly considered, presently it has to be kept in mind that crushed salt backfill exhibits several functions in a radioactive waste repository in the operational phase as well as in the post closure phase. They are listed below, whereas function (1) – (6) are already discussed in /MLY 99/.

Operational phase:

1) Radiation protection
2) Fire protection
3) Explosion protection

Post-closure phase:

4) Heat transfer (starts in the operational phase and ends in the post closure phase)
5) Void volume reduction
6) Stabilization of mine openings
7) Re-establisment of the rock salt barrier

Function (7) is addressed since at least the safe confinement of radioactive waste within a containment bearing rock zone (CRZ) is required /BMU 17/.

Regarding the different functions (1) – (7) of crushed salt backfill main functions and other functions are distinguished for simplification issues. Requirements on crushed salt backfilling derived from main functions cover other functions which are not considered furthermore.

From the operational phase of the radioactive waste repository it turns out that the cross-section of the backfilled cavity must be closed, e.g. a gap at the roof due to settling is not permitted. If a gap is avoided reliably functions (1) - (3) of the operational phase are fulfilled as well as function (6) of the post-closure phase.

In principal, functions (4), (5), and (7) require a porosity as low as possible in order to maximize heat conductivity and to minimize void volume and permeability. As the porosity decreases with time it is evaluated which porosity state is most unfavorable to fulfil function (4), (5), and (7). In the case of function (5) “heat transfer”, the range of high porosity, i.e. the initial porosity, is of interest because heat conductivity is low at high porosity (Fig. 2.4) and for repository design agreement with the temperature criterion at

the container surface has to be demonstrated. Consequently, low porosity does not determine the repository design and was not investigated in the past. Furthermore Fig. 2.4 clearly shows the linear relationship of heat conductivity and porosity. Thus, the conclusion is drawn that impreciseness in the temperature prediction is small in the range of low porosity, too.

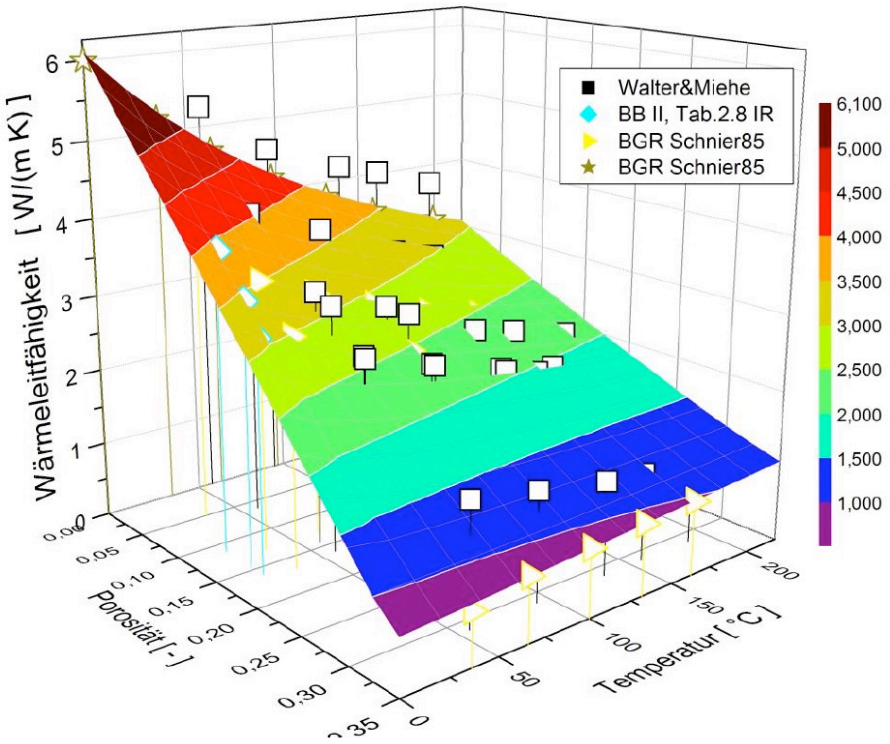

Fig. 2.4 Heat conductivity of crushed salt as a function of porosity and temperature /WIE 12/

In the past – before VSG was performed – function (5) "void volume reduction" covered very conservatively the long–term safety aspect of limited radionuclide release by

- Limiting the amount of brine being able to intrude into the repository and
- Constituting a barrier limiting radionuclide release according to the former radiation protection ordinance

To achieve this goal according to the former radiation protection ordinance a permeability k ~ 1E-14 m² was sufficient denoting a permeability range where permeability is strongly correlated to porosity (Fig. 2.5). In this context knowledge on the crushed salt´s compaction behavior in the high and medium porosity range was necessary in order to assess the amount of potentially contaminated brine squeezed out of the repository to check

whether the radiation protection goals were met. Thus, the initial porosity of the crushed salt and its compaction behaviour in the high and medium porosity range (40 – 10%) were investigated in research projects before safe confinement was required /BMU 10/. In this context several backfill technologies were tested in order to minimize the initial porosity.

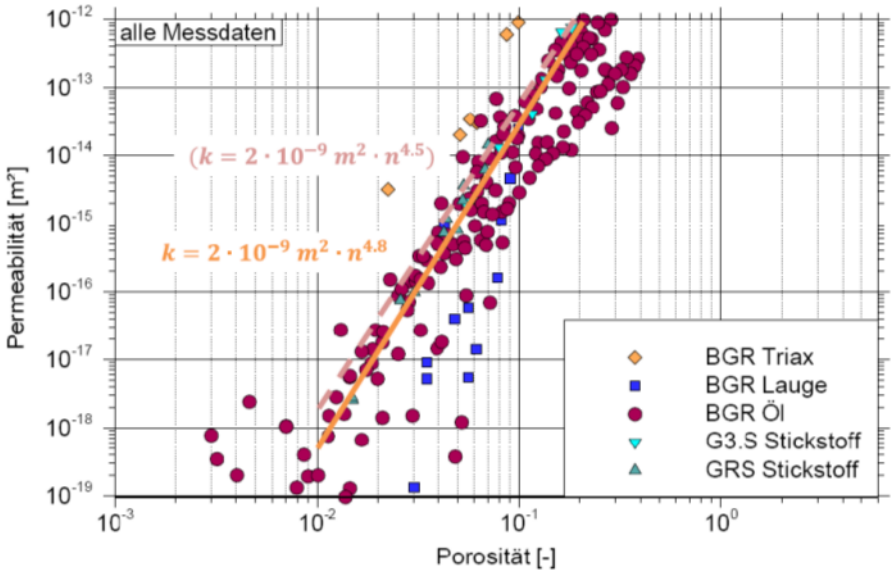

Fig. 2.5 Permeability versus porosity of crushed salt, curve fitting for a porosity – permeability relation /KRÖ 09/ /WIE 12/

Presently, function (7) "re-establishment of the rock salt barrier" became the main aspect of R&D due to the requirement of safe confinement. Obviously, the barrier function is related to the low porosity range well below 10 % (Fig. 2.5). The range of 5 – 1 % is of main interest (Fig. 2.6) because permeability decreases significantly below 5 % porosity converging to permeability values of intact rock salt (Fig. 2.6) and constitutes a tight barrier.

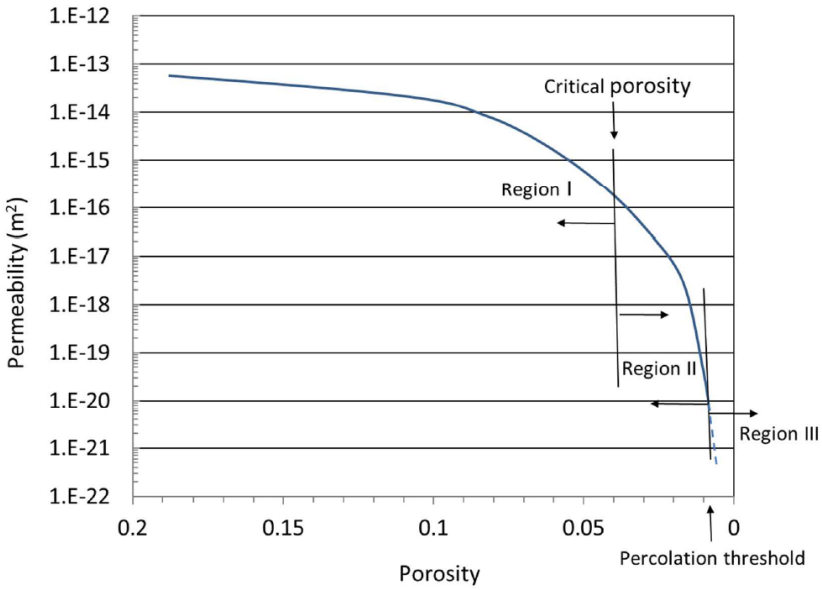

Fig. 2.6 Proposed generalized permeability – porosity response of crushed salt in response to consolidation /STO 17/

In this range however it seems that small variations of porosity lead to significant changes in permeability (Fig. 2.5). The data shown in Fig. 2.5 permit two interpretions. First, in the small porosity range the inaccurcy of the measurements cause the wide range of results. Second, the correlation between permeability and porosity is lost in the low porosity range and crushed salt behaves similar to (slightly) damaged rock salt. Then, permeability in the very low porosity range ~ 1 % is mainly a function of differential pressure (Fig. 2.3).

This transition from crushed salt to a low-porosity material (with transport properties comparable to slightly damaged rock salt has to be verified experimentally. Potential experimental setups and procedures are identified in Section 4 and their prerequisites are discussed.

Constitutive models applied to the high and medium porosity range must be checked to their ability to capture the low porosity range. They must be able to reproduce stress dependent behaviour as well as porosity dependent behaviour. Available constitutive models are considered with respect to their capability to capture the porosity stress transition in Section 5. Further, capabilities of availble constitutive models are demonstrated by benchmark calculations in order to test their capabilities in modelling practice.

2.3 Some remarks on quality assurance of crushed salt backfill during emplacement

In general, crushed salt is a favorite backfill material in salt mines because it can be produced by run-of-mine salt and is of low cost. Several emplacement technologies are available, e.g. pneumatic, slinger, and gravity stowing. As the initial porostiy should be rather low slinger stowing was selected as best available technology for backfill emplacement in drifts.

Within the TSS-experiment in the Asse mine crushed salt emplacement was tested using slinger truck technology /BEC 04/. The initial porosity of the emplaced crushed salt backfill lay in a range between 0.3 and 0.4. The mean value was calculated to 0.35 by recording the mass of emplaced backfill and the volume of the drift. The density of the salt was assumed 2160 kg/m³ uniformly (Tab. 2.1). For example, the range of the grain size distribution of emplaced naturally dry backfill within the TSS-experiment is given in Fig. 2.7.

Tab. 2.1 In-situ QA-data of crushed salt backfill within the TSS-Experiment /WIE 12/

	Southern drift	Northern drift
Backfill material [10^3 kg]	1,347	1,363
Drift volume [m^3]	963	966
Initial bulk density [kg/m^3]	1,399	1,411
Specified deviation [%]	+2 … -2.6	+2 … -2.6
Range of initial density [kg/m^3]	1,363 …1,427	1,374 … 1,439
Porosity [-]	0.34 … (0.35) … 0.37	0.33 … (0.35) … 0.36
Void ratio [-]	0.52 … (0.54) … 0.58	0.50 … (0.53) … 0.57

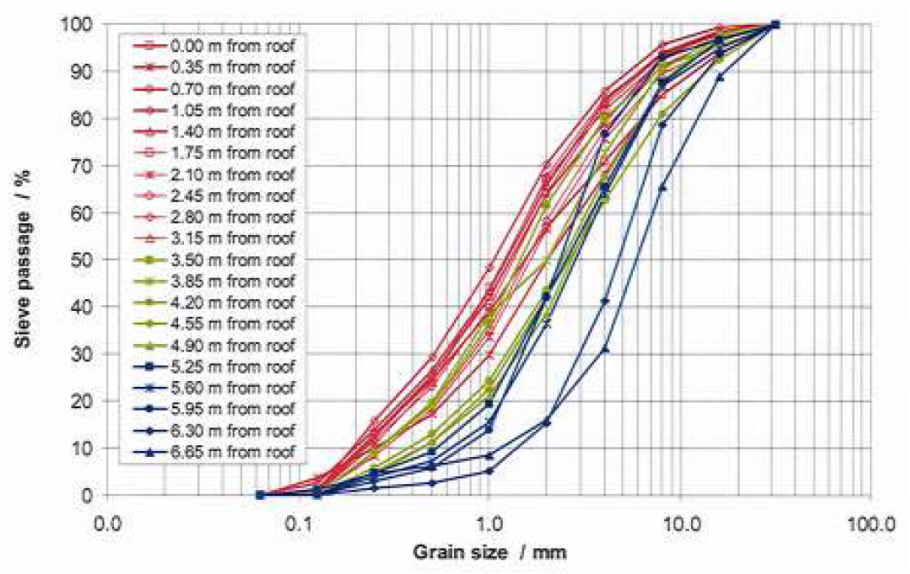

Fig. 2.7 Grain size distribution of 20 backfill samples taken from the top to the bottom over the whole backfill slope at the entrance of a drift /BEC 04/

Up to now, the following QA-measures were applied during emplacement of the crushed salt backfill:

- Initial porosity by recording mass of emplaced crushed salt and volume of cavity
- Grain size distribution curves

Furthermore, the following QA-measures may be applied if required

- Moisture content (surface moisture) /ENG 12/
- Mineral composition
- Emplacement temperature

It has to be kept in mind that these QA-measures describe the knowledge on the initial conditions of crushed salt after backfilling. The resulting uncertainties in initial conditions must be managed in the modelling approach.

3 Natural and technical analogues and microstructural relevance

This section describes the importance of natural and technical analogues referenced to the microstructural relevance of crushed salt, the methodology used in the microstructural investigations and lists additional techniques that have been applied in a salt context elsewhere. In general, it is distinguished between the examination of pores and grains (amount, shape, spatial and size distributions). The section further reports the achieved results by summarizing the found microstructural deformation indicators.

3.1 Importance of natural and technical analogues

A key uncertainty for granular salt consolidation is the necessary time scale reaching a state of residual porosity which ensures its function as technical and, fortunately, salt-specific long-term barrier for sealing necessary entrances (drifts or shafts) to the repository. Due to the limited duration of laboratory tests long-lasting a time gap exists to demonstrate that disaggregated salt readily consolidates into an impermeable solid under a wide range of modest stress and temperature conditions. On the other hand, experiences from conventional mining (over more than some 100 years) may act as technical analogues, that the applied emplacement techniques work, and that consolidation takes place, despite not optimized crushed salt mixtures are used. In addition, natural analogues, e.g. salt precipitation and consolidation processes, which formed historically the salt rock deposits, give strong empirical evidence that this process of densification in crushed salt works.

As argued by /HAN 17/ taking the state of the practice as a whole, including analogues, a robust concept for future salt repositories can put forward. The synopsis of analogues presented here gives a summary of already published information and new results. Although analogues are imperfect renditions of salt repository seal elements, long-term processes and properties of underground workings can be related to the functionality of salt repository seal systems, which amplifies the confidence that the seal works.

3.1.1 Natural analogues – primary genesis of salt rocks

Natural geologic deposits themselves provide evidence that high porosity evaporite crystals solidify readily into salt rock with negligible porosity. Petrography studies, as pub-

lished e.g. by /CAS 89/ and /WAR 06/, of modern saline pan halite and Quaternary shallow-buried (0 – 200 m) halite sediments demonstrate that the diagenetic modification of halite begins contemporaneously with deposition, is most intense within the upper few meters of burial, and is essentially complete within the first 45 m of burial or, at least, within 100 m. The phenomenological evolution of pore space during sedimentation is exemplarily shown for Dead Sea sediments in Fig. 3.1. The salt of the coastal Dead Sea area is revealed in 10.2 – 10.8 ka (10,200 – 10,800 years old). The halite layer was deposited during the Earlier Holocene, owing to the development of extremely arid conditions in the shrinking phase between the Lisan Lake and the present Dead Sea.

The initial processes of sedimentation probably include (1) evaporative concentration of groundwater brines and (2) cooling of surface brines when they sink below the sediment surface. At shallow burial depths, halites retain many textural features of 'mature' modern saline pan halite. Halites below the first few meters are no longer susceptible to dissolution from floodwaters but continue to be cemented by clear halite. Most important, the mechanisms for cementation and displacive growth of halite at shallow-burial depths are accompanied with a significant porosity loss due to early post depositional diagenetic cementation by clear halite. Other mechanisms of porosity loss by chemical or mechanical compaction were dismissed by /CAS 89/ for lack of evidence. However, in addition to these primary sedimentation processes of evaporite precipitation, most ancient evaporites show strong evidence of secondary or diagenetic textural overprints indicating displacive crystal growth, recrystallisation, back reactions and replacement of grains /WAR 06/.

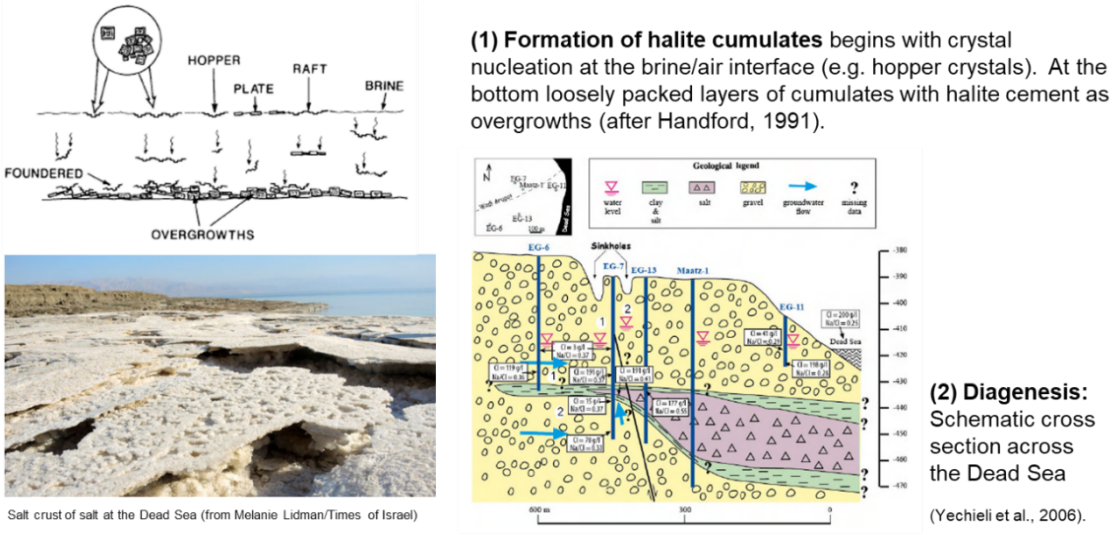

Fig. 3.1 Synoptic view of formation of halite beds (example: Dead Sea)

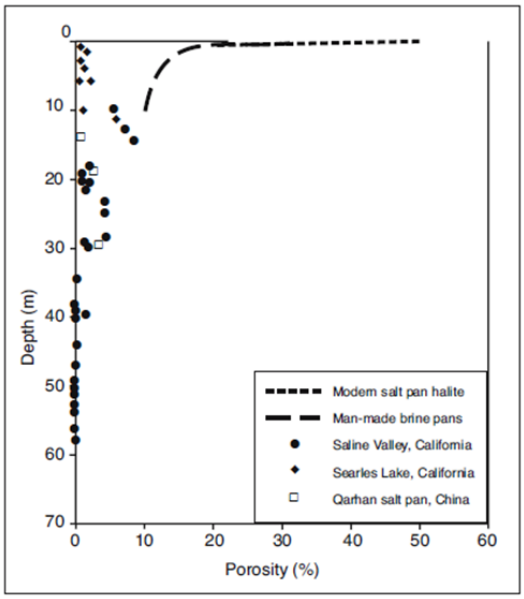

Fig. 3.2 Porosity in Quaternary halite beds versus depth /CAS 89/

In summary, independently from the acting process, it is generally accepted that pore space cementation reduces the porosity of halite crusts from more than 50 % near the surface to less than 10 %, within the first 10 m of burial /CAS 89/. The remaining pore spaces are completely filled by burial depths of approximately 45 m. This leads to a porosity value of essentially zero by 100 m depth (Fig. 3.2). Diagenetic processes will take place with further sedimentary sinking and, in addition, remaining fluids will be squeezed out at great depth and re-distributed in the deposit.

Thereby it is important, to note, e.g. by /CAS 89/, that undeformed halites from the Permian Salado and Rustler Formations of New Mexico contain delicate syndepositional textures and abundant clear halite cements that are comparable to those observed in modern saline pan halites and shallow-buried halites. The Permian halites are interpreted to have undergone a depositional and early diagenetic history similar to the modern and Quaternary analogs.

3.1.2 Natural analogues – diagenetic changes of petrophysical properties

The diagenetic induced loss of porosity, mainly due to mineralogical/chemical changes (cementation) and minor to textural effects (mechanical induced compaction) in the pore space of deposited salt aggregates is also documented in associated changes of petrophysical properties. /EZE 14/ investigated Dead Sea (DS) salt sediments measuring geophysical parameters such as compression wave velocities (Vp), shear waves (Vs) and

electrical resistivity (ρ_x) in laboratory and field conditions, and their relationship, in addition, to porosity / permeability interrelations.

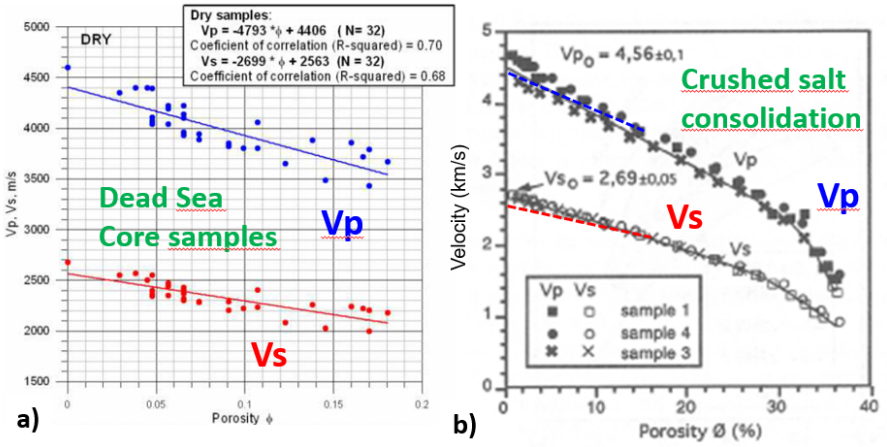

Fig. 3.3 Ultrasonic wave velocities vs porosity of consolidated halite. A) Core measurements from Quaternary halite beds of Dead Sea sediments (after /EZE 14/); b) Consolidation tests with syndeformational velocity measurements on table salt /POP 98/

Depending on the inherent porosity the ultrasonic wave velocities of core segments show a nearly linear trend of decrease, which nicely corresponds to earlier lab measurements during consolidation tests on table salt (Fig. 3.3). The velocity changes correspond to density changes in the range of 1,681 – 2,116 kg/m^3 in wet samples and between 1,638 – 2,106 kg/m^3 in dry samples /EZE 14/. The latter authors performed also permeability measurements on cores, which are depicted in Fig. 3.4a as single measurements and in Fig. 3.4b in relation to measurements presented in the framework of the REPOPERM II-project /KRÖ 17/.

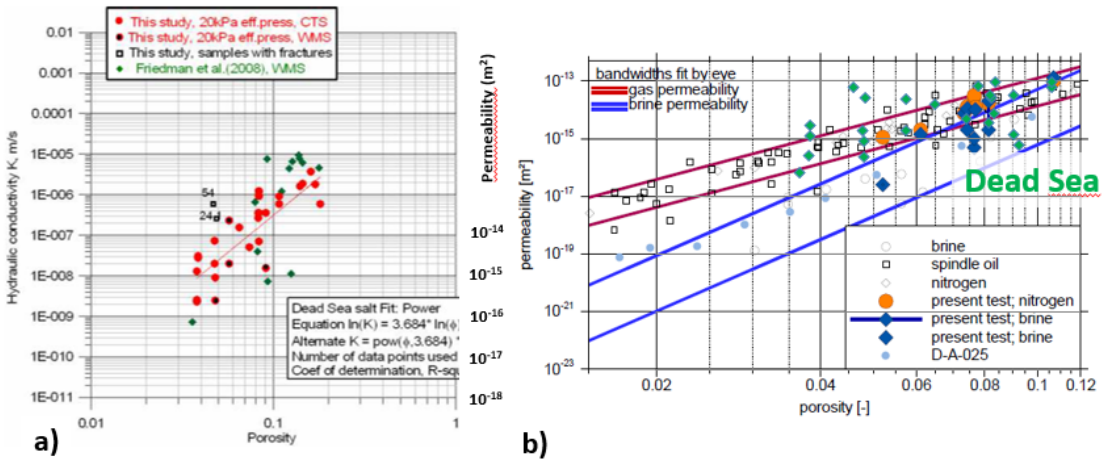

Fig. 3.4 Permeability / porosity relationships. a) core measurements from Quaternary halite beds of Dead Sea sediments (after /EZE 14/); b) lab measurements on crushed salt with single data and bandwidths, in addition, with the results from a) (modified after REPOPERM-data sets from /KRÖ 09/)

The core data show a significant scattering which is higher than values observed in the lab measurements on synthetical compacted material but, in general, the trend is more or less equal to that which was measured using gas. Importantly, lab measurements with brine show a different, significant lower permeability range related to the respective porosity. Although the reasons are not well understood the differences imply that not only mechanical compaction (e.g. grain fragmentation and/or intracrystalline deformation processes such as glide) are acting but also hydro-mechanical-chemical deformations mechanisms. In addition, if brine is used 2-phase-flow effects can occur which may pretend a low permeability. /KRÖ 09/ therefore attributed measurements carried out with the "inert" fluids (gas, oil), especially because of their agreement, as the "relevant" measured values (Fig. 3.4). However, for these measurements, even with a porosity of 1 %, the resulting permeability still varies between 10^{-17} and 10^{-18} m^2, which is comparatively high in view of necessary barrier function of crushed salt. In contrast, the permeabilities estimated for 1 % porosity, which are determined with the simultaneous action of the pressure solution processes, show a permeability that corresponds to that of virgin rock salt (< 10^{-22} m) (Fig. 3.4).

3.1.3 Technical analogues

In salt mines long-lasting experiences demonstrate that convergence of underground openings is a fact, due to the plastic salt behaviour, as shown by investigations of compacted backfill material /BRE 99/ /BRA08/. In addition, also closure of underground rooms associated with “self-backfill” processes are helpful as analogue studies.

The initial drift state of drift closure is characterized by significant contour damage resulting in spalling and brecciation of the salt with fragments, usually of different grain sizes between several decimetres to centimetres. The average residual porosity of this “self”-backfill is estimated in the order of < 30 % which is assumed to be progressively reduced due to the time and stress dependent convergence, ending probably in a state comparable to the virgin salt mass. However, the degree of closure and the time dependence of this “self-backfill” process are unknown. Depending on the site conditions this could be a very efficient process as it was demonstrated in the underground vicinities of the Teutschenthal mine (D), where old drifts were re-mined (for details see /POP 18/). Although the following observations are made for underground openings in the potash seam with carnallite bearing rocks (and not in rock salt environment) it represents in general salt properties which are characterized by creep, amplified by humidity effects. Thus, the case situation at the Teutschenthal mine may act as a technical analogue of crushed salt consolidation.

The former potash salt mine Teutschenthal is operated by the company GTS (Grube Teutschenthal Sicherungs GmbH & Co. KG), performing back-filling operations as stabilization measures to avoid rock bursts. For backfilling of the former mining chambers, it becomes necessary that GTS has to work over the access drifts because they are progressively closed in the vicinity of the collapsed mining East field mining area. Due to the acting convergence, amplified by the high-stress zone around the collapsed mine areas the self-backfill in the former drifts looks qualitatively like the undisturbed host rock (Fig. 3.5). Only, larger salt fragments indicate the brecciated nature of the material due to the acting convergence. However, since self-sealing respectively -healing is attributed to the development of cohesion and tightness between formerly crushed salt fragments created during contour disturbance, the current conditions observed in the Teutschenthal mine offer a unique opportunity to proof the general assumption of self-healing capacity of salt rocks. As parameter, strength as well as permeability testing was performed after sampling several big rock blocks (0.4 m x 0.4 m x 0.4 m) from the massif exposed in the former drift.

Fig. 3.5 Image of re-mining a completely closed former access drift with a road-header situated close to the collapsed East field at Teutschenthal. The originally several square-meters cross-sectional area is converged, as indicated by impurities around the former drift contour, Image of re-mining a completely closed former access drift with a road-header situated close to the collapsed East field. The originally several square-meters cross-sectional area is converged, as indicated by impurities around the former drift contour, and, a significant floor-heave occurred, as is documented by the encapsulated wirelines.

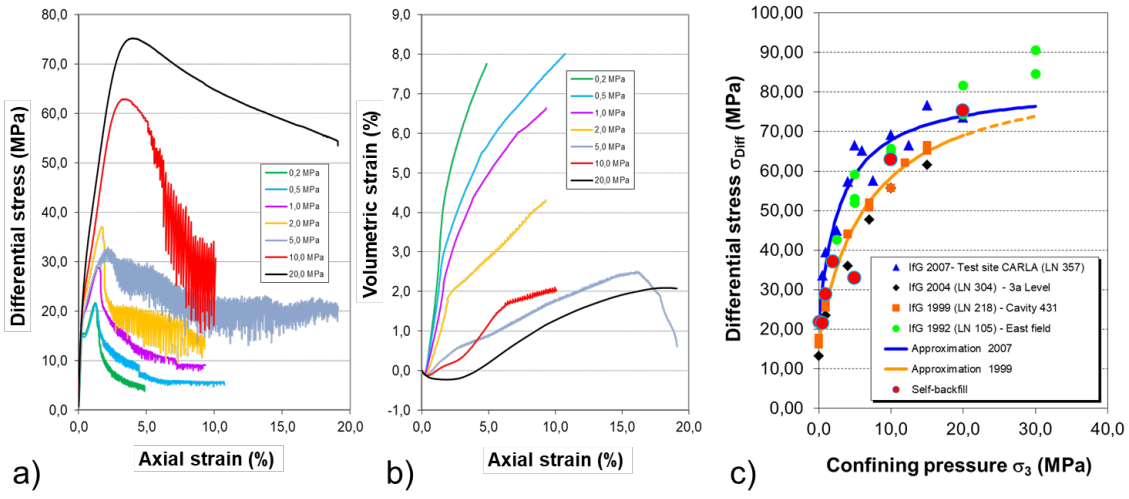

Fig. 3.6 Summary of triaxial strength test on re-compacted self-backfill samples at 23 °C. a) stress- and b) dilatancy-curves as a function of axial strain. c) Evaluation of the general strength and dilatancy behaviour in comparison to triaxial failure strength boundaries as a function of confining pressure (σ_1 vs σ_3) of camallitite from various locations at the Teutschenthal mine.

The material-specific stress-strain and dilatancy behaviour of the re-consolidated carnallitite material was measured with a servo-hydraulic testing machine of the IfG (Fig. 3.6). Seven triaxial compression tests were carried out by applying confining pressures in the range of $1 \leq \sigma_3 \leq 15$ MPa with a constant deformation rate of $\dot{\varepsilon} = 2.5 \cdot 10^{-5}\ 1/s$. The test samples showed the well-known brittle behaviour of natural carnallitite, i.e. macroscopically no difference to virgin rock material was visible. This is confirmed if the respective strength and dilatancy data are compared with existing data sets, which IfG has determined from triaxial strength test series of material sampled at various sites in the mining field of Teutschenthal. The rock mechanical properties of tachyhydrite bearing carnallitite are variable, but the data of the re-consolidated material lie in the usual range of data scattering.

In addition, gas permeability testing was performed on two rock specimens. In both tests initial permeability-values in the order between 10^{-18} m^2 to 10^{-19} m^2 were measured at hydrostatic confinement of 5 MPa. Increase of confining pressure up to 10 MPa, followed by a waiting period of 12 hours lowered the permeability by more than 2 orders. This clearly confirms the establishment of intact rock properties.

3.2 Microstructural processes and hydromechanical interactions

Models that reproduce the actual material behaviour during crushed salt reconsolidation need to be based on a sound understanding of the governing microstructural processes. Similar to intact salt, experimental work on granular salt began in the 1970's, and this work largely focused on the use of granular salt as backfill material in a waste repository. Because the deformation of both intact and granular salt varies with time, many experimental studies have focused on understanding the rate-dependent deformation of these materials. The mechanical processes and hydromechanical interactions in question have been recently discussed in detail by /HAN 14/ which is summarized in the following paragraphs. As prerequisite methods of microstructural investigations are described, which delivers an understanding of relevant microstructural processes and complex hydro-mechanical interactions during granular salt reconsolidation. This information provides the fundamental underpinnings for describing the evolution of the crushed salt seal element from a porous material into the equivalent of an impermeable solid.

3.2.1 Overview of experimental methods

In the scope of this report, results from light microscopy investigations by BGR and Sandia are presented (compare also work from /HAN 97/, /SCH 04/, /HAN 14/, /HAN 16/, /THI 16/, /KRÖ 17/ and /MIL 18/). However, BGR recently also accomplished Scanning Electron Microscopy (SEM) (compare to /PEN 07/, /THI 16/, /KRÖ 17/, /MIL 18/) and Computed X-Ray Tomography (CT) (compare to /KRÖ 17/), on which will be reported in an upcoming study. Next to these methods, there are also techniques of gamma-ray decoration, Electron BackScattered Diffraction (EBSD), low-angle Ion-etching by Broad-Ion-Beam (BIB) milling and etching of thick sections by a slightly undersaturated NaCl-solution, all of which help in identifying sub-grain boundaries. Focussed-Ion-Beam (FIB) and microtome tools can help in Transmission Electron Microscopy (TEM) preparation to get a high-resolution insight to crystal structures such as lattice plane widths and intracrystal compaction fringes. Energy-dispersive X-ray spectroscopy gives insight to the spatial distribution of elements, while X-ray crystallography identifies mineral phases. This list gives an overview only and is by no means exhaustive.

3.2.2 Optical microscopy

Identification of the acting microstructural mechanisms, as illustrated in the following, results mainly from classical light microscopy investigations performed by Sandia and BGR in the framework of KOMPASS. Capped thin sections (~5x7 cm, ~30 µm thick) and polished thick sections (~ 250 µm) are prepared for polarization microscopy. Microstructures were evaluated on parts of the prepared samples (~ 5x5 mm to ~ 300x300 µm), with a resolution in the order of ~ 1 – 10 µm /DES13/. Therein, the original samples were inevitably destroyed during the preparation process, so that only post-mortem analysis was possible.

The optical microscopes used were a Zeiss AxioScope 5, equipped with ZenCore imaging software (Sandia) and a LEITZ DMRM with the microscope-camera Leica DPC 450C (BGR). The following 10 features can be distinguished: (1) grain and (2) pore sizes as well as (3) grain and (4) pore shapes, (5) deformation indicators, such as (6) grain contacts, (7) cracks and (8) micro faults, (9) impurities and (10) fluid inclusions. These features help in the identification and quantification of deformation mechanisms, such as cataclasis, diffuse mass transfer by dissolution, neoformation or intracrystalline plasticity (Section 3.2.3, /BLE 02/).

3.2.2.1 Sample preparation by Sandia

To prepare thick sections, specifically for reflected light analysis, the samples were prepared as follows. First, the small oedometer samples were cut into slabs length wise, using a low damage Isomet saw with isopropanol as the cutting fluid. This was to maintain the variable porosity profile. Due to the overall length of the sample profile, two thick sections were fabricated from each sample slab; top to middle and middle to bottom. After cutting adequately sized blocks for a standard thin section, they were each vacuum impregnated with a two-part epoxy with added rhodamine B dye for contrast. A semi-automatic grinder/polisher was used first with 600 grit SiC paper to create a parallel surface, followed by 1200 grit, both with alcohol-based lubricant. The polishing steps are outlined in Tab. 3.1, and also used an alcohol-based lubricant for each diamond suspension. After each polishing step, the thick sections were cleaned in an ultrasonic bath of isopropanol. The large oedometer cell sub-sample sections were made similarly, however, profile orientation was not as meticulous.

Tab. 3.1 Polishing steps used for thick section preparation

Step	Surface and Suspension	Speed (RPM) Head/platen	Normal Force [N]	Time [min]
1	Non-woven pressed, 9 μm diamond	50/100	10	5
2	Soft woven synthetic, 3 μm diamond	50/100	10	10
3	Soft woven synthetic, ¼ μm diamond	30/50	5	5

3.2.2.2 Sample preparation by BGR

Capped thin sections (~5x7 cm, ~30 µm thick) were prepared for reflected light microscopy. All sawing (band saw) and polishing (polishing machine TF 250, comp. JEAN WIRTZ) were performed dry. For coloured resin impregnations, Araldite 2020 A / B, comp. Huntsman with EpoDye, comp. Struers was used under low vacuum (~30 minutes).

The uncompacted crushed salt was moulded into blocks of coloured resin first, which were glued on glass slides for cutting and polishing. The compacted crushed salt was also saturated with coloured two-component resin first. Subsequently, the dried samples (24 h drying time) were glued (24 h at 35 °C, using an adhesive press) on polished glass

slides, then cut (fine band saw, comp. EXAKT) and polished (polishing machine Mikroschleifsystem 400CS, comp. EXAKT).

3.2.3 Fundamentals: Deformation mechanisms – dry/wet conditions

Mechanisms of salt densification have been extensively described in the literature as cited throughout (see above). As illustrated in Fig. 3.7, micromechanical processes depend on many external boundary conditions and extant internal conditions. The initial porosity of a disaggregated natural geomaterial, including salt, is usually between 30 and 40 %. Granular salt consolidation is essentially pore volume reduction, where the amount and nature of final pore volume depends on multiple factors. Time dependent granular salt consolidation results primary from the acting stress and can be significantly amplified with increasing fluid content. Factors of secondary importance are temperature, grain size distribution and quantity of impurities (e.g. clay, anhydrite).

Under in-situ conditions, the convergence of the mine openings (drifts or shafts) provides the driving boundary condition for the operative processes. Material properties of the consolidating mass are inextricably tied to the inward creep of the native formation, that means granular salt reconsolidation results directly from time-dependent deformation processes in the surrounding salt. The convergence itself is increasingly influenced by reduction of the backfill porosity and attendant stress increase in the backfill.

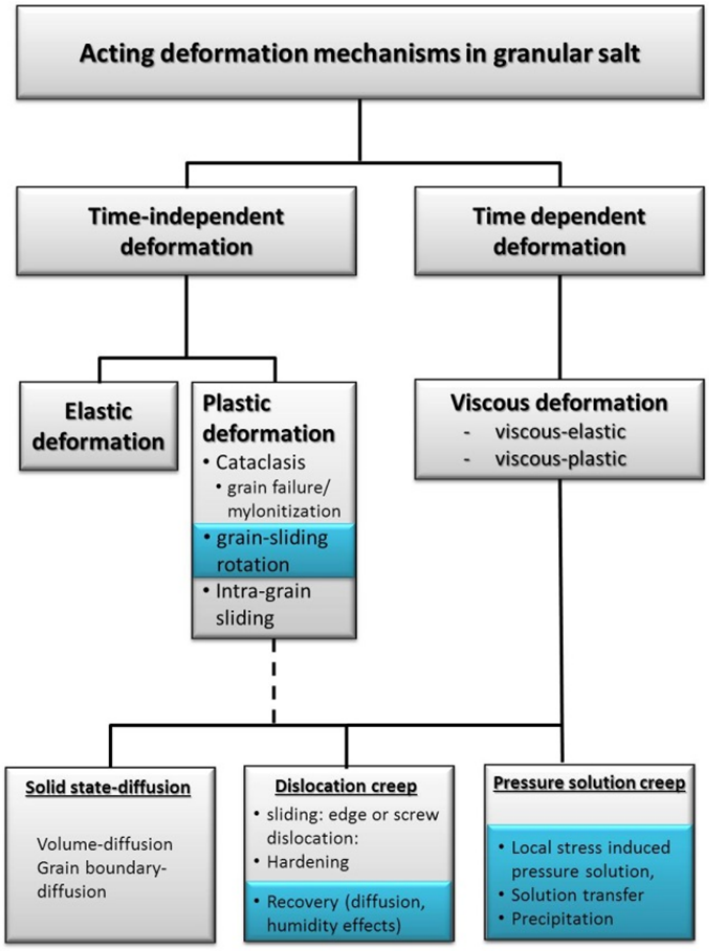

Fig. 3.7 Acting deformation mechanisms in salt (modified after /ELL 03/)

The complexity of deformation mechanisms during crushed salt consolidation is illustrated by exemplary microstructural investigations performed on thin sections prepared from uncompacted and compacted crushed salt showing a variety of microstructures. In the following the fundamental deformation mechanisms and structures for the Sondershausen material are presented, sorted by following the classification scheme of Blenkinsop /BLE 02/.

The convergence-driven consolidation sequence of crushed salt proceeds thusly. Initial compaction processes at high porosity are accomplished by brittle processes involving instantaneous grain rearrangement (e.g., grain sliding and rotation) and cataclasis (brittle failure of grains due to local stress concentrations or frictional slip):

- Cataclasis / microcracking
  - Intragranular Microcracks (Fig. 4.7 to Fig. 4.50)
  - Microfaults (en-échelon, Fig. 4.4, Fig. 4.7 and Fig. 4.51)
  - Trans-granular Microcracks (particle breakage, Fig. 4.7 and Fig. 4.52)

- Intracrystalline plasticity
    - Bended, unbroken grains (Fig. 4.58)
    - Compaction fringes (Fig. 4.56)
    - Bended grain boundaries (Fig. 4.58)

With progressive consolidation, i.e. as void space is eliminated, the main acting mechanisms change whereby differences in microstructure become obvious between samples tested at high and low stresses and, especially, if free water is available, as demonstrated by studies of /SPI 93/:

- wet material densified at stresses below 5 MPa, abundant grain-to-grain indentations and contact truncations were observed, and little evidence was found in these samples for plastic deformation or for marginal dissolution or undercutting at grain contacts
- occasional evidence was found for grain boundary migration and contact cataclasis in highly compacted samples tested at 4.2 MPa
- in the wet-densified samples tested at 6-8 MPa microstructures and overgrowths were widely developed in the pores

In foregoing investigations several potential deformation mechanisms in the low-porosity range were already identified but the individual importance or contribution to the overall deformation is unknown:

- *Intracrystalline deformation mechanisms* similar to those acting in natural salt, including dislocation multiplication, glide, cross slip, climb. During natural salt deformation hardening occurs via lattice distortion and obstructed movement of dislocations as indicated by increasing dislocation density. Because the creep mechanisms are thermally activated recovery processes may take place at higher temperatures. In addition, stress recovery due to humidity may play a major role.
- *Pressure solution creep*; Highly stressed parts of halite grains, such as domains adjacent to grain contacts, are prone for being dissolved. The dissolved material can be transported and removed by grain boundary fluids finally becoming redeposited from the latter at sites of low stress e.g. /SCH 99/; /URA 07/.
- *Dynamic recrystallization* in terms of (strain-induced) grain boundary migration (GBM) (e.g. /URA 86/) plays a significant role for the plastic deformation of salt grains. GBM is driven by differences in dislocation density across grain boundaries and significantly supported by grain boundary fluids /PEA 01/; /URA 07/.

At given stress conditions brine content seems to be the key factor which varies with respect to formation and impurity quantities. Bedded salt formations tend to have elevated impurities thereby increasing brine content from a few thousandth to several weight percent /FIN 92/. Domal formations nominally have less brine (0.01 to 0.1 wt.%) /ROE 81/ and minor amounts of impurities.

In granular salt aggregates pressure-solution creep and plasticity-coupled pressure solution are considered to be the important mechanisms, as schematically illustrated in Fig. 4.57. If moisture is available in the contact area, even very small amounts are sufficient to activate pressure solution processes characterised by material dissolution and reprecipitation. In addition, fluid assisted grain boundary migration is an efficient process of reducing dislocation density and hence removing the stored energy of dislocations, even at room temperature. Thus, the grain boundary diffusional pressure mechanism dramatically enhances the densification rate in the crushed salt /SPI 90/; /CAL 96/; /CAL 98/.

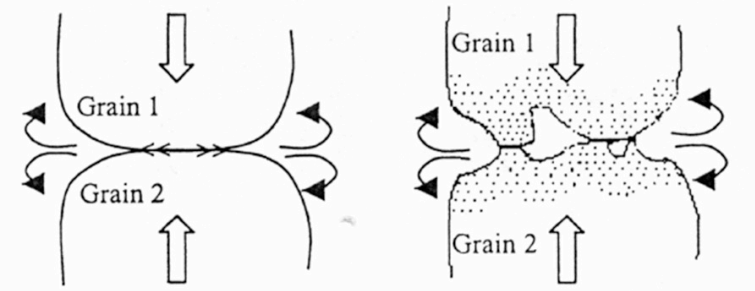

Fig. 3.8 Schematic representation of pressure solution. Left: Grain boundary diffusional pressure mechanism; Right: Plasticity-coupled pressure mechanism with plastically-deformed region shaded. Figure taken from /HAN 14/

Occurrence of fluids in the virgin salt and, in addition, comparable deformation structures were identified in the Sondershausen material:

- Diffusive mass transfer by solution
    - Fluid inclusions
        - Planes (Fig. 4.5, Fig. 4.7 and Fig. 4.53)
        - Lines (Fig. 4.6, Fig. 4.7 and Fig. 4.51)
        - Connected fluid inclusions (Fig. 4.55)
    - Grains with rounded edges and even, flush grain-to-grain contacts (indicator for pressure solution, Fig. 3.8 and Fig. 4.56 /HAN 14/)

In summary, because the above described processes have been documented in laboratory experiments on natural and artificial salt aggregates and in deformed natural salt,

they can be attributed as a fact, i.e., ambient reconsolidation of granular salt with a small amount of moisture is well understood mechanistically as underpinned by large-scale tests, laboratory measurements, and microscopic documentation of deformational processes. Empirical evidence indicates that fluid-aided processes will be operative in typical bedded salt as porosity reduces below 10 %, even if no construction moisture is added. Nominally, domal salt contains much less moisture than bedded salt, so enhanced compaction and reconsolidation may be facilitated by addition of small amounts of water during construction. As cited throughout this paper, observations concerned with bedded salt show adequate moisture from negative crystals, grain boundary fluid and hydrous minerals to sustain fluid-assisted processes.

3.2.4 Synoptic view of hydro-mechanical interactions and microstructure

One of the key technical issues concerning properties of reconsolidating granular salt is the mobility of fluids in the residual pore space. It is well known from nature and laboratory experiments that small amounts of residual brine will be present at grain boundaries in granular salt. Intact salt grains exhibit thin fluid films with a thickness of a few nanometres, which can be seen under the microscope as channels or pores. Grain boundary structure is believed to change during dynamic recrystallization in presence of fluids, such that grain boundary migration is assisted by thin fluid films residing on the grain boundaries /URA 86/, /DRU 90/.

In addition to mechanical aspects, grain boundaries play a critical role in percolation phenomena within rocks referring to its hydraulically integrity /GHA 15/. The presence of brine strongly affects microstructural evolution and the mechanical and transport properties of the material (e.g. /SCH 06/), although the structure of the halite grain boundaries which contain water is still a matter of debate. One model proposes a thin fluid film transmits the contact stress, therefore diffusion transports dissolved material. On the other hand, the thin film fluids may be squeezed out resulting in islands of solid-solid contact, through which the contact stresses are transmitted. Water-filled channels surround islands of solid-solid contact and are conduits through which material diffuses.

A simplified summary, suggested by Christopher Spiers (personal communication with Till Popp), microscopic findings provide a consistent picture of fluid distribution and mobility inside granular aggregates, as schematically shown in Fig. 3.9. The nominal 35 % void space is almost completely air-filled, which stands in strong contrast to the intact state of natural salt: both, negligible moisture content (up to 1.0 wt. %) and porosity. If

granular salt is wetted to improve compaction and reconsolidation behaviour, the secondary moisture is mainly distributed at salt grain surfaces as a thin wetting solution film or isolated as fluid droplets in grain interstices. Intracrystalline fluid inclusions captured during crystallization from the formation waters would remain inside the crystal structure, perhaps to be moved to the grain boundary by crystal plasticity. During isostatic compaction salt is transported by fluid-assisted diffusion processes, specifically dissolution and precipitation due to differences in chemical potential between points in the solid at grain boundaries under high stress and those under lower stress (Fig. 3.9). As mentioned before, additional driving force (chemical potential drop) both along and across grain boundaries can be provided by internal plastic deformation of the grains, giving rise to combined grain boundary migration and solution-precipitation creep.

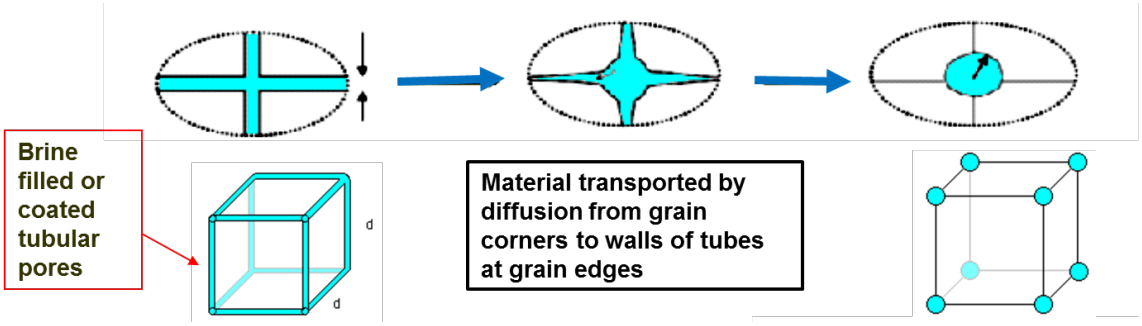

Fig. 3.9 Schematic of fluid redistribution in granular aggregates during compaction. (left) initial situation with cubic grains and pore fluid channels along cube edges; (right) isolated spheres at cube corners.

However, there is experimental evidence from analogue investigations on crystalline materials that the fluid topology in a low porosity mono-phase polycrystalline aggregate (as it is the case for crushed salt) is controlled by the balance between solid-solid and solid-fluid interfacial energies, and hence the dihedral angle θ (e.g. /HOL 97/). In the case of $\theta > 60°$ the fluids will be present inside isolated inclusions, whereas for $\theta < 60°$ the fluid forms an interconnected network of grain boundary triple junctions. Based on this approach /GHA 15/ postulated that even natural salt may become permeable at specific PT-conditions. However, this assumption is only based on theoretical considerations which correspond not to the reality. It is a fact that natural salt rocks remain tight, also at these PT-conditions, as argued already in the respective statement of the DAEF /DAE 16/ and as it was recently experimentally demonstrated in the research project PeTroS /IFG 20/.

Referring to crushed salt conditions there is no doubt that if the fluids existing in the primary pore space (mostly air and water vapor) are compressed, they may be partially

squeezed out during the transition to a low-pore-space regime. However, migration out of the consolidating material continues as long as a connected porosity and adequate permeability exists. All observations confirm effective reconsolidation until only a few % porosity remains. At that point, the relative saturation within the intergranular pore space increases. As the granular salt continues to consolidate, further fluid transport out of the consolidating mass would undoubtedly involve two-phase flow of both brine and trapped air. Empirical results indicate that intrinsic medium permeability approaches zero as the porosity of the consolidating salt reduces /HAN 14/. As this condition is approached the brine or air effective permeability are even lower than the intrinsic permeability and the mobility of fluids in highly compressed salt is very low. Of course, this range of conditions is very challenging to interrogate experimentally and remains an area of active research.

4 Experimental work

4.1 Overview and discussion of existing experimental database

The laboratory investigations on crushed salt compaction carried out in the past years have been extensively documented in the literature and described in summary form /KRÖ 09/ /WIE 17/. As a consequence, and with reference to selected sources /KOR 96/, /CAL 99/, /BEC 99/, /BEC 04/, /KRÖ 09/, /KRÖ 17/, /WIE 17/, /LAM 18/ a repetitive presentation can be dispensed with. The evaluations within the scope of the present research report are rather limited to those aspects which were of particular importance in the subsequently documented planning of the demanded laboratory test program. Fig. 4.1 shows a striking sketch of the historical development of the focal points, objectives and results of selected studies on crushed salt compaction.

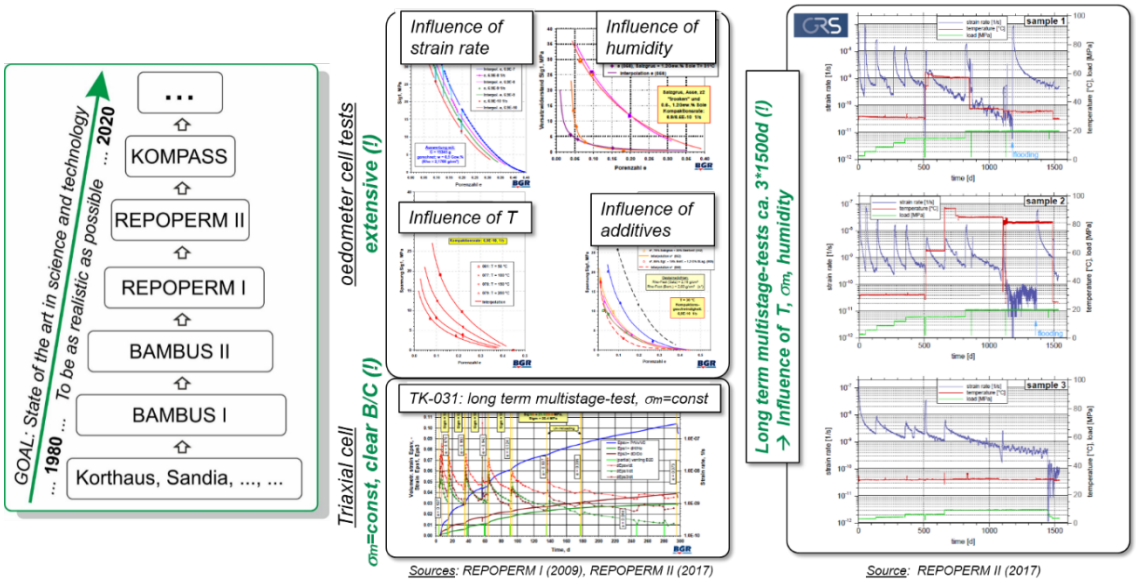

Fig. 4.1 History of selected projects on the material behaviour of crushed salt

Fundamental experience from completed projects on crushed salt compaction can be characterized by:

- The extensive oedometer tests carried out in the past have identified important factors influencing the compaction process and allow a rough quantitative assessment of the respective influencing factor on the compaction behaviour.
- A major disadvantage of the oedometer tests, as described above, is the fact that the test results can only be used to a limited extent for the validation of functional relationships and for the determination of constitutive model-related parameters

and to an even lesser extent for the (further) development of constitutive models. The reason for this is the way in which the tests are carried out, in which on the one hand the boundary conditions are not completely known, since the confining stress is usually not measured, and on the other hand the processes are superimposed in such a way that the isolation of individual processes for clear assignment and interpretation is hardly possible. While the first disadvantage can be remedied by monitoring the horizontal stress by measurement, the second disadvantage remains in principle, since active control of the horizontal stress in the oedometer test is not possible by design.

Fig. 4.2 shows a comparison of the mechanical processes in the oedometer test and in the triaxial test. The advantage of the triaxial tests is a higher flexibility of the possible load paths and the resulting possibility of a specific isolation of individual processes or influencing factors.

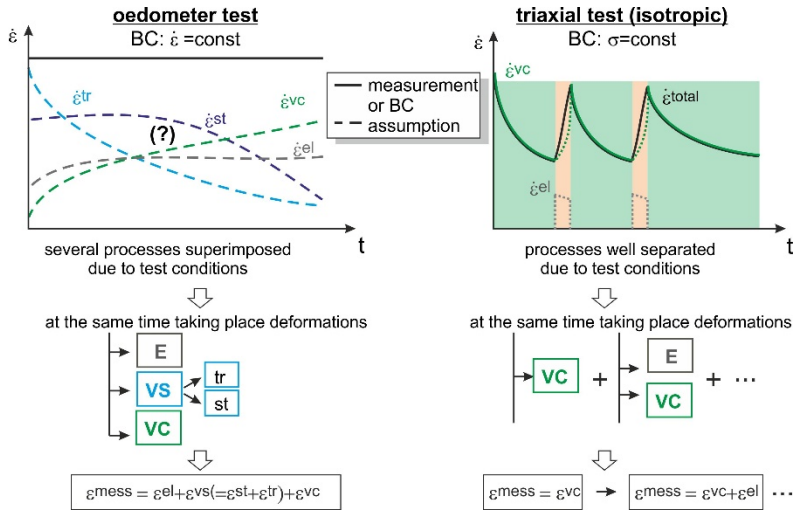

Fig. 4.2 Comparison sketch of the mechanical processes in an oedometer test and in a triaxial test

The number of currently available triaxial experiments on crushed salt compaction is comparatively small. The above statement applies in particular to triaxial tests for long-term crushed salt compaction with small porosities of less than 5 %. The same statement applies to experimental data on the dependence of permeability and porosity. Based on the aforesaid collocation of experience regarding experimental data appropriate to analyse and validate in detail the load bearing behaviour of crushed salt in space and time, merely two triaxial test conducted by BGR and one triaxial test conducted by TUC on crushed salt samples have been estimated to be appropriate for further investigations into the suitability and validation of currently available constitutive models to image the

thermal-hydraulically-mechanic coupled behaviour of crushed salt taken into account the new demands induced by the concept of an isolating rock zone. The tests mentioned above, named TK-031 and TK-033 will be documented, described and integrated within the approach for an experimental laboratory program, appropriate to analyse and quantify systematically the dependencies between crushed salt compaction and stress level, stress geometry, mean stress, deviatoric stress, stress rate respectively strain rate, etc. in the following chapters.

4.2 Material selection

4.2.1 Synthetic crushed salt mixture /lithological reference parameters

Compacted crushed salt is most advantageous as backfill and long-term sealing material for closure measures of underground openings in salt formations. Because of its lithological characteristics it guarantees a maximum of compatibility with the host rock and, in addition, it is easily available as residual material during underground excavation. However, its compaction behavior depends primarily on the material conditions at the site, e.g. regarding lithological composition (e.g. NaCl-content and impurities, such as anhydrite or clay) and humidity. Whereas domal salt is attributed to be naturally dry (e.g. around 0,02 wt.-% for the Gorleben-Hauptsalz) may bedded salt has significant higher water content (between 0.1 and > 1 wt.-%). In addition, also the type of recovery during underground working (e.g. cutting with a rod-header or blasting) and further conditioning, e.g. sieving, grain surface wetting or adding additives, like clay, will have an important impact with respect to the grain size distribution and intergranular conditions. Thus, the pre-selection of granular salt material is a prerequisite for the experimental work.

The following guiding principles underlie the choice of the KOMPASS-reference material:

- easy availability and permanent reproducibility of the relevant properties, e.g. grain size distribution and water content:

  With respect to later investigations a crushed salt material has to be selected, that could act as a reference material for the different experimental investigations, not only in the KOMPASS-project but also for other generic investigations.

- preferred investigation of crushed salt from a bedded salt formation:

In the past, in Germany most long-term compaction tests have been carried out with material from steep inclined salt structures, i.e. mainly from the Asse mine and with respect to the Gorleben site but with different material properties, e.g. grain size distributions and humidity content /KRÖ 17/.
However, due to its favored properties the Staßfurt-formation seems to be the most promising host rock for a repository (independently, if domal or bedded salt will be considered in the future).

– establishing a preferred grain size distribution, i.e. the used sieve line with special respect to the role of the over-sized grains (maximum grain size):

  As shown in past studies, e.g. in the framework of the REPOPERM projects, the backfill resistance of mined grain size fractions for drift backfilling (e.g. recovered by a road header with a maximum grain size d = 31.5 mm) is quite similar to a material where grain size fractions larger than 8 mm have been removed (e.g. DEBORA material). This confirms the assumption that the compaction behavior is largely controlled by the grain fractions of little grain diameters, i.e. the over-sized grains are only swimming in the matrix[1].

➔ Selection of commercially available salt fractions from the GSES-salt mine, which represents the Staßfurt-sequence in a bedded Zechstein salt formation[2].

➔ Optimization of the grain size distribution with preparation of a synthetic crushed salt mixture. The maximum grain size to 8 mm was set to 8 mm, which also facilitates the use of smaller the specimen sizes.

[1] The use of oversized grains has also some drawbacks from the experimental point of view. For example, the investigations of /GLA 16/ demonstrate, that the coarse fraction of such mixtures clearly tends to segregate due to handling of the material during production and installation. Furthermore, thin section investigations on highly compacted samples showed a tendency for the oversized fraction to break which finally results in smaller grain size fractions.

[2] The GSES salt mine („Glückauf Sondershausen Entwicklungs- und Sicherungsgesellschaft mbH“) was opened in 1893 and is actually the oldest active potash mine in the world. It lies on the northern edge of the Thuringian basin and south of the Harz Mountains. This border region of the central German Zechstein basin is characterized paleogeographically by several effective swells and depressions (e.g. the Eichsfeld swell, but also smaller carbonate and sulfate walls, created in the Zechstein Ages). This situation causes, in addition due to the nearby former mainland, locally strong lateral and vertical changes in thickness and facies within the Zechstein strata. The sequences of Z1 to Z4 are developed in the area and reach a primary thickness of over 100 m, which can be locally amplified by salt movements. The rocksalt production in Sondershausen (ca. 200,000t per year, mostly used as road salt) is situated in the more than 100 m thick Staßfurt-formation, due to its low content of accessory minerals (i.e. NaCl-content is in the order of 98%) in a depth of around 700 m. At the top of the salt formation an up to 20 m thick potash seam (hard salt/sylvinite and carnallitic facies) is embedded, which was preferably mined.

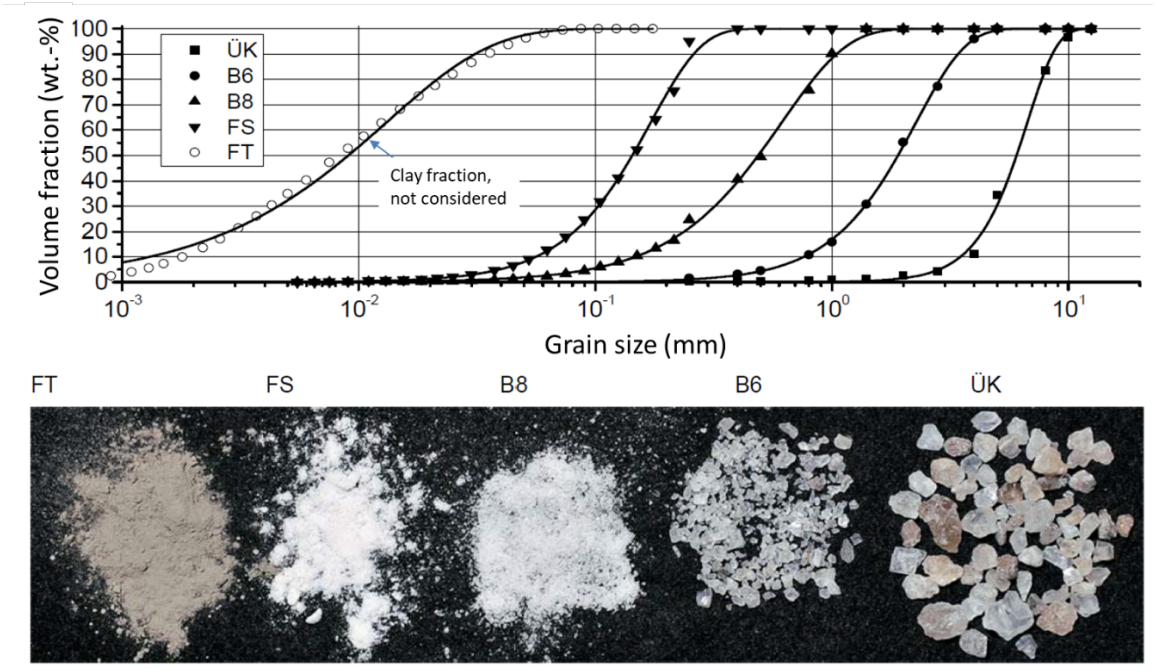

Fig. 4.3 Salt grain fractions and grain size distributions

Tab. 4.1 Grain size fractions in the raw salt material and the optimized mixture

Material-fraction	Grain size distribution d_5-d_{95} [mm]	d_{50} [mm]	m [-]	Optimized mixture [wt.-%]
Überkorn (ÜK) – oversized grains	3 - 10	6.03	3.44	-
Band 6 (B6) – production line 6	0.4 - 4	1.90	2.06	65.6
Band 8 (B8) – production line 8	0.1 -1	0.49	1.58	20.2
Feinsalz (FS) – fine salt	0.03 -0.3	0.14	2.01	14.2
			sum	100.0
Materials from other investigations or sources				
REPOPERM	0.1 - 30	2.35	0.81	
ESCO - salt	0.1 - 8	1.48	1.02	

The used crushed salt variety from the GSES, respectively the KOMPASS-reference material, is characterized as follows:

- different grain fractions are available, which are summarized regarding their grain size properties in Tab. 4.1 respectively graphical presented as sieve lines and grain fractions in Fig. 4.3.
- Following the outcome of intensive pre-tests, performed by the TU BAF in the framework of the ELSA-Project II /GLA 16/ the crushed salt mixture is composed by different weight fractions of the available grain size fractions, roughly representing a so-called Fuller-curve. The respective weight fractions are given in Tab.

4.1. As typical for bedded salt the initial humidity content of the GSES-material varies from 0.06 to 0.18 (from coarse to fine material) with an average content of around 0.1 wt.-%, as outcome of extensive material investigations.

- The measured (average) mineral density (dry material) is 2.1655 ±0.0005 g/cm^3 /GLA 16/.

At least 2 t of crushed salt mixture were ordered by the GSES. The material mixture was prepared manually in the mine and delivered in 4 big packs.

4.2.2 Porosity

The reliable determination of the porosity before, during and after the test is an important prerequisite for reliable statements regarding the salt crust properties and its suitability as sealing material. In the REPOPERM projects /KRÖ 09/ and /KRÖ 17/ a suggestion was that direct measurements of the porosity in low-porosity granular salt aggregates (e.g. with the gas porosimeter or by pycnometer tests) are not useful for determining porosities of lab samples with larger dimensions. In the KOMPASS project the sample sizes vary:

- Minimum: IfG-creep test samples) - 340 ml
- Average: triaxial cells of TUC, BGR and IfG: up to 2,000 ml
- BGR-oedometer: ca. 10.6l
- Maximum: large IfG-oedometer cell: ca. 160l.

Therefore, porosities are determined from the average solid density of the sample material as measured by the TU Bergakademie Freiberg (rock salt density, ρ_s = 2.1655 g/cm^3) as a target parameter with the calculated value $\varepsilon = \emptyset = 0$.

$$\phi = \frac{V - V_s}{V} = \frac{V_P}{V} = 1 - \frac{\rho_{S_{gr}}}{\rho_s} \quad (4.1)$$

where $$\rho_{S_{gr}} = \frac{m}{V} \quad (4.2)$$

V_0 initial volume of sample [cm^3]
V actual volume of sample [cm^3]
V_s volume of sample after complete compaction (rock salt) [cm^3]
m crushed salt mass (weight) [g]
ρ_s rock salt density [g/cm^3]
σ_{gr} density of crushed salt [g/cm^3]

4.3 Microstructural analysis of loose crushed salt material

The loose crushed salt from the Sondershausen mine was investigated as raw material, using polarization microscopy. The objective was to distinguish microstructures, which are already present before compaction. These are: (1) Microcracks, such as intra- (Fig. 4.8) and transgranular fractures (Fig. 4.7), often in an en-échelon fashion (Fig. 4.4 and Fig. 4.5) as well as (2) fluid inclusions. The latter either as planes or lines Fig. 4.5 to Fig. 4.7, each sometimes exposing a connected network (Fig. 4.55).

The en-échelon microcracks in Fig. 4.4 are following the lattice planes but show also an acute angle to the grains' corner. Therefore, it can be presumed that they are caused by load to the tip of this corner only. Such a force distribution is attributed to the mining process itself, while in-situ deformations are suspected to be more evenly distributed throughout the entire grain boundaries. Fluid inclusions, on the other hand, are likely not related to the rapid mining but indicators of past tectonic loading. It is planned to investigate carefully sampled in-situ material to better distinguish these indicators.

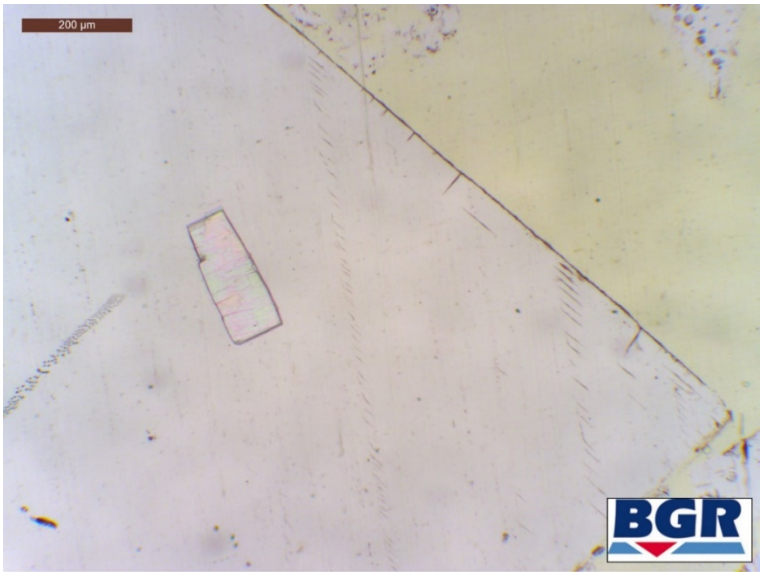

Fig. 4.4 Halite grain in uncompacted crushed salt with en-échelon, a fluid inclusion plane and a grain of anhydrite as a sloid inclusion. Scale bar is 200 µm.

Fig. 4.5 Halite grain in uncompacted crushed salt with en-échelon and fluid inclusion planes. Scale bar is 100 µm

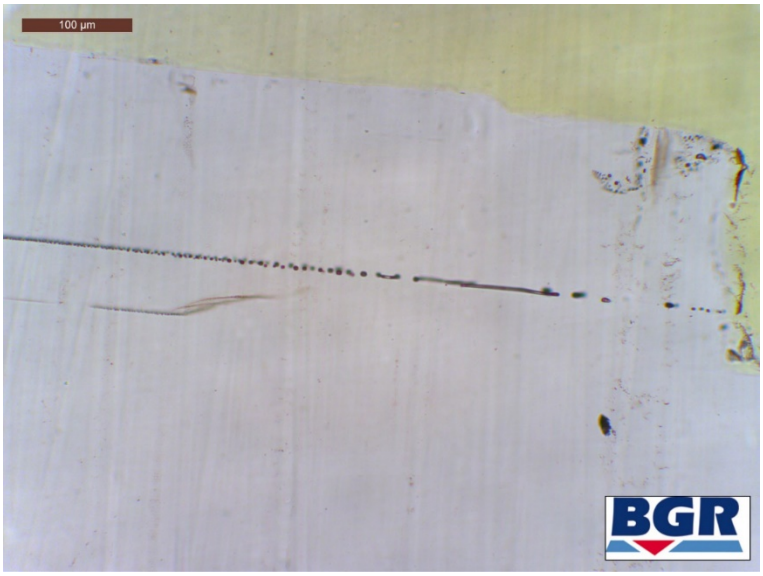

Fig. 4.6 Halite grain in uncompacted crushed salt with two fluid inclusion lines, connected by a relay. Scale bar is 100 µm

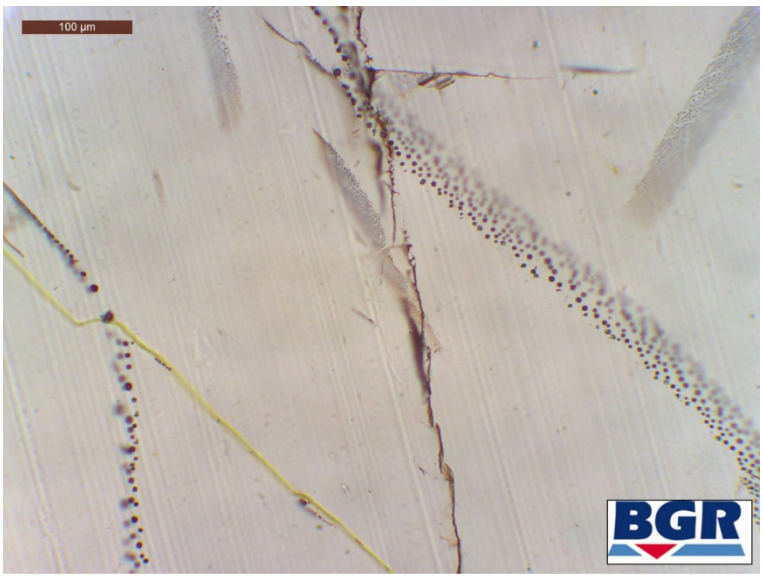

Fig. 4.7 Halite grain in uncompacted crushed salt with different types of microstructures present. Fluid inclusions (planes and lines), en-échelon (centre of the grain) intra- (top of the grain) and transgranular fractures (yellow coloured crack) were observed. Scale bar is 100 µm

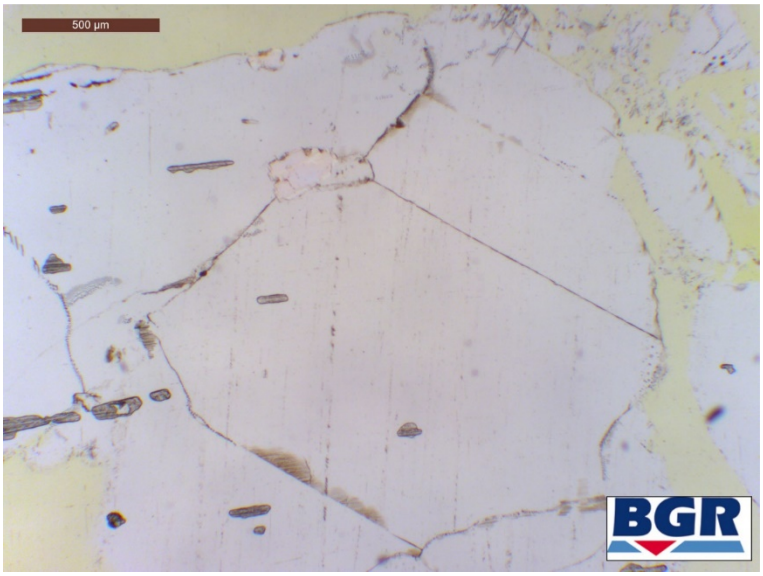

Fig. 4.8 Halite grain in uncompacted crushed salt with a grain of anhydrite as inclusion, surrounded by intragranular fractions. Scale bar is 500 µm

4.4 Oedometric tests on two crushed salt samples from bedded salt layers in Teutschenthal, Germany

4.4.1 Introduction

Previously, the search for a salt-based disposal of radioactive waste focused on vertically oriented strata, e.g. in diapirs. Consequently, former research on crushed salt backfilling used material from such locations, for instance in the joint research programs BAMBUS I + II /BEC 99/, /BEC 04/ and REPOPERM I + II /KRÖ 09/, /KRÖ 17/. In turn, this report section records the findings for crushed salt retrieved from horizontally bedded salts of the Teutschenthal mine in Germany, as flat-lying deposits are now also regarded as potential host rock candidates for nuclear waste disposal.

The main objective is to evaluate (1) the reduction of porosity and (2) the increase in corresponding backfill resistance during oedometric compaction of initially loose crushed salt. These two parameters are crucial in assessing if and under which time and stress conditions a low porosity is achievable by in-situ compaction.

4.4.2 Material and methodology

4.4.2.1 Properties of the starting material (loose crushed salt)

The crushed Teutschenthal salt (Fig. 4.9a) was sent in 2017 by the Institut für Gebirgsmechanik (IfG-Leipzig) in two so-called “big bags”. It derived from the Zechstein “z2HS” formation. The materials’ humidity was measured by oven drying at 105 °C for at least 5 days until approximate weight constancy.

Tab. 4.2 Averaged humidity of crushed salts from Asse, Gorleben and Teutschenthal. N gives the number of measurements.

Teutschenthal z2HS		Asse z2HS	Gorleben z2HS
as-received [m-%]	designed [m-%]	as-received [m-%]	as-recieved [m-%]
0.35 (*N* = 4)	0.34 (*N* = 9)	0.12 (*N* = 1)	0.13 (*N* = 2)

When re-examined several days after drying, the Teutschenthal material regained in humidity to match values of its as-received status. This regain indicates the salts’ general tendency for water uptake from humid air. Hence, the materials’ comparably high “as-

received” humidity is not inevitable resulting from unfortunate earlier outside storage conditions.

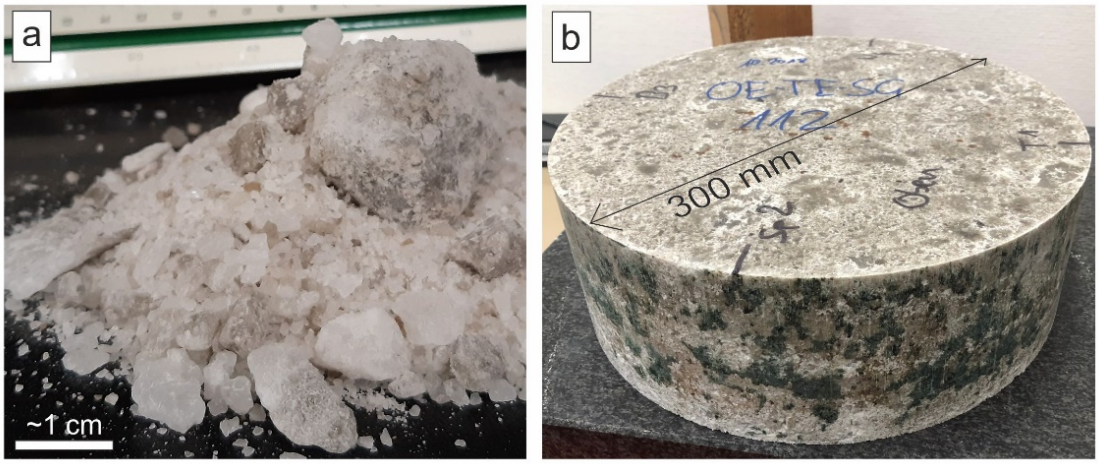

Fig. 4.9 a) Loose crushed salt from the z2HS formation of the Teutschenthal underground salt mine. b) Test specimen after oedometric compaction, diameter is 300 mm, height is 102.21 mm. It was compacted from a pile of loose crushed salt almost one third taller than its final height (compacted from 144.23 mm to 102.21 mm)

Oven drying also reduced grain adhesion (clumping) to ensure accurate subsequent sieving. Therein, the used mesh sizes ranged from 31.5 mm to 0.063 mm, with a total of 11 meshes. Crushed salt from all sieving fractions was subsequent mixed to create a designed grain size distribution material. Therein, it is aimed for the designed material to fall within the range of crushed Asse salt from previous “TSS-tests” in the above mentioned BAMBUS project (Fig. 4.10). This artificial distribution enables better comparison to previous tests and considers a scaling effect: Compared to underground backfilling in galleries, the oedometric cell is limited in size and might not hold a representative amount of largest grains without disturbing the experiments’ outcome (see also /AST 16/).

The designed material was divided for three separate examinations: (1) mineralogical analysis via X-ray diffraction (XRD, 10 samples), (2) humidity determinations via oven drying (9 samples, see Tab. 4.2) and (3) one oedometric compaction test.

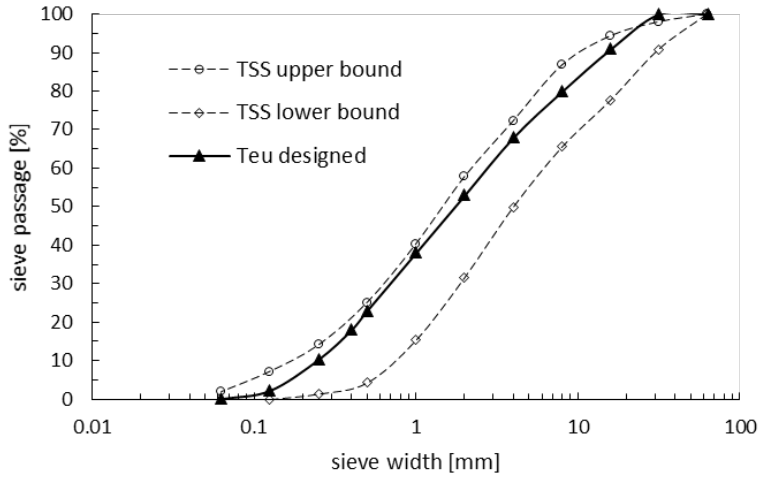

Fig. 4.10 Grain size distribution curves. Solid line = designed crushed salt from Teutschenthal material, dashed lines = upper and lower bound of grain size distributions from crushed Asse salt as used in previous "TSS-tests" of the BAMBUS project.

Test (1) was performed by the BGR sub-department "B2.1 – Technical Mineralogy", with each of 10 samples being 30 g in weight. This mineralogical Rietveld analysis was essential for the estimation of the solid matter density, which, in turn, was crucial for the porosity evaluation. The solid matter density (ρ_S) for each XRD-sample was derived by

$$\rho_S = \sum_{i=1}^{n} \rho_i * N_i \tag{4.3}$$

ρi literature density value [g/cm^3]
Ni mass-percentage for a given mineral phase i

Identified phases, averaged abundances and used densities were: Halite (85.31 m-%; 2.168 g/cm^3), Anhydrite (8.58 %; 2.97 cm^{-3}), Polyhalite (3.49 %; 2.78 cm^{-3}) and unidentified material (2.62 %). The latter was neglected by normalizing identified phases to a full 100 %. Following this procedure, the averaged solid matter density ($\overline{\rho_S}$) was 2.261 g/cm^3, the smallest ($\rho_{S\text{-}MIN}$) was 2.226 g/cm^3 and the largest ($\rho_{S\text{-}MAX}$) was 2.327 g/cm^3. Further, considering the salts' humidity (0.34 %, Tab. 4.2) gained from test (2), the density (ρ_S^f) was determined as

$$\rho_S^f = \overline{\rho_S} * 1.0034 \tag{4.4}$$

resulting in a best estimate of 2.268 g cm^{-3} (range from 2.233 g cm^{-3} to 2.335 g cm^{-3}).

4.4.2.2 Oedometric testing

To compact loose crushed salt in an oedometric cell causes unwanted stress inhomogeneity and hence an uneven compaction grade throughout the sample. As a countermeasure, the designed crushed Teutschenthal salt was filled stepwise in three sections of approximately 60 mm, 50 mm and 35 mm height. Each section was slightly press-compacted by hammer strokes to a fitting metal disk before filling the next section. The resulting overall filling height was 144.23 mm. The oedometers' diameter was 300 mm, resulting in an initial sample volume (V_{tot}) of 10,195.04 cm³. The sample mass (m) was 15,345 g, hence resulting in an initial bulk density (m / V_{tot} = $\rho_{bulk,\,0}$) of 1.505 g/cm^3.

Using the best estimate for solid matter density, the initial porosity (ϕ) was 33.6 % (e = 0.506), as calculated by

$$\phi = 1 - \frac{\rho_{bulk}}{\rho_S^f} \tag{4.5}$$

For comparison to earlier tests the pore number or void ratio (e) is given, which is derived by:

$$e = \frac{\phi}{1 - \phi} \tag{4.6}$$

The evolution of porosity and void ratio was determined throughout the experiments. Therein, three independent linear variable displacement transducers (LVDTs) recorded changes in the samples' height to update its bulk volume and thus its bulk density.

Next to porosity, the evolution of the samples backfill resistance is recorded. This resistance is interpreted as a dynamic threshold: It is the minimum applied uniaxial stress that is necessary to constantly compact the sample at a given strain rate and a given bulk density. Therein, the uniaxial stress was servo-controlled by the LVDT-signal to match a user-defined compaction speed. This speed was set in an alternating, multi-step manner, ranging from 0.36 mm/h to 0.00036 mm/h for test Oedo-112. Corresponding to the initial sample height, this speed resembles strain rates ($\dot{\varepsilon}$) of $6.9 \cdot 10^{-7}$ s^{-1} to $6.9 \cdot 10^{-10}$ s^{-1}. Test Oedo-113 was designed for more rapid rates ranging from 3.6 mm/h to 0.0036 mm/h ($\dot{\varepsilon}$ = $6.9 \cdot 10^{-6}$ s^{-1} to $6.9 \cdot 10^{-9}$ s^{-1}). For reasons of practicability the multi-step procedure is chosen: compacting the same volume at an in-situ realistic deformation rate (e.g. for Asse-conditions at $\dot{\varepsilon}$ approximately equal to $6.9 \cdot 10^{-10}$ s^{-1}, /BEC 99/) would have

yielded an experiment runtime of 13.3 years. Hence, periods of higher compaction speeds are inserted and further relaxation intervals were added. The latter in order to allow any possible impact of foregoing rapid phases to decay. Tab. 4.3 lists the order of user-defined experiment phases for test Oedo-112.

As a drawback, increasing uniaxial forces implied an increasing frictional resistance of the sample with the oedometers' inner surfaces. This unwanted effect could not be eliminated and likely lead to an inhomogeneous distribution of stress and compaction. On the other hand, the determined uniaxial stress values were mathematically corrected by accounting for these frictional forces. This feat was achieved by placing load cells underneath the oedometers' cell walls. The thereby measured load must have been transferred by and hence were proportional to the frictional resistance.

Please refer to /STÜ 17/ for a more detailed explanation of this accredited testing procedure (DAkkS No.: D-PL-20434-01-00). The tests' BGR-internal identifier number are Oedo-112 and Oedo-113 (LIMS Nr.: 18001 and 18021). In both experiments the used oedometric apparatus was "M5" operating at constant 48.8 °C. Test Oedo-112 was performed from January, 25th 2018 to October, 10th 2018 (258 days) and Test Oedo-113 was performed from October, 29th 2018 to November, 14th 2018 (16 days).

4.4.3 Results and discussion

The oedometric test Oedo-112 on crushed Teutschenthal salt resulted in a cohesive block (Fig. 4.9b). Its final bulk density is ρ = 2,123 g/cm³, its remaining porosity is about 6.4 % (e = 0.068), i.e. 27.2 % porosity was diminished in 258 days of compaction. As expected from previous tests (see references to REPOPERM and BAMBUS projects above), the load resistance changed with (1) compaction state, i.e. bulk density / porosity, and (2) applied compaction speed. In two occasions, we needed the full machines' capability of almost 35 MPa in order to maintain the desired speeds. Fig. 4.11a displays the applied uniaxial stresses throughout the experiment and Fig. 4.11b shows the evolution of porosity. The colouring corresponds to the experiment phases.

Tab. 4.3 Experiment phases and respective key values. The short phases 6, 7, 13 and 14 are due to machine readjustments.

Phase-Nr	Type	Δt	*v*	Porosity Reduction	Remaining Porosity	Backfill Resistance Average	Backfill Resistance Range Width
		[d]	[mm/h]	[%]	[%]	[MPa]	[MPa]
1	compaction	3.14	0.34929	15.03	18.13	4.88	15.48
2	relax	6.76	0.00171	0.20	17.93	5.44	12.54
3	compaction	11.25	0.00038	0.07	17.86	2.82	0.30
4	compaction	16.75	0.00312	0.89	16.97	8.04	7.41
5	compaction	5.25	0.03433	3.24	13.73	17.36	11.03
6	relax	0.73	0.00597	0.08	13.65	16.52	5.61
7	compaction	0.31	0.33125	1.97	11.68	27.61	13.60
8	relax	11.71	0.00136	0.31	11.36	15.23	22.22
9	compaction	17.00	0.00037	0.12	11.24	8.94	0.51
10	compaction	20.12	0.00304	1.22	10.02	19.47	14.37
11	compaction	2.00	0.02766	1.14	8.88	31.56	11.30
12	relax	18.04	0.00122	0.46	8.42	20.46	20.21
13	compaction	2.75	0.00039	0.02	8.40	14.85	0.58
14	relax	3.08	0.00035	0.02	8.37	14.34	1.04
15	compaction	41.98	0.00030	0.26	8.11	15.05	2.80
16	compaction	18.03	0.00290	1.12	6.99	28.65	17.50
17	relax	12.00	0.00067	0.17	6.82	26.43	11.32
18	compaction	56.92	0.00036	0.44	6.38	22.59	1.23
19	End of Test	6.00	-0.00007	-0.01	6.39	1.60	22.78

Tab. 4.3 gives remaining porosity and porosity reduction for each experiment phase. The vast amount of pores was diminished at the very onset of the test. The initial 33.6 % porosity was reduced by 15.03 % in the first three days of compaction, while only 0.43 % reduction occurred in the latest phase that lasted 63 days at a compaction rate 0.00036 mm/h. Bear in mind that the porosity reduction is a user-defined value, set by the designated speed and duration of a compaction phase.

A material intrinsic property is the salts' resistance to compact, i.e. the minimum stress needed to keep a constant compaction speed. Tab. 4.3 notes the averaged load resistance and its range (maximum – minimum value) per phase. It is evident that load resistance increases with increasing density and compaction speed. The value range becomes wider with compaction speed, illustrating the comparably weak strength of salt at low strain rates. Each increase in compaction rate causes a drastic increase in load resistance first until it deviates to a gentler slope with a constant, linear appearance (Fig. 4.11a). The phases with the slowest compaction of 0.00036 mm/h show no such drastic

increase. This lack is due to higher stresses in the foregoing relaxation phases. During the latest compaction (phase 18), only a constant 23 MPa have been necessary to maintain the steady compaction speed.

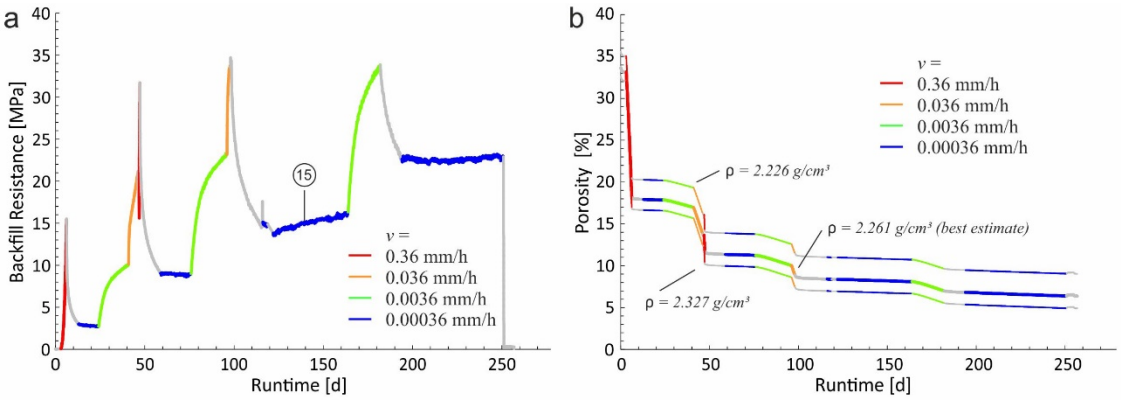

Fig. 4.11 Evolution of load resistance (a) and porosity (b). Colours represent the differing compaction speeds (v), grey illustrates the evolution during relaxation periods, see Table 2. The number “15” marks phase 15, see text for details.

Fig. 4.12a shows the key diagram of this study. It illustrates the materials backfill resistance versus its porosity, stating the load necessary to compact the sample at a given compaction state and – in colour – at a given compaction rate. It stands to reason to connect each phase of the same compaction speed, as done by the dashed lines. However, bear in mind that this connection is subjectively drawn and neither a valid mathematical nor a valid rheological proven description. Even temping for the interpreter, it is yet speculative if the same set and ratio of deformation mechanisms do apply for each phase. In other words, the early compaction in phase 3 (0.00036 mm/h) might be caused more by rigid grain reorientation, while the latest compaction in phase 18 (also 0.00036 mm/h) might hypothetically be accomplished more by moving dislocations and recrystallization events. The latter possibly enabled by the salts’ comparably high humidity of 0.34 m-%. For a better understanding, knowledge on each mechanisms’ intensity is essential. Therefore, currently the abundance of microstructural indicators were investigated (see also Section 3 of this report). Fig. 4.11a and Fig. 4.12a shows a differing evolution of load resistance within each compaction phase. This finding supports the hypothesis of differing mechanism intensities at play. Particularly interesting is the evolution of load resistance in phase 15, which increases linearly, while all other phases with 0.00036 mm/h compaction speed remain at a constant stress value, i.e. show a compaction creep behaviour. We also like to stress that extrapolation to even lower compaction speeds can be subjectively anticipated by the trend in interpreted lines but remains unverified.

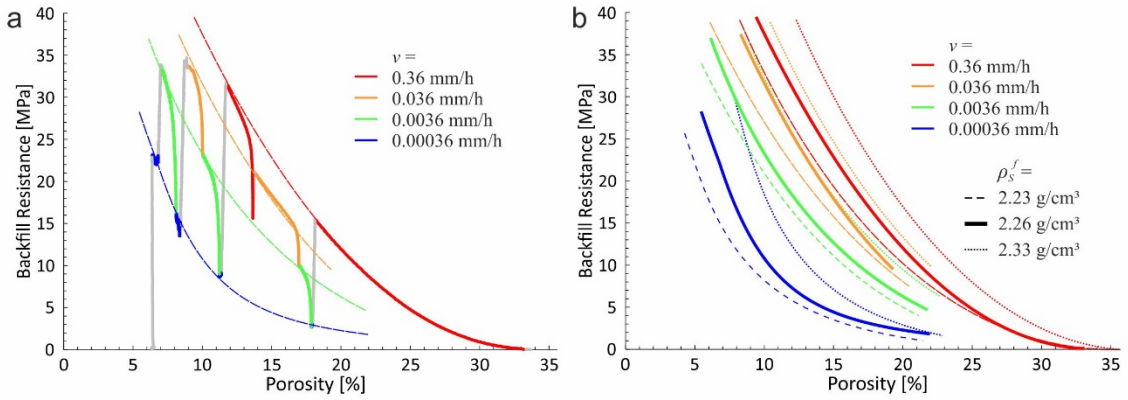

Fig. 4.12 (a) Load resistance versus porosity values at given compaction speeds (in colour), wherein porosity is derived by the best estimate for solid matter density. (b) Illustrates differing interpreted lines for each case of best estimate (solid), lowest (dashed) and largest (dotted) solid matter density. Note that interpreted lines in both, (a) and (b) are subjectively drawn.

The error margin due to imprecise solid matter density estimation is drastic. Given the full margin of ρ_S^f = 2.233 g/cm^3 to ρ_S^f = 2.335 g/cm^3, the initial porosity ranges from 32.6 % to 35.5 %, and the remaining porosity from 4.89 % to 9.02 %. This gives an error span likely wider than the actual value. Note further, that this porosity range falls close to the percolation threshold, which defines a strict reduction in permeability /JOB 15/. Hence, we stress the importance for a precise remaining porosity quantification. However, since original crushed salt is a natural product, its density varies. And it is this natural raw material that is planned to be used as backfilling. The imprecision in solid matter density further effects the ratio of load resistance to porosity. It states that either more force (in the case of higher solid matter density) or less force (in the case of lower solid matter density) is needed for the same volume of compaction. Fig. 4.12b illustrates the effect of imprecise solid matter density estimation. It shows a set of interpreted curves that display the relation of load resistance to remaining porosity, compaction speed (in colour) and solid matter density values. It is elaborated on the difficulty of precise porosity determination in current investigations.

Comparison to other oedometric crushed salt tests

Next to the above reported oedometric test Oedo-112, a second test was accomplished, Oedo-113. Oedo-113 lasted only for 14 days, as it was designed to reproduce the Oedo-112 results but at higher compaction speeds, ranging from 3.6 mm/h to 0.0036 mm/h. The test results are shown in Fig. 4.13a and match those achieved by the Oedo-112 test.

This suggests that early rapid compaction of 3.6 mm/h does affect later experiment stages to the same extend as early compaction at 0.36 mm/h.

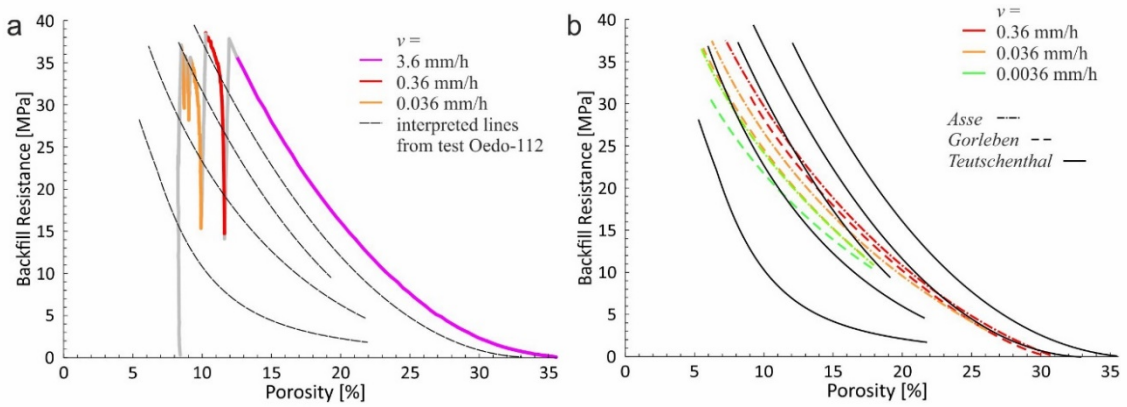

Fig. 4.13 Load resistance versus porosity values given for differing strain rates (in colour) of test Oedo-113. Note that the recorded values match the interpreted curves from test Oedo-112 (black dashed lines, compare to Fig. 4.12a). b) Interpreted lines of crushed Asse and crushed Gorleben salt behaviour at different compaction speeds (in colour). Interpreted curves from Oedo-112 and Oedo-113 (solid black lines) show a distinctively weaker load resistance at lower compaction speeds. The black curves range from 0.00036 mm/h to 3.6 mm/h, compare to left Figure. Note that crushed salt differs also in moisture content (Tab. 4.2). This content has a drastic effect on both: porosity estimation and – which is more significant in long-term evaluation – material deformation behaviour.

Fig. 4.13b compares interpreted ratio curves of backfill resistance to porosity from differing “z2HS” Zechstein locations. It shows results from oedometric tests on Teutschenthal (Oedo-112, Oedo-113), Asse (Oedo-049) and Gorleben (Oedo-081) material. The latter two described in /STÜ 02/. The Figure shows a set of compaction rates, each determined using the best estimate for solid matter density and humidity of each location. In general, the tested crushed Teutschenthal salt behaves as expected from previous tests: A lower compaction speed results in a lower backfill resistance curve. However, Teutschenthal material covers a wider range and shows distinctively weaker backfill resistance at lowest compaction speeds. This effect is possibly related to its comparably higher humidity (compare to Tab. 4.2). A hypothesis, which is supported by earlier studies on artificially humidified samples /STÜ 98/. Yet, the influence of other parameters such as solid matter density and impurities are also at play. Hence, it is difficult to state an effect resulting from bedded salt only, i.e. from tectonic overprints such as dislocation densities and (sub)grain size distributions.

4.4.4 Conclusion on crushed salt tests from the bedded salt deposits Teutschenthal

Based on two oedometric compaction experiments (Oedo-112 and Oedo-113), a similar compaction pattern of the Teutschenthal material, representing bedded salt, to crushed salt gained from domal salt deposits is concluded. However, the Teutschenthal material exposes a wider range in backfill resistance development. Therein, crushed salt achieves a weaker backfill resistance for lower compaction rates, which is attributed to its comparably higher humidity. In any case, there is a general behavioural variance corresponding to the origins of crushed salt. This variation is typically not just owed to microstructural differences, e. g. differing dislocation densities and differing grain sizes from past tectonic loading (diapirism / bedding reorientation) but most likely due to inter-facies differences in degree of saturation, impurity abundance and solid matter density.

The Teutschenthal tests, Oedo-112 and Oedo-113, were performed at the same test setup but at differing strain rates. Both show congruent results, which suggests that a rapid early compaction of 3.6 mm/h does not significantly alter later phases in the here applied oedometric testing procedure.

4.5 Pre-compaction tests

The majority of the laboratory investigations performed to date on the THM behaviour of crushed salt have been carried out with the aim of generating the lowest possible residual porosity, starting from an initial porosity of > 30 %. Compared to the situation in-situ, either the required loads are unrealistically high, or the desired residual porosity is only achieved after a very long period of time due to convergence. A new approach is pursued with the investigations on the short-term production of pre-compacted test specimens of crushed salt under in-situ loading conditions. The aim is to produce a starting material with low porosity and natural grain structure corresponding to the in-situ compacted material, which can be used for further long-term tests to investigate the THM behaviour of crushed salt characterized by very small porosities (≈ 1 % – 5 %). The special requirements in this new approach are that already during pre-compaction the load level and the load direction must correspond to the actual in-situ conditions to a large extent, but at the same time a time-lapse effect is achieved. Within the research project different techniques have been investigated regarding their possibility to fulfil the mentioned demands above.

Tab. 4.4 gives a brief overview.

Technique	Resulting sample size	Controlled by strain rate / load	Stress re-gime	Runtime	Re-maining po-ros-ity	Material	Number of tests
Plain Strain (TUC)	d = 90 mm h = 180 mm	Radial load (σmax = 5/10/15 MPa)	Plain strain (long-est axis fixed)	3 d	2 – 11 %	Preliminary tests on not classified crushed salt w = 0.5/1/2/3 %	8
		Radial load (σmax = 2/4/5/10/ 15 MPa)		2 – 7 d	2 – 19 %	KOMPASS reference mate-rial w = 0.1/0.3/0.5/1 %	23
Small Cell (IfG)	d = 80 mm h = 100 mm	Axial load, step-wise (σmax = 20 MPa)	Oe-dome tric	1 – 5 d	10 – 20 %	KOMPASS reference mate-rial	3
Big Cell (IfG)	d = 500 mm h = 620 mm	Axial load, step-wise (σmax = 20 MPa)	Oe-dome tric	< 28 d	10 – 20 %	KOMPASS reference mate-rial w = dry/1 %	2
BGR	d = 100 mm h = 200 mm	Strain rate, step-wise ($\dot{\varepsilon}_{max}$ = 9.1*10-6 1/s) (σmax = 20 MPa)	Oe-dome tric	< 28 d	~ 15 %	Various (shown in this study: ASSE/DEBORA)	> 40 (2 shown in this study)

Tab. 4.4 Brief comparison of pre-compaction techniques. *) Porosity values are not unconditionally comparable. They show intra-sample variance and are subjected to drastic measurement errors, foremost imprecise solid matter density determination

Technique	Resulting sample size	Controlled by strain rate / load	Stress regime	Runtime	Remaining porosity	Material	Number of tests
Plain Strain (TUC)	d = 90 mm h = 180 mm	Radial load (σ_{max} = 5/10/15 MPa)	Plain strain (longest axis fixed)	3 d	2 – 11 %	Preliminary tests on not classified crushed salt w = 0.5/1/2/3 %	8
		Radial load (σ_{max} = 2/4/5/10/15 MPa)		2 – 7 d	2 – 19 %	KOMPASS reference material w = 0.1/0.3/0.5/1 %	23
Small Cell (IfG)	d = 80 mm h = 100 mm	Axial load, stepwise (σ_{max} = 20 MPa)	Oedometric	1 – 5 d	10 – 20 %	KOMPASS reference material	3
Big Cell (IfG)	d = 500 mm h = 620 mm	Axial load, stepwise (σ_{max} = 20 MPa)	Oedometric	< 28 d	10 – 20 %	KOMPASS reference material w = dry/1 %	2
BGR	d = 100 mm h = 200 mm	Strain rate, stepwise ($\dot{\varepsilon}_{max}$ = 9.1*10^{-6} 1/s) (σ_{max} = 20 MPa)	Oedometric	< 28 d	~ 15 %	Various (shown in this study: ASSE/DEBORA)	> 40 (2 shown in this study)

4.5.1 Plain strain compaction by TUC

The plain strain compaction technique is based on the idea that the compaction conditions in-situ can be idealized by a plane strain state. These conditions correspond to the crushed salt compaction in a drift with stresses and deformations in radial direction (creep of the rock onto the offset), while the deformation in axial direction of the drift is negligible (encumber of axial deformation and passive build-up of the axial stress induced by the axial deformation restraint). This load boundary condition can be realized according to the schematic sketch shown in Fig. 4.14 by an extension test with constrained axial strain in a laboratory test.

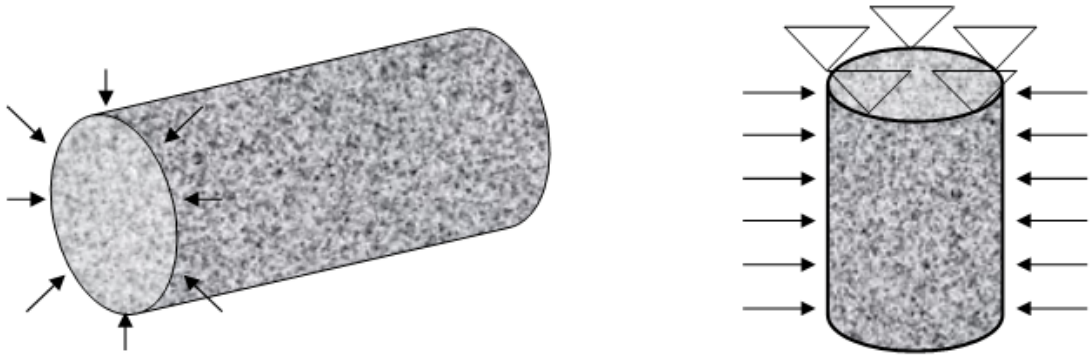

Fig. 4.14 Schematic sketch for the transfer of the in-situ stress of crushed salt in a section (left) to the triaxial stress of a cylindrical test specimen in an autoclave (right)

In order to realize a triaxial extensional stress (TE) with prevented axial strain (plain strain / plane strain state), autoclaves available at the Chair of Waste Disposal Technologies and Geomechanics of TU Clausthal for the ageing-resistant storage of clay rocks under pore pressure were modified. The triaxial cells, originally configured for isostatic and axially and radially movable support of cylindrical test specimens, were modified by locking the axial pressure pieces in such a way that loosely introduced crushed salt displacement in the radial direction can be subjected to a defined load by the experimental specification of a confining pressure and at the same time axial elongation is prevented (TE load with reduced axial elongation = plane strain state). Fig. 4.15 shows a photographic view of the pressure bearing cells used for the pre-compaction of crushed salt in the research project after completion of preliminary tests on test specimens.

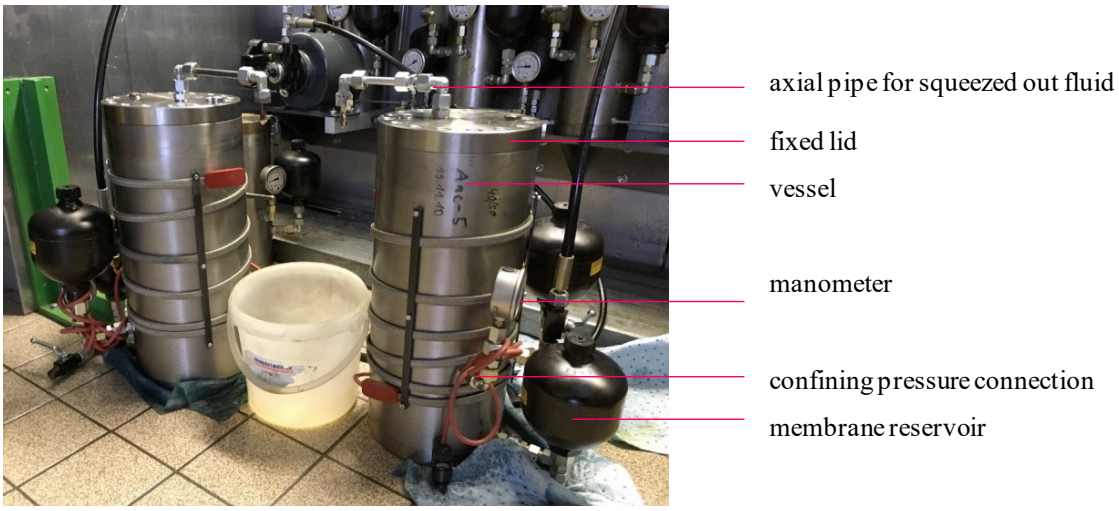

Fig. 4.15 Pressure storage cells for the pre-compaction of crushed salt under plain-strain conditions

In order to be able to produce pre-compacted, cylindrical crushed salt test specimens with the dimension diameter d = 90mm / height h = 180 mm after completion of the pre-compaction, the pre-compaction is carried out on test specimens of loosely poured crushed salt with the dimension d0 = 120 mm / h0 = 240 mm. According to the photographic documentation in Fig. 4.16, the crushed salt is filled in layers into a cylindrical Perbunan jacket onto the bottom pressure piece of the autoclave and lightly compacted without destroying the grain structure in such a way that the initial porosity calculated from the crushed salt mass filled in, cylinder volume and salt grain density is approximately 20 % – 25 %.

Fig. 4.16 Production of crushed salt test specimens for the pre-compaction by layer installation with moderate pre-compaction

After completion of the crushed salt filling, the top pressure piece is placed on as shown in Fig. 4.17, the Perbunan jacket is connected to the upper pressure piece by means of a band clamp and the cover plate of the autoclave is screwed on.

Fig. 4.17 Installation of crushed salt test pieces in autoclaves

Flooding of the annular space between the crushed salt test specimen and the autoclave with hydraulic oil is carried out by means of an electric hydraulic pump until hydraulic oil escapes via a vent hole on the front face. The venting bore is then closed, and the radial pressure specified in the test is generated by means of a hand pump (Fig. 4.18). To compensate for the decreasing jacket pressure in the annular space as a result of crushed salt compaction, the autoclaves used for pre-compaction have a membrane reservoir as shown in Fig. 4.18.

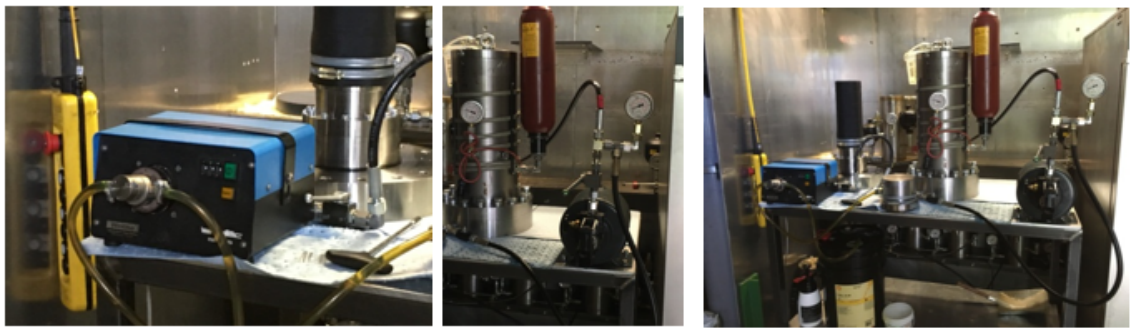

Fig. 4.18 Oil hydraulics for the generation of experimentally specified radial compaction pressure

For the validation of the above-described test technique with regard to its basic suitability for the production of pre-compacted crushed salt test specimens of defined porosity and for the development of first findings on the quantitative dependence of the pre-compaction on the level of stress, on the duration of the stress and on the moisture content of the crushed salt, preliminary tests were first carried out with systematic variation of the confining pressure (s_c = 5 MPa, 10 MPa, 15 MPa) and water content (w = 3 %, 2 %, 1 %, 0.5 %) with a uniformly specified compaction time at t = 3 d. For the preliminary tests documented below, unclassified crushed salt (crushed salt grit, which is produced during the machining of rock salt drill cores on a lathe) was used. Fig. 4.19 shows the stress boundary conditions realized in the preliminary tests and the test specimens generated

from pre-compacted crushed salt. Fig. 4.19 shows that the test technique was suitable in each individual case to compact the loosely introduced crushed salt at least to such an extent that stable, cylindrical test specimens were obtained.

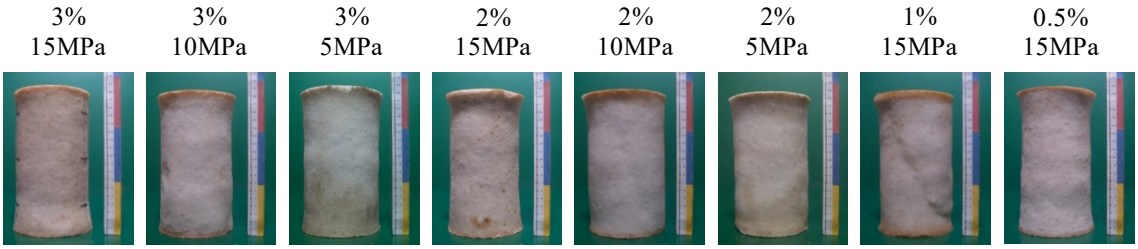

Fig. 4.19 Preliminary tests on the producibility of pre-compacted crushed salt test specimens

The porosity of the salt samples calculated from mass, volume and crushed salt density (assumption: Na = 2.16 g/cm^3) before and after pre-compaction is documented in Fig. 4.20. According to this, even under the concession of a small and statistically not representative number of individual tests, it can be estimated that:

(a) with increasing confining pressure and increasing water content the compaction increases and vice versa the porosity decreases and

(b) the applied experimental technique is suitable to generate porosities of 1 % – 5 % within comparatively short experimental times.

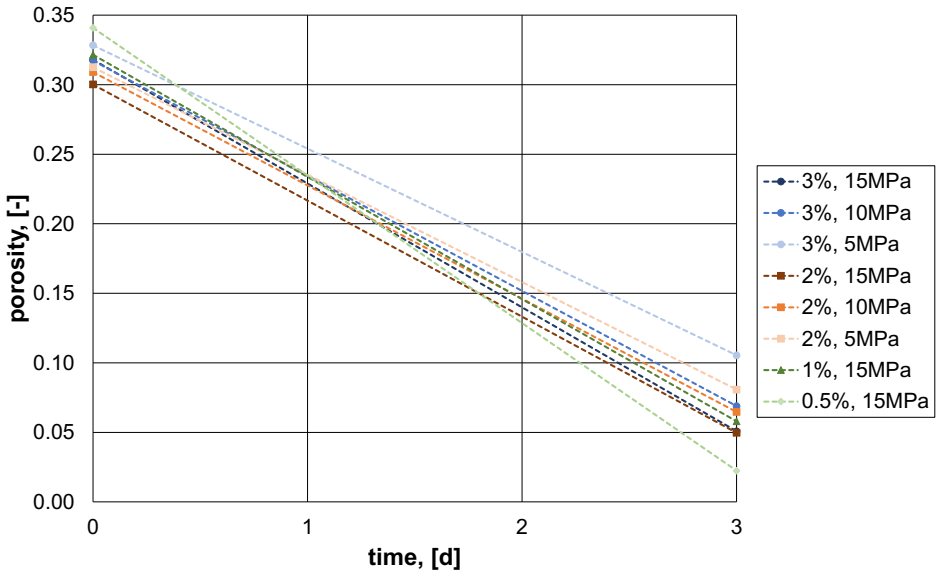

Fig. 4.20 Preliminary tests for crushed salt compaction. Porosity of crushed salt before and after pre-compaction under plain strain conditions

Fig. 4.21 shows an analysis of the ultrasonic wave velocities of the pre-compacted crushed salt specimens, according to which there is a systematic correlation between the porosity of the pre-compacted crushed salt specimens realized in the preliminary tests and the longitudinal ultrasonic wave velocity v_p.

A comparison of these results with a correlation between the porosity and the ultrasonic wave velocity of compacted crushed salt published in /POP 98/ shows significant differences according to Fig. 4.21b, which, subject to further investigations, are causally attributed to the different type of pre-compaction (TUC: TE-plain strain; /POP 98/: TC-oedometer) and as a consequence is presumably an indicator for the influence of the stress geometry on the compaction behaviour and the directional dependence of the material behaviour of compacted crushed salt.

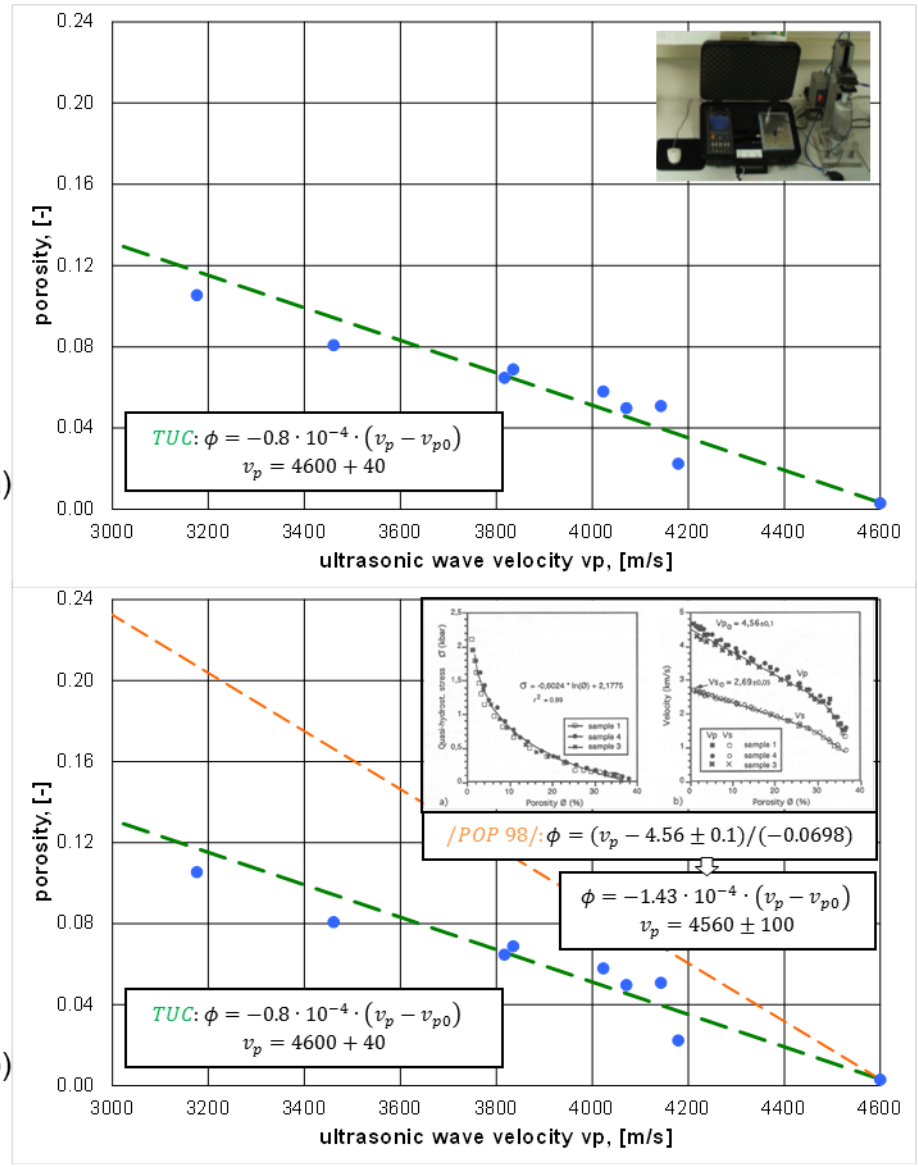

Fig. 4.21 Correlation between ultrasonic wave velocity vp and the porosity of pre-compacted crushed salt test specimen

The question to be clarified in the preliminary tests, whether cylindrical test specimens with plane-parallel end faces and smooth lateral surface can be produced from the pre-compacted test specimens for subsequent tests on the THM behaviour of compacted crushed salt, was carried out by means of preparation tests using a lathe. As a result of the preliminary tests and with reference to the photographic documentation in Fig. 4.22, it could be confirmed that the consistency of the pre-compacted crushed salt is basically suitable for producing cylindrical test specimens with plane-parallel end faces and a smooth outer surface from the salt specimens on a lathe.

Fig. 4.22 Cylindrical test specimen with plane-parallel end faces and smooth lateral surface after machining on a lathe

Nevertheless, it should be noted that the test specimens made of pre-compacted crushed salt react, as expected, much more sensitively to the preparation process than drill cores made of rock salt, so that within the framework of the calculation of laboratory tests it must be taken into account that every third test specimen is destroyed during lathe processing. A similar statement applies on the basis of the previously available examination results also to the pre-compaction itself, i.e. at about every third pre-compaction test, a penetration of jacket pressure oil into the test specimen is observed, because either the band clamp used for sealing between the Perbunan jacket and the pressure piece was not locked sufficiently tightly or the locking of the band clamp does not enable the demanded axial movement of Perbunan jacket induced due to the radial constriction of the specimens by the compression and, as a consequence, a penetration of jacket pressure oil into the test piece results due to tensile failure of the Perbunan jacket in the transition area between the top pressure piece and the frontal sample cross-sectional area. The above-described causes for a penetration of jacket pressure oil into the crushed salt could also be eliminated only partially by constructive measures (e.g. rounding off the pressure pieces) so far.

After the fundamental feasibility and functionality of time-lapse tests for the pre-compaction of crushed salt could be proven by the work described above, it was still to be clarified within the scope of the preliminary tests how the required adjustment of defined crushed salt moisture levels could be realized. Of particular importance here is that

- the initial moisture content of the starting material must be taken into account,
- a trial-related homogenisation of the moisture content within the crushed salt used for the test specimen production must take place,
- at least at water contents of w > 1%, the possibility of free water (free brine) being squeezed out cannot be excluded and, as a consequence, drained pre-compaction with the possibility of absorbing the squeezed-out liquid without evaporation must be provided,
- in the case of pressed liquids, the salinity of the liquid must be determined to ensure that the water content can be determined exactly,
- the addition of fresh water to set a defined water content leads to a dissolution and redissolution of salt minerals and consequently the necessary addition of water has to take place in the form of a saturated solution, taking into account the amount of salt in the solution

As a result of the above preliminary considerations, two basic procedures for the adjustment of defined water contents were worked out as follows:

Method 1:

(a) Production of saturated brine by mixing water and crushed salt with natural moisture

(b) Production of wet crushed salt by mixing crushed salt with natural moisture and saturated brine

The procedure according to method 1 required for the production of m_p = 4,000 g crushed salt with a water content of w = 0.3 % is characterized by

(1) Calculation of the mass of crushed salt with natural water content a and calculation of the mass of saturated brine b for m_p = 4,000 g crushed salt with a water content of w = 0.3 %:

$$a + b = m_p \tag{4.7}$$

a = mass of crushed salt with natural water content (w = 0.122 %) [g]
b = mass of saturated brine (35.9 g salt in 100 g water / 35.9 %)
m_p =mass sample with w = 0.3 % / m_p = 4000 g

$$0.00122 * a + \left(\frac{1}{1.359}\right) * b = 4000g * 0.003 = 12g \tag{4.8}$$

Inserting Equ. (4.7) in Equ. (4.8) returns:

$$0.00122 * (4000g - b) + \left(\frac{1}{1.359}\right) * b = 12g \tag{4.9}$$

$$\Leftrightarrow\ b = 9.692g$$

Inserting Equ. (4.9) into Equ. (4.8) provides:

$$a = 4000g - b = 3990.308g \tag{4.10}$$

(2) Calculation of the crushed salt quantity and the water quantity for the production of b = 9.692 g saturated brine using crushed salt with a natural water content of w = 0.122%.

$$\frac{(0.00122 * c + d)}{b} = \frac{1}{1.359} \tag{4.11}$$

$$(1 - 0.00122) * \frac{c}{b} = \frac{0.359}{1.359} \tag{4.12}$$

$$c + d = b \tag{4.13}$$

c = salt quantity [g]
d = water quantity [g]

From Equ. (4.12) follows directly with b = 9. 692 g according to Equ. (4.9):

$$c = 2.563g \tag{4.14}$$

Inserting Equ. (4.14) into Equ. (4.13) gives:

$$d = 7.129g \tag{4.15}$$

Method 2:

(a) Drying of crushed salt with natural moisture up to a water content of w ≈ 0 %

(b) Production of saturated brine by mixing dry crushed salt (w = 0 %) with water

(c) Mixture of dry crushed salt (w = 0 %) with brine

The procedure according to method 2 required for the production of 4 kg of crushed salt with a water content of 0.3 % is characterized by

(1) Calculation of the mass of water required to produce 4 kg of crushed salt with a water content of w = 0.3%.

$$4000g * 0.003 = 12g \tag{4.16}$$

(2) Calculation of the mass of dry salt to produce a saturated brine (35.9 g salt in 100 g water = 35.9 %) with 12 g water:

$$\frac{35.9}{100} * 12g = 4.308g \tag{4.17}$$

(3) Calculation of the mass of saturated brine for 4 kg of dry crushed salt and saturated brine from Equ. (4.16) and Equ. (4.17):

$$4.308g\ salt + 12g\ water = 16.308g\ brine \tag{4.18}$$

(4) Calculation of the mass of dry salt required to produce 4 kg of crushed salt from dry crushed salt and saturated brine:

$$4000g - 16.308g = 3983.692g \tag{4.19}$$

A comparison of the processes described above with Method 1 and Method 2 for the production of crushed salt mixtures with defined water content shows that, despite the somewhat more complex calculation of the required partial quantities of crushed salt, water and brine in Method 1, both processes require approximately the same amount of experimental work for weighing, drying and mixing the partial components. In view of the fact that the natural water content of crushed salt is not a fixed numerical value but scatters around an average value and, in particular, is to be regarded as variable depending on the storage conditions and storage time, it is recommended that the water contents specified in the tests be adjusted by Method 2, which is considerably less sensitive in this respect.

Performance of pre-compaction tests on classified crushed salt

A FULLER-optimised mixture formulation developed in the ELSA research project /ELSA 16/ and designated as OBSM was used as the classified crushed salt. The mixture is characterized by a synthetic combination of three fractions of rock crushed salt, which accumulate in the deicing salt production of GSES mbH (Glückauf Sondershausen Entwicklungs- und Sicherungsgesellschaft) in the Sondershausen mine. With the characteristic values documented in /ELSA 16/, the particle size distribution of the individual fractions can be determined according to Fig. 4.23.

For the laboratory investigations to be carried out by the project partner TUC, 500 kg of the crushed salt material packed by GSES in a big bag on a pallet was taken over in the shaft hall of the Glückauf Sondershausen mine on 22 May 2019 and transported to Clausthal by car.

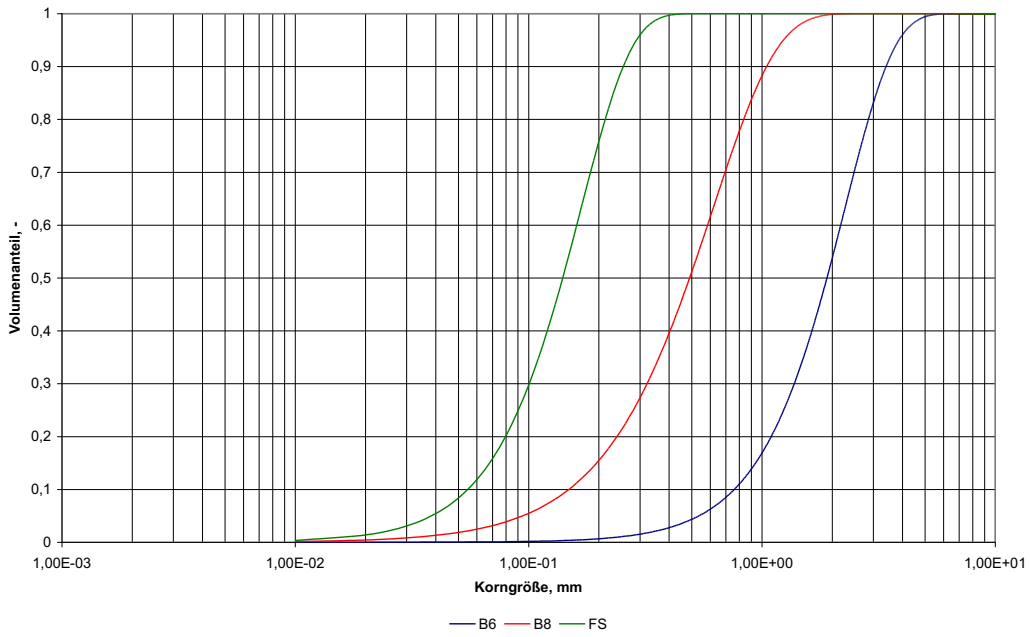

	denomination	graine size distribution d_5 - d_{95}	d_{50}	m	ratio
fraction 1:	band 6 (B6)	0,4mm bis 4,0mm	1,90mm	2,06	65,6 M%
fraction 2:	band 8 (B8)	0,1mm bis 1,0 mm	0,49mm	1,58	20,2 M%
fraction 3:	fine salt (FS)	0,03 mm bis 0,3 mm	0,14mm	2,01	14,2 M%

Fig. 4.23 Particle size characteristics of crushed salt mixture type OBSM

Fig. 4.24 documents the compaction tests carried out with the classified crushed salt material. In contrast to the preliminary tests on unclassified crushed salt, significantly lower water contents of minimum w = 0.1 % to maximum w = 1.0 % have been used. With regard to the effectiveness of the test specimen production, it can be stated with reference to Fig. 4.24 that a test specimen could only be generated from about every third crushed salt sample, since either the oil under pressure penetrated the test specimen during the compaction or the pre-compacted specimen broke during the production of the test specimen on the lathe. Nevertheless, it can be stated that even for the classified crushed salt material, which is characterized by significantly lower water contents, test specimens with defined porosity can be produced, depending on the level of compaction stress and the compaction time.

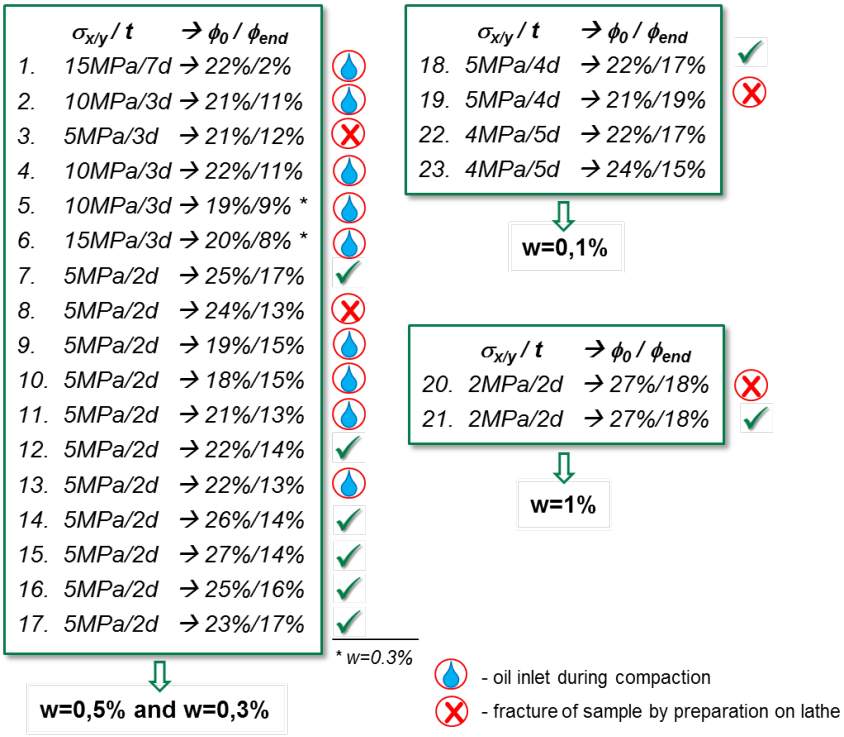

Fig. 4.24 Compaction tests on classified crushed salt

A first overview of the dependence of the compaction stress (confining pressure), compaction time and water content on the porosity of the pre-compacted crushed salt is shown in Fig. 4.25. Thereafter it is obvious, that the porosity decreases with increasing confining pressure, increasing compaction time and increasing water content. However, quantifiable correlations between porosity, confining pressure, compaction time and water content cannot yet be derived from the test results available to date.

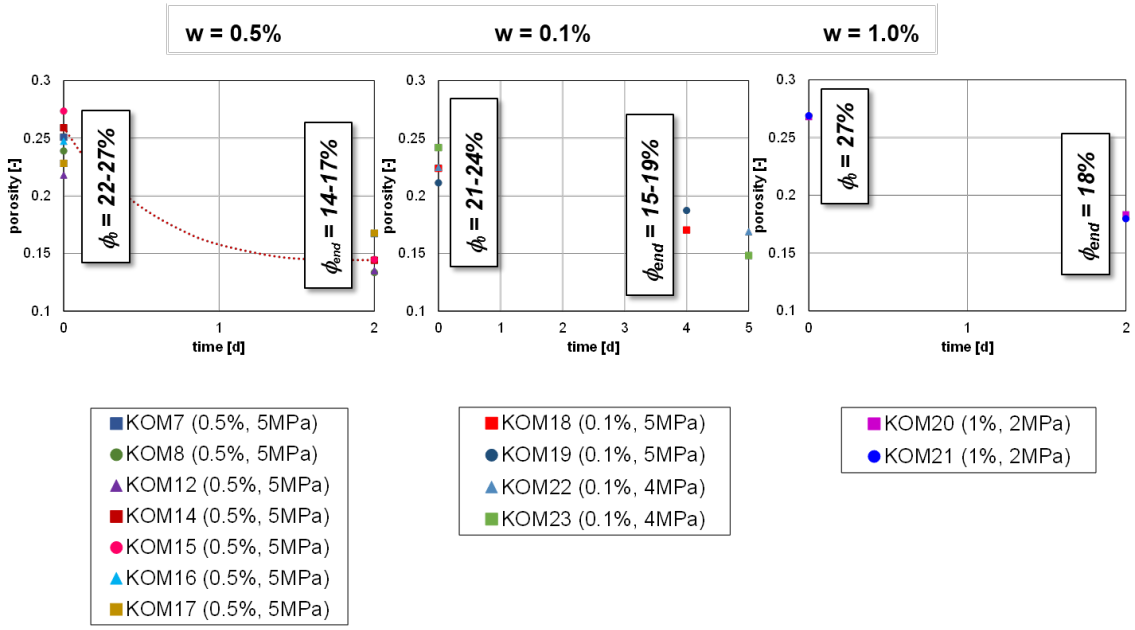

Fig. 4.25 Investigation findings on the influence of confining stress, compaction time and water content on the porosity of classified crushed salt

With regard to the correlation between porosity and ultrasonic wave velocity, Fig. 4.26 shows a finding analogous to the investigations of unclassified crushed salt. This means that there is a systematic correlation between porosity and ultrasonic wave velocity, which presumably differs from the correlation published in /POK 98/ due to the different stress geometry of the "plain-strain-compaction" performed here compared to oedometer tests.

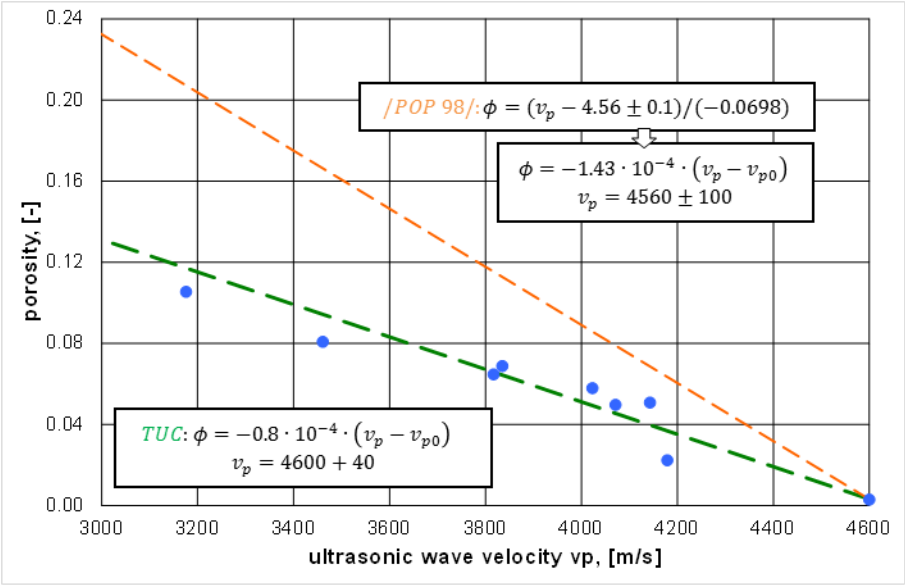

Fig. 4.26 Correlation between ultrasonic wave velocity vp and the porosity of pre-compacted crushed salt specimen

Fig. 4.24 shows that a total of 8 pre-compacted test specimens were produced within the framework of the research project and are available for further investigations. These test specimens can be used both for microscopic investigations to verify their homogeneity and, in particular, the fundamental suitability of the "time-lapse tests" and for further macroscopic investigations of the compacting behaviour at low porosity. Two of the test specimens were used for triaxial compaction tests within the framework of the research project (tests with the designation TUC-V2 and TUC-V3). The special features, objectives and results of these two tests are explained in detail in Section 4.8.2.

Two further test specimens (test specimens No. 14 and 15, Fig. 4.24) were axially halved and sent to the composite partners BGR and Sandia for microscopic examinations.

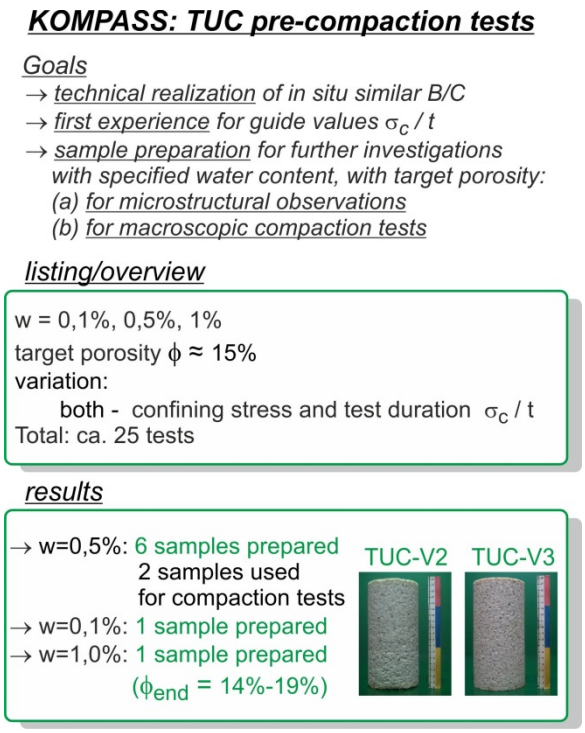

Fig. 4.27 Overview about the pre-compaction tests performed and the test specimens of classified crushed salt available for further investigations

4.5.2 Pre-tests by IfG – Small compaction cell

As pre-tests, using the suggested crushed-salt mixture, IfG performed uniaxial compaction tests in a quasi-oedometer cell (“small-compaction cell”) aiming on:

(1) Preparation of compacted specimens at defined loading conditions for microstructural investigations: Clarification of the influence of stress / time / temperature regime to receive reliable microstructure conditions at comparable strain

(2) Examination of the axial homogeneity using ultrasonic velocity measurements

The so-called “small-compaction cell” (Fig. 4.28) was constructed by the IfG especially for dynamic compaction experiments in the framework of the ELSA II-project for the investigation of pre-compacted crushed salt bricks, prepared at loading and temperature conditions up to around 100 MPa and 200 °C within a time span of some few minutes. To reduce the edge friction (silo effect), it is a steel pipe that opens out at the bottom with a cone of approx. 0.6 °. The bottom opening is closed with a base plate and the loose material is filled in from above. The piston is then passed through a brass bushing from above and the material is heated to the desired temperature in the cell. The material is then compacted in the RBA 2500 test system.

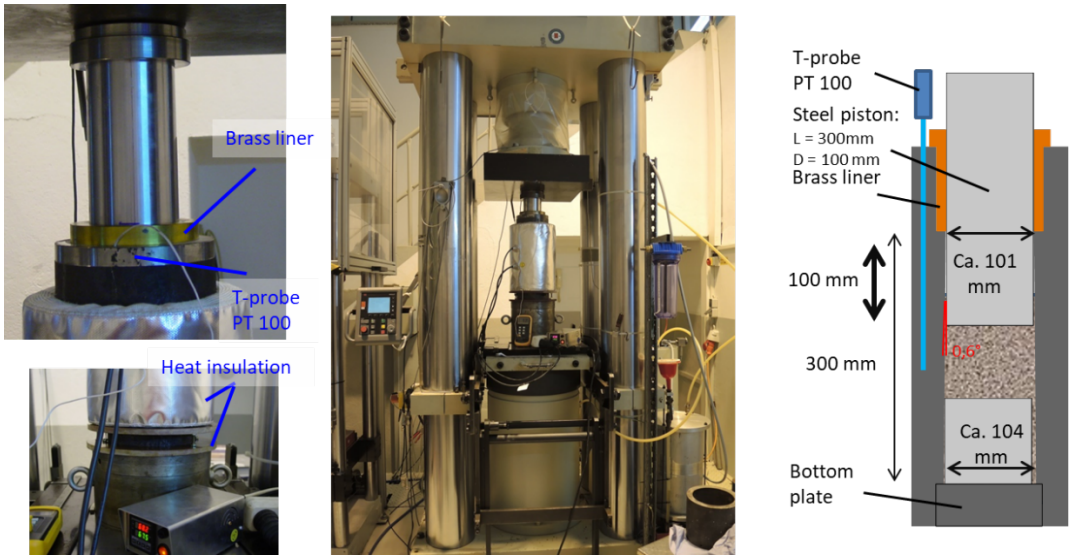

Fig. 4.28 The heated (up to 250°C) “small-compaction cell” of IfG. Left: details of the piston and the heating system; middle: the cell in the 2500 kN-load frame; right: schematic sketch

The following loading and sample, pre-consolidation and general boundary conditions are realized during the loading tests:

- Initial density as uniform as possible (ca. 1.4 g/cm^3) – initial sample height is around 150 mm
- Comparable loading path until the maximum stress of σ_{max} = 20 MPa
- Different temperatures and time conditions
    - Oedo2: short-term test (1 d loading) / high temperature: ca. 94 °C
    - Oedo3: long-term test – cold: 5 d loading at room temperature
    - Oedo1: long-term test – warm: 5 d loading at high temperature: ca. 94 °C

The specific load conditions are depicted in Fig. 4.29. After the samples were pressed out, they were photo-documented and measured with ultrasound. With the help of the

ultrasound measurement, a statement could be made about the compaction within the salt body.

The porosities are calculated according to /POP 98/, who performed similar compaction attempts, but with simultaneous transmission, based on the formula:

$$\varphi = (Vp - 4{,}56 \pm 0{,}1)/(-0{,}0698) \qquad (4.20)$$

φ = porosity [%]
Vp = P-wave velocity [km/s]

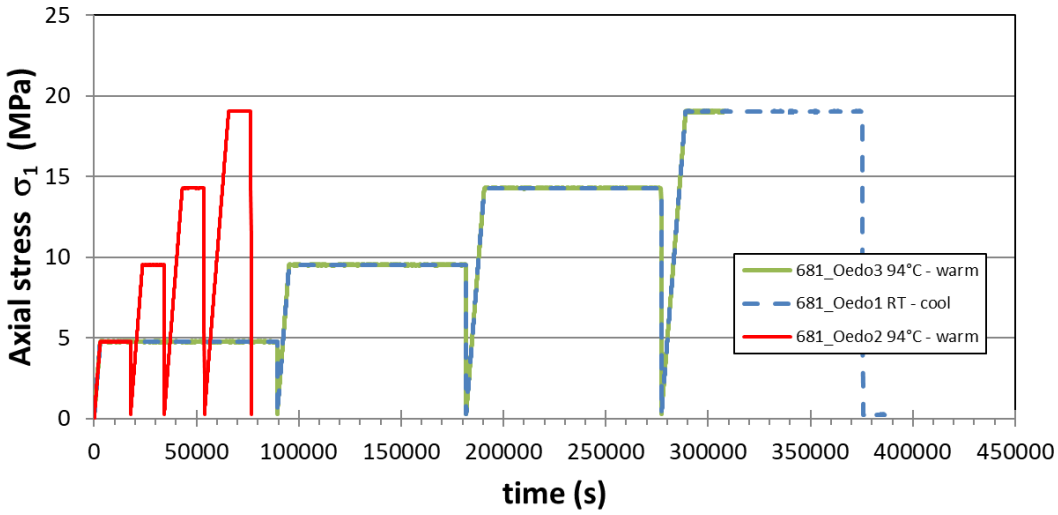

Fig. 4.29 Loading conditions during the pre-tests: axial stress vs. time

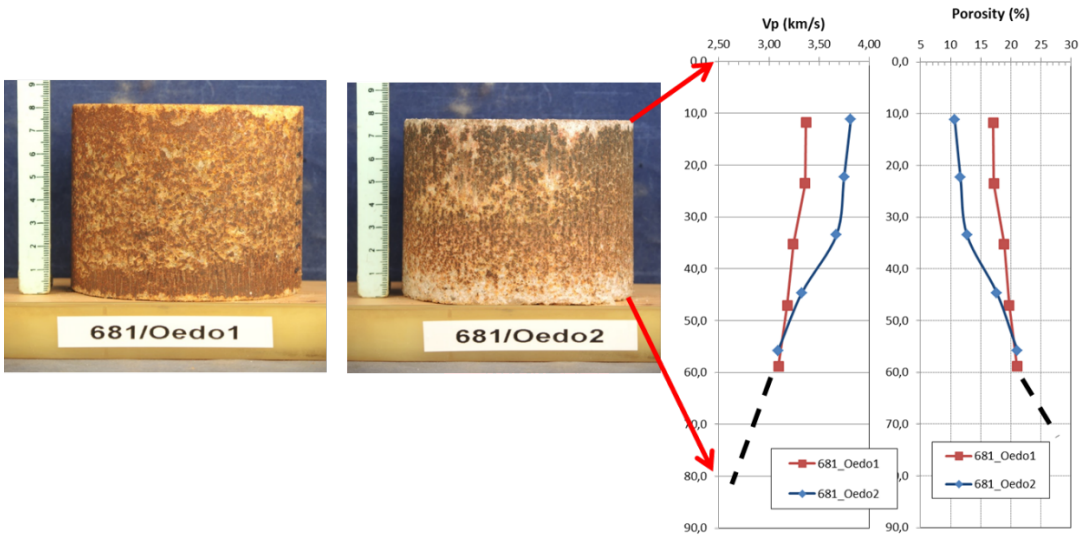

Fig. 4.30 Pre-test specimens – test of homogeneity: (left) deformed specimens at 94°C; (right) Ultrasonic wave velocity across the sample axis (radial measuring direction) at different heights and the resulting porosity

The data evaluation of the measured ultrasonic wave velocities respectively the so-derived porosity data clearly demonstrate that in the small-scale sample compaction tests the grain structure or consolidation state is significantly by the so-called “silo-effect”, i.e. friction between the crushed salt and the cell wall. Despite in the “warm” sample (94 °C) the consolidation is much higher than the room temperature samples the derived porosity varies from around 10 % at the top to estimated up to 20 % at the bottom.

This is interpreted as scale-effect, which means that, despite an initial height/diameter ratio of around 1.5, small “oedometer-cells” with diameters of around 10 cm are not adequate to simulate sufficiently consolidation processes of crushed salt, due to the bad random conditions. This shows the need to examine larger sample volumes, with the objective that the stress gradients in the sample are relatively smaller.

4.5.3 Big-compaction cell by IfG

The so-called “Big-compaction cell” of the IfG is normally used to investigate special geomechanical problems in mining, i.e. the compaction behaviour of granular backfill materials (e.g. crushed salt, crystalline gravel or sand, building materials). In contrast to the usual oedometer cell, where the diameter-to-height ratio of the sample is about 2, the diameter/height-ratio in the compaction cell is 0.5. Accordingly, the samples used in the compaction cell are 780 mm high and 514 mm in diameter which delivers a pre-compacted sample volume of ca. 160 l.

This facilitates (1) the controlled pre-compaction of a significant crushed salt mass to a specified final porosity and (2) the preparation of a number of cylindrical samples with different orientations (referring to the loading direction) and geometry (according to the requirements of the partners). The target-porosity in the pre-tests was, at least, < 15 %.

4.5.3.1 The cell and sample preparation

The principle of the backfill compaction cell is shown in Fig. 4.31. A servo-hydraulic testing machine is used to apply a vertical load up to 5,000 kN, which is equivalent to a vertical stress σ_1 of around 20 MPa. The induced stress in the steel wall depends on the magnitude of the lateral deformation caused by the horizontal stress. In addition, friction occurs between the backfill body and the steel wall, although a plastic foil fixed with grease on the wall is used. The friction can be calculated by determining the difference in the stress applied by the machine and the horizontal stresses measured by strain

gauges which are fixed in three layers on the outer steel wall in the middle of the backfill body. As estimate for the acting mean stress, in the following the mean value of the axial stress and the measured stress values of the three DMS-sections is used, which is roughly in the order of 40 % of the applied axial stress. An inductive displacement transducer measures the vertical compaction displacement.

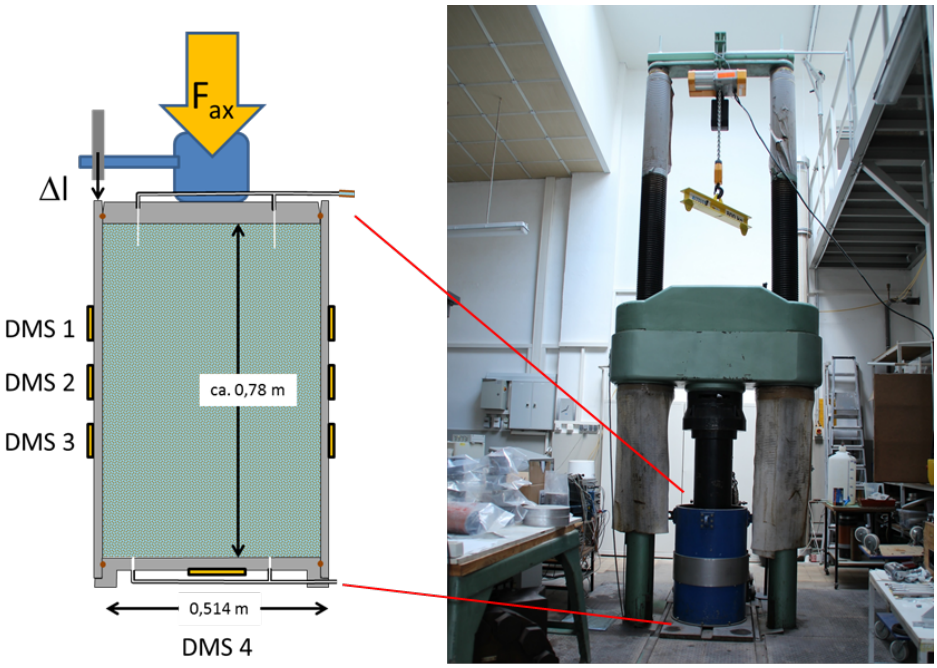

Fig. 4.31 The "Big-compaction cell" of IfG. Left: the cell with DMS-section; right: the cell in the 5,000 kN load frame

The preparation of the sample consists different steps (Fig. 4.32):

- Step 1 (a): Preparation of the cell (to minimize friction a foil is attached with grease at the wall; weighting of the empty cell)
- Step 2 (b - e): Stepwise manual filling (defined material weights) and compaction of the crushed salt in the cell, each to a specified layer height (15x). The totally emplaced material mass is checked by measuring the total weight of the filled cell; in the case of the “wet” pre-compaction tests the emplaced material was additionally moistened with a defined amount of water (1 wt.-%) using a spray bottle and stirred in a container. The nominal installation density for the wet test corresponded to the dry test.
- Step 3: quasi-uniaxial consolidation of the salt volume in the 5,000 kN load frame with a multi-step procedure until a maximum axial force (σ_1) of around 20 MPa (see chapter 4.5.3.2)
- Step 4 (f – g): Remove of the lower load plate and pressing out of the cylindrical

sample. The height and weight of the specimen are checked. Then, the sample is cut with a chainsaw in two halves (corresponding to a lower and upper level). After further stepwise segmentation sample cylinders are drilled out and prepared on a lathe with a specified geometry.

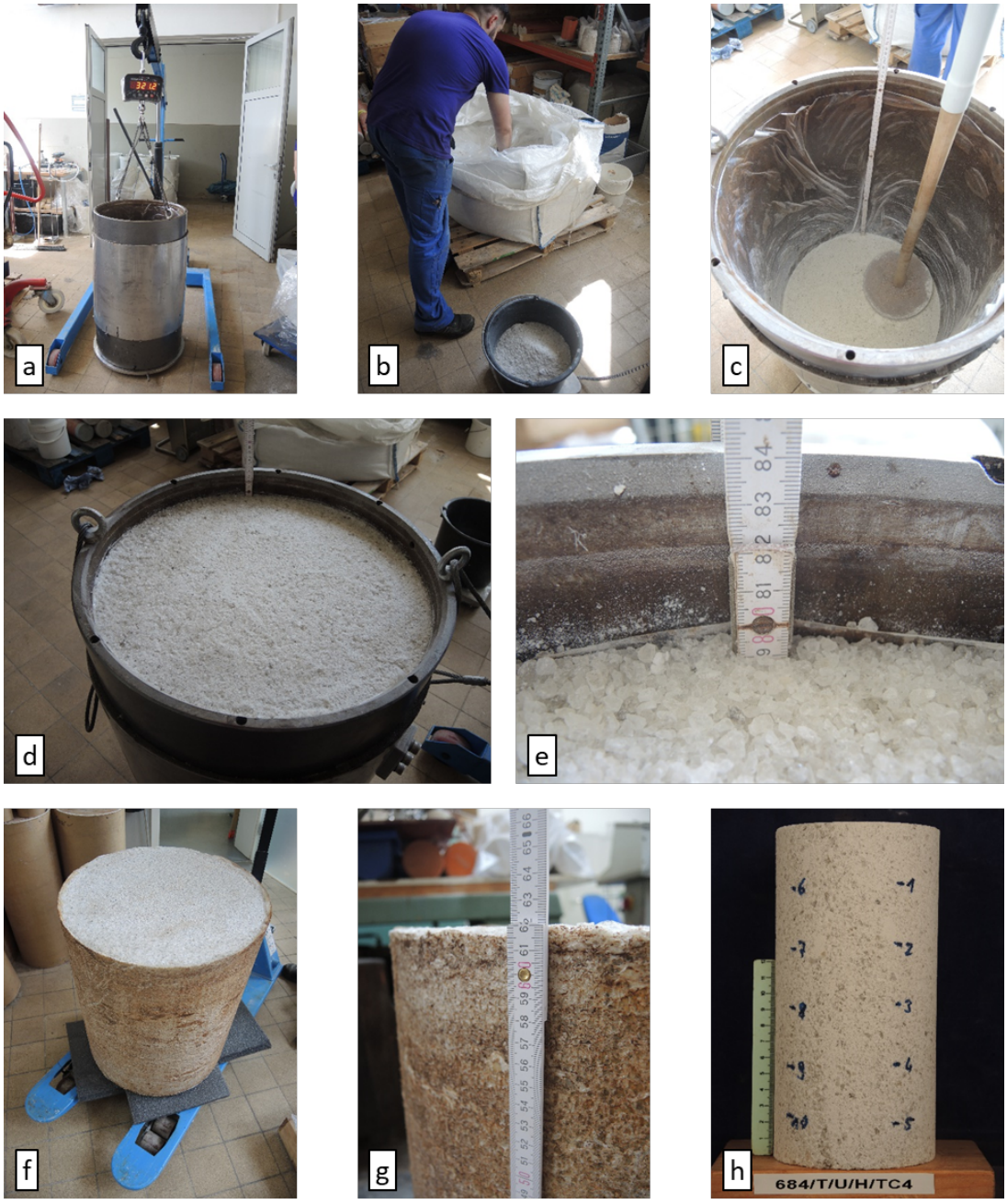

Fig. 4.32 Stepwise sample preparation

4.5.3.2 Test execution and results

At room temperature the cell was filled for the “dry” test to a specific height of 795 mm (equivalent to 237.6 kg backfill material and an initial nominal density ρ_0 of 1.405 g/cm³

with the initial porosity ϕ_o = 33.75 %) respectively for the “wet” test to 807 mm height (equivalent to 232.01 kg backfill material and 2.32 kg water resulting in an initial density ρ_0 of 1.435 g/cm³ with the initial (dry) porosity ϕ_o = 34.34 %). In the case of the wet sample the open pore space is partly filled with brine whereby dissolution effects of the water have to be considered[3]).

Both pre-tests (dry and 1 wt.-% added water) were performed as long-term multi-step test (1-month duration) with various loading steps, up to average backfill pressures of around 10 MPa. In all stages, the load was applied by increasing the axial force (around 10 kN per minute) in the vertical direction to the specific value. Then, a creep phase followed, taking at least 7 days. During the test the possible axial displacement is limited by the used strain sensor (around 100 mm), which requires unloading of the test at irregular time intervals. The specific loading steps with the measured volumetric strain are depicted for both tests in Fig. 4.33.

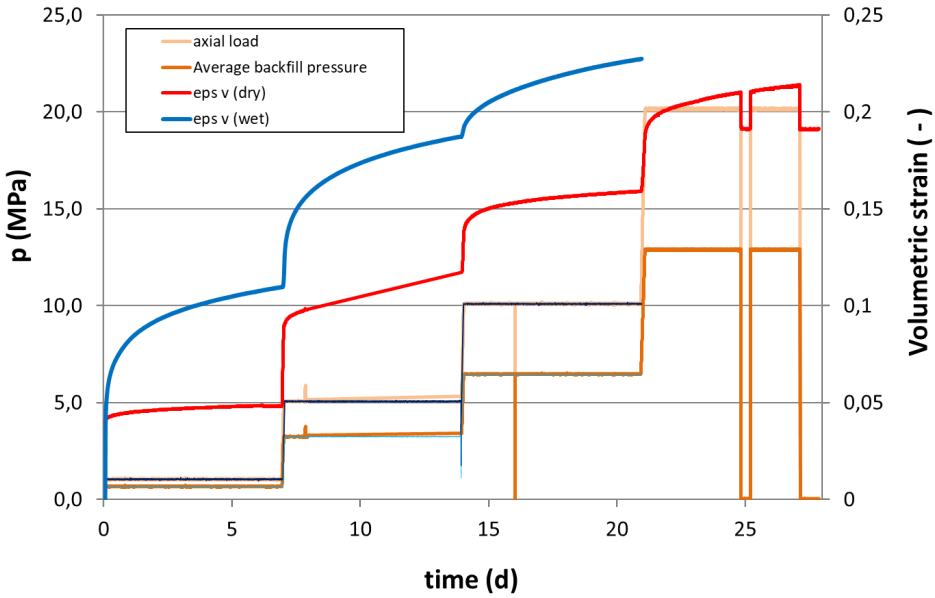

Fig. 4.33 Multistep load tests in the “Big compaction cell” with different initial water contents (0 – red curve - and 1.0 wt.-% - blue curve): volume strain and axial load respectively average backfill pressure vs. time

[3] Quantification of dissolution processes of halite by pure water is regarding the pore space volume in granular salt not simple. At 25°C, approx. 360 g of halite dissolve in 1,000 g H_2O /SAN 88/. With a density of 1.198 kg/m³ for the saturated NaCl solution and 2.165 kg/m³ for the halite, it follows that for 1 m³ of initial void volume - taking into account the water added - 0.171 m³ of halite are dissolved. However, when halite is dissolved until saturation in NaCl, the total volume balance is negative, i.e. the volume of saturated NaCl solution is smaller than the volume of water and halite required for its formation. Thus, the porosity increases more than the initial water volume. The factor of the volume increase regarding pore space volume due to the added amount of water is around 1.04.

Tab. 4.5 Test parameters for both pre-tests in the "Big-compaction cell"

IfG - Lab- test-no. (compaction tests)	**Humidity state**	**Axial load σ_1**	$\sigma_{iso\text{-}mean}$	stage duration	Creep phase	
					$\varnothing_{initial}$	$\varnothing_{end}$
		[MPa]	[MPa]	[days]	[%]	[%]
GV1_dry	**dry**	1	0.4	7.0	33.75	28.92
	dry	5	2.0	7.0	25.03	22.03
	dry	10	4.0	7.0	20.13	17.86
	dry	20	8.0	7.0	14.81	12.36
GV2_wet	**wet (1%)**	1	0.4	7.0	30.50	23.40
	wet (1%)	5	2.0	7.0	21.70	15.60
	wet (1%)	10	4.0	7.0	15.20	11.60
	wet (1%)	20	8.0			

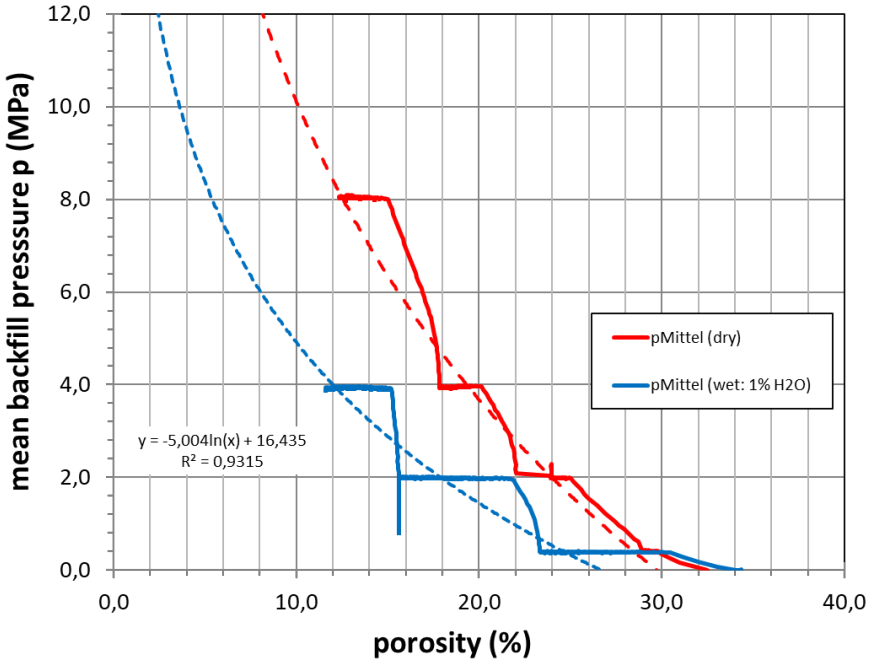

Fig. 4.34 Backfill pressure vs. porosity (pre-tests with dry and wet conditions)

It becomes obvious that the deformability of the crushed salt is significantly enhanced by adding some water. As outcome the respective relation between backfill pressure (i.e., the mean value of the principal stresses) and porosity for both tests was determined. The results are depicted in Fig. 4.34. They show that with decreasing porosity the backfill resistance increases as can be seen from the increase in the gradient of the logarithmic curve. It is worth to note that (1) for the “wet” material the general inclination is much lower and (2) that at constant load conditions creep deformation occurs. Whereas for the “dry” sample after 1 month loading a remaining (nominal) porosity of around 13 % was reached beyond the target aim of < 15 %, was the “wet” test in the loading state of 4 MPa interrupted (because of a machine breakdown with stuck of the 5,000 kN-cylinder), but

already in this state a porosity in the order of 12 % is reached. Extrapolation for the next foreseen loading step (at $\sigma_{iso} \approx 8$ MPa) delivers a final porosity in the order of around 6 %, which is realistic and can be used as target of the pre-consolidation in the next project phase.

4.5.3.3 Material conditions - homogeneity

Checking the validity of porosity values and the material homogeneity of compacted crushed salt material obtained during the pre-compaction tests is essential for future planning of the further pre-compaction procedure. Due to the ratio between height and diameter of the "Big-compaction cell" (of 2 : 1) friction effects at the wall may result in different compaction grades along the sample height, and, in addition, in anisotropy effects, as already observed in the pre-investigations Section 4.5.2.

This was checked by preparation of 6 cylindrical specimens, three each from the lower and upper segment half (drilling direction parallel to the deformation axis). As can be seen from Tab. 4.6 the samples have lower densities than expected from the final porosity reached during the compaction test (Tab. 4.1). This is related to inelastic volume expansion during and after unloading the cell. However, despite some scattering the average porosity in the top part is only 14.3±1.3 % and in the lower part is 15.9±0.4 %, i.e. 1.5 % difference exists which is significant but seems to be acceptable for the pre-compaction of a larger number of samples.

Tab. 4.6 Specimen parameters for both pre-tests in the "Big-compaction cell"

IfG - Lab- test-no. (all drilled perpendicular to the oedometer axis)	**position** (oedometer load)	**length**	**diameter**	**weight**	**density**	**porosity**
		[mm]	[mm]	[g]	[g/cm^3]	[%]
684/OEDO1/TCC1	**top**	120.66	63.58	710.2	1.854	14.39
684/OEDO1/TCC2	**top**	121.67	63.59	706.5	1.828	15.57
684/OEDO1/TCC3	**top**	120.13	63.52	717.6	1.885	12.94
684/OEDO1/TCC4	**lower**	120.83	63.55	702.2	1.832	15.39
684/OEDO1/TCC5	**lower**	121.29	63.65	701.7	1.818	16.03
684/OEDO1/TCC6	**lower**	120.12	63.68	693.8	1.814	16.24

4.5.4 BGR pre-compaction

The pre-compaction of the loose crushed salt takes place with the odometer principle. Its purpose is to generate manageable, cohesive samples for mounting in a triaxial cell.

Thereby, the initial void ratio in the triaxial experiments can be determined from the sufficiently accurate cylinder geometry of the pre-compaction cell, from the materials' solid matter density and from its humidity. Typically, the used loose crushed salt is prefabricated by a designated grain size distribution in an earlier process. Target size are samples with 100 mm diameter, 200 mm height and with a void ratio of e = 0.2 (16.7 %). The pre-compaction operates by a servo-controlled uniaxial loading that ensure a continuous, user-defined compaction speed.

In contrast to the usual oedometer cell of BGR, where the diameter-to-height ratio of the sample is about two, the target diameter to height-ratio in the compaction cell is approximately 0.5. The crushed salt was uniaxial loaded in a steel cylinder consisting of four quarter sleeves that encased an internal diameter of 100 mm. The quarter sleeves were removed when pre-compaction has been completed so that the sample was extracted without damaging it. Fig. 4.35 illustrates the apparatus used for pre-compaction of crushed salt under oedometric conditions.

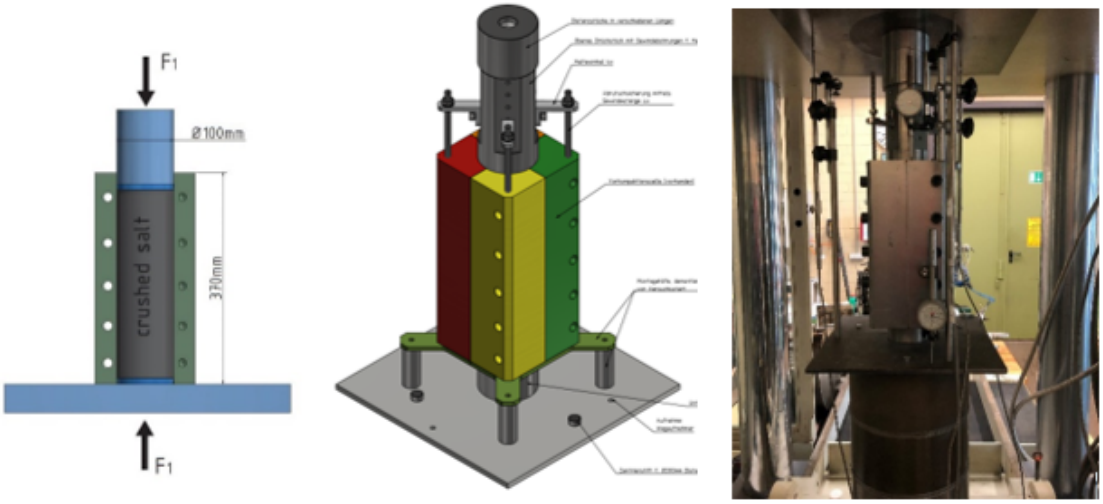

Fig. 4.35 Sketch and picture of the pre-compaction cell and its load frame

In order to achieve a homogeneous sample, the crushed salt gravel was poured in the cylinder in fife equal layers using a funnel and tube. This precaution aims to avoid segregation, i.e. a separation of grain sizes during the filling. Each layer was levelled with a fitting disk, giving it a hammer stroke before filling the next layer. Subsequent, the load piston was lowered on top of the thereby poured column of loose crushed salt.

For experiments with synthetically humidified crushed salt, the calculated amount of saturated brine was added to the crushed salt by spraying and subsequent mechanical mixing immediately before filling.

To ensure that the compaction was as homogenous as possible, the sample got compacted from both sides by reversing the cylinder after 50 % of targeted compaction. As a drawback, this sample flip implicates an interruption of the loading phase allowing the sample to elastically expand during a short (several minutes) relaxation. Next to the above-described apparatus, BGR recently uses also a second pre-compaction cell, wherein the axial loading was applied on both sample ends, top and bottom (Fig. 4.35 middle and right). This setup allows for a more homogeneous stress distribution inside the sample, making the unwanted sample reorientation obsolete.

For the axial loading during this pre-compaction, the user-defined compaction speed is depending on the sample density, i.e. depending on its compaction state. This speed should not exceed the in-situ rock stress that is expected for that corresponding density. Hence, for the most pre-compaction experiments, a maximum axial stress of 20 MPa was applied. This value is considered to mimic the in-situ like repository stress regime at a depth of approximately 850 m.

The pre-compaction procedure typically last about two to four weeks. After removal, the compacted specimens were measured with a calliper-gauge to derive its volume, its weight and hence its initial porosity. When not directly used for subsequent triaxial testing, it is stored in a vacuum-tight plastic foil.

4.6 Long-term triaxial tests

Using the samples derived by pre-compaction, several long-term tests evaluate the rheological behaviour (foremost the creep rate), the evolution of backfill resistance and porosity of compacting crushed salt. Tab. 4.7 provides a brief overview. The following sections describe each experiment individually. Note that the BGR-tests TK-031 and TK-033 derive from the previous REPOPERM project. They are again reported here as a recall for the numerical work (Section 5.4) that uses these tests for model parametrization and verification.

Tab. 4.7 Brief comparison of long-term experiments within this report. w = water content, GSD = grain size distribution, see text for details. *) Porosity values are not unconditionally comparable. They show intra-sample variance and are subjected to drastic measurement errors, foremost imprecise solid matter density determination. **) samples were subjected to 30 MPa load during pre-compaction ***) volume strain in the TUC-V3 pilot test was not carried out via EMC cylinder, but via significantly less precise synchronous cylinder, so that the values of the porosity may still be incorrect and, as a consequence, a repetition of the test with the use of EMC measurement technology is planned for the next project phase.

Experiment	Initial sample size	Material	Stress regime	Runtime	Temper-ature	Strain rate	Initial and final porosity*
TK-031 & TK-033	d = 100 mm h ≈ 200 mm	Asse "z2SP" w ≈ 0.05 wt.-% GSD = "DEBORA"	Multistep isostatic (σ_{max} = 20.4 MPa**)	295 d & 400 d	50 °C	$7*10^{-8}$ – $1.5*10^{-9}$ 1/s & $1.5*10^{-7}$ – $2.4*10^{-9}$ 1/s	16.48 → 7.76 % & 16.77 → 5.08 %
684/Oed1/TCC1 – TCC3	d = 60 mm h = 120 mm	KOMPASS reference material Dry & w ≈ 1 wt.-% GSD = Fig. 4.3	Multistep triaxial creep test (4 stages) (isostatic: σ_{max} = 1 to 30 MPa)	≈ 200 d	25 °C & 60 °C	10^{-4} – 10^{-9} 1/d	Around 16 % to 8 % Details Tab. 4.9
684/Oed1/TCC5 /TCC6	d = 60 mm h = 120 mm	KOMPASS reference material Dry	Multistep triaxial creep test (3 stages) (isostatic: σ_{max} = 5 to 30 MPa)	≈ 200 d	25°C	10^{-3} – 10^{-7} 1/d	Around 16 % to < 1 %
TUC-V2	d = 90.1 mm h = 180 mm	KOMPASS reference material w = 0.5 wt.-%	Multistep isostatic and deviatoric (σ_m ≈ 4/8/12/16/20 MPa, σ_v = 0.5/8.0 MPa)	150 d	30 °C	volumetric: $\dot{\varepsilon}_{vol} = 7.5*10^{-8} – 8.7*10^{-10}$ 1/s effective: $\dot{\varepsilon}_{eff} = 6.5*10^{-8} – 1.6*10^{-9}$ 1/s	16.7 → 9.5 %
TUC-V3	d = 90 mm h = 180 mm	KOMPASS reference material w = 0.5 wt.-%	Const. axial strain rate & isostatic	20 d	30 °C	axial: $\dot{\varepsilon}_z = 4.2*10^{-8}$ 1/s	13.5 → 1.4 %***

4.6.1 Triaxial compaction tests TK-031 and TK-033

4.6.1.1 Material

In both tests, loose crushed salt underwent an oedometric pre-compaction first in order to achieve cohesive, manageable samples (Section 4.5.4). Subsequent, the samples underwent a triaxial test phase. As raw material, crushed salt “z2SP” from the Asse mine (“Speisesalz”) was used. It resembles the grain size distribution of a previous “DEBORA” test, wherein the largest grains are below 8 mm. The solid matter density for dried “z2SP” salt was 2.169 g/cm³ with an average moisture content of w ≈ 0.05 wt.-%. The density of the moist salt is then ρ_{Sf} = 2.170 g/cm³. These densities have been determined by oven-drying at 105 °C until approximate weight constancy and X-ray crystallography. In the latter, mineral composition was quantified by a Rietveld analysis and multiplied by literature density values of each phase.

4.6.1.2 Pre-compaction

For pre-compaction, we followed the procedure described in Section 4.5.4. Tab. 4.8 complies characteristic data of the pre-compaction procedure. Fig. 4.37 shows the course of axial stress and loading rate and the resulting void ratio for the pre-compaction of both samples.

Tab. 4.8 Pre-compaction parameters of the sample preparation for tests TK-031 and TK-033

	TK-031	**TK-033**
Pre-compaction	VK-020	VK-022
Sample weight	2800.6 g	2800.2 g
Time	2 x 8 days	12 + 20 days
Loading rate $\dot{s}$	0.136 mm/h	Variable from 0.088 to 0.029 mm/h
Maximum axial stress including frictional resistance	29 MPa	30 MPa
sample height h_0 - h_E	24.9 - 19.65 cm	24.8 - 19.71 cm
void ratio e_0 - e_E	0.518 - 0.196 [-]	0.512 - 0.201 [-]

4.6.1.3 Triaxial testing

Both tests were performed in a triaxial apparatus (test unit: “M6”). Fig. 4.36 shows the system with its load frame, a sketch of the pressure cell based on the Kármán principle and a burette system. The latter to measure gas outflow during the experiment. The unit

holds samples with D = 100 mm and H ≤ 250 mm and can be loaded with a jacket pressure of up to 50 MPa below up to 100 °C. The axial force F (max. 1000 kN) is generated by the master cylinder below the pressure cell. The maximum internal cell pressure of 50 MPa is supplied by an external pressure intensifier. The test temperature is controlled by three independently working heating baths.

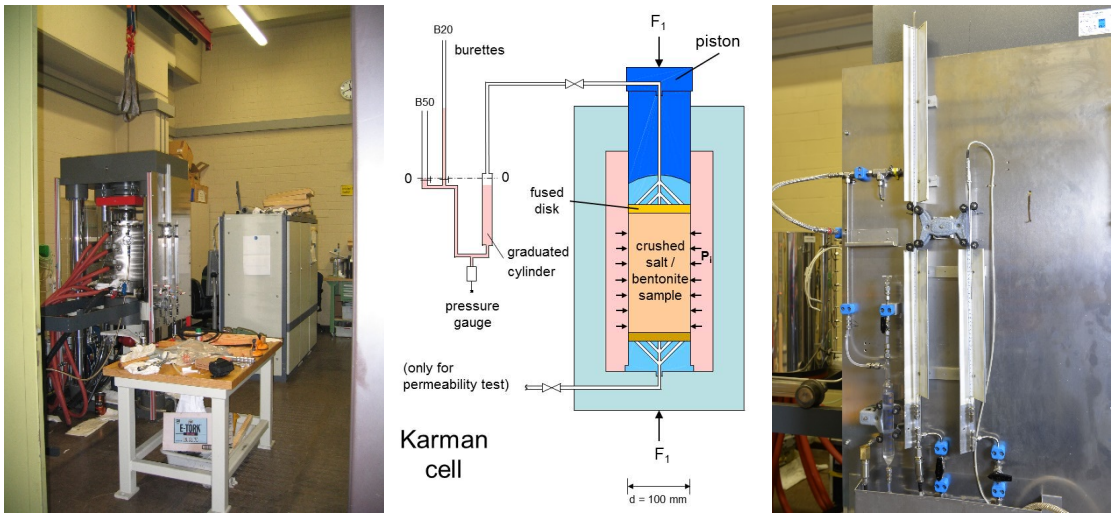

Fig. 4.36 Triaxial testing system with load frame, sketch of the pressure cell and the burette system

The triaxial compaction test TK-031 /STÜ 13/ was carried out as part of the REPOPERM project. The test included five loading phases, differing in mean stress ($\sigma_m = (\sigma_1 + \sigma_2 + \sigma_3)/ 3$): σ_m = 10.3; 12.3; 15.3; 18.4 and 20.4 MPa. The associated creep compactions lasted 7, 19, 26, 27 and 202 days, respectively. The loading rate during each phase was set between 1 and 3 MPa/d.

The second triaxial test (TK-033) was accomplished with the same raw material, a similar pre-compaction procedure (Tab. 4.8) and at the same test unit (M6). The test lasted for 400 days with only two loading stages with σ_m =15.3 for 34 days and a very long phase at σ_m =20.4 MPa for nearly one year.

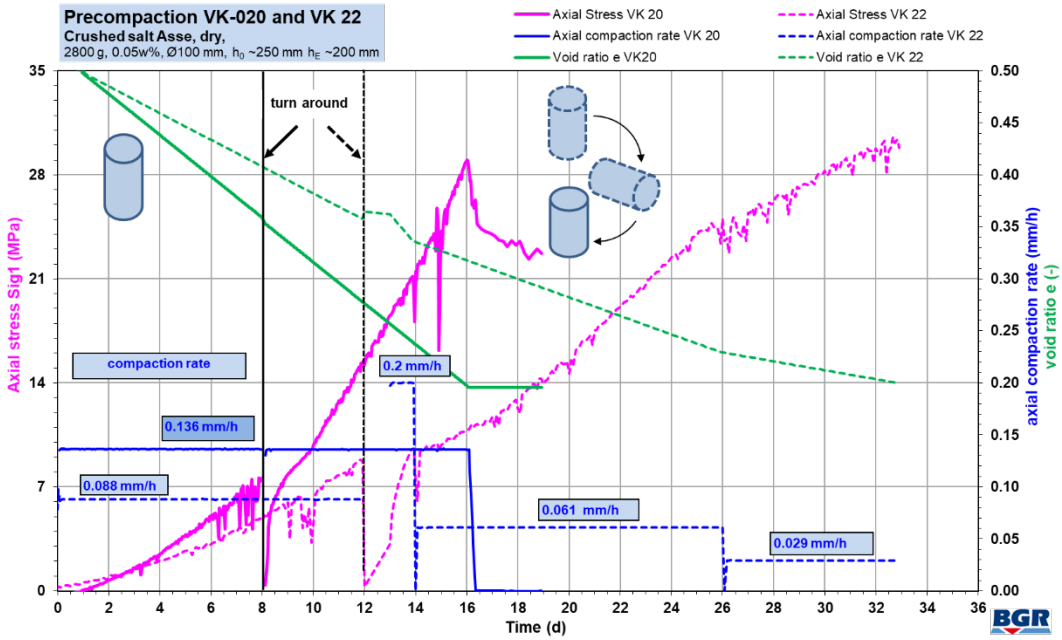

Fig. 4.37 Pre-compaction behaviour of the tests TK-031 and TK-033: Loading rate, axial stress and void ratio over time

The uniaxial pre-compacted specimen with the dimension d/h = 100/196.5 mm was further compacted in the triaxial test TK-031 from e_0 = 0.1973 (Φ = 16.48 %) to e_E = 0.0840 (Φ = 7.76 %). For test TK-033, the pre-compacted specimen had the dimensions d/h = 100/197.0 mm, yielding a void ratio of e_0 =0.2014 (Φ = 16.77 %). At the end of the test (day 400), its height was h= 188.31 mm, yielding a void ratio of e_E =0.0535 (Φ = 5.08 %).

In addition to the initial and final state parameters, where the samples were in an unloaded condition, we also measured the amount of air escaping from the samples during the test. Therefore, we used a burette system (Fig. 4.36).

Fig. 4.39a and b show for both tests the volumetric strain ε_v and respective strain rates $\dot{\varepsilon}_v$ as a function of time. Fig. 4.39b provides a more detailed resolution on an exemplary data inset. It shows void ratios, which were calculated before the start of a new loading stage, as well as at some additional values during the test.

For test TK-031, the last stage with σ_m = 20.4 MPa was carried out as a long-term test on creep compaction (202 days). It provides the material parameters in the residual porosity range ($2.1 \cdot 10^{-9} > \dot{\varepsilon}_v > 1.5 \cdot 10^{-9}$ 1/s). For technical reasons, the TK-031 test was unfortunately interrupted three times with short periods of unloading and reloading, which made the evaluation and the numerical benchmarking more difficult.

Test TK-033 is characterized by only two load phases with related creep. In comparison to test TK-031, the first two hydrostatic stress states are skipped, starting with a 34-day creep phase at an average stress of 15.29 MPa. The second creep phase then had a desired maximum stress of 20.4 MPa, similar to the test TK-031, but for a much longer duration. Consequently, test TK-033 achieves a larger compaction – as evident in the smaller final void ratio of 0.054, which corresponds to a porosity of 5.12 % (0.084 / 7.75 % for test TK-031). Likewise, the volumetric strain rate in the residual porosity range for the test TK-033 is smaller with $\dot{\varepsilon}_v > 2.4 \cdot 10^{-10}$ 1/s to $\dot{\varepsilon}_v > 1.5 \cdot 10^{-9}$ 1/s.

a.

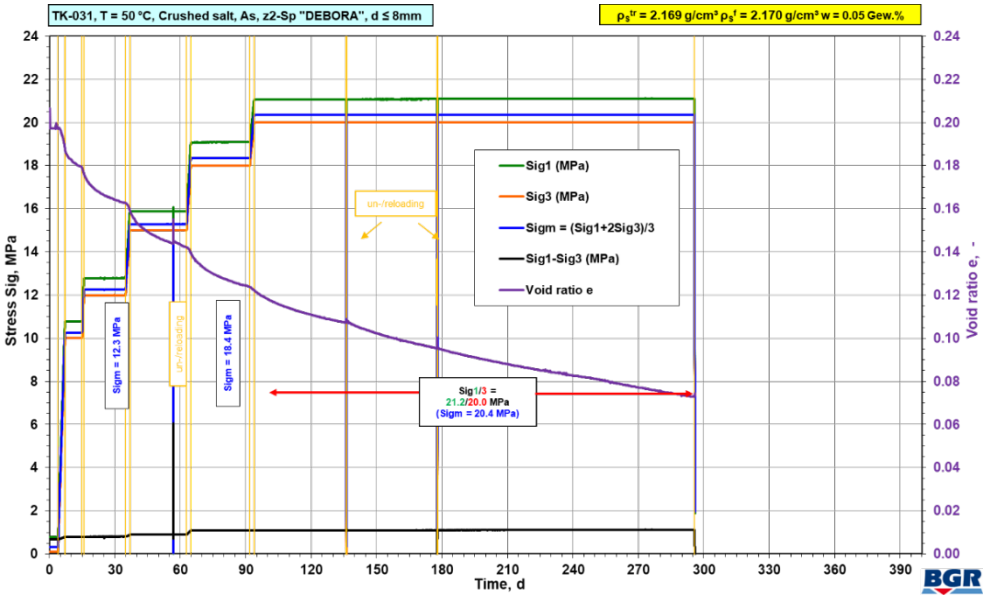

b.

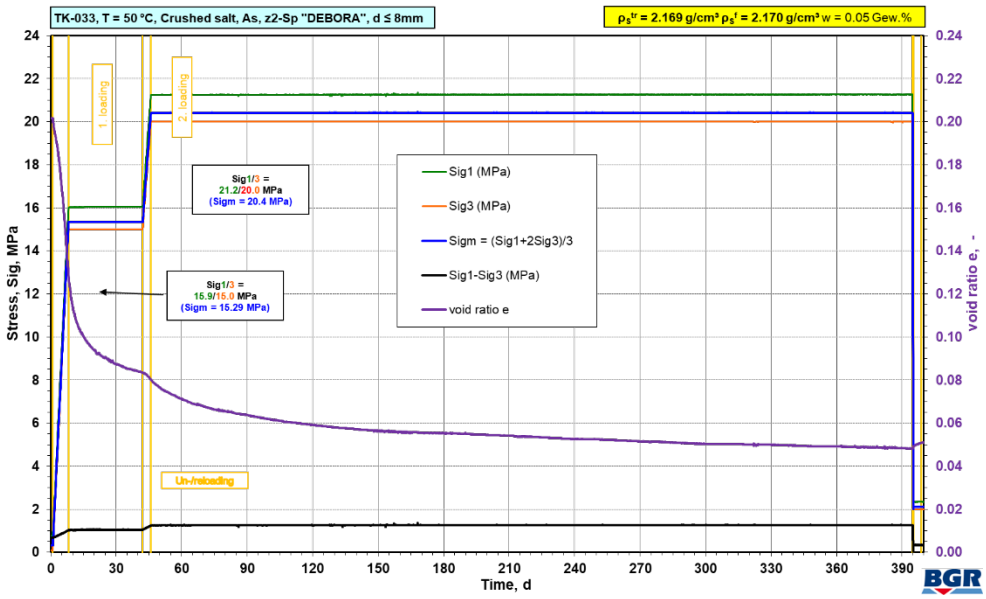

Fig. 4.38 Development of stress and void ratio over time for a) TK-031 and b) TK-033

a.

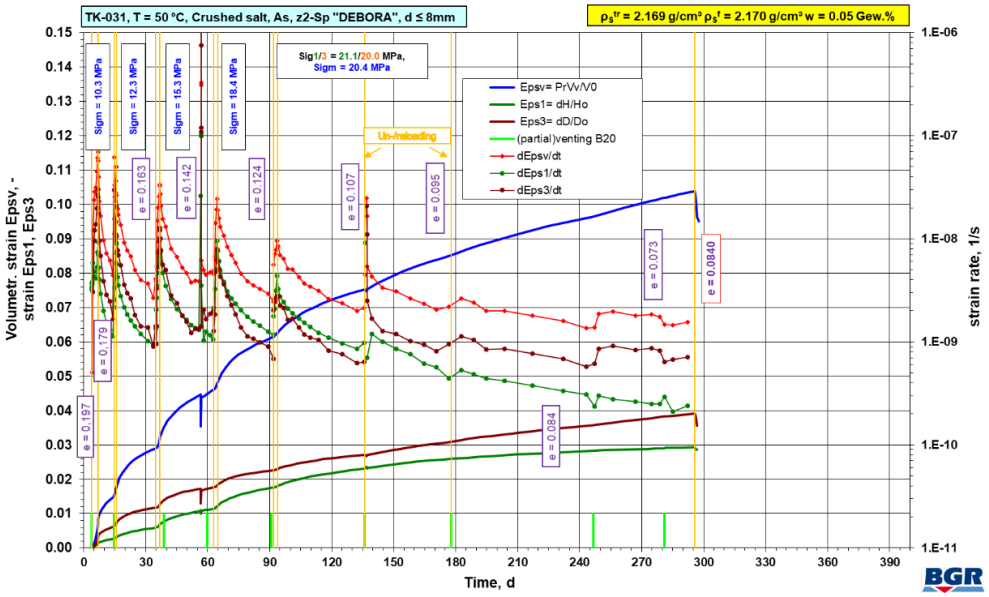

b.

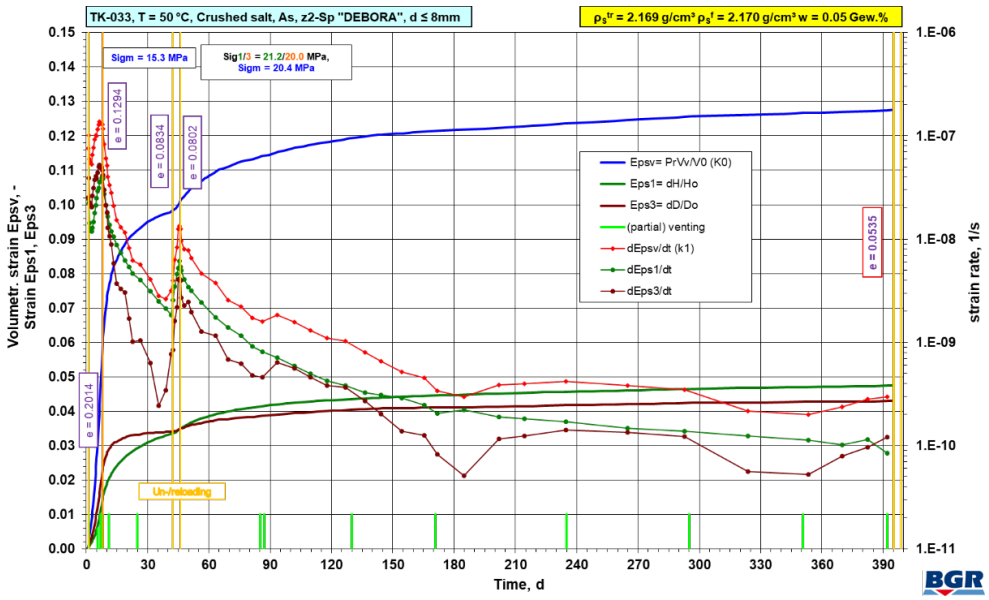

Fig. 4.39 Development of strain and strain rate versus time for a) TK-031 and b) TK-033

a.

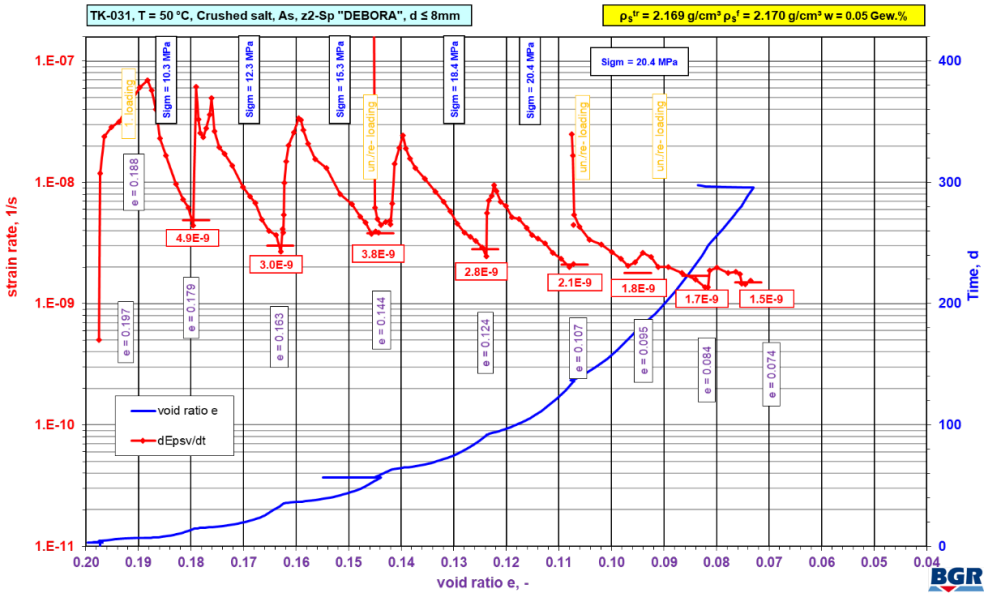

b.

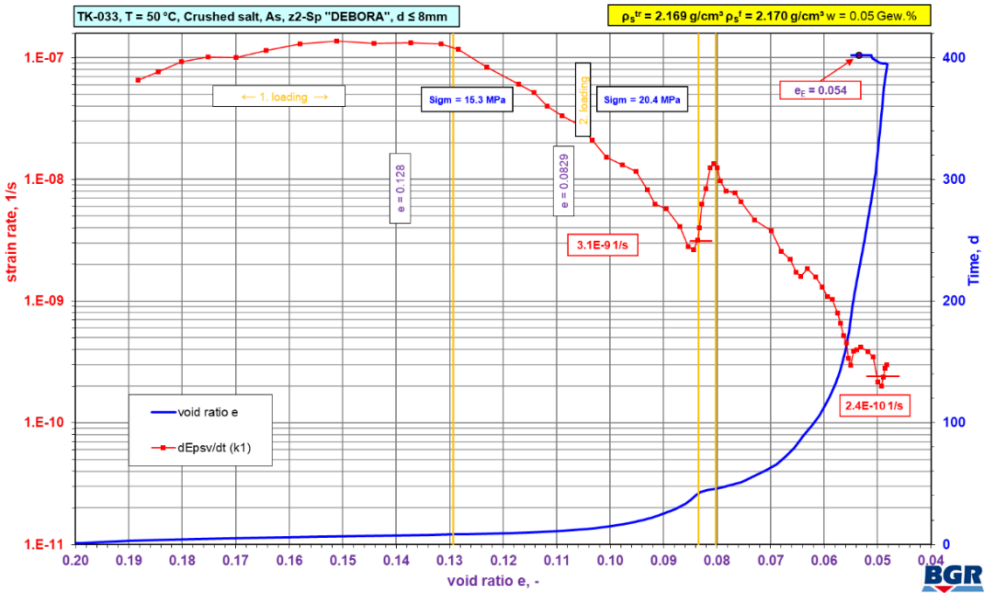

Fig. 4.40 Development of strain rate versus void ratio for a) TK-031 and b) TK-033

4.6.2 Isostatic long-term compaction test by IfG

One key objective of the KOMPASS-project is the development of a sophisticated strategy to derive necessary material parameters for the various modelling approaches. In anticipation of a coordinated procedure for that, the existing pre-compacted sample material has already been used for execution of long-term creep tests. Creep tests on salt samples are a well proven standard approach for determining creep properties of natural salt rock specimens at deviatoric conditions but allows also investigation of the isostatic compaction behavior of crushed salt. At least, 5 isostatic compaction creep tests were performed, whereby different loading conditions ($1 \leq \sigma_{iso} \leq 30$ MPa), different humidity

contents (initial dry and wet: 1 wt.-% H_2O) and two temperatures (T= 25 °C and 60 °C) were applied (for the individual experimental conditions see Tab. 4.6). The outcome facilitates preliminary conclusions regarding the following topics:

- Influence of the mean stress on compaction creep
- Moisture- and temperature-dependent compaction behavior (e.g. determination of the activation energy)
- Checking the validity of extrapolations from the obtained creep respectively porosity-development curves in comparison with the results of the pre-compaction tests

In addition, the deformed samples are very suitable for microstructural analysis, because they are representing a wide range of loading conditions respectively different porosities and the (the last loading state) is sufficient long, so during the long lasting test the specific subgrain structure should be developed.

4.6.2.1 Experimental approach

The quasi-hydrostatic compaction of the prepared samples is realized during creep tests in conventional triaxial cells after the “Kármán principle”, i.e. the confining pressure ($\sigma_2 = \sigma_3$) and the axial stress σ_1 can be controlled independent of each other. The cell itself is located typically in a loading frame to sustain the axial forces (Fig. 4.41). The axial stress comes from a hydraulic cylinder, which can be used in a range up to around 250 kN, while the confining pressure reaches up to 30 MPa. The axial load (according to the acting hydraulic pressure) is determined by a calibrated load cell before each experiment. The confining pressure was checked by digital pressure transducers. Both parameters are kept constant by a hydraulic system with pressure accumulator, ensuring an accuracy of ± 1 % during the tests.

IfG – Lab.-test-no. (isostatic creep tests)	humidity	σ_{iso}	stage duration	creep phase - porosity range -	
				$\Phi_{initial}$	Φ_{final}
		[MPa]	[d]	[%]	[%]
684/OEDO1/TCC1	dry	5	31.9	14.39	14.32
(25 °C)	dry	10	35.1	13.94	13.82
	dry	20	92.0	13.07	11.09
Total test time: 197 d	+T (60 °C)	20	38.0	-	-
684/OEDO1/TCC2	dry	10	31.9	15.60	15.49
(25 °C)	dry	20	35.1	14.43	12.83
	dry	30	92.0	12.03	7.77
Total test time: 197 d	+T (60 °C)	30	38.0	-	-
684/OEDO1/TCC3	dry	1	31.9	12.90	12.84
(25 °C)	dry	5	35.1	12.24	12.33
	dry	10	92.0	11.90	11.70
Total test time: 197 d	+T (60 °C)	10	38.0	-	-
684/OEDO1/TCC5	wet (1%)	5	31.9	16.00	7.82
(25 °C)	wet (1%)	10	35.1	7.66	3.98
Total test time: 197 d	wet (1%)	20	92.0	4.18	1.36
684/OEDO1/TCC6	wet (1%)	1	31.9	16.21	10.80
(25 °C)	wet (1%)	5	35.1	10.43	5.01
Total test time: 197 d	wet (1%)	10	92.0	4.71	0.88

Tab. 4.9 Test matrix for creep tests on pre-compacted crushed salt

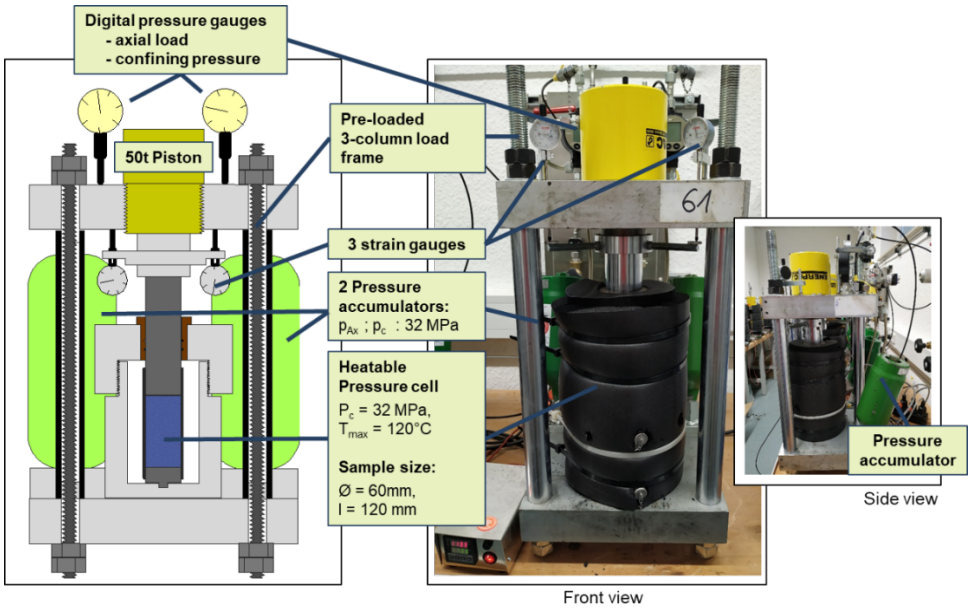

Fig. 4.41 The long-term creep test device. Left: schematic sketch of a hydraulic test rig. Right: Test rig with heatble triaxial cell

After installing the test samples in the triaxial cell, both, the axial and the radial stresses are increased simultaneously with a rate of $\dot{\sigma}_i$ = 0.1 MPa/min. When the desired stress level is reached, both, confining pressure and axial stress, are kept constant. In order to analyze the compaction behavior, the stress induced axial deformation is measured over time. The deformation measurement is carried out using three dial gages fixed around the samples, each one 120° hocked. The accuracy of the measured deformations is around ± 0.001 mm. All test parameters like axial deformation, confining pressure and temperature were checked and recorded daily.

4.6.2.2 Creep test results

As outcome of each multi-stage compaction creep test a three-part creep curve (strain vs. time) is obtained (followed by a kinking curve branch, in the case of a temperature increase), as exemplarily shown in Fig. 4.42. After hydrostatically loading of the specimen (resulting in an elastic compaction) the material starts to deform with time, i.e. creeps, depending on the acting mean stress. As a preliminary approach the measured axial strain is converted directly in the "hypothetical" volumetric strain: $\varepsilon_V = 3 \cdot \varepsilon_1$. Especially, in the 3rd loading stage (here at σ_{iso} = 20 MPa) it becomes obvious, that the compaction behavior is dominated by hardening, i.e. despite the high stress level and a test duration of ca. 100 days, no stationary creep is reached and the slope of the curve becomes with time more or less continuously smaller.

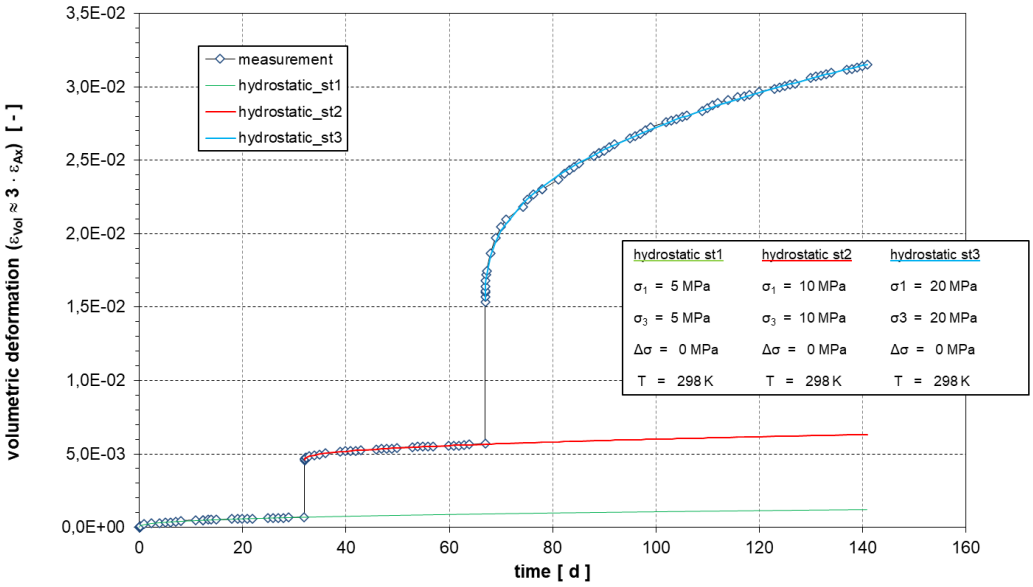

Fig. 4.42 Creep curve – sample 684/OEDO1/TCC1 (only the room temperature cycle is shown). Note the fitted curve segment using a power law

For further test evaluation, the volumetric strain curve of each creep phase (corresponding to the respective loading stage) was individually fitted by a simple power law function (with $t_{i = 1 \text{ to } 3} = 0$):

$$f(t_i) = \varepsilon_{vol} = a + b * t_i^c \tag{4.21}$$

a initial creep curve offset

b, c coefficients which were estimated using TableCurve2D®

This allows an easy determination of the slope of the measured curve based on the derivative: $f(t_i) = b * c * t_i^{c-1}$. The respective fitting parameters (a, b, c) of all test stages are summarized in Tab. 4.10.

Tab. 4.10 Fitting parameters based on a power-law relationship for creep curves of pre-compacted crushed salt

Sample/ Test-Conditions	σ_{iso}	T	Initial porosity ($Ø_{init}$)	Calculation of the porosity: $Ø_{f(t)} = Ø_{init} - a + b^{(c * t)} * 100$ with time t (d)		
	[MPa]	[°C]	[%]	**a**	**b**	**c**
684/OEDO1/TCC1	5.0	25.0	14.4	0.000	0.00018	0.379
	10.0	25.0		0.005	0.00024	0.417
	20.0	25.0		0.015	0.00306	0.385
684/OEDO1/TCC2	10.0	25.0	15.6	0.000	0.00034	0.337
	20.0	25.0		0.012	0.00504	0.329
	30.0	25.0		0.037	0.01202	0.274
684/OEDO1/TCC3	1.0	25.0	12.9	0.000	0.00024	0.254
	5.0	25.0		0.005	0.00028	0.317
	10.0	25.0		0.010	0.00019	0.523
684/OEDO1/TCC5 **(wet)**	5.0	25.0	16.0	0.001	0.02074	0.396
	10.0	25.0		0.083	0.00522	0.491
	20.0	25.0		0.118	0.00793	0.282
684/OEDO1/TCC6 **(wet)**	1.0	25.0	16.2	0.002	0.01219	0.420
	5.0	25.0		0.056	0.01209	0.437
	10.0	25.0		0.114	0.00546	0.433
"Big-compaction cell" **(dry)**	0.4	25.0	33.85	0.037	0.00791	0.196
	2.0	25.0		0.130	0.01971	0.195
	8.0	25.0		0.187	0.01515	0.327
"Big-compaction cell" **(wet)**	0.4	25.0	33.3	0.019	0.06421	0.184
	2.0	25.0		0.113	0.04566	0.258
	4.0	25.0		0.188	0.01703	0.435

4.6.2.3 Data-evaluation / discussion

Using the derived parameter sets, compaction creep curves and compaction rates were calculated as a function of time, respectively for the duration of the tests and a time period > 1,000 years (Fig. 4.43). For a better overview, in addition, the compaction behavior is also shown as figure, using a logarithmic time scale (Fig. 4.44). Despite only some few tests were performed the available data sets allow preliminary conclusions regarding the reliability and the long-term prognosis of the test results.

Depending on the applied test conditions significant differences regarding the time dependent compaction of crushed salt exist. Taking in mind, that the consolidation already at 15% remaining porosity starts the following conclusions can be drawn:

- The compaction behavior of “dry” crushed salt is generally dominated by time-dependent hardening (no stationary creep), which is likely due to dislocation creep or the mechanical displacements in the grain structure /WIE 17/. This results in a continuous decrease of compaction rate; already in the experimental time scale of some months the compaction rates range over more than 3 orders, respectively for the period of 1,000 years over more than 6 orders. In detail the spreading corresponds to the following conditions (referred to the 1,000 years period)
    - At dry conditions, increase of the isostatic stress (σ_{iso}) from 1 MPa to ≥ 20 MPa results in an increase in compaction rate by around 3 orders.
    - At σ_{iso} ≥ 20 MPa the differences between the two tests are within one order.
    - At σ_{iso} = 5 to 10 MPa there is a significant scattering over more than 2 orders, but, surprisingly, as outcome from three tests the compaction rate seems to be highest for the lowest porosity.
    - At σ_{iso} = 1 MPa the compaction creep is quite low, i.e. no significant compaction is obtained.

➔ For dry samples the residual target porosity of around 1 % is only reached if the acting stress is significantly higher than 10 MPa; at σ_{iso} ≥ 20 MPa porosities in the order of 1% are reached in the order of some few 100 years.

- Adding of water enhances drastically the efficiency of the compaction process due to the efficiency of hydro-chemical based intergranular deformation processes.

- At remaining porosities higher than around 5 – 10 % the compaction rates are high and only weakly affected by the order of the acting stress.
- As an important observation it is worth to note that for the wet samples in a porosity range of around 5 – 10 % the compaction rates become lower, obviously due to the effect of the minimized residual porosity.

➔ An estimate of the necessary time span until reaching porosities in the order of some few percent (Fig. 4.44) shows that in all cases for the wet tests this state can be reached within some few years already at low stresses (σ_{iso} = 1 MPa).

– If the same evaluation procedure is performed for the available data from the two pre-consolidation tests in the “Big compaction cell” (Fig. 4.44), the results for the “wet” test are quite comparable with the “long-term creep tests”, resulting in a residual porosity of the target of around 1 % in ca. 1 year. However, extrapolation of the compaction process at “dry conditions” with $\sigma_{iso} \approx 8$ MPa results in unrealistic fast compaction. The test duration for the compaction with one week is obviously too short.

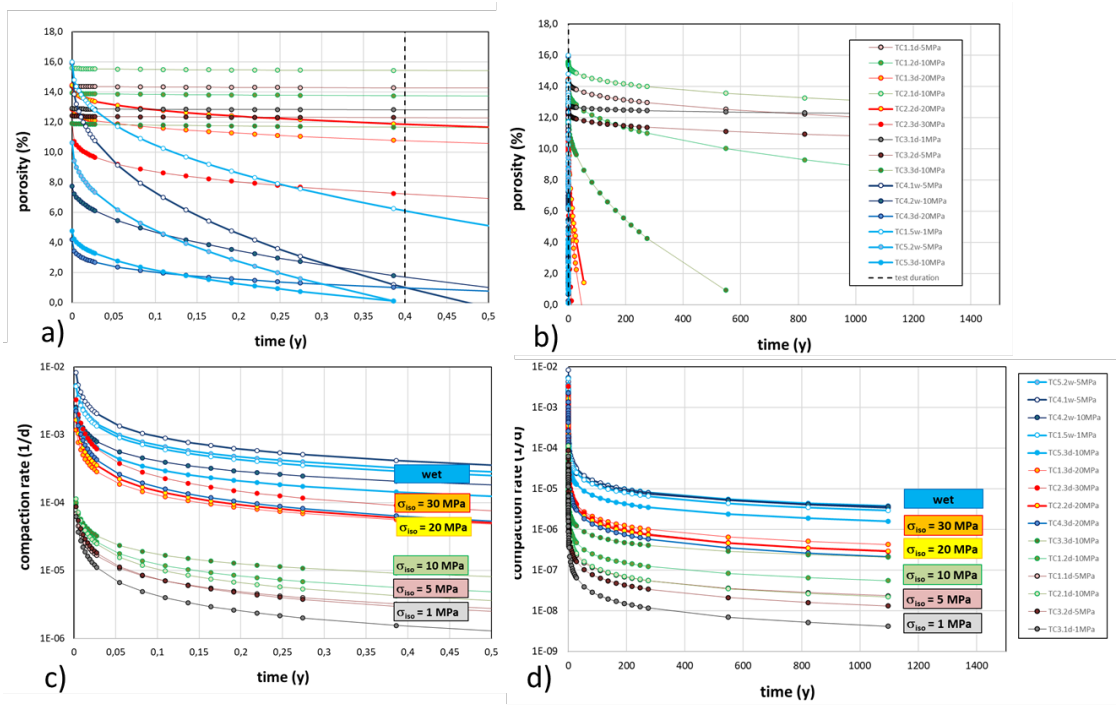

Fig. 4.43 Calculated compaction and compaction rate curves, based on the experimental parameter sets given in Tab. 4.10: a) and c) for the experimentally investigated test duration; b) and d) extrapolated for a time scale > 1,000 years

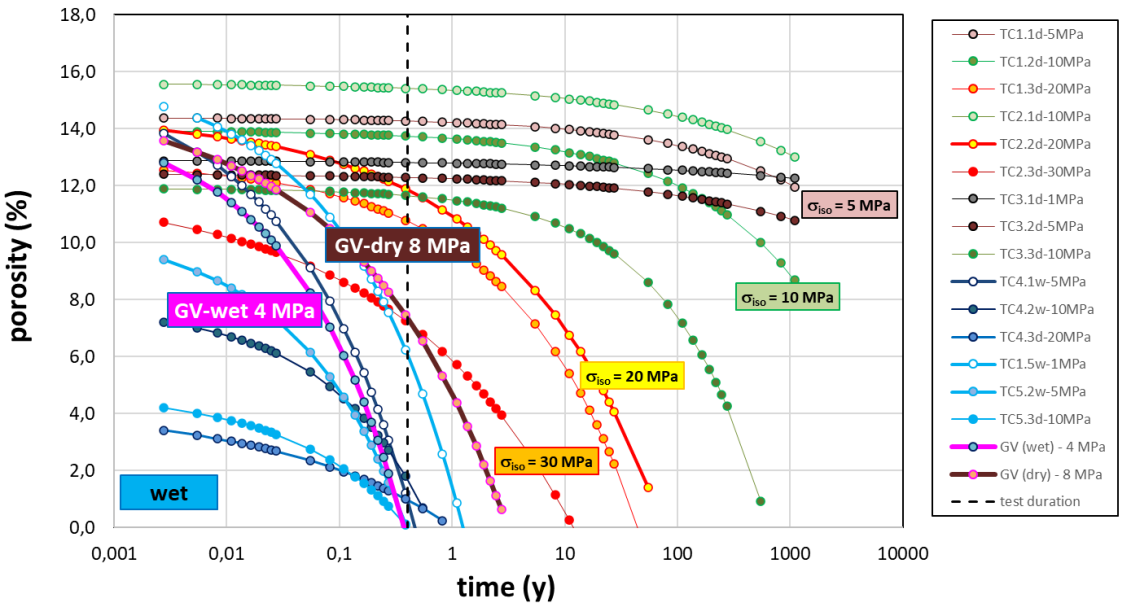

Fig. 4.44 Calculated compaction (porosity decrease) as function of time in a logarithmic scale

Additionally, in the dry experiments the temperature was varied in the final creep stage (from 25 °C to 60 °C) which allows an estimate of the activation energy. The measured values of Q are in the order of 20±5 kJ/(mol*K) for samples in a porosity range ranging from 12 to 8 %. These values are significantly lower than those given for rock salt measured during (mostly uniaxial) creep tests (e.g. /HUN 94/).

In summary, the preliminary test results show the suitability of long-term compaction tests (creep conditions) to derive reliable information on the time- and stress-dependent compaction behaviour. Despite the usually limited test duration of up to some months to few years, an extrapolation of the different datasets to longer time scales should be possible.

However, it has to be mentioned, that the volume deformation is the crucial parameter to describe the efficiency of compaction resp. porosity change. Since only the axial deformation of the creep specimen is measured this parameter need to be interpreted as part of the overall volumetric compaction. An often-used rough approximation is $\varepsilon_V = 3 \cdot \varepsilon_1$ but /IFG 06/ demonstrated based on creep tests of pre-compacted bricks that this value may be too high due to friction between frontal planes of the sample and the pistons. They found that the ratio $\varepsilon_v/\varepsilon_1$ is significantly lower than 3 and varies between 1.9 and 2.6, whereby a weak tendency of an increase depending on the stress conditions is observed. Therefore, the determination of a proportional factor is a fundamental aim in

the appraisal of the creep test results and needs to be intensively investigated in the future.

4.7 Microstructural analysis of experimental compacted crushed salt

4.7.1 Microstructures in pre-compacted samples

Over the duration of the KOMPASS project, four pre-compacted sub-samples were sent to Sandia National Laboratories (USA) from the IfG, as shown in Tab. 4.11. The table lists the sample identification number, oedometer ring's inner diameter, sample temperature during pre-compaction, axial stress applied by the oedometer piston, pre-compaction duration, and final average relative porosity. All four test specimens were pre-compacted under dry conditions. The starting material characterization, oedometer compaction curves, and general definitions on deformation microstructure mechanisms can be found in Section 3 and 3.2, respectively. Three samples, of equal initial density, were compacted in a small oedometer cell of 0.1 m diameter (Fig. 4.45 a.-c.) and one in a larger cell of 0.514 m diameter (Fig. 4.45d.), noted as 'big compaction cell' in Section 4.5.3. Rather than send the entire large cell sample, the IfG sent Sandia two 100 mm diameter by roughly 25 mm thick cylindrical sub-samples. For the small oedometer samples, porosity decreases along the sample axis from bottom to top due to less force available for compaction from side friction of the sample cell wall.

Tab. 4.11 Test parameters for pre-compacted samples from oedometer experiments

Sample ID	Oedometer Inner Diameter [m]	Temperature [ºC]	Axial Stress [MPa]	Duration [d]	Final Rel. Porosity [%]
681/Oed 1	0.1	Ambient	20	5	14.8
681/Oed 2	0.1	94	20	1	10.5
681/Oed 3	0.1	94	20	5	10
Big Oed cell Dry (sub-sampled)	0.514	Ambient	20	28	13.6

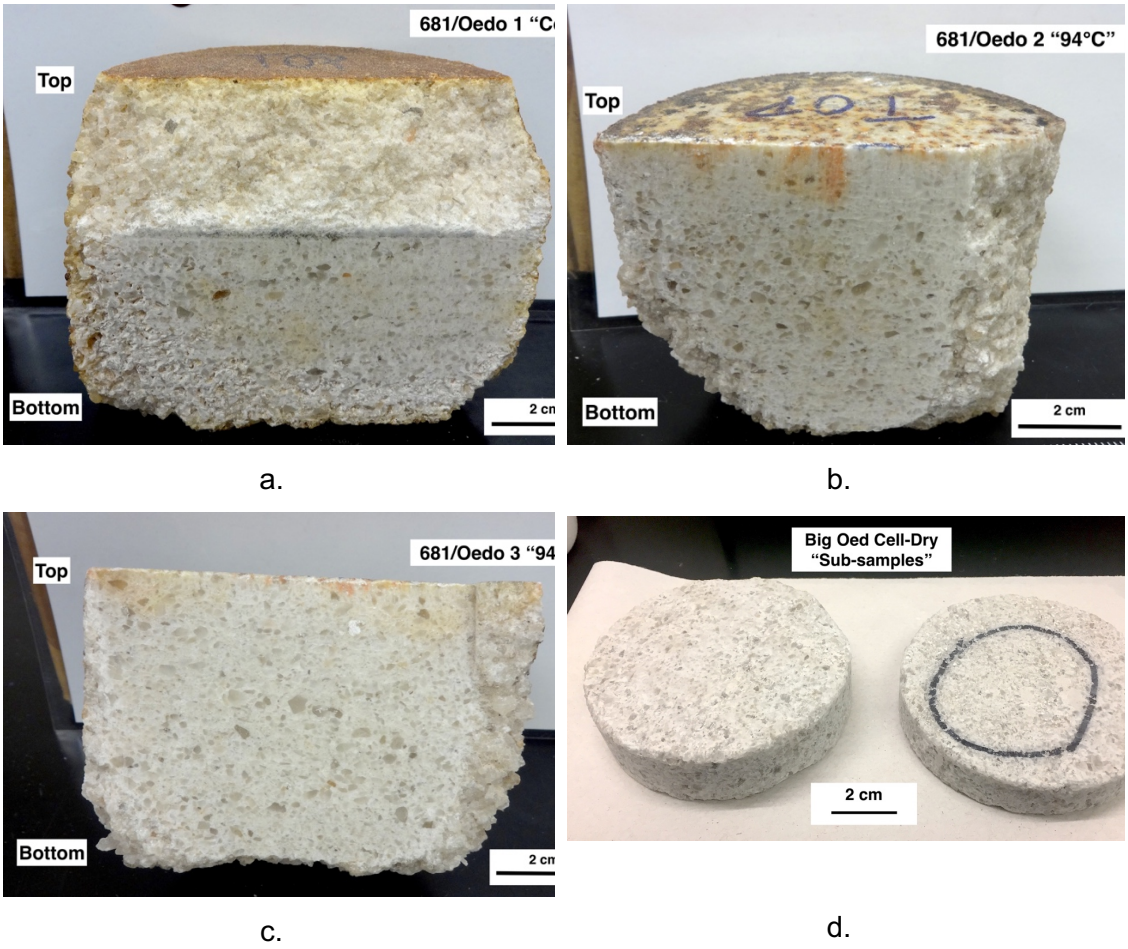

Fig. 4.45 Oedometer test samples as received from IfG, prior sample preparation of thick-thin sections

Microstructural investigations

After preparation, all thick-thin sections were examined under a Zeiss AxioScope 5 optical microscope, equipped with ZenCore imaging software, in both reflected and transmitted light. Reflected light was utilized to observe grain sizes, shapes, boundaries, and pore structures, while transmitted light was utilized to view fluid inclusion planes and bands with any attributable microcracks in the grain structure from deformation.

Fig. 4.46 through Fig. 4.49 are the resulting photomicrographs for each respective sample. Each of the four samples experienced mechanical grain rearrangement and cataclastic grain deformation indicated by cracking across and through grains, as shown in Fig. 4.46 c.-f., Fig. 4.47 c.-d., Fig. 4.48 c.-d., and Fig. 4.49 a.-c. & e, which can also be seen from areas of fluid inclusions forming linear patterns within grains. Contact points between grains, or at grain boundaries, mostly appear to be cohered together from reflected light images (Fig. 4.46 – Fig. 4.48, a. & b.), instead of surrounded by smaller particles due to abrasion or grinding.

The effect of pre-compaction temperature can be seen by comparing the three smaller oedometer test samples. The two pre-compacted at 94 ºC exhibit areas of plastic deformation at grain boundaries, as displayed in Fig. 4.47b. and Fig. 4.48a.-b, which could indicate pressure solution redeposition or dislocation motion. The ambient temperature sample exhibits relatively little cohesion between grains in Fig. 4.46a-b. This comparison is consistent with the 94 ºC samples' significantly lower relative porosity in Tab. 4.11.

Samples 681/Oed2 and 681/Oed3 were pre-compacted at 94ºC and up to 20 MPa axial stress, yet for different durations. The 5 times longer pre-compaction of 681/Oed3 did not lead to any qualitative microstructural differences, which is consistent with the minor difference in final relative porosity between the two samples in Tab. 4.11. Although this result is encouraging, it may be useful to compare pre-compaction durations at ambient temperature, where dislocation motion and any pressure solution redeposition would occur more slowly.

Grains from the big oedometer sample, pre-compacted at ambient temperature over a long duration, experience a high degree of cracking and damage (Fig. 4.49 a., b., & e.), as well as abrasion among grains (Fig. 4.49 5d.). The subgrain structure from the large oedometer sample can be seen in Fig. 4.49f. showing a polygonal substructure.

a.

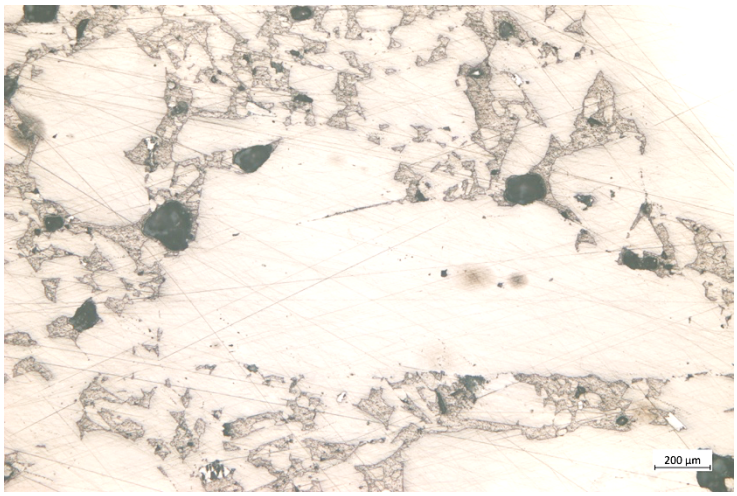

b.

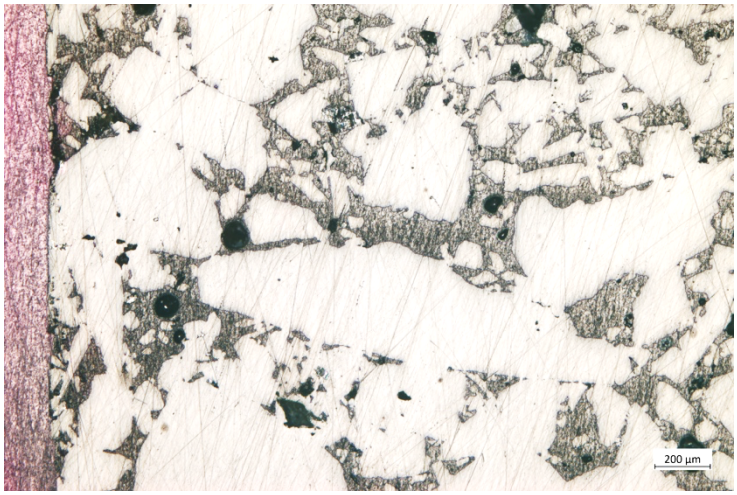

c.

d.

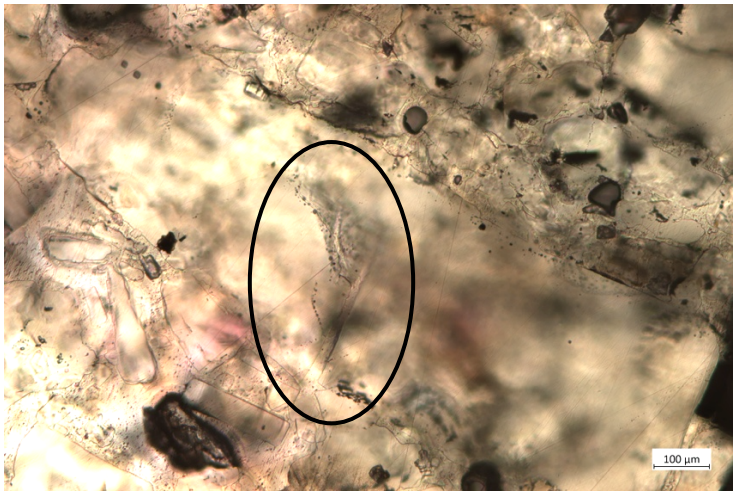

e.

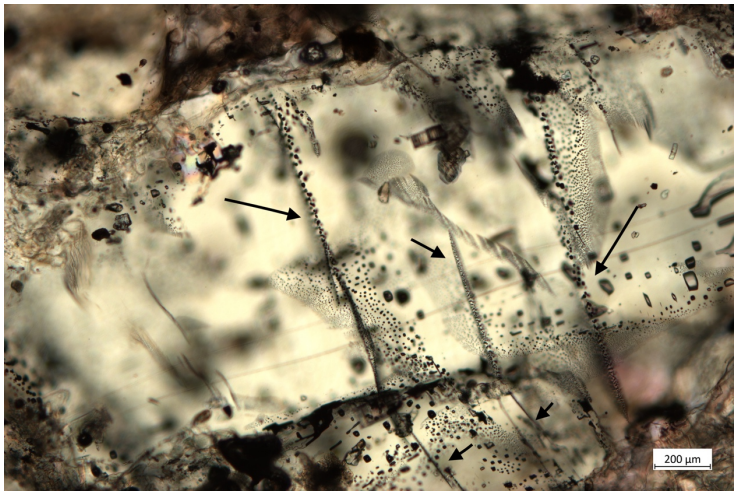

f.

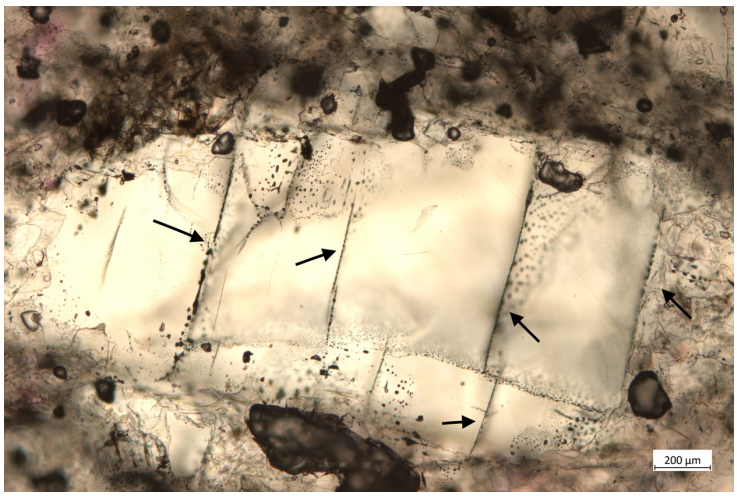

Fig. 4.46 Sample 681/Oed1 a.& b. Low magnification photomicrographs to observe pore structure and grain shapes and sizes. c. Crack propagating through grain in reflected light. d. Same location as image c., in transmitted light, to observe fluid inclusions near crack. e.& f. Fluid inclusions in propagated micro-cracks (arrows) in transmitted light.

a.

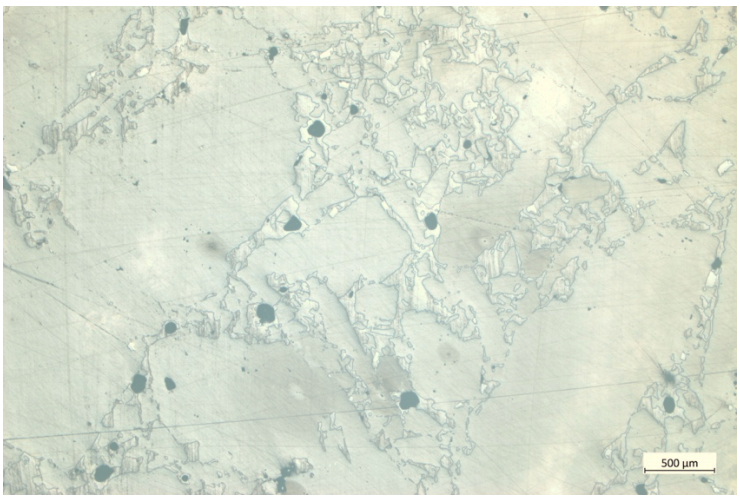

b.

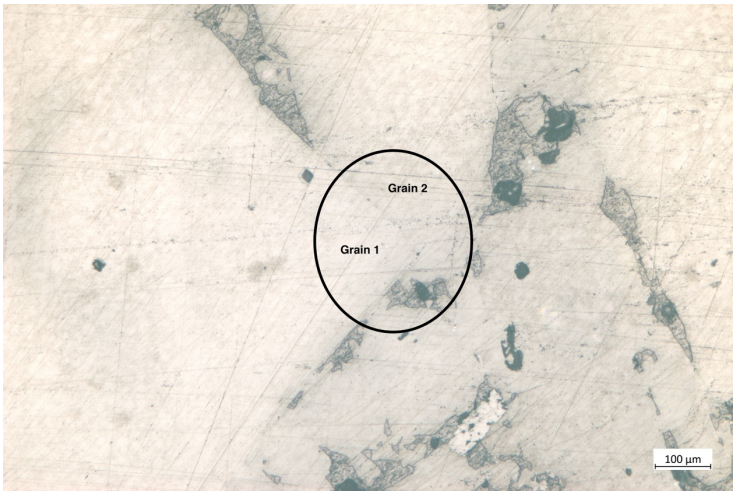

c.

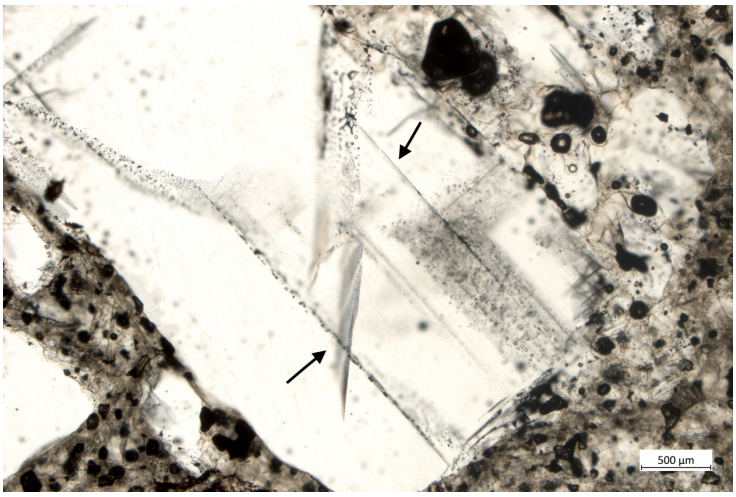

d.

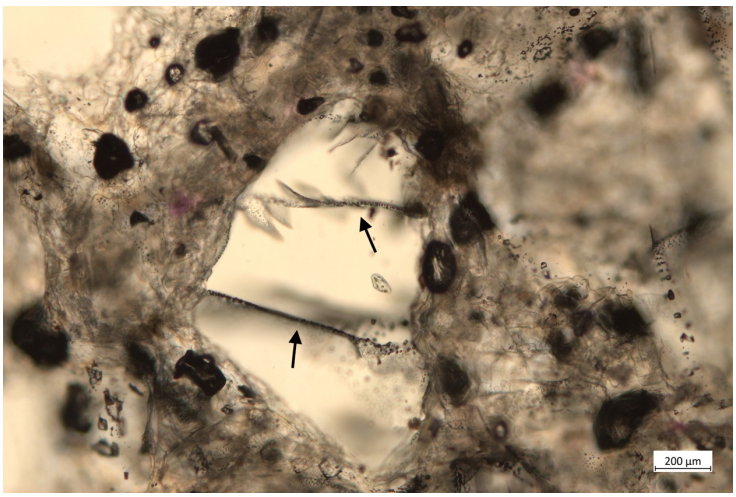

Fig. 4.47 Sample 681/Oed2 a. Low magnification photomicrograph to observe pore structure and grain shapes and sizes. b. Plastic grain deformation at center. c.& d. Fluid inclusions in propagated micro-cracks (arrows) in transmitted light.

a.

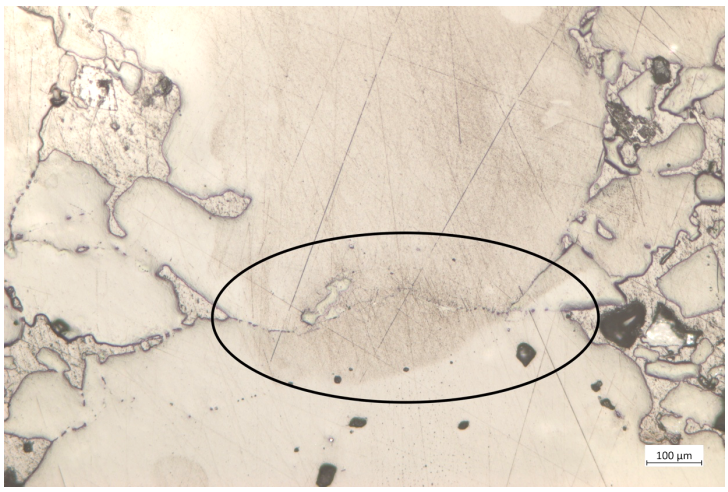

b.

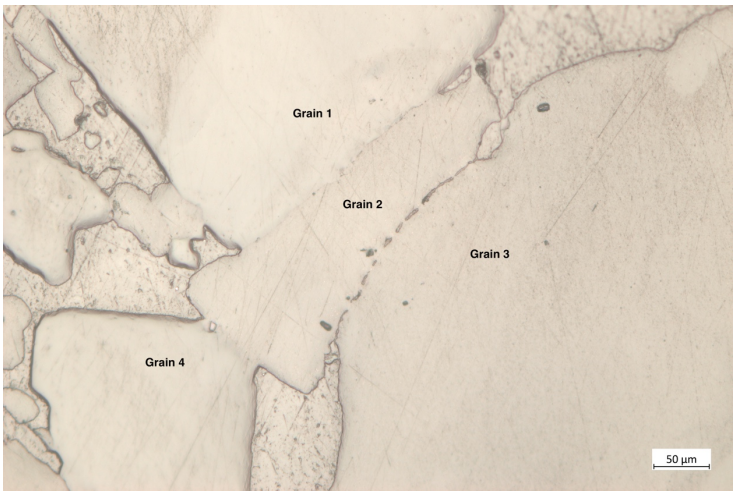

c.

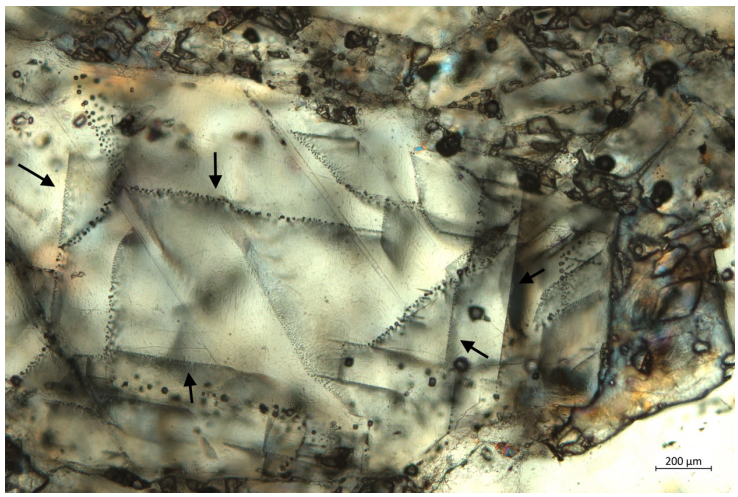

d.

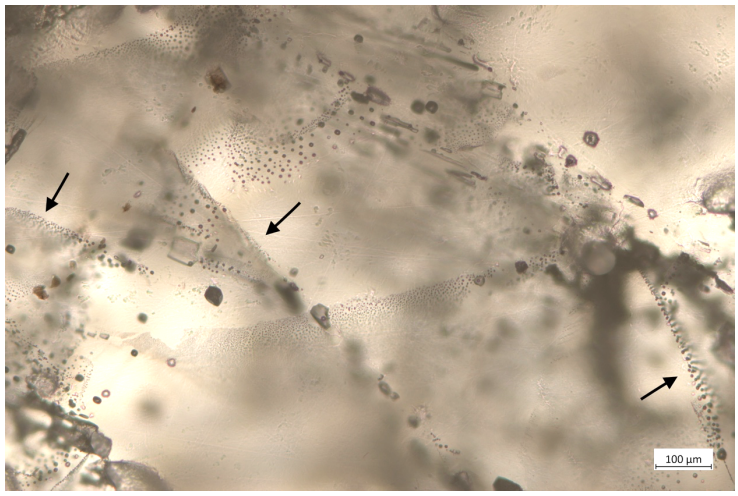

Fig. 4.48 Sample 681/Oed3 a. Low magnification photomicrograph to observe pore structure as well as grain boundary diffusional pressure mechanism b. Plastically-coupled pressure solution grain deformation at centre (Grain 2). c.& d. Fluid inclusions in propagated micro-cracks (arrows) in transmitted light.

a.

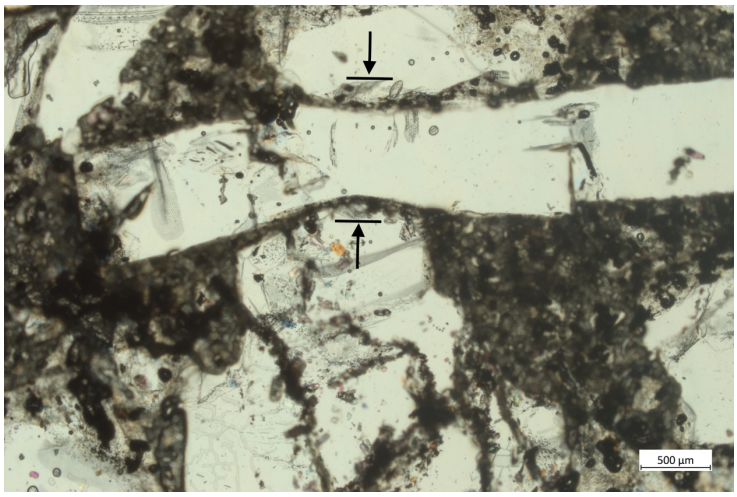

b.

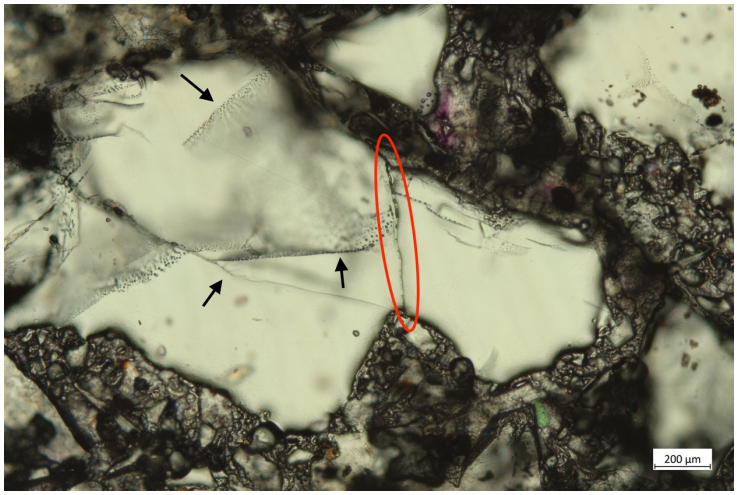

c.

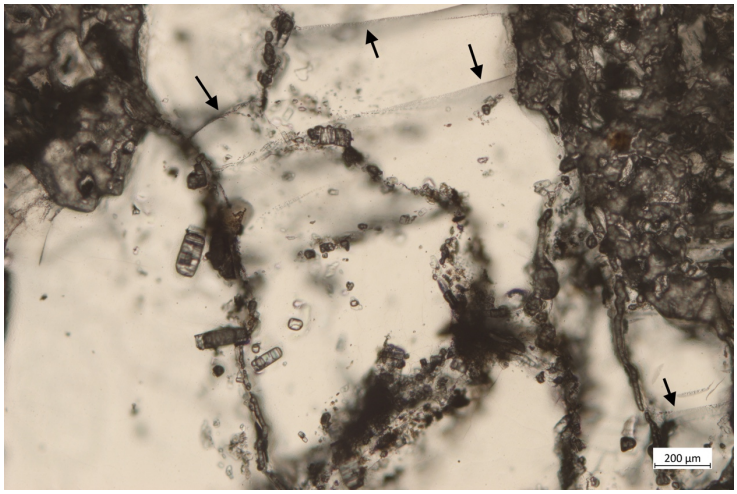

d.

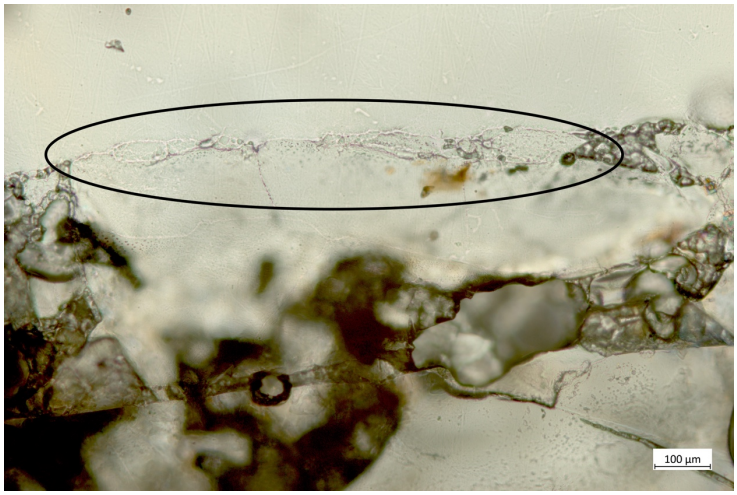

e.

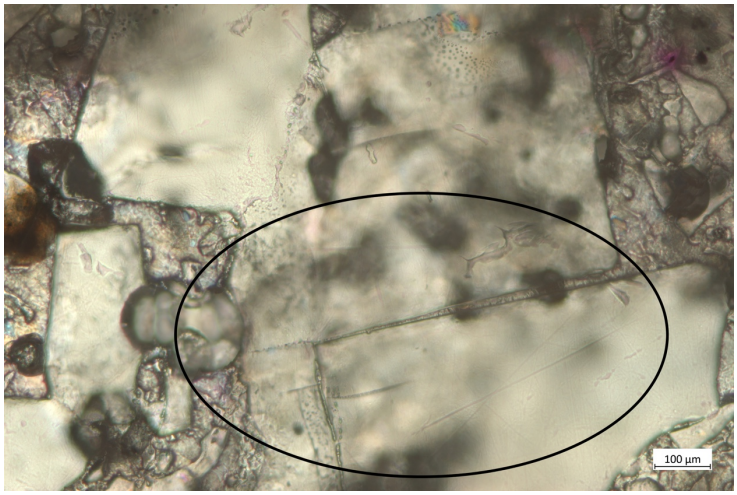

f.

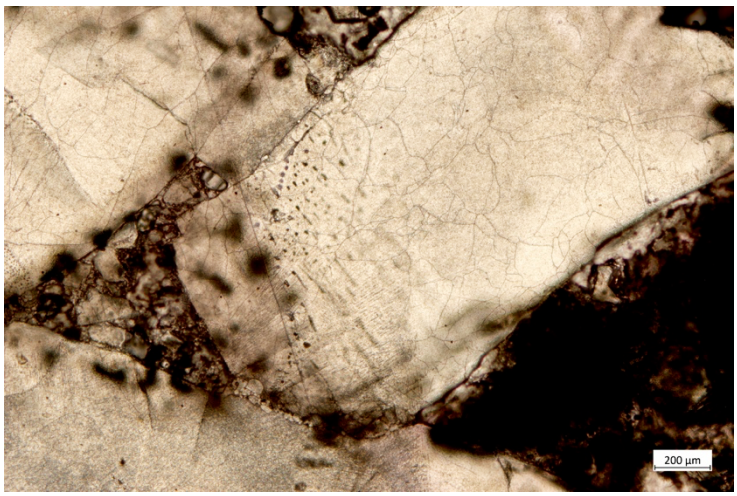

Fig. 4.49 Big oedometer sample a. Impinged grain at center experiencing cataclastic deformation. b. Microcracks through grain, with transgranular crack at center (red circle). c. Microcracks (arrows) through grains in transmitted light. d. Mechanically abraded surface between grains. e. Large crack propagating through grain (center right going left) f. Polygonal subgrain structure ranging in sizes from 50 µm to 250 µm.

4.7.2 Microstructures in long-term compacted samples

Fig. 4.50 to Fig. 4.56 and Fig. 4.58 are derived from a sample that underwent the multi-stage oedometric compaction test Oedo-117 ($6.9\text{-}10^{-7}$ mm/s to $6.9*10^{-10}$ mm/s). Therein, the sample was reduced in void volume from e = 0.448 (Φ = 30.94 %) to e = 0.073 (Φ = 6.80 %) within 133 days at 50 °C. The uniaxial load reached a maximum of 34.6 MPa.

Indicators for grain boundary diffusion (rounded grain edges with even grain contact, (Fig. 4.56), compaction fringes (Fig. 4.56) and bended grain boundaries (Fig. 4.58) occurred in the compacted samples only. Indicators found in loose crushed salt, such as intragranular fractures (Fig. 4.8 and Fig. 4.50), en-échelon fractures (Fig. 4.4, Fig. 4.5 and Fig. 4.51), transgranular fractures (Fig. 4.7 and Fig. 4.52) and fluid inclusions (Fig. 4.5 to Fig. 4.7 and Fig. 4.53 to Fig. 4.55), subjectively occur in a larger abundancy.

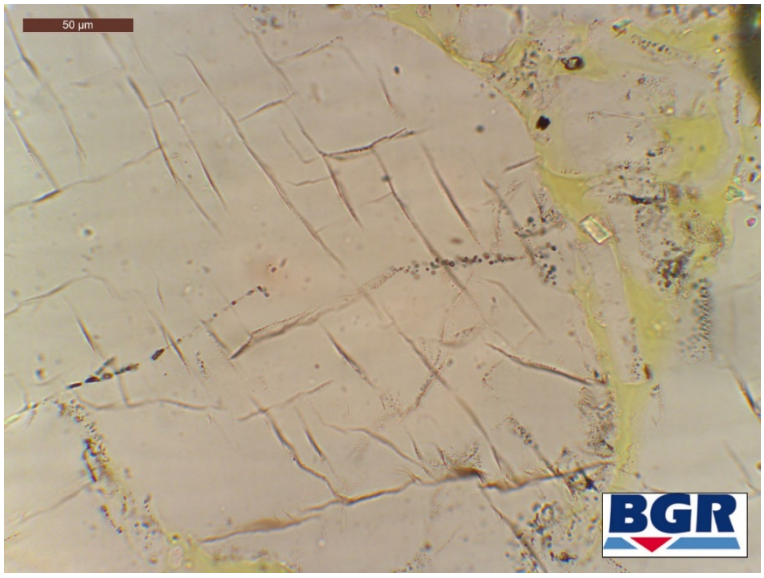

Fig. 4.50 Halite grain compacted crushed salt with intragranular fractures (microcracks). Scale bar is 50 µm

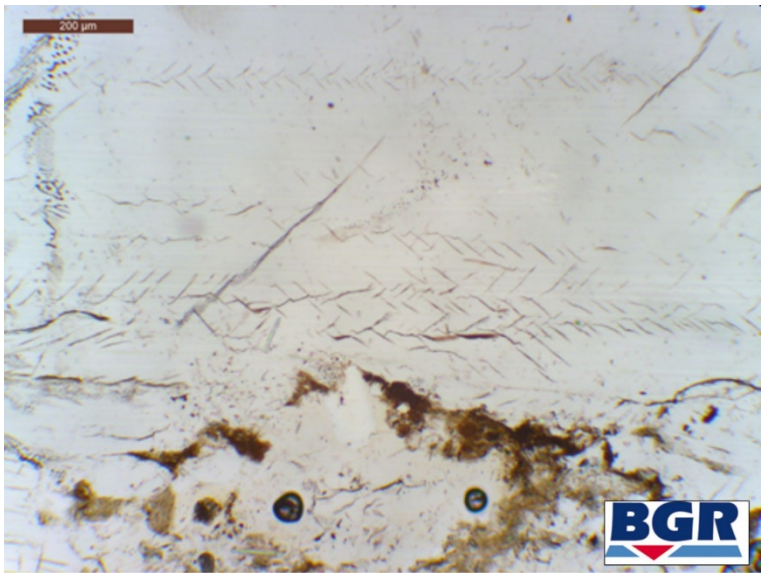

Fig. 4.51 En-échelon fractures in compacted crushed salt. Scale bar is 200 µm.

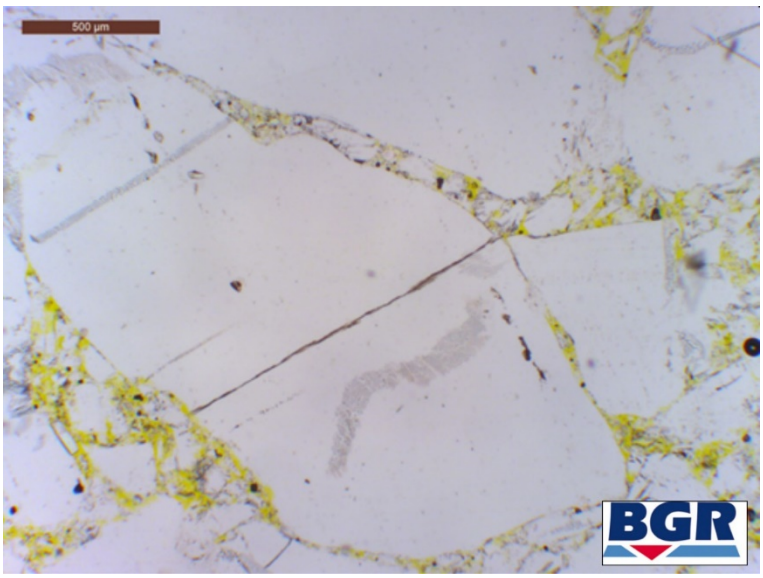

Fig. 4.52 Transgranular cataclasis in compacted crushed salt. Scale bar is 500 µm

Fig. 4.53 Fluid inclusion planes (red circle) in compacted crushed salt. Scale bar is 100 µm.

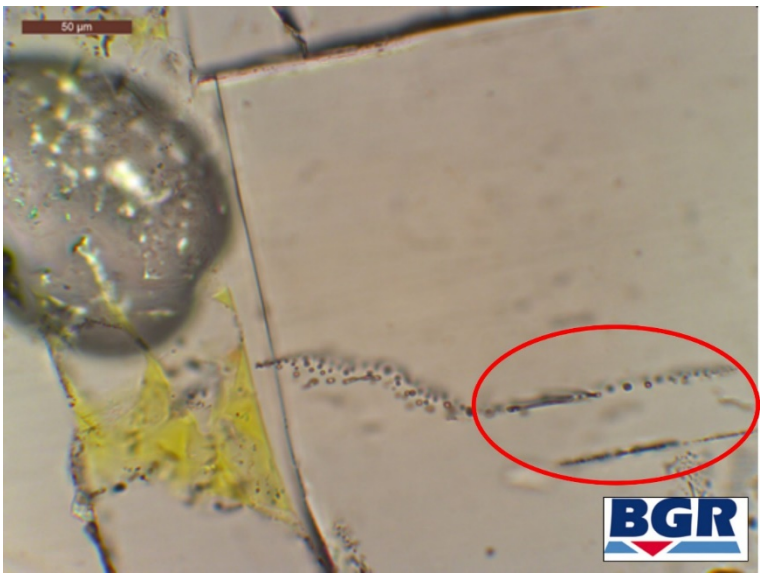

Fig. 4.54 Fluid inclusion lines (red circle) in compacted crushed salt. Scale bar is 50 µm

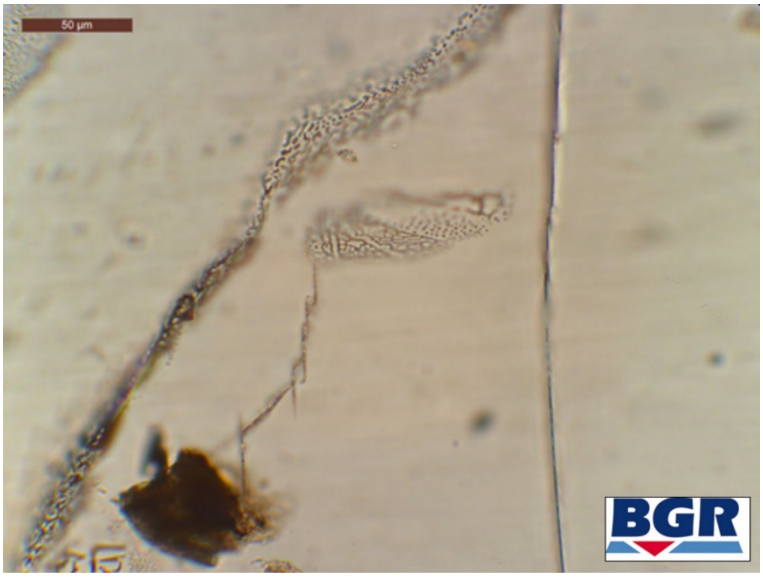

Fig. 4.55 Connected fluid inclusions in compacted crushed salt. Scale bar is 50 µm

Fig. 4.56 Indicators for grain boundary diffusion (rounded grain edges with even grain contact, red circle) and compaction fringes in compacted crushed salt. Scale bar is 200 µm

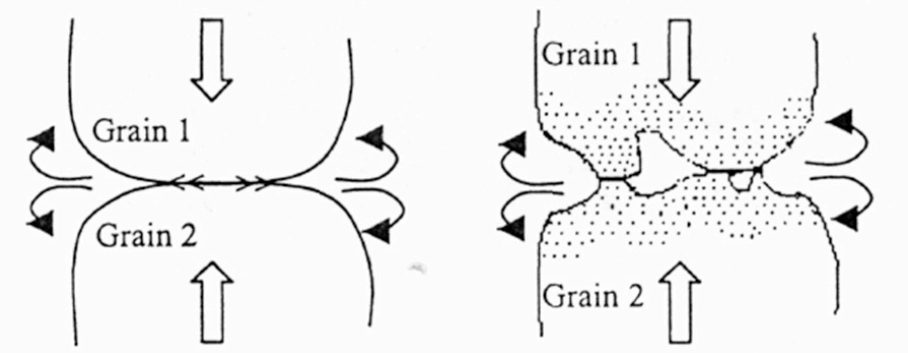

Fig. 4.57 Schematic representation of pressure solution. Left: Grain boundary diffusional pressure mechanism; Right: Plasticity-coupled pressure mechanism with plastically deformed region shaded. Figure taken from /HAN 14/

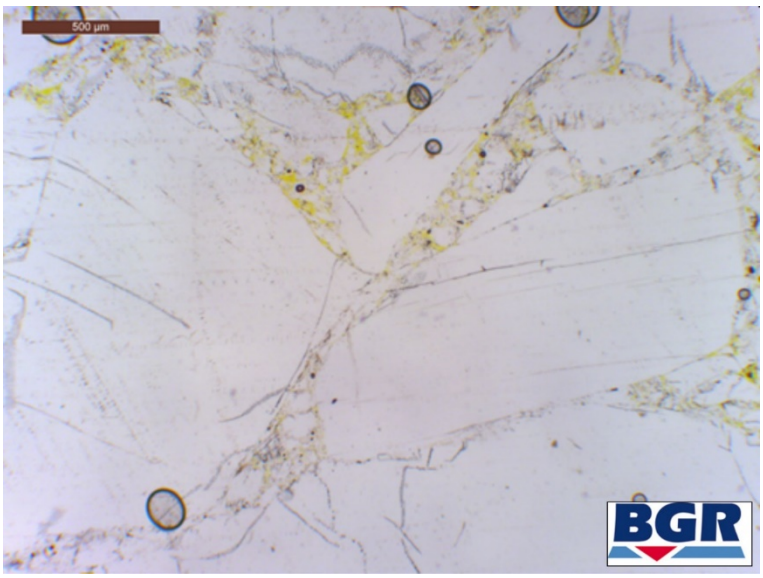

Fig. 4.58 Bended grain boundaries which are indication for intracrystalline plasticity, in compacted crushed salt. Scale bar is 500 µm.

4.8 New experimental methods for the determination of THM-coupled long-term behaviour

4.8.1 Design and construction of the new compaction cell

4.8.1.1 Pre-considerations

Development of new experimental equipment tailored for the given requirements from the various numerical approaches and related to the repository concept (e.g. emplacement of dry backfill material or constructing long-term seals of defined prepared (humid) crushed salt mixtures in drifts or shafts) is an important part of a sophisticated strategy. However, also the experimental feasibility and the already available equipment has to be included in these considerations. Tab. 4.12 summarizes several aspects of parameters which should be measured during crushed salt compaction and discussed them regarding their relevancy for cell construction.

Tab. 4.12 Pre-considerations for cell construction – requirements / conclusions

Parameter / Exp. approach	Relevancy	Degree of technical requirements	Remarks / conclusions
Sample material / pre-conditioning	++	o	➢ **Backfill reference material:** ▪ origin: domal or bedded salt, ▪ grain size distribution / maximum grain size ▪ initial water content: dry / wet ▪ pre-consolidation (time-lapse experiment); facilitation of defined specimen preparation ➔ **A reference material has been selected** *(see Section 4.2)* ➔ **The results from Section 4.5.3 (pre-compaction)**
Size of the load cell, i.e. representativity			➔ **Sample size / -geometry:** *Design of the cell, as large as possible but limited corresponding to the maximum grain size, i.e. diameter of the cell around 100 – 120 mm seems sufficient* *(see Section 4.2)*
Experimental test strategy / complexity: - loading / stress path / - loading geometry - pore pressure state - time	+	o	➢ **Test matrix according the different random conditions.** **The test number will be limited, but two different approaches for test execution exist, i.e.** ▪ long lasting single test series with individual boundary conditions for each test represent the best approach to derive material parameters, ▪ multi-step tests which allow an evaluation and estimate of the influence of parameter changes ➔ **Customized and tailored experimental set-ups have to be used according to the different requirements** ➢ **Test strategy to derive reliable experimental data:** ▪ Isostatic / deviatoric: compression/ extension ▪ Strain- or stress-controlled (e.g. creep test) ▪ Humidity state (initial, adding of water/brine) ▪ Pore pressure conditions (drained / undrained) ▪ Test duration / number of tests ➔ **Test conditions have to be defined according the requirements given by the modelling approaches** ➔ **Extensive test series must be supplemented by individual examinations with respect to special questions, e.g. permeability (see below)**

Volumetric strain / porosity	++	++	➢ **Direct measurement ➔ oedometer** ➢ **Indirect measurement ➔ triaxial cell** ▪ Measurements of sample volume changes: evaluation of cell-oil volume balance ➔ problem: possible leakage ▪ Porosity: Squeezed-out pore fluid / gas-porosimeter ➔ problem: the resolution and accuracy are limited due the delayed fluid-escape and the remaining dead-volume of non-accessible porosity ▪ Ultrasonic wave velocities, as indirect approach ➔ problem: calibration / homogeneity due to texture-effects / resolution due to damping ▪ alternatively: optical measurement methods / laser triangulation on sample surface / circumferential strain gauges ➔ problem: experiences regarding long-term stability and resolution are not available. ➔ **No absolutely satisfactory and technically easy to implement method for measuring the volumetric strain or the porosity is available, which means some uncertainty regarding this value during the tests remains.**
Permeability - gas /brine	+	++	➢ **Direct measurement with gas or brine ➔ pulse- or stationary test:** ▪ Pore pressure effects regarding the load conditions ▪ Hydro-chemical effects: - drying or wetting of the sample - inert vs. reactive fluid ▪ Two-phase flow phenomena (absolute or relative permeability values) ➔ **Permeability measurements during execution of a compaction test on crushed salt delivers special problems which requires tailored equipment and test procedures**
Temperature	(+)	o	➢ **The impact of temperature depends on the repository concept regarding the use and position of the crushed salt, e.g.:** ▪ Backfill material in the vicinity of the casks ▪ Construction of a long-term sealing element ➔ Temperature determines the efficiency of (intracrystalline) creep and (humidity-assisted) diffusion processes, but in a different way and extent. Thus, this aspect has to be considered but in a moderate way to temperatures up to around 100°C.

As result of both evaluations the following conclusions can be drawn:

- Due to the apparent deficits of the various approaches no unique measuring approach exists to quantify volumetric strain changes or the porosity directly during the test, but combination of methods respectively parameters to be measured is constructive. But some uncertainties regarding the resolution of the various parameters remains. Thus, a final proof of the reliability of the results can be only obtained by measurements of the sample density after the test (see Section 4.5.3.3)

– Due to the apparent difficulties measuring reliable permeability during loading without influencing the mechanical test conditions in a negative way it is recommended to focus on different aspects of the various test, e.g. (1) a series with execution of isostatic creep tests and (2) execution of single loading tests for investigating transport and pore space properties.

Taking these requirements in mind a simple quasi-isostatic cell is designed which a allows a multi-parameter monitoring of various parameters during the compaction test (Fig. 4.59).

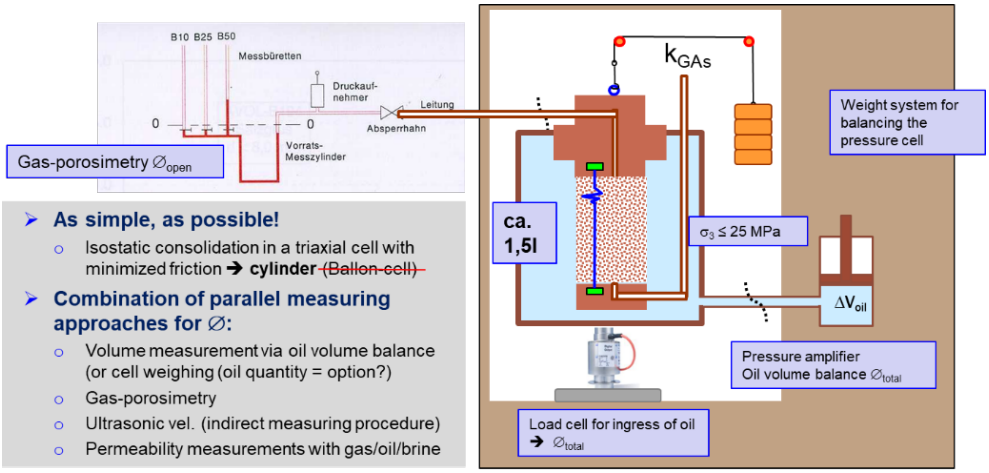

Fig. 4.59 General design concept of the “New IfG-compaction cell”

Tab. 4.13 Comparison of experimental approaches for the design of the test equipment

Experimental approach	Dilatancy	Stress-field	Permeab.	Flexibility	Advantages	Disadvantages
Oedometer	+++	- -	+	o	▪ Defined sample volume for every deformation condition ▪ Simple geometry ▪ One-dimensional flow possible ▪ Stress or displacement controlled	▪ One-dimensional (axial) deformation ▪ friction on the wall (silo effect) or end surfaces ➔ no ideal hydrostatic stress condition
Triaxial apparatus (KÁRMÁN-principle)	+	+ (-)	++	+	▪ Hydrostatic/deviatoric stress states can be realized (Compression / Extension) ▪ Flexible sample geometry for flow (radial/axial) ▪ Different volume measurement methods can be combined	▪ Load frame as abutment required ▪ Indirect volume measurement ▪ Initial sample geometry problematic with non-compacted samples ▪ Long-term stability with oil tightness problems - leakage (e.g. into the sample) ▪ End surface friction
Isostatic compaction cell	++	(-)	++	(-)	▪ Nearly isostatic stress conditions ▪ Simple construction ▪ Otherwise how **KÁRMÁN apparatus**	▪ Only isostatic stress state ▪ Otherwise how **KÁRMÁN apparatus**
Multi anvil apparatus / true-triaxial pressure apparatus (KIT, BGR)	(+)	(+)	-	(-)	▪ Any (hydrostatic/ deviating) stress conditions can be realized	▪ Friction at the piston surfaces; no ideal hydrostatic stress state ▪ No flow tests possible ▪ High preparative effort ▪ Problems between the pistons: gap / edges ▪ High apparatus costs

4.8.1.2 The new cell – construction and pre-testing

The new test facility has been specially developed for the routine and long-term testing of cylindrical test specimens (solids and plastic materials). The cell consists of a stiff steel tube with the inner dimensions of 200 mm diameter and 360 mm length. The cylindrical sample has a diameter of 110 mm and a maximal length of 250 mm. Compared to classical triaxial cell, it offers the advantage that the load condition is almost isotropic and that dimensions can be used to produce samples regardless of the test facility. Unfortunately, no deviatoric stress conditions can be realized. As functional improvement the new cell considers the main principles summarized in Fig. 4.59.

As a functional principle, a cylindrical test specimen sealed with an oil-tight rubber jacket is pressurized quasi-isostatically in the cell via the hydraulic oil and thus compacted, whereby pore fluid can escape via a drainage line or alternatively permeability measurements are possible. The pressure-dependent compaction of the test specimen is determined by measuring the hydraulic oil quantity introduced into the cell.

Fig. 4.60 The new pressure cell developed by IfG

The pressure cell is designed for a maximum test pressure of up to 200 bar. The cell pressure is generated by means of a pressure intensifier, in which the oil volume introduced can be determined very precisely by measuring the displacement of the separating piston. The volume resolution of the measuring systems used is < 0.1 ml. The following test procedures can be realized:

- Pressure – Approaching a defined pressure state via a time-controlled ramp or maintaining this pressure. At the same time, the amount of oil volume is measured, which results in the sample compaction depending on the pressure.
- Oil volume – By regulating the oil volume over a time ramp up to a constant value, defined compaction states of the test specimen can be set or kept constant (if the system compressibility is known); this is a prerequisite for constant boundary conditions in a flow measurement.

During the test, the cell pressure and the displacement of the pressure intensifier are recorded by means of the data logging system for defined time intervals, which allows the oil volume quantity to be determined via the cross-sectional area of the respective pressure generator used. For the quantitative determination of the sample compaction, the compressibility of the pressure cell and the oil used was measured before using a steel cylinder (in the sample dimensions), which was taken into account as inherent deformation in the pressure-dependent evaluation of the compaction experiments to determine the net sample volume:

$$\Delta V = \Delta S_{\mathrm{PI}} \cdot A_{\mathrm{PI}} - c \cdot p_i \tag{4.22}$$

ΔS_{PI}	axial piston displacement of the pressure amplifier
A_{PI}	piston cross section of the pressure amplifier
c	correction factor (compressibility of the pressure cell / system)
p_i	acting oil pressure in the cell

In addition, a pressure loop is run after the execution of each test, which determines the correction factor c for each individual test. During the compaction test, the permeameter can be used to measure the parameter permeability as a function of the compaction (porosity). The permeability was calculated according to the Equ. (4.23) depending on the test medium (gas or salt solution):

In the pre-tests only the gas-permeability is measured on the initial dry sample. The investigation method used at IfG for the determination of gas permeability by means of technically dry N_2 is based on the DARCY equation for laminar gas flows by measuring the flow rates q at a defined pressure gradient between inlet and outlet of the sample (primary or secondary pressure):

The permeability is calculated by means of:

$$k = \frac{2 * p_0 * q_0 * \eta * l}{A(p_1^2 - p_2^2)} \tag{4.23}$$

k	permeability [m^2]
l	sample length [m]
q_0	flow rate under room pressure [m^3/s]
p_0	pressure at the flow meter [N/m^2]
A	cross section [m^2]
η	dynamic viscosity [Pa*s]
p_1	pressure inlet [N/m^2]
p_2	pressure outlet [N/m^2]

Actually, two cells are constructed, which are in the testing phase.

4.8.2 Two pilot tests from the laboratory program approach with innovative operational modes TUC-V2 and TUC-V3

4.8.2.1 Objective and selection of experiments

Within the framework of the research project, two pilot tests were carried out with the aim of verifying the technical feasibility of new types of operation for the isolated analysis of individual functional dependencies between stress and crushed salt compaction in the triaxial test and subsequently investigating the dependence between the deviatoric stress and volume compaction, which has only been investigated to a limited extent so far. These tests are one small part of the planned extended systematic laboratory program described in Section 6.2.3.

1) Pilot test TUC-V2: The objective of the pilot test designated in the following TUC-V2 is the isolated analysis of the influence of deviatoric stresses on viscous volumetric deformations and the influence of porosity on viscous shear deformations.
2) Pilot test TUC-V3: The objective of the pilot test designated in the following TUC-V3 is the testing of a new type of control in which the confining stress is continuously controlled to a level corresponding to the axial stress in the triaxial test in addition to the strain-controlled load increase. As a result of the simultaneous control of the axial strain rate and the confining pressure, a strain-controlled isotropic stress curve with exclusive generation of volumetric deformations results, i.e. shear deformations are completely eliminated due to the avoided deviatoric

load components. The test designated TUC-V3 corresponds to the tests planned with series S3 in Fig. 6.16.

As test specimens for the pilot tests, two specimens produced within the framework of the pre-compaction tests were used as follows:

TUC-V2: sample KOM7

TUC-V3: sample KOM12

4.8.2.2 TUC-V2: multi-stage test with isotropic and deviatoric load stages

The load history realized in the TUC-V2 test is shown in Fig. 4.61. According to this, a total of 5 load stages were realized with a test period of 30 days each and an equidistantly increasing mean stress of σ_m = 4.2 MPa/8.2 MPa/12.2 MPa/16.2 MPa/20.2 MPa from load stage to load stage. Each load stage is characterized by a 10-day approximately isotropic load with σ_v = 0.5 MPa, followed by a 10-day deviatoric load with σ_v = 8.0 MPa, again followed by a 10-day isotropic stress with σ_v = 0.5 MPa. The test specimen temperature was kept constant at a level of T = 30°C for the entire test duration of 150 days.

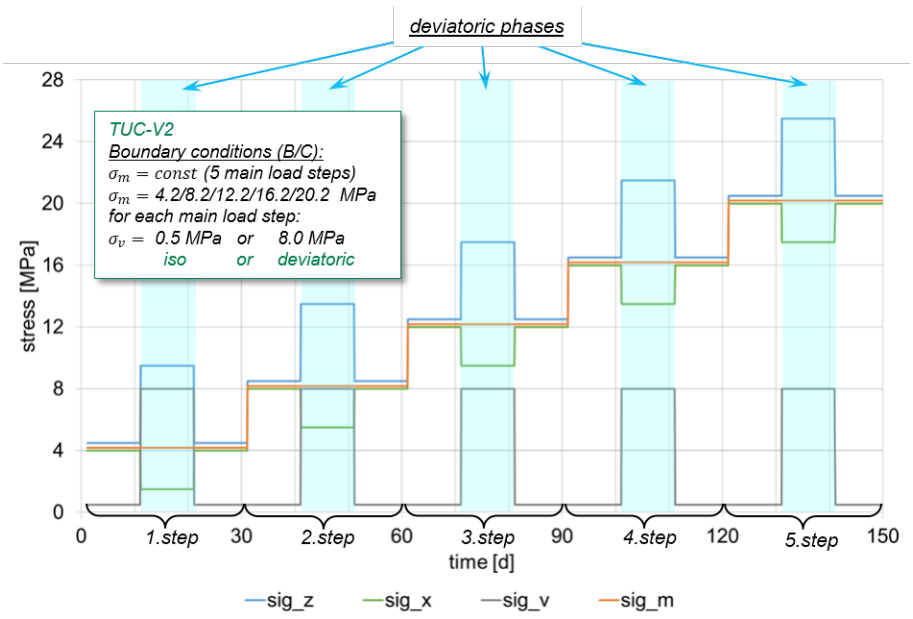

Fig. 4.61 Loading history for the multi-stage long-term test TUC-V2

Fig. 4.62 shows the measurement results for the volumetric strain and for the axial strain as well as for the volumetric and effective strain rates. For the volumetric strain, both the original measured values and a smoothed variant of the measurements are plotted. The

purpose of the smoothing is to derive an unambiguous functional dependency between the metrologically determined compaction rates or volume strain rates and the respective influencing factor (mean or deviatoric stress, porosity, etc.). Fig. 4.63 shows a comparison of the ultrasonic wave velocities measured during the test with the ultrasonic wave velocities determined on the pre-compacted crushed salt test specimens prior start of triaxial test and the theoretical compensation function between porosity and ultrasonic wave velocity according to Section 4.5. According to this, the ultrasonic wave velocities measured during the test correlate comparatively well with the load-free ultrasonic wave measurements on pre-compacted crushed salt test specimens.

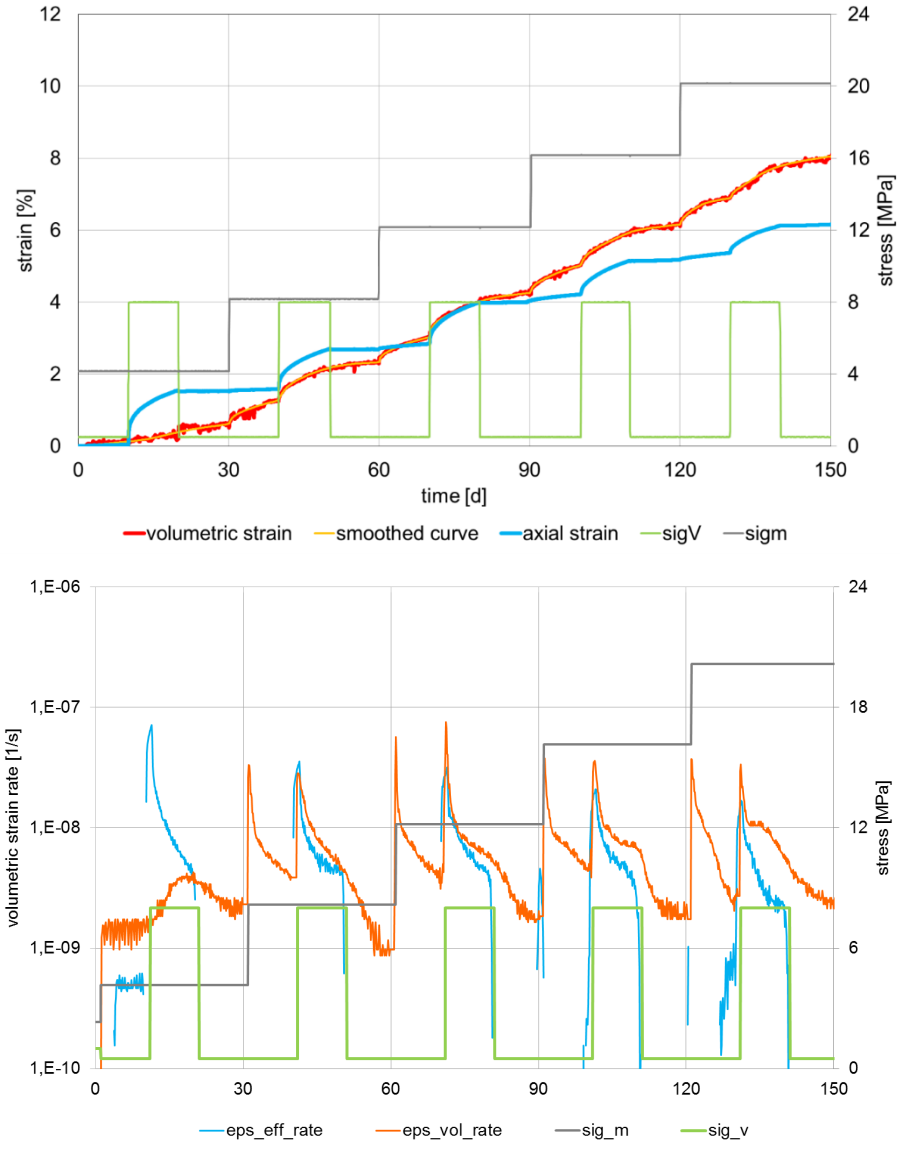

Fig. 4.62 Measurement results for the multi-stage long-term test TUC-V2

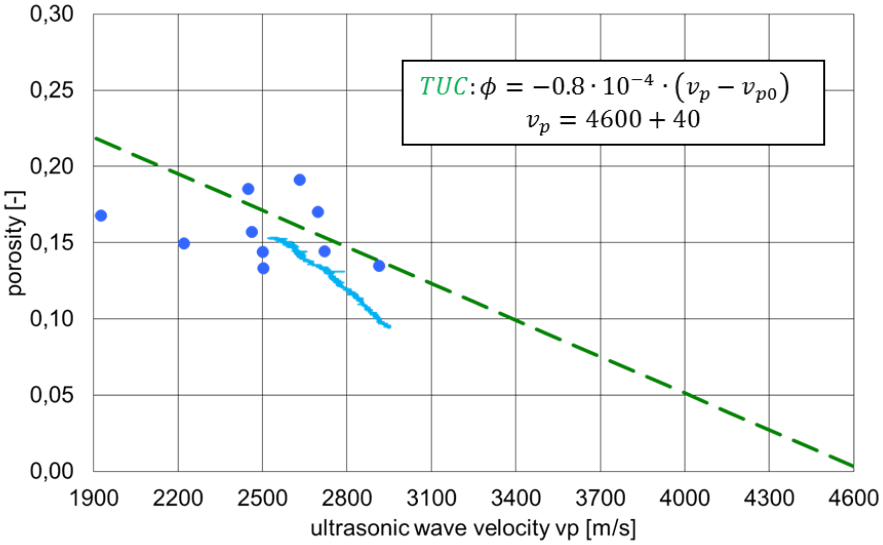

Fig. 4.63 Course of the ultrasonic wave velocity in the TUC-V2 experiment in comparison to load-free measurements on pre-compacted crushed salt test specimens and the theoretical functional dependence

After the 5 load stages of the TUC-V2 pilot test already implemented and had clearly confirmed both the feasibility and the usefulness of the new test technology, the loading history for a planned continuation of the TUC V2 test was determined as follows, as can be seen from Figure 4.62:

a) Specification of a second loading phase – only deviatoric loads are varied (switched on and off) while the mean load is kept constant;
b) Specification of a third loading phase – the mean load is still kept constant and the deviatoric load is switched off, i.e. loading is characterized by isotropic conditions.

The aim of the second loading phase is the isolated measurement and recording of the dependence of the viscous shear deformations on the porosity. The aim of the third loading phase is the determination of long-term compaction behaviour under an in-situ similar loading (without abrupt change of the stress) up to the range of small porosity values of less than 5 %, possibly up to 1 %.

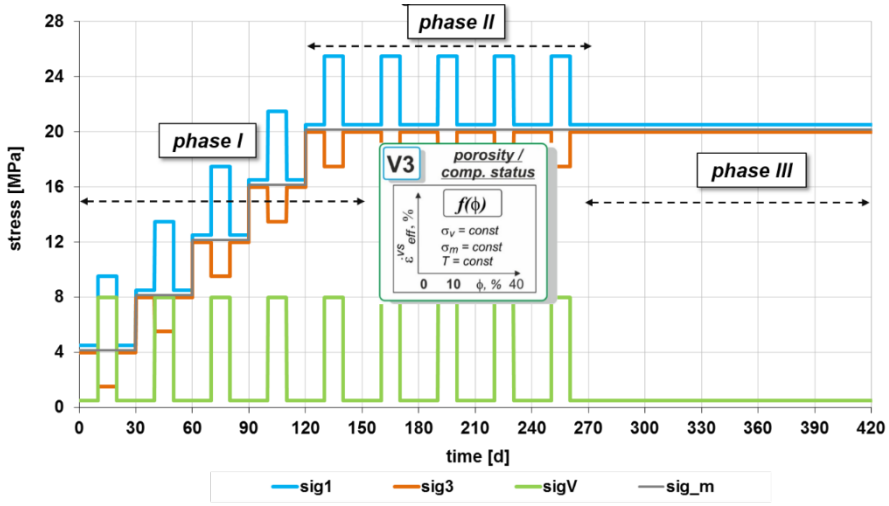

Fig. 4.64 Proposal for the continuation of the TUC-V2 experiment

4.8.2.3 TUC-V3: single stage distortion controlled isotropic triaxial test

The pilot test designated TUC-V3 was carried out with a comparatively low strain rate of 4.2e-8 1/s (= 0.00025 %/min) over a test period of 20 days. The experimental difference between the axial stress and the confining stress was 1 MPa. The test specimen temperature was kept constant at a level of 30 °C during the entire test period. The measured values for axial stress, confining stress and volume strain recorded during the TUC-V3 pilot test are shown in Fig. 4.65. According to this, the feasibility of the proposed new type of test control with strain-regulated isotropic load can be considered as verified, even with further specification of comparatively low strain rates from ε = 0.00025 %/min. With regard to the final porosity of approx. 1.4 % realized in the test as shown in Fig. 4.65, it should be noted that the measurement of the volume strain in the TUC-V3 pilot test was not carried out via EMC cylinder (in contrast to the TUC-V2 experiment), but by means of a significantly less precise synchronous cylinder, so that the absolute numerical values of the porosity may still be incorrect and, as a consequence, a repetition of the test with the use of EMC measurement technology is planned for the next project phase or if the re-search work is continued.

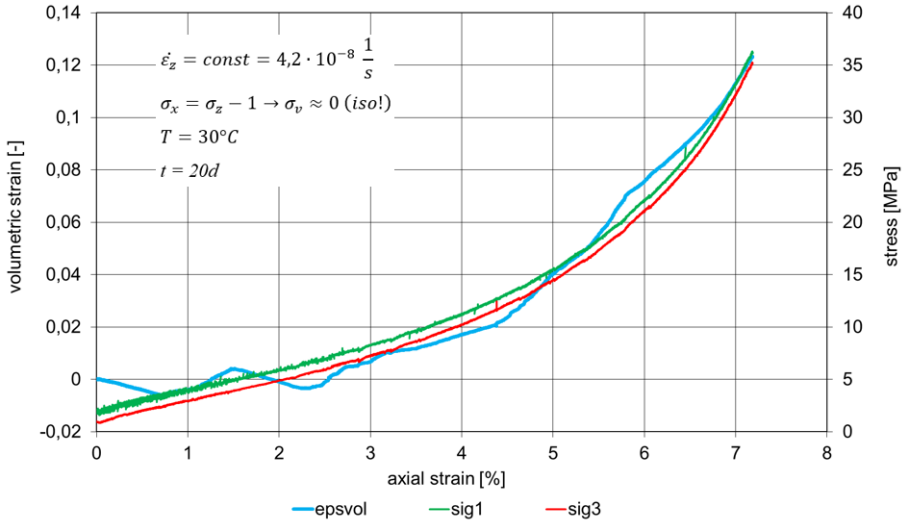

Fig. 4.65 Results from the TUC-V3 experiment

5 Modelling work

5.1 Requirements

The aim of this chapter is twofold: There are requirements for the constitutive models described in Section 5.2, which result from physical considerations and material investigations, and totally, there are requirements for the constitutive equation if THM calculations are carried out on a more complex scale in the context of repository design.

5.1.1 Requirements from repository layout

With regard to the final disposal of radioactive waste, the actions on the granular salt are a consequence of the repository design. The design for current variants of drift disposal and borehole disposal has been developed in /BOL 12/, /BOL 18/, /MÖN 20/ (Fig. 5.1). It is largely independent of the salt formation as a dome, cushion or flat bedding. Individual design variants such as e. g. the length of the borehole must be adjusted.

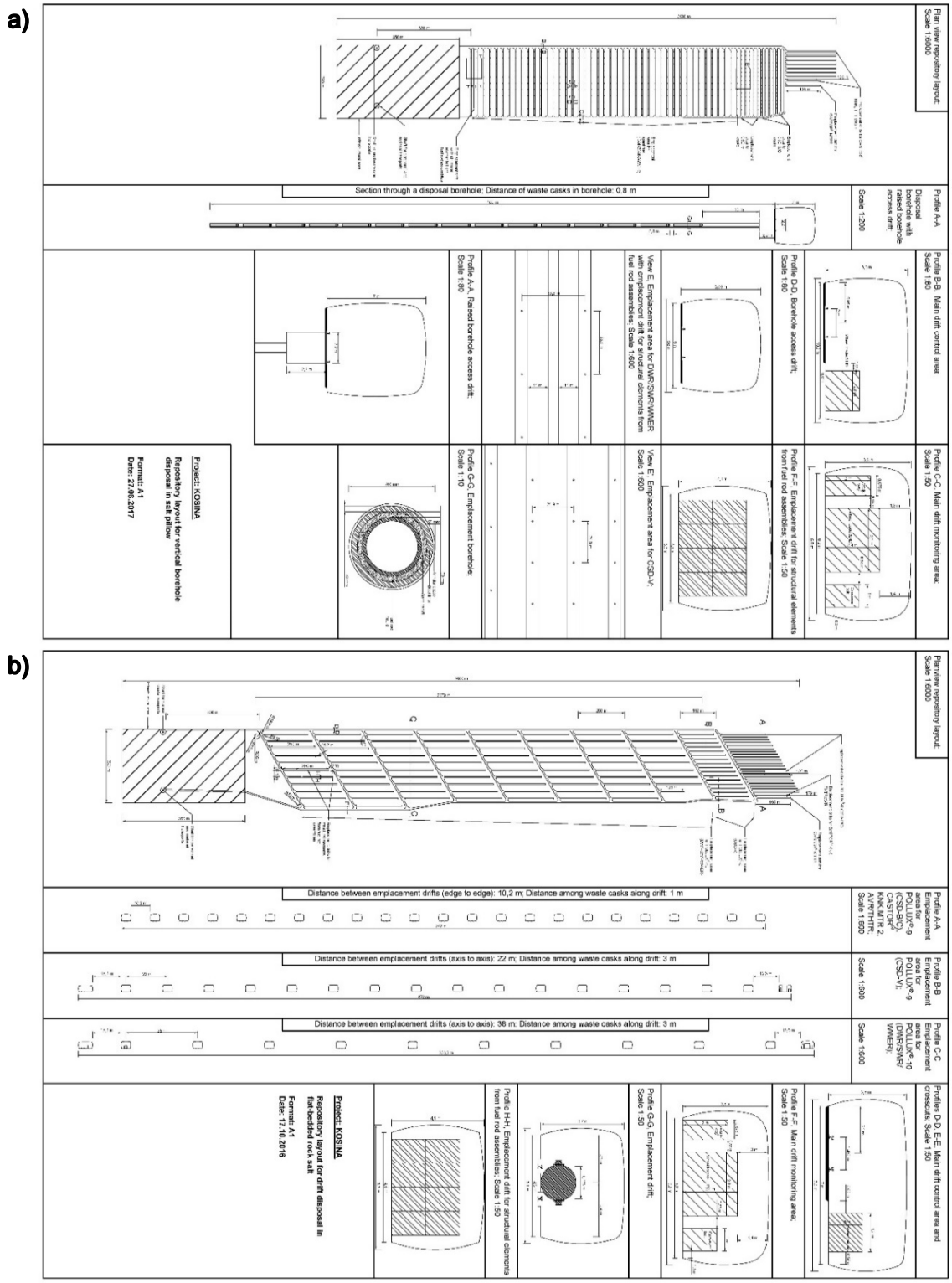

Fig. 5.1 Design variants for the emplacement of radioactive waste /BOL 18/ a) Vertical borehole disposal. b) Horizontal drift disposal.

In the concepts for drift emplacement the waste container is placed on a bedding from rock salt and then encased in granular salt (Fig. 5.1a). In the concepts for borehole emplacement, granular salt is only used outside the liner and thus at some distance from the waste. This is independent of whether disposal is vertical (Fig. 5.1b), or horizontal. Correspondingly, thermal loading in these variants for borehole emplacement is lower than in the case of drift emplacement, where granular salt directly surrounds the waste containers.

For precautionary reasons, the site selection law /BMU 17/ currently specifies a temperature limit of 100°C for the container surface. Scientific findings may lead to different thermal limitations in the future. The appropriateness between emplacement work and retrievability effort is required in /BMU 20/, which also results in thermal limitations.

To summarise the thermal limitations, it must be assumed that design temperatures of 200 °C, as used in /BOL 12/, are difficult to implement. Starting from a design temperature of 100 °C, this temperature is reached in granular salt only in the case of drift emplacement in the immediate vicinity of the casks. Regardless of the disposal concept, a temperature increases with a maximum temperature of approx. 60 °C is expected at drift seal locations and a temperature increase with a maximum to slightly more than 40 °C in the shafts can be assumed.

Temperature has a particular influence on dislocation creep. The basis for the following estimation is a North German domal rock salt in the state of stationary creep rate. The comparison is carried out using the BGR_b constitutive model with the parameters for activation energy and pre-coefficient according to /HUN 94/. The reference temperature is 33 °C, which in Northern Germany is a normal temperature of a depth of approx. 800 meters. Dislocation creep rate becomes much faster with temperature increase, particularly in the upper temperature range (Tab. 5.1). Temperature could be a starting point for time optimization in experiments, if dislocation creep is the dominant mechanism; however, there is a substantial shift in the deformation mechanisms towards dislocation creep, if it is not.

Tab. 5.1 Thermally activated dislocation creep rate compared to a reference temperature of 33 °C

Temperature	[°C]	33	100	175	200	250
Relative creep rate	[-]	1	37	8.3E3	40.6E3	634.E3

In /BOL 12/ it was assumed that the emplacement drifts and the cross-cuts are backfilled with naturally dry crushed salt in the case of drift disposal as well as borehole disposal, while the access drifts are filled with slightly moistened granular salt to facilitate compaction. The target value of humidification is the equilibrium moisture content of approx. 0.6 % wt. In contrast, current plannings /BOL 18/ assume that the access drifts will be filled with naturally dry granular salt also. Moistened backfill with a humidity content of about equilibrium moisture is only used for shaft backfilling and in a specific area of drift sealing.

Thus, as a profile for humidity and thermal loadings it can be summarized, that the upper temperature limit is 100°C for the naturally dry salt granulate and for a moistened granulate with approximately equilibrium moisture is of approx. 50 °C.

A limitation of the mechanical stress can only be carried out to a limited extent. The driving force for the mechanical load is the dynamic stress equilibrium initiated by the excavation in the host rock. The result is a deviatoric stress in the host rock, which results in the convergence rate and, over time, the convergence at the excavation contour. The convergence is accompanied by the compaction of the backfill material, from which a support pressure on the contour results. This leads to the reduction and finally to the complete elimination of the deviatoric stress and thus to static equilibrium again. The initial convergence rate is essentially the result of overlying rock mass and state-dependent creep rate of the host rock.

5.1.2 Requirements for the numerical model

The processes occurring during the compaction of granular salt in a repository can be assigned to a single process class or can be assigned to the coupling between process classes. The term “process class” and in the following the term “state variable” is to be

understood in the sense of numerical calculation methods and not in that of thermodynamics. The work within this project is limited to the thermal (T), the hydraulic (H) and the mechanical (M) process class and thus the corresponding couplings. Other process classes such as the chemical (C) and radiological (R) process classes are not considered (Fig. 5.2). Processes which are connected with one of these two process classes but have to be considered within the framework of the THM-coupled approach, are only recorded in their effects as they are assigned to one of the three process classes considered. This applies, for example, to the dissolution, which would have to be considered in the THMC context but is reduced here solely to its effect in the mechanical sub-material model.

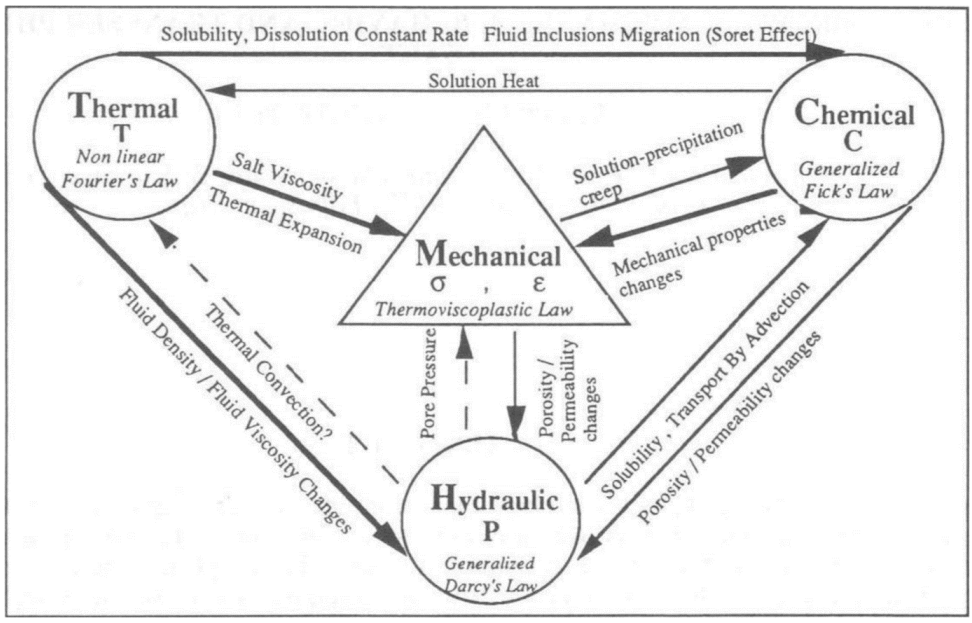

Fig. 5.2 Main coupled processes in salt /COS 93/

5.1.2.1 Grain structure

There are state variables, which have an influence on the material behaviour, but their determination is complex for systems on and off the laboratory scale. One such quantity is the geometry of the granular salt structure, which is caused due to both the material itself and the complexity of the geometry.

Granular salt is extracted during drift excavation, with different stratigraphic units being passed through during the process. The material is temporarily stored in bunkers or even above ground. It is broken by crushing mills and, if necessary, sieved, in order to be dried

or moistened. Finally, it is installed, cooled if necessary, to compensate for initial subsidence of the backfill itself. Thus, already the industrial excavation process, the preparation process, and finally the backfilling process is a material handling that leads partly to deformations as they also occur later during the compaction process (Section 4.3).

Regardless of the process class, the grain structure and thus the porosity has a decisive influence on the development of each individual material property. Already from the grain size distribution (Fig. 2.7) it can be seen that in an industrial used backfill material a few large grains are surrounded by many smaller and smallest grains (Fig. 5.3).

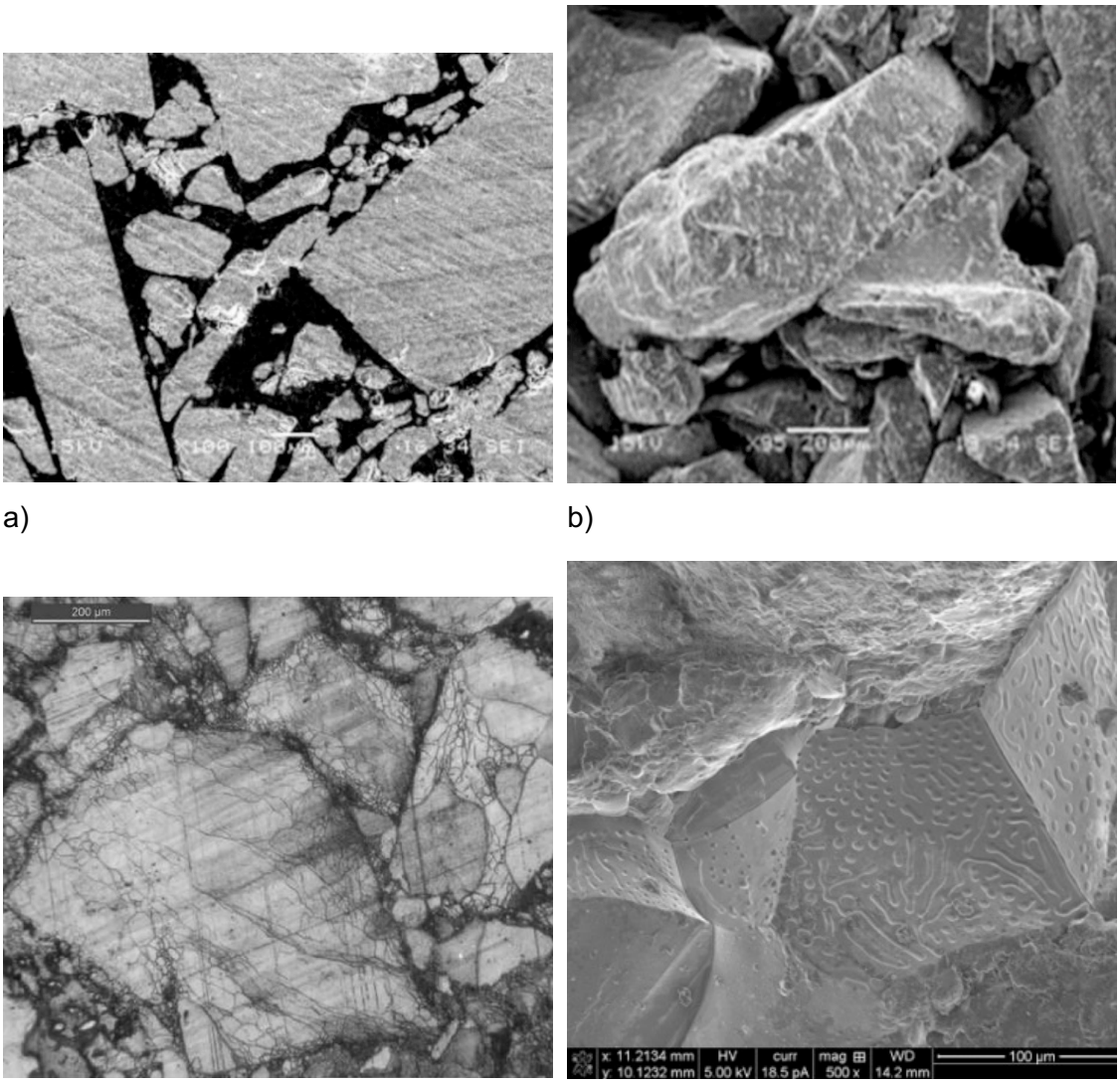

a) b)

c) d)

Fig. 5.3 Micro-structures of consolidated crushed salt. a) and b) with 20.7 % porosity /HAN 14/. c) and d) with 1.67 % porosity (point counted) /STO 17/

Characteristic parameters of a granular material include:

- Maximum grain size
- Grain size distribution
- Grain shape
- Coordination number

The maximum grain size and the grain size distribution are components of the sieve analysis; the grain shape describes the geometry type, the extension in orthogonal directions, and the characteristics of its corners and edges; the coordination number (mean value) describes the number of contacts between a grain and its neighbours /HEI 91/. In principle, the coordination number increases as the material is compacted. In addition, fracture processes can increase the number of grains. On the other hand, outer grain boundaries can also become inner ones and disappear completely in the further development /STO 17/. The significance of individual variables for the overall process therefore changes with compaction. It becomes clear that the description of the grain structure is a multidimensional quantity from its geometric side.

The maximum grain size is described as an important property /HAN 14/ with reference to /DAV 96/. The other geometric properties such as grain size distribution, the coordination number and the initial porosity of the loosest bulk material are less important. However, this is in case of dry crushed salt in contrast to findings in /BEC 99/ and /KRÖ 09/ where fine-grained crushed salt proves to be stiffer in oedometer tests compared to coarse granular salt and where the initial porosity of a more sieved material is higher than that of a material with a wider grain spectrum (Fig. 5.4). The complexity of the grain structure comes clear by the result in Fig. 5.4. It is the same basic material, where oversize and dust content are extracted and otherwise only the maximum grain size differs. However, as the finer sieves do not differ, the width of the grain-size curve changes and the fine grain distribution shows a higher tendency to a material with single grain size.

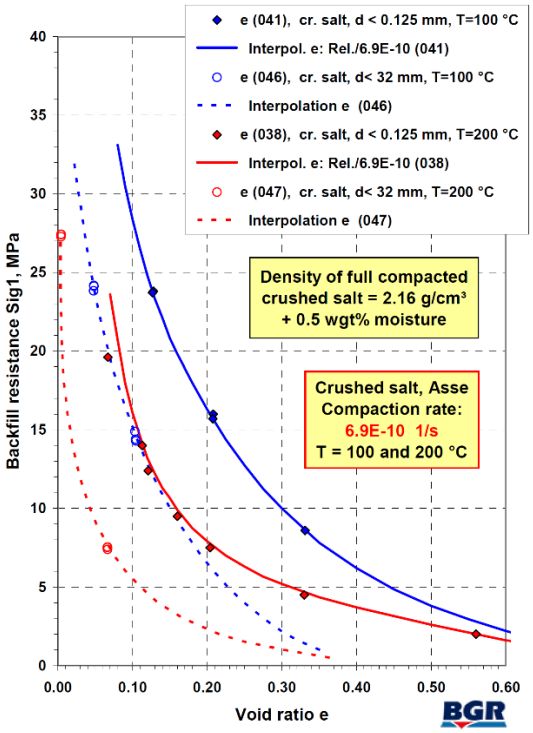

Fig. 5.4 Influence of the grain-size curve on the Backfill resistance with d < 31.5 mm and d < 0.125 mm /KRÖ 09/

Another aspect is the anisotropy in the grain shape. As already shown in Fig. 5.3, the length of a grain in the individual spatial directions can vary. Under the influence of gravity, such grains will tend to lie flat, which, despite isotropic stress conditions, results in a transversely isotropic deformation behaviour /BEC 99/ and in the presented results in Section 4. A piece of the backfill material of the BAMBUS test field is shown in Fig. 5.5a, giving an impression of the layered structure under real conditions of drift backfilling. A variation in the porosity distribution, measured in a horizontal horizon above the heat producing casks /BEC 04/ is also given in Fig. 5.5b.

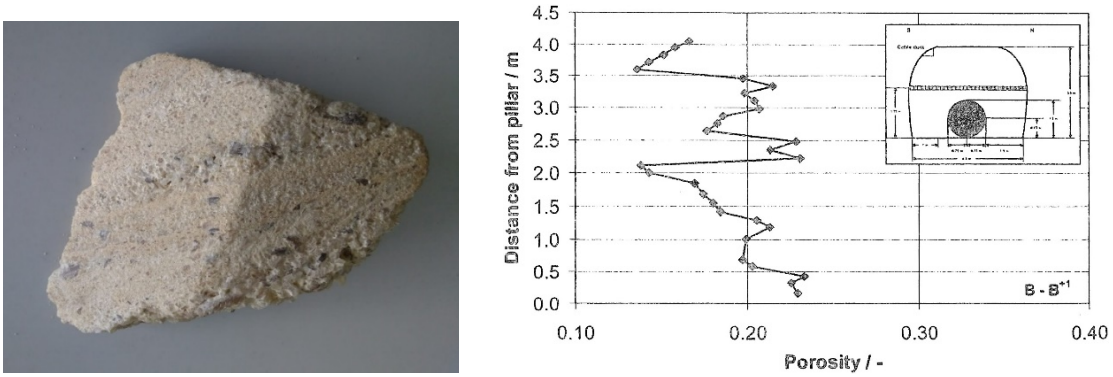

a) b)

Fig. 5.5 Distribution of grains: a) Layered structure of backfill material - Sample from the BAMBUS test field /HEE 19/. b) Horizontal porosity distribution in cross section B+1 (1 m behind central plane) /BEC 04/

Another aspect is the description of the discontinuous properties of the granular salt. To be able to use the concept of continuum mechanics, the approach of the representative volume element (RVE) is used. There are variations of the RVE-concept within numerical approach, which need not be considered here. The representative control volume is chosen in such a way that the overall effect of the locally individual behaviour in the RVE can be described by a mean behaviour. An example is an isotropic external stress, which causes local shear stresses within the grain structure, but the shear stresses compensates itself when averaged over the grains in the RVE. This aspect of representation also applies to the grain structure and its development respectively their influence on the observed behaviour.

In summary, the description of the grain structure is complex. With respect to the reproducible measurement results, a clear characterization of the granular salt is required. This can also be done on laboratory scale. Under the conditions of a repository, however, the situation is more difficult. It must be assumed that in the context of the proof, the concept of varied data sets is applied rather than that of a geometric description. Irrespective of this, a constitutive model may explicitly contain an approach to describe the grain structure or the influence is implicitly considered within the chosen approaches and their different parameter sets.

5.1.2.2 Requirements to mechanical models

Independent of the process class (Fig. 5.2) a process can be characterized by two quantities: time (instantaneous or time consuming) and energy consumption (reversible or

dissipative) (Fig. 3.7). Four combinations are possible, but in the THM processes for crushed salt, only three of them exist; there is no reversible time-consuming process. From a mechanical point of view, the following terms are synonymous: time consuming and viscous, reversible and elastic, dissipative and plastic; instantaneous is not specifically named. Accordingly, viscoelasticity is the mechanical sub-process that does not occur with crushed salt. The influence of field quantities is subordinated to this classification. Field quantities in the THM context are essentially stress, displacement and strain as well as their time rates, temperature and moisture. The resulting processes are listed in Fig. 3.7. In the case of moisture, a distinction must be made between freely available moisture available on the grain surfaces and moisture trapped in pores, since different deformation mechanisms are used. Furthermore, moisture can be a prerequisite for a deformation process or just a supporting parameter. Finally, the note from Section 3.2.3 resumed, according to which the weighting of the deformation mechanisms may change during the course of compaction and depending on the current state of the process variables.

Time-independent, i. e. instantaneous elasticity ε_{ij}^{el} is the basis for the stress development. Although it only plays a minor role from the deformation point of view, its effect cannot be neglected. There is no influence from moisture w, just from porosity φ (Tab. 5.2). At complete compaction, the stiffness tensor $\mathbb{C}$ should be approximately the same as for rock salt. "Approximately" results from deviations in the microstructure of the granular salt compared to rock salt, where these deviations were caused by the mechanical manufacturing process and may not have been completely eliminated.

$$\varepsilon_{ij}^{el} = f\left(\sigma_{ij}, \varphi\right) \tag{5.1}$$

(Time-independent) plasticity is the mechanical process that is required when the external load can be compensated not only by elasto-viscoplastic internal reactions. Plasticity is attributed to two basically independent mechanisms: grain rearrangement $\varepsilon_{ij}^{pl,ra}$ and grain fracture $\varepsilon_{ij}^{pl,fr}$.

Grain rearrangement is a rigid-body movement initiated by overcoming the external frictional forces acting on the grain. A rigid body motion is decomposed into a displacement component and a rotation component. The localization of the deformation is the distinguishing feature of the deformation mechanism in Fig. 3.1. Cataclastic flow is a spatially narrow band with shear deformation. Under these conditions, the grain movement leads

more to a dilatant behaviour. In the other case, the volume is reduced if the grain structure is rather loose and there is enough free pore space available for movement. Correspondingly, the external stress during grain rearrangement may be isotropic and deviatoric, whereby the influence from isotropic stress will disappear with decreasing porosity. Both variants take advantage from the friction-reducing effect of superficial moisture w and its hydraulic pressure p_{fl}. The moisture reduces the friction within the grain structure and the hydraulic pressure the contact force between grains.

$$\varepsilon_{ij}^{pl,rb} = f\left(\sigma_{ij}, \varphi, w, p_{fl}\right) \tag{5.2}$$

Inter- and intra-granular fracture is a structural overload. Possibly, it may be the prerequisite for the rearrangement of the aborted or broken pieces. In the case of a cataclasis, the above-mentioned narrow band contains shear fractures. In the case of the much looser material, fractures are the reaction to the local increase in stress resulting from the distribution of the external stress over the less pronounced contact surfaces. Since the stress increase decreases with the growth of the contact areas, this failure mode disappears with a decrease in porosity. With rearrangement, the external stress leading to the breakage may be isotropic and deviatoric, where the isotropic influence disappears with the decrease in porosity. Moisture typically has no influence on fracture. As note, fractures has an impact on the geometric description $\overline{D}$ of the grain structure (Section 5.1.2.1).

$$\varepsilon_{ij}^{pl,fr} = f\left(\sigma_{ij}, \varphi, \overline{D}\right) \tag{5.3}$$

Since granular salt is produced from rock salt, the viscoplastic deformation mechanisms of rock salt must also remain valid for crushed salt. Thus, the most important deformation for the overall process of granular salt compaction is viscoplastic deformation ε_{ij}^{vpl}. It contributes most significantly to achieving the goal of safe confinement and contains the greatest number of deformation mechanisms. Its individual main components are dislocation creep $\varepsilon_{ij}^{vpl,dc}$, solid-state diffusion $\varepsilon_{ij}^{vpl,ss}$, and pressure solution creep $\varepsilon_{ij}^{vpl,ps}$ (Fig. 3.7).

Dislocation creep results from the crystal structure of halite and consists of hardening and recovery. Dislocation creep exhibits a steady-state deformation rate if the rate of both components is equivalent. Numerical approaches without these two components and accordingly without the associated evolutionary equations are not able to represent

laboratory tests such as oedometer tests with realistic material parameters, /BEC 99/ and /KRÖ 17/.

The steady state of dislocation creep is disproportionately dependent on stress. On the basis of a Norton approach, a stress exponent in the range between 3 and 6 is expected. Thus, the local stress increase has a strong effect in the range of high porosity, because the load transfer occurs via small contact areas and partly small grains with small cross sections (Fig. 5.3). In this porosity range, dislocation creep is preferably carried out by the small grains. Large grains with comparatively low stress, at the level of the external acting, contribute to dislocation creep essentially only in the surroundings of the contact area. As the porosity decreases, the rate of dislocation creep reduces by two processes: recovery, which reduces the difference from hardening, and an increase in the number of contacts and contact areas between the grains, which reduces the stress increase.

As in the instantaneous plastic processes, both external isotropic and deviatoric stress can activate dislocation creep over a wide range of porosity. However, the isotropic stress influence disappears in the transition area to compact rock salt. A fully compacted granular salt has a higher number of grain boundaries, thus, comparable to natural virgin rock salt the dislocation creep rate is reduced, but recrystallization will take part over time (Tab. 5.2).

From the participation of the small grains in the deformation, the importance of the grain size distribution becomes evident. The advantage is the higher deformation rate compared to a mixture with reduced size distribution and the disadvantage is a possible segregation during insertion.

The deformation behaviour is determined at the beginning of the compaction by the behaviour of the loose grain structure and the local stress increase, later on by the further development of the contact areas. If the compaction is more advanced, the deformation behaviour approaches that of a single pore in a surrounding salt. Therefore, in total, three phases with two transition areas can be identified. During the first two phases, the external stresses have a similar effect on the internal deformation behaviour. Hence, the relationship between the volumetric deformation rate and the effective deformation rate should also be similar (Tab. 5.2). With the transition to single pore, the volumetric deformation rate must therefore approximate the behaviour of the void ratio rate $\dot{e} \propto e$, which means an asymptotic approximation to zero in this case (Tab. 5.2). Near complete compaction, in contrast, the equivalent strain rate remains in the order of magnitude of that

of intact rock salt. However, the deviatoric creep rate shows a functional change caused by the geometrical influence at the transition from loose bulk material to a material with a single pore structure.

In addition to the geometric and mechanical influence, the temperature and the pore pressure have an effect on the dislocation creep rate. Temperature has a particular influence on dislocation creep (Tab. 5.1). The influence of pore pressure p_p on deformation rate has hardly been included in constitutive models at present, /STO 17/. It is a current object of research to determine the extent and development of the influence of pore pressure. This applies to the same extent to the liquid path as to the gas path. It is assumed that pore pressure starts to become significant in the porosity range between 2 % and 5 %, /STO 17/, what is a complementary evaluation of Fig. 2.1. The upper value applies more to the fluid path, the lower value to the gas path. The systemic behaviour caused by the entry of gases and liquids from outside is not the subject of consideration here. If compaction reaches the above mentioned range, the determination of the effective stress in the sense of Terzaghi and Biot is of further importance.

$$\dot{\varepsilon}_{ij}^{vpl,dc} = f\left(\sigma_{ij}, \varphi, T, \overline{D}, p_p\right) \tag{5.4}$$

Solid-state diffusion takes place, in contrast to the pressure solution that still follows, without moisture. It consists of three parts: volume diffusion, grain boundary diffusion, surface diffusion. The process benefits from free spaces, which is higher along grain boundaries than in the lattice and even more at the surface. Therefore, surface diffusion is the dominant sub-process of solid-state diffusion. However, it must be taken into account that naturally dry salt from domal salt already contains pore solution (Section 3.1.1). This solution can be released and distributed on the grain surface. And even a very small amount of surface moisture is sufficient to activate pressure solution creep which increases deformation significantly.

$$\varepsilon_{ij}^{vpl,ss} = f(T, \overline{D}, \sigma_{\perp ss}) \tag{5.5}$$

A liquid phase is the necessary prerequisite for the mechanism of pressure solution. The mechanism consists of three steps - the dissolution of the solid granular salt into the fluid, the transport within the fluid and finally the precipitation as solid phase. The transport takes place in the direction of the potential gradient from an energy-rich place to a low-energy place.

Granular salt with naturally increased moisture content from bedded salt must be distinguished from moistened salt. When crushed salt is moistened, the moisture is on the grain surfaces and can become effective there immediately via the deformation mechanisms. In the other case, the moisture must be released by time-consuming deformation or hydraulic processes or acts during inner-crystalline deformation processes.

In case of sufficient available moisture on the surface, pressure solution is a very essential deformation process when stresses and temperatures are low and porosity is high. The stress dependency is nearly a linear function, which leads to this dominance for small stresses compared to the disproportionate stress dependence of dislocation creep. A slightly disproportionate stress dependence at pressure solution, at least in some range, is a subject of research. Contact areas are still small at the beginning of the compaction and therefore the transport distance is short. In addition, the gradient to the free surface is high because of the local stress increase.

At local level, the contact normal stress is the decisive stress component. However, due to the grain structure, it can be caused by both external isotropic and deviatoric stress. In addition to local stress and temperature, the grain size, the number of contacts and the contact area as well as the pore pressure have an effect (Equ.(5.6).

$$\varepsilon_{ij}^{vpl,ps} = f\left(\sigma_{ij}, T, \overline{D}, w, p_{fl}\right) \tag{5.6}$$

Recrystallization and healing is not a deformation process in the strict sense, but rather, from the numerical point of view, the process of developing an inner state variable in the evolution equation of constitutive models. The aim of recrystallization and healing is the recovery of cohesion between the surfaces of cracks in case of rock salt, /HAM 16/, and transferred to crushed salt for the surfaces of cracks and between grains. In addition, a weakened formulation was used in /HAM 16/ under the concept of damage regression, which considers the reduction of dilatancy in addition to the aspect of cohesion also. From this point of view, the compaction of granular salt is a single process of damage regression. Another aspect is the change in the grain structure of the granular salt, the crushed salt has already going through during its production and processing, and finally the further changes during its compaction process. Finally, the aspect of healing may play a specific role in connection with the proof of long-term safety.

In some of the above processes, healing is an integrated part of these processes, but the focus was on deformation processes. The influence of moisture on recovery has already been pointed out for dislocation creep (Fig. 3.7). The rate of dislocation creep

increases because of dynamic recrystallization. The reorganization is already part of the process description of pressure solution creep.

Recrystallization and healing are not homogeneous processes with the same state at the same time everywhere (Section 4). Therefore, within limits, they can also be seen inversely to percolation.

$$f(T, w, \overline{D}) \tag{5.7}$$

Tab. 5.2 Behavioural characteristics and their mathematical representation of selected deformation processes

Elasticity – Closing up to rock salt behaviour with low residual porosity	$\mathbb{C}(\varphi) \xrightarrow{\varphi \to 0} \sim \mathbb{C}_{rs}$
Creep I – Closing up to rock salt behaviour with low residual porosity	$\dot{\varepsilon}_{ij}^{vpl,dc}(\sigma_{ij}, \varphi, T, \overline{D}) \xrightarrow[\overline{D} \to \overline{D}_{RS}]{\varphi \to 0} \dot{\varepsilon}_{ij}^{vpl,dc_{rs}}(\sigma_{ij}^{d}, T)$ $\hat{\dot{\varepsilon}}^{vpl,dc}(\sigma_{ij}, \varphi, T, \overline{D}) \xrightarrow[\overline{D} \to \overline{D}_{RS}]{\varphi \to 0} \hat{\dot{\varepsilon}}^{vpl,dc_{rs}}(\sigma_{ij}^{d}, T)$
Creep II – Deviatoric rate and compaction rate are similar over a wide range of porosity	$\frac{\dot{\varepsilon}_{0}^{vpl,dc}(\sigma_{ij}, \varphi, T, \overline{D})}{\hat{\dot{\varepsilon}}^{vpl,dc}(\sigma_{ij}, \varphi, T, \overline{D})} \propto c \; \forall \varphi \gg 0$
Creep III - Compaction rate tend to 0 with low residual porosity	$\dot{\varepsilon}_{0}^{vpl,dc}(\sigma_{ij}, \varphi, T, \overline{D}) \xrightarrow{\varphi \to 0} 0$

5.1.2.3 Notes on numerical aspects of thermal and hydraulic behaviour

The main objectives of backfilling open cavities in a repository with granular salt are listed in Section 2. These are to transfer the heat resulting from the decay process of the waste away from the emplacement casks into the host rock and to ensure the integrity of the containment barrier over the entire period. The essential properties of granular salt with respect to proof are therefore its thermal and hydraulic properties. Other properties are necessary to describe the achieved state reliably. In order to carry out the proofs successfully, it is sufficient if the description of the condition covers the essential characteristics - it does not necessarily have to be complete. Some short remarks are given in the next two subchapters: first on thermal behaviour, then on hydraulic behaviour.

5.1.2.3.1 Thermal behaviour

In Section 2 the need to describe the thermal behaviour has been pointed out. In the concept of drift disposal, the thermal behaviour of the salt granulate is of particular importance. It results from the direct contact between the disposal cask and the backfill material.

If a largely dry salt granulate is assumed, the heat transport in the salt granulate is essentially determined by two processes: heat conduction within the grain structure and a further process in the porous space. To the extent that the pore volume decreases, the contact surfaces are enlarged, respectively new contacts are being established. Accordingly, the thermal conductivity within the grain structure improves and the additional process loses importance. If the grain structure is fixed, the heat conduction decreases as the temperature increases whilst the radiation proportion increases with the temperature (Fig. 2.4), where both sub-processes have a non-linear behaviour.

In case of calculations such as those carried out in the context of this project, heat transport is described solely by means of the equation of heat conduction. In the simplest case, the parameter for heat conduction consists of a constituent in combination with a porosity function; two constituents contribute to the total amount in more complex models. The one constituent is generally identified as that of the intact rock salt. For pure rock salt (halite), Birch & Clark /BIR 40/ specifies the thermal resistance in the temperature range between 0 °C and 400 °C as a linear function of the temperature, resulting in the temperature-dependent coefficient of thermal conductivity λ_{RS}.

$$\lambda_{RS} = \frac{\lambda_0}{1+a\,\vartheta} \tag{5.8}$$

a	material parameter
λ_0	thermal conductivity at 0 °C [W/m/K]
ϑ	temperature [°C]

In case of halite $\lambda_0 = 6.1\ W/m/K$ and $a = 0.00483\ 1/°C$. Polynomial approximations are found in /BEC 99/ and /BEC 04/ as well as a compilation in /STO 17/ as alternative to Equ. (5.8). Partly, the parameters were adapted to specific facies. An exponential approach can be found in /STO 17/ as an additional approach.

Approaches for granular salt, which refer only to one constituent, are a multiplicative decomposition of a single substance approach with a porosity function, cf. compilation in

/STO 17/. The porosity function is mostly polynomial, but an exponential approach is also included. A further approach to this type can be found in /HEI 91/ with a rational porosity function given by geometrical reason. The measurement data presented in Fig. 2.4, however, indicate that single substance approaches are able to represent the range of low porosity to a limited extent only. Approaches with two constituents, which contain in addition to the thermal conductivity of rock salt λ_{RS} another constituent λ_1 are e.g.

/KOR 91/ $$\lambda_{CS} = \frac{\varphi}{\varphi_0}\lambda_1 + \left(1 - \frac{\varphi}{\varphi_0}\right)^m \lambda_{RS} \quad (5.9)$$

/BGR/ $$\lambda_{CS} = \frac{\lambda_{RS}\,(1-\varphi)}{1 + a\,\frac{\varphi}{(1-\varphi)}\,\frac{\lambda_{RS}}{\lambda_1}} \quad (5.10)$$

/MAC 15/ $$\lambda_{CS} = \lambda_1^{\varphi}\,\lambda_{RS}^{1-\varphi} \quad (5.11)$$

a	material parameter
m	material parameter [-]
φ	current porosity [-]
φ_0	porosity from non-compacted granular salt [-]

The second constituents λ_1 in Equ. (5.9) is a polynomial approach of 3rd order in /KOR 91/ and /BEC 04/, the adjustment in /WIE 12/ was done by means of a linear function (Fig. 2.4). Another note refers to the porosity from non-compacted granular salt φ_0. This porosity is not the initial or built-in porosity but more a theoretical value as the porosity of a loose bulk. The reason is that the results for the same material at the same state differ with its initial porosity.

5.1.2.3.2 Hydraulic behaviour

The aspect of hydraulic tightness is mentioned in Section 2. A hydraulically tight barrier is present if an adequate hydraulic resistance is reached. Typically, the hydraulic flow is described based on Darcy flow.

A number of permeability models for rock salt are listed in /ALK 08/ and /KUH 14/. The overwhelming number of models listed describe permeability either as a function of porosity or stress. Only a few of the models listed include porosity and stress dependence both. In principle, these models can also be applied to granular salt, if granular salt is considered to be loosened rock salt at low porosity, e. g. /HEE 04/. However, there are differences in the network, which is also reflected in the development of permeability (Fig. 2.1).

In rock salt, the stress tensor in its spatial expression is decisive for the unloading at grain boundaries as well as the arise of cracks and crack networks. In contrast, granular salt initially contains a non-oriented pore network, which is closed due to the viscoplastic behaviour of host rock and thus the resulting compaction of the salt granulate.

The approach in /POP 07/ (Equ. (5.15) was applied to slightly damaged rock salt (Fig. 2.3, red curve). Its reference parameters are $\Delta k = 5.1$, $\mathrm{b}_t = 0.8\,1/MPa$, $n = 0.04\,1/MPa$, $\eta = 3 \cdot 10^{-10}\ m^2$, $\epsilon = 0.0023$, and $\xi = 4.16$.

/SER 93/ $$k = k_0 \left(\frac{\sigma_{min}}{p}\right)^{2\lambda} \left(\varepsilon_{vol}^{ir}\right)^{s} \tag{5.12}$$

/HEE 04/ $$k = \frac{k_{tp}}{\left(\frac{\varphi_{tp}}{\varphi}\right)^{n_1} + \left(\frac{\varphi_{tp}}{\varphi}\right)^{n_2}} \tag{5.13}$$

$$k_{tp} = a_k\, e^{b_k\, \hat{\sigma}} \tag{5.14}$$

$$\varphi_{tp} = a_\varphi\, e^{b_\varphi\, \hat{\sigma}} \tag{5.15}$$

k_0, a_k permeability parameter [m²]
Δk logharithmized value of the permeability contrast [-]
η permeability parameter [m²]
λ, s material parameter [-]
n_1, n_2 material parameter [-]
a_φ material parameter [-]
a, b, c material parameter [-]
b_k, b_φ material parameter [1/MPa]
b_t, ϵ, n material parameter [1/MPa]
σ_{min} minimum stress [MPa]: pressure (+), tension (-)
$\hat{\sigma}_{12}$ effective confining stress perpendicular to fractures [MPa]
p normalizing stress [MPa]: $p = 1\ MPa$
$\hat{\sigma}$ Terzaghi effective stress [MPa] – $\hat{\sigma} = \sigma_{min} - \alpha_B\, p_{fl}$
α_B Biot coefficient [-] – for reasons of conversatims: $\alpha_B = 1$
ε_{vol}^{ir} dilatancy [-]
$\varepsilon_{vol,0}^{ir}$ initial dilatancy [-]
φ current porosity [-]
φ_0 porosity of non-compacted granular salt [-]
$E_i(x)$ exponential integral [-]: $Ei(x) = -\int_{-x}^{\infty} \frac{e^{-t}}{t}\, dt = \int_{-\infty}^{x} \frac{e^{t}}{t}\, dt$
$\langle X \rangle$ Macauleay brackets: $\langle X \rangle = X\ \forall\ X > 0\ \wedge\ \langle X \rangle = 0\ \forall\ X \leq 0$

Some notes:

- The different behaviour along a load path, which means compaction versus damage, as shown in Fig. 2.1, is not yet included in the models.
- The model in /KUH 14/ is a simplified form given by Stormont, which can be adopted to crushed salt condition by e. g. $\varepsilon_{kk}^{pl} = \frac{\varphi}{1-\varphi_0}$
- Some more constitutive models exist whose stress dependence results from a dilatancy condition – they have to be checked whether they are suitable in the context of granular salt or not.

5.2 Existing constitutive models for crushed salt

5.2.1 BGR-CS3 model

The BGR-CS3 model considers elastic and creep deformation of crushed salt as well as deformation due to grain rearrangement and humidity creep. The constitutive model as well as its implementation in BGR´s proprietary FEM code JIFE are currently being reviewed both from a theoretical point of view and in terms of applicability. Here a condensed version of the detailed documentation published in /KRÖ 17/ is given.

The formulation of the BGR-CS3 constitutive model is based on a geometrical idealization (Fig. 5.6) presented in /STE 85/. The elastic component of crushed salt deformation is described by Hooke's law where the Young's modulus E is piecewise linearly related to the void ratio e. In the following chapters, the models for the creep deformation, the grain rearrangement and the humidity creep of crushed salt are presented.

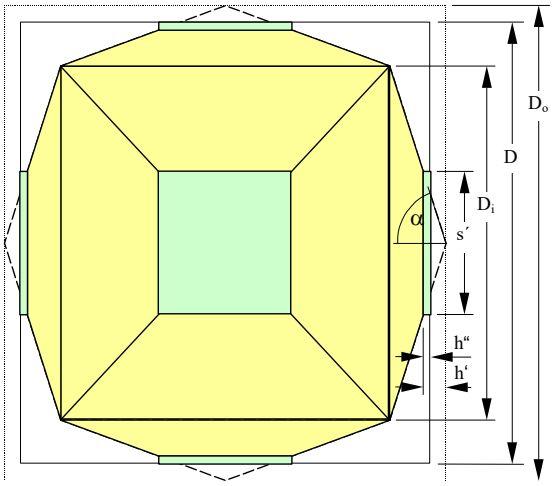

Fig. 5.6 Idealized model of a unit crystal with peak to peak contact to six adjoining crystals

5.2.1.1 Creep

The volumetric creep rate of the crushed salt is given by Equ. (5.16) as a function of the local stress σ^{local} and a dynamically developing frictional hardening stress σ^{rv} which in a stationary state tends to $\sigma^{rv} \rightarrow z\,\sigma^{local}$. The local stress at the contact zones is computed from the hydrostatic pressure p, the deviatoric stress q (= von Mises equivalent stress) and the extended relative contact area U'. $\frac{1}{k}$ represents the ratio between deforming solid mass and total solid mass of the crushed salt.

$$\dot{\epsilon}_{vol} = -2A\exp\left(-\frac{Q}{RT}\right)\left(\frac{\sigma^{local}-\sigma^{rv}}{1-z}\right)^{n-1}\cot(\alpha)\sqrt{U}\left(\frac{p}{U'}\right)e^{\frac{\frac{1}{k}+e}{1+e}} \tag{5.16}$$

$$\sigma^{local} = \sqrt{\left(\frac{p}{U'}\right)^2 + b\left(\frac{q}{U'\beta}\right)^2} \tag{5.17}$$

α	angle (Fig. 5.6)
e_0	initial void ratio [-]
e	void ratio [-]
β, b	fit parameters close to 1 [-]
z	ratio of frictional stress over local stress [-]
A	structural parameter for Norton law [d^{-1}]
Q	activation energy for Norton law [kJ mol^{-1}]
n	stress power for Norton law [-]
R	universal gas constant [kJ mol^{-1} K^{-1}]
T	temperature [K]

The differential equation for evolution of the frictional hardening stress in the contact zone (“geometric hardening”) is given by:

$$d\sigma^{rv} = \frac{z\,\sigma^{local} - \sigma^{rv}}{m\,\epsilon_{vol}}\, d\epsilon_{vol} \tag{5.18}$$

m fit parameter [-]

The relative grain contact area U and its extension U' satisfy the following functions of initial and current void ratio derived from the geometrical idealization ($U = 0$ for virgin uncompacted crushed salt and $U \to 1$ for complete compaction):

$$U = \left(\frac{3}{2}\frac{1}{\cot(\alpha)}\right)^2 \left(\left(\frac{1+ke_0}{1+ke}\right)^{\frac{1}{3}} - 1\right)^2 \tag{5.19}$$

$$U' = (\kappa U)^{\gamma} \tag{5.20}$$

$$\cot(\alpha) = \sqrt{1 + ke_0} - 1 \tag{5.21}$$

κ, γ artificial fit parameters close to 1 [-]

For small void ratios volumetric creep is decreasing linearly with void ratio thus fulfilling theoretical expectation and avoiding negative porosity.

Deviatoric creep comprises the creep due to the effect of the voids as well as creep of the inner bulk of the grains including a frictional hardening stress σ^{rn}.

$$\dot{\epsilon}_{dev} = 2A\exp\left(-\frac{Q}{RT}\right)\left(\frac{\sigma^{local} - \sigma^{rv}}{1-z}\right)^{n-1} cot(\alpha)\sqrt{U}c\left(\frac{q}{U'^{\beta}}\right) e^{\frac{\frac{1}{k}+e}{1+e}} + A\exp\left[-\frac{Q}{RT}\right]\left(\frac{q-\sigma^{rn}}{1-z}\right)^{n} \tag{5.22}$$

c fit parameter close to 1 [-]

The differential equation for evolution of the frictional hardening stress due to Norton creep is given by Equ. (5.31):

$$\frac{d\sigma^{rn}}{d\epsilon^{dev}_{Norton}} = \kappa_{rn}\left[\frac{q-\sigma^{rn}}{\sigma^{rn}} - \left(\frac{1-z}{z}\right)^2 \frac{\sigma^{rn}}{q-\sigma^{rn}}\right] \tag{5.23}$$

κ_{rn} fit parameter [-]

Combining the approaches of volumetric and deviatoric creep the tensorial expression for creep of crushed salt results in:

$$\dot{\epsilon}_{dev} = 2A\exp\left(-\frac{Q}{RT}\right)\left(\frac{\sigma^{local}-\sigma^{rv}}{1-z}\right)^{n-1}\cot(\alpha_0)\sqrt{U}e\frac{\frac{1}{k}+e}{1+e}\left[-\frac{p}{U'}\frac{\delta_{ij}}{3}\right.$$
$$\left.+\frac{3}{2}c\left(\frac{q_{ij}}{U'^{\beta}}\right)\right]+\frac{3}{2}A\exp\left[-\frac{Q}{RT}\right]\left(\frac{q-\sigma^{rn}}{1-z}\right)^{n}\frac{q_{ij}}{q} \quad (5.24)$$

5.2.1.2 Grain rearrangement

Fracturing occurs when the local stress in the contact zone exceeds a given stress limit σ^{frac}. Since experimental results indicate that this limit is inverse proportional to the root of grain diameter, the following scaling has been suggested:

$$\sigma^{frac} = \sigma_F\sqrt{\frac{0.01m}{D_i}} \quad (5.25)$$

σ_F fit parameter [MPa]

D_i grain width [m] (Fig. 5.6)

For a diameter of about 1 cm, the parameter σ_F should be about that of fracture stress for compact rock salt. As a reference value for the grain diameter the fraction with the lowest grain diameter has to be taken.

Hence, deformation due to fracture and grain rearrangement will happen as soon as the function $\langle\sigma^{local}-\sigma^{frac}\rangle$ is getting positive. The local effect due to fracturing is given by:

$$\dot{\epsilon}_{ij}^{frac} = B^{frac}\langle\sigma^{local}-\sigma^{frac}\rangle\cot(\alpha)\sqrt{U}e\frac{\frac{1}{k}+e}{1+e}\frac{1}{\sigma^{local}}\left(\frac{p}{U'}\frac{\delta_{ij}}{3}+\frac{3}{2}\sqrt{b}\frac{q_{ij}}{U'^{\beta}}\right) \quad (5.26)$$

δ_{ij} Kronecker delta

B^{frac} fit parameter [-]

5.2.1.3 Humidity creep

The modelling of humidity creep is assuming diffusion of salt ions having a pressure gradient on the contact areas between the grains as driving force. The macroscopic creep rate is then given by:

$$\dot{\epsilon}^{diff} = \frac{D^{diff}}{R^{contact}D_i\left[1+\cot(\alpha)\right]^{\frac{1}{3}}} * \frac{(1+ke)^{\frac{2}{3}}}{k(1+e)} * \exp\left(-\frac{Q^{diff}}{RT}\right)$$
$$* \sinh\left(\frac{3\kappa'\sigma^{local}}{TR^{contact}}\right) \quad (5.27)$$

The radius $R^{contact}$ results from a radial symmetric capture of the contact area.

$$R^{contact} = \zeta \frac{s'}{2} = \zeta \frac{3}{4} \frac{D_i[1+\cot(\alpha)]}{\cot(\alpha)} \left[1 - \left(\frac{1+ke}{1+ke_0}\right)^{\frac{1}{3}}\right] \tag{5.28}$$

ζ fit parameter [-]
s' width of the contact area [m]
Q^{diff} activation energy for diffusion process [kJ mol^{-1}]
D^{diff} parameter [m^2 d^{-1}]
κ' parameter [K m MPa^{-1}]

The scalar creep rate is then generalized including deviatoric components:

$$\dot{\epsilon}_{ij}^{diff} = \frac{D^{diff}}{R^{contact} D_i [1+\cot(\alpha)]^{\frac{1}{3}}} * \frac{(1+ke)^{\frac{2}{3}}}{k(1+e)} * \exp\left(-\frac{Q^{diff}}{RT}\right) * \sinh\left(\frac{3\,\kappa' \sigma^{local}}{TR^{contact}}\right) * \left(-\frac{p}{\sigma^{local}}\frac{\delta_{ij}}{3} + \frac{3}{2} c_d \frac{q_{ij}}{\sigma^{local}}\right) \tag{5.29}$$

c_d fit parameter [-]

$$\dot{\sigma}_{ij} = 2G\dot{e}_{ij}^{e} + K\dot{\varepsilon}_{kk}^{e}\delta_{ij} = 2G\left(\dot{e}_{ij} - \dot{e}_{ij}^{c}\right) + K(\dot{\varepsilon}_{kk} - \dot{\varepsilon}_{kk}^{c})\,\delta_{ij} \tag{5.30}$$

5.2.2 Callahan model

This description of the WIPP crushed salt constitutive model is primarily based on information provided in /CAL 99/. Most of the model is presented in an infinitesimal strain setting for simplicity, but, in actual practice, the model is extended into the finite deformation realm using hypoelasticity as described in Section 2.4 of /REE 18/. Note that the following description uses the convention that tensile stresses and strains are positive.

5.2.2.1 Model equations

The WIPP crushed salt constitutive model, the total strain rate is additively decomposed into elastic strain rate $\dot{\varepsilon}_{ij}^{e}$ and inelastic (creep) strain rate $\dot{\varepsilon}_{ij}^{c}$ contributions, as shown in Equ. (5.31).

$$\dot{\varepsilon}_{ij} = \dot{\varepsilon}^{e}_{ij} + \dot{\varepsilon}^{c}_{ij} \tag{5.31}$$

5.2.2.2 Elastic behaviour

The elastic strain rate may be decomposed into deviatoric $\dot{e}^{e}_{ij}$ and volumetric $\dot{\varepsilon}^{e}_{kk}$ contributions:

$$\dot{\varepsilon}^{e}_{ij} = \dot{e}^{e}_{ij} + \frac{1}{3}\dot{\varepsilon}^{e}_{kk}\delta_{ij} \tag{5.32}$$

In this model the stress rate $\dot{\sigma}_{ij}$ is related to the elastic strain rate by the isotropic linear-elastic relation:

$$\dot{\sigma}_{ij} = 2G\dot{e}^{e}_{ij} + K\dot{\varepsilon}^{e}_{kk}\delta_{ij} = 2G\left(\dot{e}_{ij} - \dot{e}^{c}_{ij}\right) + K(\dot{\varepsilon}_{kk} - \dot{\varepsilon}^{c}_{kk})\,\delta_{ij} \tag{5.33}$$

G shear modulus [Pa]
K bulk modulus [Pa]

Following the work of /SJA 87/, these elastic moduli are assumed to be functions of the crushed salt density ρ. No temperature dependency is included in the functional form of the elastic moduli. The functional forms for these elastic moduli are:

$$G = G_0 e^{G_1 \rho} \tag{5.34}$$

$$K = K_0 e^{K_1 \rho} \tag{5.35}$$

G_0, K_0, material parameters [Pa]
G_1, K_1 material parameters [m^3/Kg]

These parameters are determined from laboratory testing.

5.2.2.3 Inelastic (creep) behaviour

The total creep strain rate $\dot{\varepsilon}^{c}_{ij}$ contains contributions from two deformation mechanism – dislocation creep $\dot{\varepsilon}^{d}_{ij}$ and grain boundary diffusional pressure solution $\dot{\varepsilon}^{w}_{ij}$:

$$\dot{\varepsilon}^{c}_{ij} = \dot{\varepsilon}^{d}_{ij} + \dot{\varepsilon}^{w}_{ij} \tag{5.36}$$

The following flow rules describe the evolution of these two creep strains

$$\dot{\varepsilon}^{d}_{ij} = \left[\dot{\varepsilon}^{d}_{eq}(\sigma^{f}_{eq})\right]\frac{\partial \sigma_{eq}}{\partial \sigma_{ij}} \tag{5.37}$$

$$\dot{\varepsilon}^{w}_{ij} = \left[\dot{\varepsilon}^{w}_{eq}(\sigma^{f}_{eq})\right]\frac{\partial \sigma_{eq}}{\partial \sigma_{ij}} \tag{5.38}$$

The terms in brackets in Equ. (5.37) and Equ. (5.38) are the equivalent creep strain rates for dislocation creep $\dot{\varepsilon}_{eq}^{d}$ and grain boundary diffusional pressure solution $\dot{\varepsilon}_{eq}^{w}$.The notation used in Equ. (5.37) and Equ. (5.38) indicates these equivalent creep strain rates are scalar functions of the equivalent stress measure σ_{eq}^{f}, which is defined in Equ. (5.47). The non-associated creep flow potential σ_{eq} is defined in Equ. (5.48). The partial derivative term $\frac{\partial \sigma_{eq}}{\partial \sigma_{ij}}$ appearing in Equ. (5.37) and Equ. (5.38) is the normal to the flow potential, which determines the creep flow direction.

Equivalent stress and flow potential

The equivalent stress and flow potential used in Equ. (5.37) and Equ. (5.38) are given by:

$$\sigma_{eq}^{f} = \left[\eta_0 \Omega_f^{\eta_1} \sigma_m^2 + \left(\frac{2-D}{D}\right)^{\frac{2n_f}{n_f+1}} (\sigma_1 - \sigma_3)^2\right]^{\frac{1}{2}} \tag{5.39}$$

$$\sigma_{eq} = \left[\kappa_0 \Omega^{\kappa_1} \sigma_m^2 + \left(\frac{2-D}{D}\right)^{\frac{2n}{n+1}} (\sigma_1 - \sigma_3)^2\right]^{\frac{1}{2}} \tag{5.40}$$

Where

$$\Omega_f = \left[\frac{(1-D)n_f}{\left[1-(1-D)^{\frac{1}{n_f}}\right]^{n_f}}\right]^{\frac{2}{n_f+1}} \tag{5.41}$$

$$\Omega = \left[\frac{(1-D_v)n}{\left[1-(1-D_v)^{\frac{1}{n}}\right]^{n}}\right]^{\frac{1}{2}} \tag{5.42}$$

$$D_v = \begin{cases} D_t & D \le D_t \\ D & D > D_t \end{cases} \tag{5.43}$$

D	current fractional density = $\frac{\rho}{\rho_{int}}$ [-]
ρ_{int}	intact salt density Kg/m3]
σ_m	mean stress = $\frac{1}{3}\sigma_{kk}$ [Pa]
σ_1	maximum principle stress [Pa]
σ_3	minimum principle stress [Pa]
$\eta_0, \eta_1, \kappa_0, \kappa_1, n_f, n, D_t$	= material parameters [-]

The functional forms of Equ. (5.39) and Equ. (5.40) are identical, but each has independent parameters so that one can specify different mean stress dependence to the equivalent stress and flow potential. This non-associated formulation allows one to control the ratio of dilation strain to distortional strain without affecting the equivalent stress definition. As crushed salt approaches full consolidation ($D \rightarrow 1$), Ω_f and Ω_2 both approach zero and the mean stress influence on the creep strain rate is eliminated. This is consistent with observed inelastic isochoric deformation characteristics of intact salt. When the salt is fully consolidated, $D = 1$, Equ. (5.39) and Equ. (5.40) reduce to

$$\sigma_{eq}^{f} = \sigma_{eq} = \sigma_1 - \sigma_3 \tag{5.44}$$

which is equal to the Tresca equivalent stress. Graphically, the flow potential resembles the shape of an American football whose axis is aligned with the hydrostat in Fig. 5.7a when $D < 1$, but it changes to a hexagon whose surface normals are perpendicular to the hydrostat in Fig. 5.7b when $D = 1$. An expanded expression for the flow potential normal $\frac{\sigma_{eq}}{\sigma_{ij}}$ is provided in Section 2.2.1 of /CAL 99/.

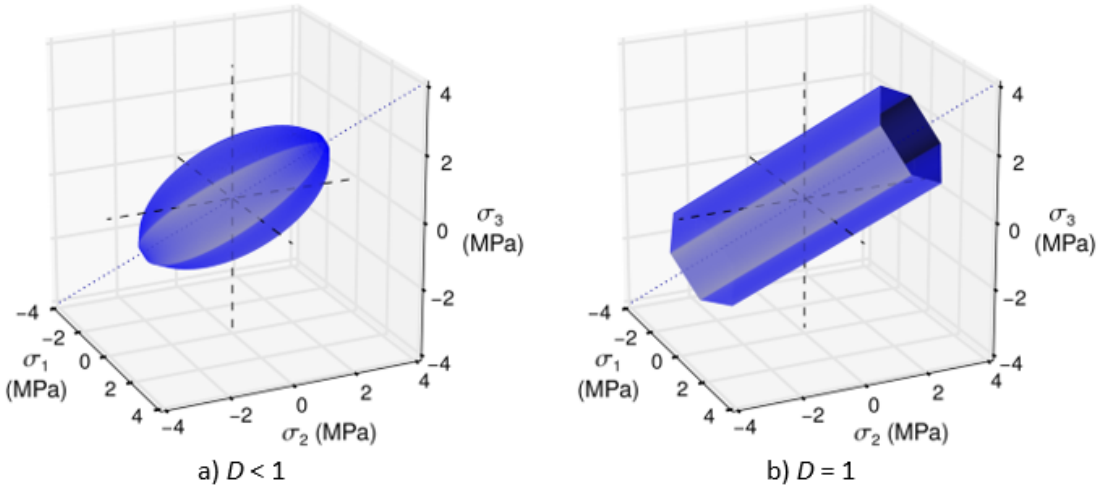

Fig. 5.7 Flow potential at two different relative densities

To complete the description of the creep strain rate, the kinetic equations (i.e. equivalent creep strain rate equations) for dislocation $\dot{\varepsilon}_{eq}^{d}$ and grain boundary diffusional pressure solution $\dot{\varepsilon}_{eq}^{w}$ need to be defined.

Kinetic equation for dislocation creep

The dislocation creep model, known as the Multi-mechanism Deformation model (MD model) originally developed by /MUN 79/ and later extended by /MUN 89/, provides the dislocation creep component of the crushed salt model. /REE 18/ recently extended the MD model to account for creep at low equivalent stress and exchanged the Tresca equivalent stress for the Hosford equivalent stress. The creep at low equivalent stress has been incorporated into the WIPP crushed salt model, but the equivalent stress has been left as Tresca for now.

The kinetic equation for dislocation creep in the MD model is given by

$$\dot{\varepsilon}_{eq}^{d} = F\dot{\varepsilon}_{s} \tag{5.45}$$

F function which accounts for transient effects

$\dot{\varepsilon}_s$ steady state dislocation creep strain rate [-]

The transient function *F* has three branches: a work hardening branch (*F* > 1), an equilibrium branch (*F* = 1), and a recovery branch (*F* < 1)

$$F = \begin{cases} exp\left[\Delta\left(1-\dfrac{\zeta}{\varepsilon_t^f}\right)^2\right] & \zeta < \varepsilon_t^f \quad \text{Transient Branch} \\ 1 & \zeta = \varepsilon_t^f \quad \text{Equilibrium Branch} \\ exp\left[-\delta\left(1-\dfrac{\zeta}{\varepsilon_t^f}\right)^2\right] & \zeta > \varepsilon_t^f \quad \text{Recovery Branch} \end{cases} \tag{5.46}$$

The choice of the particular branch depends on the transient strain limit ε_t^f and the internal variable ζ. The legacy MD model used a single mechanism to describe the stress and temperature dependence of the transient strain limit. /REE 16/, however, analysed the data from /SAL 15/ and /DUE 15/ and discovered larger transient strain limit values for equivalent stress < 8 MPa than would be expected from extrapolating from higher stresses. Therefore, an additional mechanism of identical form to the legacy model was added to capture the transient creep at low equivalent stress.

The new transient strain limit as prescribed by /REE 18/ is given by:

$$\varepsilon_t^f = \sum_{i=0}^{1} \varepsilon_i^f \tag{5.47}$$

$$\varepsilon_i^f = K_i e^{c_i T} \left(\frac{\sigma_{eq}^f}{\mu} \right)^{m_i} \tag{5.48}$$

K_i, c_i, m_i, material parameters
T absolute temperature [K]
M shear modulus of intact salt [Pa]

Subscript "0" identifies the low stress transient strain limit term and subscript "1" the legacy transient strain limit term.

The internal variable ζ, used in the calculation of the transient function *F,* is obtained by integration of the evolution equation:

$$\dot{\zeta} = (F - 1)\dot{\varepsilon}_s \tag{5.49}$$

The quantities Δ and δ, appearing in Equ. (5.46), are the work hardening and recovery parameters and are given by Equ. (5.50) and Equ. (5.59), respectively. In these equations α_h, β_h, α_r, and β_r are material parameters. The recovery parameter δ is often taken to be constant (i.e. $\delta = \alpha_r$) because of insufficient data.

$$\Delta = \alpha_h + \beta_h \log_{10} \left(\frac{\sigma_{eq}^f}{\mu} \right) \tag{5.50}$$

$$\delta = \alpha_r + \beta_r \log_{10} \left(\frac{\sigma_{eq}^f}{\mu} \right) \tag{5.51}$$

In the current MD model, four steady state dislocation mechanisms are considered. The steady state dislocation mechanism associated with low equivalent stress is denoted $\dot{\varepsilon}_{s_0}$. The actual micro-mechanical origin for the low stress behaviour has not been conclusively identified but is believed to be pressure solution redeposition along the grain boundaries /BER 19/. The other three steady state dislocation mechanisms are the same as in the legacy MD model: dislocation climb $\dot{\varepsilon}_{s_1}$, an unidentified but experimentally observed mechanism $\dot{\varepsilon}_{s_2}$, and dislocation slip $\dot{\varepsilon}_{s_3}$. Because these mechanisms are assumed to act in parallel, their contribution to the steady state dislocation creep strain rate is simply the sum of the four:

$$\dot{\varepsilon}_s = \sum_{i=0}^{3} \dot{\varepsilon}_{s_i} \tag{5.52}$$

$$\dot{\varepsilon}_{s_i} = A_i \left(\frac{\sigma_{eq}^f}{\mu}\right)^{n_i} exp\left(-\frac{Q_i}{RT}\right) \; for \; i < 3 \tag{5.53}$$

$$\dot{\varepsilon}_{s_3} = H\left(\sigma_{eq}^f - \sigma_0\right) \sum_{i=0}^{2} B_i e^{-\frac{Q_i}{RT}} \sinh\left[q\left(\frac{\sigma_{eq}^f - \sigma_0}{\mu}\right)\right] \tag{5.54}$$

A_0, A_1, A_2, B_0, B_1, B_2 = structure factors [1/s]
Q_0, Q_1, Q_2 = activation energies [J/mol]
R = universal gas constant = 8.31446 J/(mol-K)
q = stress constant [MPa]
σ_0 = stress limit [-]
H = Heaviside function with argument $(\sigma_{eq}^f - \sigma_0)$

The low stress mechanism has the same functional form as the first and second mechanisms in the legacy MD model. The first mechanism (dislocation climb) dominates at low equivalent stress and high temperature. The second mechanism (unidentified or unnamed) dominates at low equivalent stress and temperature. The third mechanism (dislocation glide) is only active at high stress when $\sigma_{\mathrm{eq}}^{\mathrm{f}} > \sigma_0$ as reflected by the Heaviside function *H*(•).

Kinetic equations for grain boundary diffusional pressure solution

This section transitions from the earlier infinitesimal strain presentation to a finite strain presentation in order to more accurately define the logarithmic volume strains in terms of densities and fractional densities.

The kinetic equation for grain boundary diffusional pressure solution, used in the WIPP crushed salt model, is a modified version of the /SPI 93/ model for moist crushed salt:

$$\dot{\varepsilon}_{eq}^{w} = \frac{r_1 w^a}{d^p} e^{-\bar{\varepsilon}_v} \left(\frac{e^{r_3 \bar{\varepsilon}_v}}{|e^{\bar{\varepsilon}_v} - 1|^{r_4}}\right) \frac{e^{-\frac{Q_s}{RT}}}{T} \Gamma \sigma_{eq}^f \tag{5.55}$$

r_1 = material parameter [m^p-K/(Pa-s)]
r_3, r_4, a, p = material parameters [-]
Q_s = material parameter [J/mol]
T = absolute temperature [K]
R = universal gas constant 8.31446 [J/(mol-K]
d = salt grain size [m]
w = moisture fraction by weight [-]
$\bar{\varepsilon}_v$ = logarithmic volume strain, relative to the original configuration [-]
Γ = geometry function [-]

Note that if the crushed salt is dry ($w = 0$) the grain boundary diffusional pressure solution contribution to the total strain rate vanishes i.e. $\dot{\varepsilon}^{ss}_{eq} = 0$.

Equ. (5.63) contains the term $e^{\bar{\varepsilon}_v} - 1$ in the denominator, which could cause problems if the volume strain were zero. The quantity $\bar{\varepsilon}_v$ is defined, however, relative to an original (fictitious) configuration, such that $\bar{\varepsilon}_v$ is always positive. To do so, the following relationships between the different fractional densities and crushed salt densities are introduced.

$$D_0 = \frac{\rho_0}{\rho_{int}} \tag{5.56}$$

$$D_* = \frac{\rho_*}{\rho_{int}} \tag{5.57}$$

D_0 = fractional density in the original configuration [-]

D_* = fractional density at emplacement time [-]

ρ_0 = crushed salt density at the original fractional density [Kg/m^3]

ρ_* = crushed salt density at emplacement time [Kg/m^3]

According to /CAL 99/, the original fractional density D_0 is typically set to 0.64, based on the approximate fractional density for random dense packing of single size spheres.

The following relationships between porosity, density, and fractional density are useful:

$$\Phi_0 = 1 - \frac{\rho_0}{\rho_{int}} = 1 - D_0 \tag{5.58}$$

$$\Phi_* = 1 - \frac{\rho_*}{\rho_{int}} = 1 - D_* \tag{5.59}$$

$$\Phi = 1 - \frac{\rho}{\rho_{int}} = 1 - D \tag{5.60}$$

Φ_0 = porosity based on assumed original fractional density [-]

Φ_* = porosity at emplacement time [-]

Φ = porosity at current time [-]

To complete the variable definitions, the relationships between the volumetric strain, density, and fractional density are summarized as

$$\bar{\varepsilon_v} = \varepsilon_v + \varepsilon_{v*} = \ln\left(\frac{\rho_*}{\rho}\right) + \varepsilon_{v*} = \ln\left(\frac{D_*}{D}\right) + \varepsilon_{v*} \tag{5.61}$$

$$\varepsilon_{v*} = \ln\left(\frac{\rho_0}{\rho_*}\right) = \ln\left(\frac{D_0}{D_*}\right) \tag{5.62}$$

Therefore

$$\bar{\varepsilon_v} = \varepsilon_v + \varepsilon_{v*} = \ln\left(\frac{\rho_0}{\rho}\right) = \ln\left(\frac{D_0}{D}\right) \tag{5.63}$$

And

$$\hat{\varepsilon}_v = e^{\bar{\varepsilon}_v} - 1 \tag{5.64}$$

ε_v = logarithmic volume strain relative to the emplacement configuration [-]

ε_{v*} = logarithmic volume strain at the emplacement configuration relative to the original (fictitious) configuration [-]

$\hat{\varepsilon}_v$ = engineering volume strain relative to the original (fictitious) configuration [-]

Thus, an emplaced volumetric strain ε_{v*}, corresponding to the volumetric strain accumulated in going from a fractional density D_0 to the fractional density at the time the crushed salt is placed D_* is included in Equ. (5.61) to avoid division by zero at the start of a calculation when $\varepsilon_v = 0$.

The geometry function Γ used in Equ. (5.55) has two functional forms given by Equ. (5.61); the choice of which one to use depends on the magnitude of the engineering volumetric strain $\hat{\varepsilon}_v$. For compressive volumetric strains less than 15 %, a constant value of $\Gamma = 1$ is used.

$$\Gamma = \begin{cases} 1 & \text{Small strain } (\hat{\varepsilon}_v > -0.15) \\ \left[\dfrac{e^{\varepsilon_v} + \Phi_0 - 1}{\Phi_0 e^{\bar{\varepsilon}_v}}\right]^{n_5} & \text{Large strain } (\hat{\varepsilon}_v < -0.15) \end{cases} \tag{5.65}$$

n_5 = material parameter

As the crushed salt density approaches the density of intact salt, the value of Γ approaches zero; therefore, $\dot{\varepsilon}_{eq}^{w} = 0$ when the salt is fully consolidated.

5.2.3 CODE_BRIGHT model

CODE_BRIGHT is a finite element code developed by the Polytechnical University of Catalunya. It was developed on a new general theory for saline media, originally, but extended with time to porous media and to thermal-hydraulic-mechanical (THM) coupled processes. The program GiD developed by the International Centre for Numerical Methods in Engineering (CIMNE) is used for pre-and postprocessing /UPC 20/.

The model for crushed salt is described through an additive approach of the elastic, creep and viscoplastic strain rates /UPC 20/.

$$\dot{\varepsilon} = \dot{\varepsilon}_{el} + \dot{\varepsilon}_{c} + \dot{\varepsilon}_{vp} \tag{5.66}$$

5.2.3.1 Elastic behaviour

In CODE_BRIGHT the elastic behaviour is described by the generalized Hooke's law in combination with a variation of Young's modulus /UPC 20/.

$$E = E_0 + (\Phi - \Phi_0)\frac{dE}{d\Phi} \geq E_{min} \tag{5.67}$$

E	Young's modulus [MPa]
E0	Reference value of Young's modulus [MPa]
Φ	Porosity [-]
Φ0	Reference value of Porosity [-]
dE/dΦ	Variation of Young's modulus with porosity [MPa]
Emin	Minimum elastic modulus [MPa]

5.2.3.2 Creep

For describing the creep behaviour of crushed salt material two mechanism are included: fluid assisted diffusional transfer (FADT) and dislocation creep (DC). This combination allows to simulate the humidity induced creep behaviour and the mechanism referred to dislocation theory including dislocation climb and glide /UPC 20/.

$$\dot{\varepsilon}_{c} = \dot{\varepsilon}_{FADT} + \dot{\varepsilon}_{DC} \tag{5.68}$$

5.2.3.3 Humidity creep

For the presence of brine humidity induced creep is an important mechanism for the mechanical behaviour of crushed salt. It describes the influence of differences in chemical potential induced by gradients in contact stresses. Salt will be dissolved in areas under high stress and will be precipitated in areas of low stress. The migration of salt is supposed to be diffusional through the liquid phase /UPC 20/ /OLI 02/.

$$\dot{\varepsilon}_{ij}^{FADT} = \frac{1}{2\eta_d^{FADT}}(\sigma_{ij}^{'} - p'\delta_{ij}) + \frac{1}{3\eta_v^{FADT}}p'\delta_{ij} \tag{5.69}$$

σ_{ij}' effective stress [MPa]

$\sigma_{ij}' = \sigma_{ij} + \delta_{ij}P_f$

p' mean effective stress [MPa]

$p = \frac{1}{3}(\sigma'_x + \sigma'_y + \sigma'_z)$

P_f fluid pressure

$P_f = \max(P_g, P_l)$

δ_{ij} Kronecker delta [-]

The functions for volumetric and deviatoric viscosity, the temperature dependent parameter containing material properties and the geometrical functions are defined by

$$\frac{1}{2\eta_d^{FADT}} = \frac{16B(T)\sqrt{S_l}}{d_0^3} g_d^{FADT}(e) \tag{5.70}$$

$$\frac{1}{\eta_v^{FADT}} = \frac{16B(T)\sqrt{S_l}}{d_0^3} g_v^{FADT}(e) \tag{5.71}$$

$$B(T) = \frac{A_B}{RT} exp \frac{g^2}{(1+e)} \tag{5.72}$$

$$g_d^{FADT}(e) = \frac{(1+e)}{(\sqrt{1+e} - \sqrt{2e/\lambda_v})^4} \tag{5.73}$$

$$g_v^{FADT}(e) = \frac{3e^{3/2}(1+e)}{(\sqrt{1+e} - \sqrt{2e/\lambda_v})^4} \tag{5.74}$$

5.2.3.4 Dislocation creep

The strain rate for the DC mechanism is described by the use of the creep power law which is already applied for the use of rock salt /UPC20/ /OLI 02/.

$$\dot{\varepsilon}_{ij}^{DC} = \frac{1}{\eta_{DC}^d} \Phi(F) \frac{\partial G}{\partial \sigma_{ij}^{'}} \tag{5.75}$$

G flow rule

F stress function

Φ scalar function

The following functions are used for specifying the flow rule and stress function, the volumetric and deviatoric viscosities, the geometrical relations in dependence of void ratio, as well as the temperature dependence.

$$F = G = \sqrt{q^2 + \left(\frac{-p}{\alpha_p}\right)^2} \tag{5.76}$$

$$\Phi(F) = F^n \tag{5.77}$$

$$\alpha_p = \left(\frac{\eta_{DC}^v}{\eta_{DC}^d}\right)^{\frac{1}{n+1}} \tag{5.78}$$

$$\eta_{DC}^v = A(T) g_{DC}^v(e) \tag{5.79}$$

$$\eta_{DC}^d = A(T) g_{DC}^d(e) \tag{5.80}$$

$$g_{DC}^v(e) = 3(g-1)^n f \tag{5.81}$$

$$g_{DC}^d(e) = \left(\sqrt{\frac{1+g+g^2}{3}}\right)^{n-1} \left(\frac{2g+1}{3}\right) f + \frac{1}{\sqrt{g}} \tag{5.82}$$

$$A(T) = A_A \exp\left(\frac{-Q_A}{RT}\right) \tag{5.83}$$

$$g = \frac{1}{(1-f)^2} = \frac{d^2}{x^2} \tag{5.84}$$

$$f = \sqrt{\frac{2e}{3(1-e^{\frac{3}{2}})(1+e)}} = \frac{\sqrt{2}s}{d} \tag{5.85}$$

q	deviatoric stress [MPa]
	$q = \sqrt{3J_2}$
p'	mean net stress [MPa]
	$p' = \frac{1}{3}(\sigma'_x + \sigma'_y + \sigma'_z)$
J_2	second invariant of the deviatoric stress tensor [MPa]

5.2.3.5 Grain rearrangement

For catching the effect of different deformation behaviour depending on the loading velocity, the viscoplastic law was applied in CODE_BRIGHT based on the critical state theory /UPC20/ /OLI02/.

$$\dot{\varepsilon}_{VP} = \Gamma \langle \Phi(F) \rangle \frac{\partial G}{\partial \sigma} \tag{5.86}$$

Γ	fluidity (inverse of viscosity) [$s^{-1}MPa^{-m}$]
$\Phi(F)$	stress function
F	viscoplastic yield function
G	flow rule

$$\Phi(F) = F^m \tag{5.87}$$

$$G = F = q^2 - \delta^2(p_0 p' - p'^2) \tag{5.88}$$

$$\Gamma = \Gamma_0 exp\left(\frac{-Q}{RT}\right) \tag{5.89}$$

$$dp_0 = p_0 \frac{1+e}{\lambda - \kappa} d\varepsilon_v = p_0 \frac{1+e}{X} d\varepsilon_v \tag{5.90}$$

With

$$p = \sigma_{oct} = \tfrac{1}{3} I_1 = \tfrac{1}{3}\left(\sigma_x + \sigma_y + \sigma_z\right) \tag{5.91}$$

$$q = \frac{3}{\sqrt{2}}\tau_{oct} = \frac{1}{\sqrt{2}}\sqrt{\left(\sigma_x - \sigma_y\right)^2 + \left(\sigma_y - \sigma_z\right)^2 + (\sigma_z - \sigma_x)^2 + 6\left(\tau_{xy}^2 + \tau_{yz}^2 + \tau_{zx}^2\right)} \tag{5.92}$$

m	power of stress function [-]
δ	parameter in flow rule [-]
p_0	initial value of hardening parameter [MPa]
Γ_0	initial value for fluidity [$s^{-1}MPa^{-m}$]
Q	Activation energy [J mol^{-1}]
R	gas constant [J mol^{-1} K^{-1}]
T	temperature [K]
X	parameter in hardening law [-]

5.2.4 C-WIPP model

The cwipp crushed salt model was developed by /SJA 87/, /CAL 91/ to describe backfill compaction for the Waste Isolation Pilot Plant (WIPP), a repository for nuclear waste connected to the US defense program. The model is implemented in the common numerical codes FLAC/FLAC3D and UEC/3DEC by Itasca. Though it is not directly used, several KOMPASS partners developed variants, and so the cwipp model is briefly described here.

The stress measures used in this formulation are the isotropic or volumetric stress

$$\sigma_0 = \frac{1}{3}\mathrm{tr}\sigma = \frac{1}{3}(\sigma_1 + \sigma_2 + \sigma_3) \tag{5.93}$$

And the effective or von Mises stress

$$\sigma_{eff} = \sqrt{3J_2} = \sqrt{\frac{1}{2}[(\sigma_1 - \sigma_2)^2 + (\sigma_2 - \sigma_3)^2 + (\sigma_3 - \sigma_1)^2]} \tag{5.94}$$

Here σ_1 and σ_3 denote the principal stresses.

Crushed salt deformation is modelled as a sum of elastic deformation, volume-preserving creep and compaction creep,

$$\dot{\varepsilon} = \dot{\varepsilon}_{el} + \dot{\varepsilon}_{cr} + \dot{\varepsilon}_{c} \tag{5.95}$$

The first two terms are similar to the ones for intact rock salt with some influence of the compaction state: Elastic deformation is given by the standard Hooke law where bulk and shear modulus are functions of density.

$$K = K_s e^{K_1(\rho-\rho_s)}, G = G_s e^{G_1(\rho-\rho_s)} \tag{5.96}$$

ρ	current density of crushed salt
ρ_s	density of intact salt

Volume-preserving creep comprises transient and stationary terms. Stationary creep is modelled as a Norton-type power law with a Kachanov factor involving the porosity P.

$$\dot{\varepsilon}_{cr,stat} \sim \left(\frac{\sigma_{eff}}{1-P}\right)^n \tag{5.97}$$

Transient creep is described as in the WIPP rock salt model, without direct influence of porosity.

Compaction creep is given by

$$\dot{\varepsilon}_c = -\frac{1}{\rho} B_0 (e^{-B_1\sigma_0} - 1) e^{B_2\rho} \left[\frac{1}{3}\delta_{ij} - \frac{1}{\sigma_{eff}} * \sigma_{ij}^d\right] \tag{5.98}$$

B_0	parameter describing the overall scale
B_1	parameter describing the stress dependency
B_2	parameter describing the density dependence

The magnitude only depends on the isotropic or mean stress $\sigma_0 = \frac{1}{3} tr\, \sigma$; the (normalised) stress deviator is included in the tensor structure such that uniaxial stress implies uniaxial compaction. The compaction rate is set to zero if σ_0 is positive (i.e. not compressive) or if $\rho = \rho_s$, so that density can only increase up to the density of intact salt. Note that the compaction rate does not go to zero for $\rho \rightarrow \rho_s$, so that complete compaction is achieved in finite time.

5.2.5 C-WIPP modified by BGE-TEC

In the numerical calculations in the project BAMBUS /BEC 99/, a similarly simply structured constitutive model as CWIPP is included in the comparison in addition to more complex material laws. As a result, it was possible to map the measured compaction behaviour comparably with this very simple material model. The motivation for the use of CWIPP in this project is to investigate the limitations further and thus possibly the limits of application of the constitutive model CWIPP. An additional motivation was the availability of the constitutive model in the calculation code FLAC3D Vers. 5 /ITA 12/, its numerically stable behaviour, and the possibility to modify it easily.

As given in Section 5.2.4, the tensor of the strain rate is an additive decomposition into an elastic part, a part of volume-preserving deviatoric creep, and a part of volumetric creep. The modification is made in the volumetric creep part. The other parts remain unaffected.

Originally, the compaction creep part is described as a multiplicative decomposition into a constant f_c, a porosity function f_φ and a stress function f_σ, Equ. (5.99). The modifications consist of interpreting the constant as an Arrhenius function and giving the stress function a more stress sensitive character. In a wide range of porosity, a dry granular salt shows a higher stress dependence than a moistened crushed salt /KRÖ 09/.

The sign convention used corresponds to the one in the program code and the description in /ITA 12/, i. e. pressure and compression is given a negative sign, while tensile stress and extension has a positive sign.

$$\dot{\varepsilon}_{ij}^{c} = f_c \, f_\varphi \, f_\sigma \tag{5.99}$$

$$f_c = \frac{B_0}{\varrho_s} \qquad \rightarrow \qquad f_T = B \, e^{-\frac{Q}{RT}}$$

$$f_\varphi = \frac{e^{B_2 \, \varrho_s \, (1-\varphi)}}{(1-\varphi)}$$

$$f_\sigma = (1 - e^{-B_1 \, \sigma_0}) \left[\frac{\delta_{ij}}{3} - \frac{\sigma_{ij}^d}{\sigma_v}\right] \quad \rightarrow \quad f_\sigma = \left(1 - e^{-\left(B_1 + B_3 \, |\sigma_0|^{B_4}\right) \sigma_0}\right) \left[\frac{\delta_{ij}}{3} - \frac{\sigma_{ij}^d}{\sigma_v}\right]$$

B	material parameter [1/d]
B_0	material parameter [kg/m^3/d]
B_1	material parameter [1/MPa]
B_2	material parameter [m^3/kg]
B_3	material parameter [1/MPa$^{(1+B4)}$]
B_4	material parameter [-]
Q	activation energy [J/mol]
R	molar gas constant [J/(mol K)]
T	temperature [K]
ρ_s	rock salt density [kg/m^3]
Φ	porosity [-]
σ_0	mean stress [MPa]: $\sigma_0 = 1/3 \; tr(\sigma_{ij})$
σ_{ij}	stress [MPa]
σ_{ij}^d	deviatoric stress [MPa]: $\sigma_{ij}^d = \sigma_{ij} - \sigma_0 \, \delta_{ij}$
σ_v	von Mises equivalent stress [MPa]
δ_{ij}	Kronecker delta, identity tensor of second rank [-]

The process of volumetric compaction creep does not contain any erratic components. Rather, the temperature and stress dependence at otherwise constant state variables must be strictly monotonous functions from a mathematical-physical point of view. The multiplicative decomposition of compaction creep into the separate functional parts allows a simple check to what extent the modifications are permissible. The condition of monotony is fulfilled for the Arrhenius function (Equ.(5.100) but not for the stress function. The stress function has an extreme value at $\sigma_{0,mx} = -\left(-B_1/\left(B_3(1+B_4)\right)\right)^{1/B_4}$. So, it depends on the parameter values B_i whether this point lies in the negative half space of the mean stress or not.

5.2.6 C-WIPP modified by the IfG

The IfG currently uses a variant of the empirical CWIPP crushed salt model (Section 5.2.4) that has been modified in several aspects:

- The porosity dependence has been changed such that the compaction rate goes to zero for small porosities. Specifically, the B_2 term in Equ. (5.98) is replaced,

  $$e^{B_2\rho} \longrightarrow e^{B_2\rho} - e^{B_2\rho_S} .$$

  This modification has little effect for high porosities and becomes relevant in the low porosity range. Thus, full compaction (zero porosity) is attained only asymptotically for long timescales.
- The tensor structure is extended to allow for a more general deviatoric component of compaction creep (or, in other words, an additional porosity-dependent creep term). The coefficient of the stress deviator is modified with two additional parameters,

  $$\frac{1}{\sigma_{\text{eff}}} \cdot \sigma_{ij}^{d} \longrightarrow \frac{2}{\sqrt{\zeta_{\text{iso}}\, \sigma_0^2 + \zeta_{\text{eff}}\, \sigma_{\text{eff}}^2}} \cdot \sigma_{ij}^{d} .$$

  The new coefficient leads to a smooth transition between uniaxial and isotropic stress and includes more flexibility to accommodate a range of deformation behaviours for general triaxial stress states.
- The model only retains the compaction creep term and the porosity dependence of the elastic moduli of the CWIPP model. To include intact rock salt behaviour, i.e. creep and damage, these terms are coupled to the visco-elasto-plastic constitutive model for rock salt /MIN 07/ /LÜD 14/.

Additionally, the model is reformulated in terms of porosity rather than density. While this does not change the physical behaviour, the interpretation is more intuitive and there are fewer conversions required when changing systems of units. The parameters in the new formulation are renamed C_0 to C_2 to avoid ambiguity.

Taking all this together, compaction creep in this model is given by

$$(\dot{\varepsilon}_{\text{c}})_{ij} = -\, C_0\left(e^{-C_1\sigma_0} - 1\right)\ \frac{e^{C_2 P} - 1}{1 - P} \left[\frac{1}{3}\delta_{ij} - \frac{2}{\sqrt{\zeta_{\text{iso}}\, \sigma_0^2 + \zeta_{\text{eff}}\, \sigma_{\text{eff}}^2}} \cdot \sigma_{ij}^{d}\right] \tag{5.100}$$

Elastic behaviour is described by the usual Hooke law, with elastic moduli depending on porosity as

$$K = K_S e^{-\kappa P}, \quad G = G_S e^{-\gamma P} \tag{5.101}$$

Note that a porosity-dependent bulk modulus (increasing with decreasing porosity) implies that after a loading–compaction creep–unloading cycle, there will be a "frozen elastic" contribution to volumetric strain proportional to

$$\Delta\sigma \cdot \left(\frac{1}{K(P_{\text{ini}})} - \frac{1}{K(P_{\text{final}})}\right) \tag{5.102}$$

Transient and stationary creep are given by, in rheological terms, Kelvin and modified Maxwell elements. The stationary creep rate is enhanced by a hyperbolic sine,

$$\left(\dot{\varepsilon}_{\text{creep,stat}}\right)_{ij} = \frac{1}{\eta}\, e^{-\frac{Q}{RT}} \sinh m\sigma_{eff}^{n} \cdot \sigma_{ij}^{d} \tag{5.103}$$

Finally, plastic deformation, dilatancy and softening are governed by the Minkley yield function

$$\sigma_{diff}^{yield} = -\sigma_D - \frac{\sigma_{MAX} - \sigma_D}{\sigma_\phi - \sigma_3}\, \sigma_3 \tag{5.104}$$

and a non-associated plastic potential. Since rock salt damage does not play an important role in this project, we will not go into detail here.

5.2.7 C-WIPP modified by TUC

Listing of designations:

- $\dot{\varepsilon}^{vc}{}_{ij}$ - individual components of the viscous compaction strain rates, in 1/s
- $\dot{\varepsilon}^{vs}{}_{ij}$ - individual components of the viscous shear strain rates, in 1/s
- $\dot{\varepsilon}^{el}{}_{ij}$ - individual components of the viscous compaction strain rates, in 1/s
- $\dot{\varepsilon}^{vc}{}_{vol}$ - scalar volumetric compaction strain rate, in 1/s
- $\dot{\varepsilon}^{vs}{}_{st}$ - scalar pre-factor for steady state strain rate, in 1/s
- $\dot{\varepsilon}^{vs}{}_{tr}$ - scalar pre-factor for transient state strain rate, in 1/s
- s_{ik} - deviatoric stress tensor, in MPa
- σ_v - von Mises equivalent stress, in MPa
- δ_{ij} - Kronecker symbol
- φ - porosity, in -

φ_0 - initial porosity, in -

$RV^{vc}{}_{ij}$ - the term determining the directional distribution of individual strain components for viscous compaction in C-WIPP/TUC, in -

$RV^{vs}{}_{ij}$ - the term determining the directional distribution of individual shear strain components for viscous shear in C-WIPP, in -

β - material parameter for the directional distribution of individual strain components, for C-WIPP original $\beta \equiv 1$, in -

$\beta_1,\ \beta_2$ - material parameters for the directional distribution of individual strain components for C-WIPP/TUC, in -

C_0 - material parameter, pre-factor for C-WIPP, in 1/s

C_1 - material parameters for influencing factor stress for C-WIPP, in 1/MPa

C_{1_m}, C_{1_v} - material parameters for influencing factor stress for C-WIPP/TUC, in 1/MPa

C_2 - material parameter for the influencing factor porosity for C-WIPP, in -

C_{2_e}, C_{2_p} - material parameter for the influencing factor porosity for C-WIPP/TUC, in -

ρ_f - density of intact salt rock, in kg/m³

K_f - bulk modulus for intact salt rock, in MPa

G_f - shear modulus for intact salt rock, in MPa

$K_1,\ G_1$ - material parameters in elastic model part in C-WIPP, in m³/kg

5.2.7.1 Objectives and guidelines/principles in the development of the model

In accordance with the briefly described statements in Sections 5.3, 4.5.1 and 6.2.4 about, with regard to the basic requirements for a material model for crushed salt, to the necessary of experimental investigations for the quantification of the functional dependencies between compaction and several known influencing factors and to the structure and performance of currently available constitutive models, it has been shown that there is currently no constitutive model available that is suitable for describing the THM-coupled material properties of crushed salt in space and time sufficiently realistically and in particular in the area of small porosities and that there are also clear deficits in the area of the experimental analysis of the material behaviour. The objective of the following explanations is first to outline the methodology used for the (further) development of the constitutive model and, based on this, to distinguish the development steps already realized within the framework of the research project for the (further) development of a constitutive model characterizing the THM-coupled material behaviour of crushed salt in space and time sufficiently realistically from the processing steps still to be realized within the framework of further research work. The methodology of constitutive model (further)

development used in the research project is characterized by a total of five processing steps as follows:

Processing step 1: Definition of qualitative requirement characteristics

- Practicability
    - The material model should have a structure that is as simple as possible and not unnecessarily complex. This means that the number of processes and influencing factors considered should be as small as possible and as large as necessary. A similar statement applies to the composition/superposition and the interaction/coupling of individual processes and functional relationships for individual influencing factors. The requirement applies in accordance with the "law of parsimony", also known as "Okcham's razor blade", /LUX 18/, which is widely used in physics.
- Functionality
    - The constitutive model should take into account all relevant processes and influencing factors for current or future intended applications. The processes must be numerically feasible/implementable and stable, i.e. functional. The possibility of optional activation and deactivation of individual processes or individual influencing factors is desirable. This enables a differentiated application of the constitutive model and a differentiated analysis of the results and statements generated with the constitutive model. Furthermore, the formulation of normalized influencing factors (no units) is desirable, which in turn result in unit-less, generally valid model parameters. Thus, the principles of dimensional analysis are also taken into account, /LUX 18/.
- Plausibility
    - All functional dependencies considered in the constitutive model should be physically meaningful with regard to the qualitative course of the state variables and with regard to the limit values of the calculated target variables. This means that the target and state variables are to be checked for each functional relationship in dependence of all relevant influencing factors by isolated analytical calculations.
- Empirical realism
    - The constitutive model should be validated as comprehensively as possible. For this purpose, a suitable experimental database must be available

or created. The maximum possible realism of the model statements according to the state of the art in science and technology is achieved/given when the validation has been successfully proven for all individual functional relationships and influencing factors, but also for the overall model, taking into account the interactions between individual processes or influencing factors. The value ranges of the influencing factors experimentally investigated and used for the validation of the constitutive model should include the in-situ relevant value ranges as far as possible.

Processing step 2: Selection of a suitable basic model

In a second processing step, a basic model was selected that was estimated to be suitable for (further) development. For the assessment of the suitability of the basic model were used in particular following indicators: availability of the constitutive model equations, clear description, suitable structure of the constitutive model equations for a modification, substitution and/or addition of individual functional thermals.

Processing step 3: Plausibility check

In a third processing step, based on systematic for each influencing factor isolated analytical calculations, the constitutive model equations are checked for plausibility and mathematical correctness. This means that it is checked whether the functional dependencies and interactions resulting from variation of the loading conditions are plausible and whether and to what extent the functional dependencies estimated to be significant can be represented by the material model.

Processing step 4: Modification of deficient equation terms and integration of missing equation terms

The deficiencies recognized as obvious in the result of the analytical investigations in processing step 3 are first eliminated in processing step 4. For the representation of relevant in-situ situations second, obviously missing dependencies are supplemented by equation terms that are considered suitable.

Processing step 5: Validation of the (further) developed constitutive model

In a fifth and initially final processing step, the validation of the first version of the (further) developed constitutive model generated in processing step 4 finally takes place. This includes in particular the validation of possibly all functional relationships considered in the constitutive model with regard to the requirement characteristic "real-ism" defined in processing step 1: a back analysis of currently available laboratory tests on crushed salt compaction and the planning and execution of further tests for the extensive largely complete validation of functional dependencies.

From the chronology of constitutive model (further) development outlined above with processing steps 1 to 5, it is clear that processing steps 3, 4 and 5 in particular are not completely independent of one another, but rather require repeated iterative processing until a finally suitable and validated constitutive model is available for a sufficiently realistic characterization of the THM-coupled material behaviour of crushed salt.

Within the framework of the research project:

1) processing step 1 and processing step 2 are realized,
2) in processing step 3, the scheme for the plausibility calculations is created and the calculations are carried out for the selected base model,
3) initial modifications and additions to the base model in processing step 4 are made and
4) in processing step 5, a selection of currently available and well interpretable tests (TK-031 and TK-033 from BGR and TUC-V2 from TUC), is very successful recalculated with the (further) developed first version of the constitutive model C-WIPP/TUC and the simulation results are compared to the measurement results.

The following sub-chapters briefly describe the results of these development steps.

5.2.7.2 Selection of the basic model and strategic/long-term planning for development scope

The constitutive model C-WIPP/Itasca was chosen as the basic model, since it presents a comparably simple structure and involves all main processes – elastic deformations, viscous shear and viscous compaction deformations.

A detailed description of the extended variant of the constitutive model C-WIPP/Itasca, which is designated C-WIPP/TUC in the following, is given below.

Fig. 5.8 shows in schematic form the strategically long-term planned development work. Subsequently, significant modifications or development steps are described:

1) Modifications to remedy functional terms identified as deficient, implausible and/or impractical as follows:
    a. Functional relationship between viscous compact deformations and porosity;
    b. Directional distribution for viscous compaction deformations as a function of the stress geometry (TC, TE, isotropic);
    c. Functional relationship between elastic compaction deformations and porosity;
    d. Functional relationship between viscous shear deformations and porosity;
    e. New version of the functional term for consideration of viscous shear deformations as a function of deviatoric stress, temperature and deformation history or loading history;
2) Introduction of new functional correlations which have been missing so far:
    a. Influence of deviatoric stresses on viscous compaction deformations;
    b. Influence of temperature on viscous compaction deformations;
    c. Influence of moisture content on viscous compaction deformations;
    d. Influence of material anisotropy induced by the pre-compaction process / loading history, if necessary;
    e. Influence of particle size distribution on the compaction process, if necessary.

Within the framework of the research project, the modifications designated 1a, 1b and 2a were realized. A detailed description of the work is given in the following.

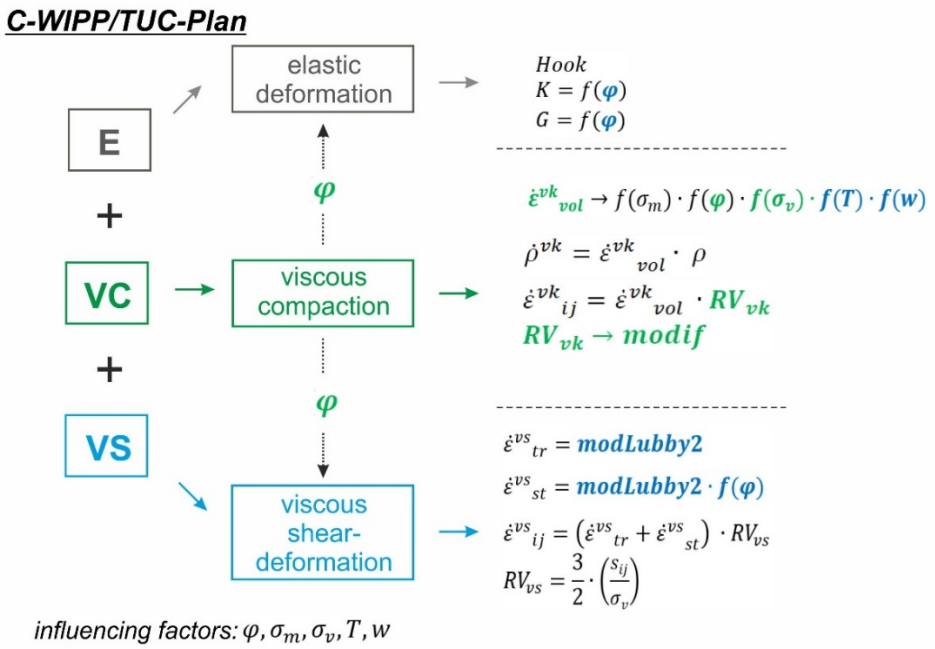

Fig. 5.8 Sketch of the planned modifications for creating the constitutive model of TUC for crushed salt based on the constitutive model C-WIPP

5.2.7.3 Development steps realized in the model within the project

1) Modification to consider the directional dependence of viscous deformations (modification 1b)

The directional distribution in the compaction part of the constitutive model approach C-WIPP/Itasca is implemented in FLAC3D according to the program code of Itasca as follows:

$$\dot{\varepsilon}^{vc}{}_{ij} = \dot{\varepsilon}^{vc}{}_{vol} \cdot RV^{vc}{}_{ij} \tag{5.105}$$

$$RV^{vc}{}_{ij} = \left[\frac{\delta_{ij}}{3} - \beta \cdot \frac{s_{ik} \cdot \delta_{kj}}{\sigma_v}\right] \tag{5.106}$$

The material parameter β mentioned above is not variable but is set to identical one by Itasca in FLAC3D. This ensures that the lateral strain components are identical zero and that the compaction occurs exclusively in the axial direction in the case of uni-axial compression stress. Thus, a plausible result is achieved in case of uniaxial loading. For triaxial loads, on the other hand, the assumption of exclusively axial deformations is not very plausible. For isotropic loads, the formulation is discontinuous (deviatoric stress in the denominator becomes identical to zero for isotropic loads). This special solution ensures that identical numerical values are calculated for the individual strain components

under isotropic load. Thus, the model C-WIPP provides the following directional distribution for three relevant load cases:

$$\text{UC: } \dot{\varepsilon}^{vc}{}_1 = \dot{\varepsilon}^{vc}{}_{vol} \cdot 1,\ \dot{\varepsilon}^{vc}{}_{2,3} = \dot{\varepsilon}^{vc}{}_{vol} \cdot 0 = 0 \tag{5.107}$$

$$\text{TC: } \dot{\varepsilon}^{vc}{}_1 = \dot{\varepsilon}^{vc}{}_{vol} \cdot 1,\ \dot{\varepsilon}^{vc}{}_{2,3} = \dot{\varepsilon}^{vc}{}_{vol} \cdot 0 = 0 \tag{5.108}$$

$$\text{Isotropic: } \dot{\varepsilon}^{vc}{}_{1,2,3} = \dot{\varepsilon}^{vc}{}_{vol} \cdot \left(\frac{1}{3} + \frac{0}{0}\right)(!) \rightarrow special\ solution\text{: } \dot{\varepsilon}^{vc}{}_{1,2,3} = \dot{\varepsilon}^{vc}{}_{vol} \cdot \frac{1}{3} \tag{5.109}$$

The extension of the constitutive model C-WIPP/Itasca in the formulation part outlined above is of particular importance, both for load cases with isotropic or approximately isotropic loading in situ and within the framework of the triaxial tests for the analysis of the functional dependencies between crushed salt compaction and isotropic stress (e.g. test TK-031with nearly isotropic load or test TUC-V2 with triaxial load).

One possibility of eliminating the deficit, which was realized within the framework of the research project, is the integration of a function of the angle $\alpha = f(I_1, J_2) = f(\sigma_v, \sigma_m)$:

$$RV^{vc}{}_{ij} = \left[\frac{\delta_{ij}}{3} - f(\alpha) \cdot \frac{s_{ij}}{\sigma_v}\right] \tag{5.110}$$

This angle takes into account the relation between the deviatoric and the isotropic components of the stress (Fig. 5.9):

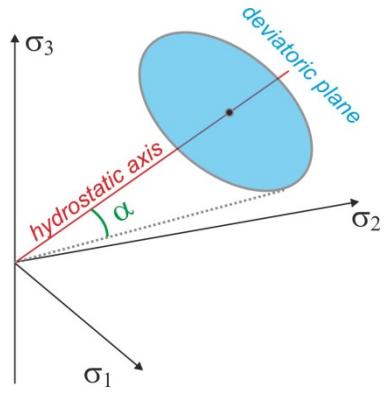

Fig. 5.9 The angle α in the principal stress space used to organize the directional distribution of the deformations

The angle α is defined here by the following relationships:

$$\cos(\alpha) = \frac{3 \cdot \sigma_0}{\sqrt{9 \cdot {\sigma_0}^2 + {\sigma_v}^2}},\ \sin(\alpha) = \frac{\sigma_v}{\sqrt{9 \cdot {\sigma_0}^2 + {\sigma_v}^2}},\ \operatorname{tg}(\alpha) = \frac{\sigma_v}{3 \cdot \sigma_0} \tag{5.111}$$

The use of a function of angle α ensures a continuous transition of the directional distribution of the strain components during a change between isotropic and deviatoric loading

conditions. The form of the function $f(\alpha)$ can be chosen variably; the values of the function parameters can then be determined on the basis of measurement data after suitable validation tests have been performed.

For the form of the function, the following variants were analysed in the research project by analytical test calculations:

$$f\ (\alpha) = \beta_1\ \cdot [\mathrm{tg}\ (\alpha)]^{\beta 2} \text{ bzw. } f(\alpha) = \beta_1\ \cdot [\sin\ (\alpha)]^{\beta 2} \tag{5.112}$$

The mode of action of both variants is very similar. The parameters $\beta_1,\ \beta_2$ ensure sufficient flexibility in the quantitative adaptation of the directional distribution to the measurement results for any stress geometries. Fig. 5.10 demonstrates the effect of the new function for the directional distribution of the strain components in comparison to the Itasca formulation in C-WIPP. It shows the individual strain components for isotropic stresses, triaxial compressive stresses and uniaxial compressive stresses.

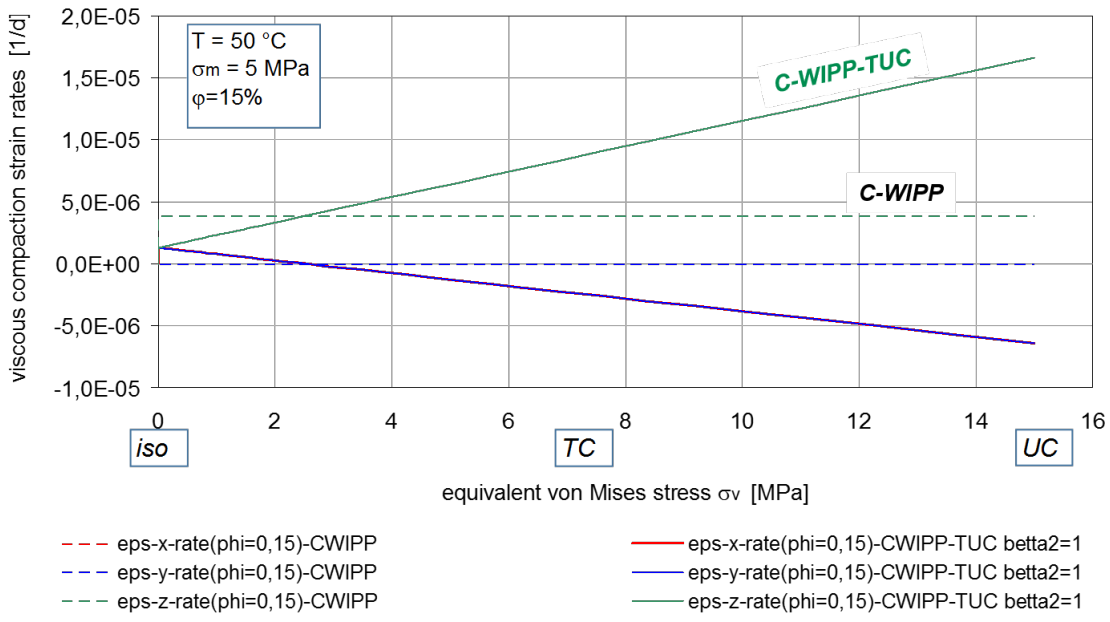

Fig. 5.10 Analytical calculation for individual strain components for different stress situations for the original formulation of C-WIPP and for the modified formulation of TUC in comparison

Since the deficit of the Itasca version of the constitutive model C-WIPP outlined above has already been known to the scientific community for some time, there are various variations of the constitutive model C-WIPP in which the deficit has been remedied by alternative modifications, e.g. C-WIPP/IfG. To confirm the similarity of the effect regarding this modification in the two constitutive model variants C-WIPP/IfG and C-WIPP/TUC,

Fig. 5.11 compares the constitutive model equations and analytical calculation results of the two variants of constitutive model approaches. The necessity and functionality of the constitutive model modifications described above is demonstrated in the following chapter by recalculating selected compaction experiments.

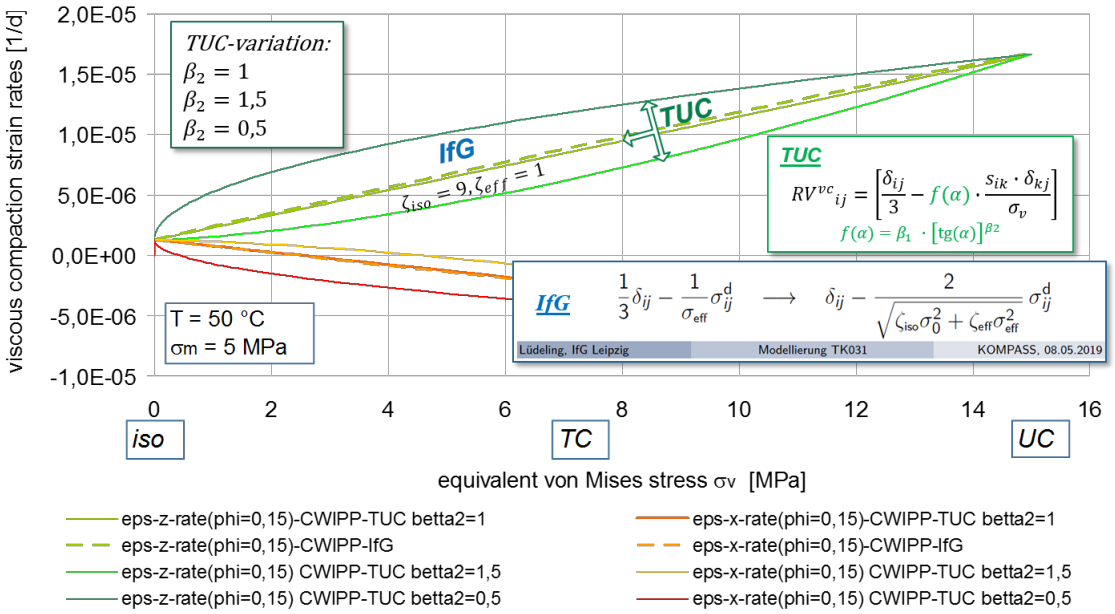

Fig. 5.11 Analytical calculation for individual strain components for different stress situations for the C-WIPP/TUC formulation and for the C-WIPP/IfG formulation in comparison

2) Introduction of deviatoric stresses as an additional influencing factor (modification 2a)

In the majority of the currently available constitutive model approaches, it is taken into account, that the compaction process is not only dependent on the isotropic stress component but also on the deviatoric stress component. In the constitutive model C-WIPP/Itasca, however, this influencing factor has not been considered so far. Since the TUC-V2 experiment, carried out within the framework of the research project, clearly demonstrated the existence of a dependency between the compaction and the deviatoric stress and since, in addition, initial information regarding an isolable quantification of this dependency is also available in the result of the experiment evaluation, consideration of the dependency of the compaction on the deviatoric stress was realized in the constitutive model variant C-WIPP/TUC as a further modification as follows:

The formulation of the connection between compaction and stress in C-WIPP/Itasca is characterized as follows:

$f(\sigma_m) = [\exp(-B_1 \cdot \sigma_m) - 1]$ in the case of formulations for density rates or (5.113)

$f(\sigma_m) = [\exp(-C_1 \cdot \sigma_m) - 1]$ for formulation for volume strain rates (5.114)

(in convention: shear stress negative).

The modified formulation looks as follows:

$$f(\sigma_m, \sigma_v) = \left[\exp\left(-C_{1\_m} \cdot \sigma_m + C_{1\_v} \cdot \sigma_v\right) - 1\right] \quad (5.115)$$

Parameter C_1 was substituted by two parameters as follows: Parameter C_{1_m} for the consideration of the dependence of the crushed salt compaction on the isotropic stress and parameter C_{1_v} for the consideration of the dependence of the crushed salt compaction on the deviatoric stress.

With reference to the chapter 5.4 with the benchmark test re-calculations, it should be noted that the constitutive model extension documented in Equ. (5.115) was successfully validated within the framework of the back analysis of the TUC-V2 experiment.

3) Modification of the functional relationship for the influence of porosity on the crushed salt reaction (modification 1a)

In the constitutive model C-WIPP/Itasca, the dependence of the compaction process on the porosity is taken into account by the equation terms given with Equ. (5.116) and Equ. (5.117):

$f(\rho) = \exp\,(B_2 \cdot \rho)$ in the case of formulations for density rates or (5.116)

$f(\varphi) = \exp(C_2 \cdot \varphi)\,/(1 - \varphi)$ for formulation for volume strain rates. (5.117)

The well-known shortcoming of this formulation is that the compaction rate does not tend towards zero when the porosity becomes zero, i.e. when the crushed salt is fully compacted. This shortcoming has already been remedied by some years in the by TUC modified version of the C-WIPP as follows:

$$f(\varphi) = \exp(C_2 \cdot \varphi) \cdot (\varphi/\varphi_0)/(1 - \varphi) \quad (5.118)$$

This formulation was now adopted and slightly extended in the frame of the validation work:

$$f(\varphi) = \exp\left(C_{2\_e} \cdot \varphi\right) \cdot (\varphi/\varphi_0)^{C2\_p}/(1-\varphi) \tag{5.119}$$

The parameter C_2 was splited here into two different parameters: parameter C_{2_e} for the exponential function and parameter C_{2_p} for the potential function.

This simple multiplicative extension of the exponential function with a potential function served the purpose of flexibilization within this functional relationship. The need for this flexibilization was recognized thanks to the systematic comparative analysis of all three as an experimental basis for model validation selected test, which is described in the Section 5.4 with the benchmark test re-calculations.

5.2.7.4 Current final variant of the constitutive model formulation and current parameter set for C-WIPP/TUC

In frame of this project phase modifications were made only in the model part for describing viscous compaction deformations, i.e. in the most essential part of the model, to produce the model C-WIPP/TUC. Thus, only this part of model is described below.

The formulation of C-WIPP/Itasca variant is shown in black colour and the modified variant C-WIPP/TUC is shown in green colour for better traceability:

$$\dot{\varepsilon}^{vc}{}_{ij} = \dot{\varepsilon}^{vc}{}_{vol} \cdot RV^{vc}{}_{ij} \tag{5.120}$$

C-WIPP→ $$\dot{\varepsilon}^{vc}{}_{vol} = -3\, C_0 \cdot f(\sigma_m) \cdot f(\varphi) \tag{5.121}$$

C-WIPP/TUC→ $$\dot{\varepsilon}^{vc}{}_{vol} = -3\, C_0 \cdot f(\sigma_m, \sigma_v) \cdot f(\varphi) \tag{5.122}$$

C-WIPP→ $$f(\sigma_m) = [\exp(-C_1 \cdot \sigma_m) - 1] \tag{5.123}$$

C-WIPP/TUC→ $$f(\sigma_m, \sigma_v) = \left[\exp\left(-C_{1\_m} \cdot \sigma_m + C_{1\_v} \cdot \sigma_v\right) - 1\right] \tag{5.124}$$

C-WIPP→ $$f(\varphi) = \exp\left(C_{2\_e} \cdot \varphi\right)/(1-\varphi) \tag{5.125}$$

C-WIPP/TUC→ $$f(\varphi) = \exp\left(C_{2\_e} \cdot \varphi\right) \cdot (\varphi/\varphi_0)^{C2\_p}/(1-\varphi) \tag{5.126}$$

C-WIPP→ $$RV^{vc}{}_{ij} = \left[\frac{\delta_{ij}}{3} - \beta \cdot \frac{s_{ik} \cdot \delta_{kj}}{\sigma_v}\right] \tag{5.127}$$

C-WIPP/TUC→ $$RV^{vc}{}_{ij} = \left[\frac{\delta_{ij}}{3} - f\ (\alpha) \cdot \frac{s_{ik} \cdot \delta_{kj}}{\sigma_v}\right] \tag{5.128}$$

$$f\ (\alpha) = \beta_1\ \cdot [\mathrm{tg}\ (\alpha)]^{\beta 2} \tag{5.129}$$

Table 5.1 summaries the compaction parameters for the constitutive model C-WIPP/TUC. These were determined on the basis of the test analysis and test recalculations for validation and due to parameter determination procedure described in the Section 5.4 with the benchmark test re-calculations.

Tab. 5.3 Compaction parameters for the constitutive model C-WIPP/TUC

$C0$	1/s	2,14E-22
$C1\_m$	1/MPa	0,66
$C1\_v$	1/MPa	0,25
$C2\_e$	-	151,9
$C2\_p$	-	0,2
$\beta 1$	-	3,6
$\beta 2$	-	1

5.2.7.5 Summary

Fig. 5.12 shows a schematic sketch of the model structures for the basic model C-WIPP/Itasca, for the current model variant C-WIPP/TUC and for the final variant C-WIPP/TUC with all modifications planned strategically/long-term within the framework of the next project phases.

This extended constitutive model variant C-WIPP/TUC was successfully validated on the basis of three selected triaxial tests TK-031 and TK-033 by BGR and TUC-V2, see detailed description in the Section 5.4. Thus, the functionality of the introduced or modified functional relationships has been confirmed. It should be emphasized that these results are only the first steps in the model development work and in the model validation work. For a comprehensive, possibly complete validation of the model, the results of all planned investigations from the proposed laboratory program are required.

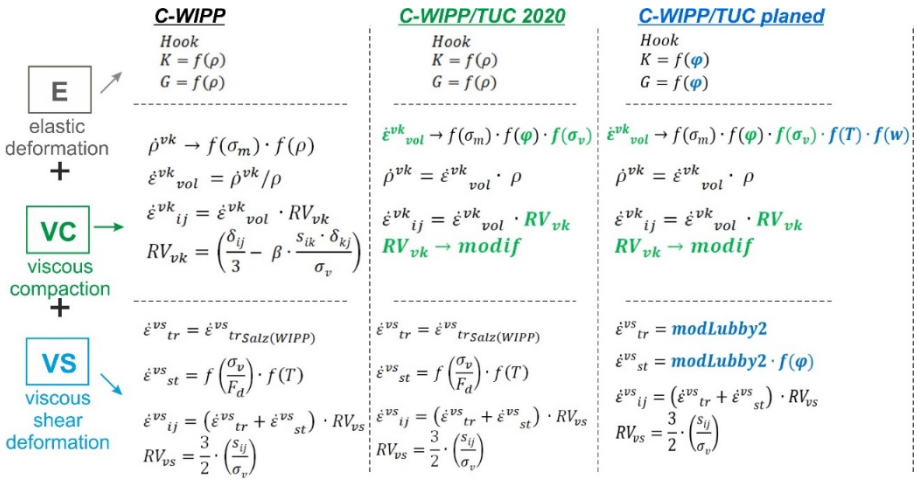

Fig. 5.12 Model structures for the basic model C-WIPP/Itasca, for the current model variant C-WIPP/TUC and for the final variant C-WIPP/TUC with all long-term planned modifications

5.2.8 Modified Hein model

Hein describes a material law for naturally dry crushed salt, /HEI 91/, which, in addition to its elastic behaviour, contains two viscoplastic deformation components - grain deformation and grain displacement.

5.2.8.1 Kinematic equations

The additive decomposition of the strain rate tensor $\dot{\varepsilon}_{ij}$ into a thermoelastic part $\dot{\varepsilon}_{ij}^{thel}$, a viscoplastic deformation part of grain deformation $\dot{\varepsilon}_{ij}^{g}$ and a viscoplastic deformation part of grain displacement $\dot{\varepsilon}_{ij}^{a}$ (Equ. (5.149) is assumed in this constitutive model

$$\dot{\varepsilon}_{ij} = \dot{\varepsilon}_{ij}^{thel} + \dot{\varepsilon}_{ij}^{g} + \dot{\varepsilon}_{ij}^{a} \tag{5.130}$$

5.2.8.2 Elastic material behaviour

The elastic material behaviour is given by Hooke's model in rate formulation with a porosity dependent stiffness tensor. A pore model is used in /HEI 91/ to derive the porosity dependent behaviour.

While the Poisson's ratio is assumed to be independent of porosity and therefore correspond to that of rock salt, the porosity dependence of the three other elasticity parameters of an isotropic material is identical, i. e. the bulk modulus (Equ. (5.131) the shear modulus and the Young's modulus. The final value of the individual quantities is that of rock salt.

$$K = K_s \, e^{-c\,\varphi \frac{1-\varphi_0}{1-\varphi}} \tag{5.131}$$

c	molar gas constant [-]
K	bulk modulus [MPa]
K_s	rock salt bulk modulus [MPa]
φ	porosity [-]
φ_0	porosity of a loose bulk [-]

The state X_0 describes the behaviour of the loosest bulk, which cannot really be measured. The material in this state corresponds more to a discontinuum. Therefore, the state "0" is more an imaginary than a real state. This state is necessary as the elastic material behaviour would otherwise depend on this initial state. This dependency becomes clear if the pre-compressed initial state X_i of an individual experiment is set instead of X_0.

In parallel, Hein /HEI 91/ describes a geometrically based approach based on a sphere model with Hertzian contacts (Equ. (5.132)

$$K = K_s \, k_1 \, M \left((1 - \varphi) \, \frac{b}{R} \right)^{k_2} \tag{5.132}$$

k_1, k_2 material parameter [-]

M coordination number [-]

$\frac{b}{R}$ ratio between contact radius b and ball radius R [-]: $\frac{b}{R} = \left(1 - \left(\frac{1-\varphi_0}{1-\varphi}\right)^{2/3}\right)^{1/2}$

Different functions are given in /HEI 91/ for the coordination number M. These models can be divided into three groups, where Group III is the most realistic one:

- Group I with fixed geometric grain arrangement with resulting constant porosity and correspondingly constant value M.
- Group II where the coordination number increases disproportionately strongly with decreasing porosity; in the vicinity of complete compaction, these models exhibit a physically incomprehensible behaviour.
- Group III with decreasing porosity degressively up to a maximum linear increasing coordination number.

The initial porosity is taken into account in the formulation according to Equ. (5.132) via the contact surface. It should also be noted that the properties of rock salt in the state of complete compaction are only achieved in the special case $k_1 \, M \, \varphi_0^{k_2/3} = 1$.

5.2.8.3 Grain deformation

A viscosity approach according to Perzyna is used for grain deformation (Equ. (5.133).

$$\dot{\varepsilon}_{ij}^{g} = \gamma(T) \, \langle \phi(F - F_0) \rangle \, \frac{\partial G}{\partial \sigma_{ij}} \tag{5.133}$$

$\langle X \rangle$ Macaulay brackets: $\langle X \rangle = X \; \forall \; X > 0 \; \wedge \; \langle X \rangle = 0 \; \forall \; X \leq 0$

F yield function

F_0 hardening function

G viscoplastic potential

T temperature [K]

γ fluidity coefficient

ϕ scalar function

σ_{ij} stress [MPa]

The following assumptions are made in /HEI 91/ related to Equ. (5.133):

- The fluidity coefficient is interpreted as Arrhenius term $\gamma(T) = \frac{A}{2} e^{-\frac{Q}{RT}}$.
- There is no hardening function, thus, $F_0 = 0$ and so flow starts at lowest stress.
- The scalar function ϕ is $\phi = F^{\frac{n-1}{2}}$, where n is the stress exponent.
- An associated flow rule is used, hence, $F = G$.

The part of grain deformation can be described as a function of a generalized equivalent stress $\hat{\sigma}$ (Equ. (5.134).

$$\hat{\sigma} = \sqrt{h_1 \sigma_0^2 + h_2 q^2} \tag{5.134}$$

h_1, h_2 porosity dependent material parameter [!/MPa^2]

q deviatoric invariant [MPa], $q = \left(\sigma_{ij}^d : \sigma_{ij}^d\right)^{1/2}$

σ_0 mean stress [MPa], $\sigma_0 = 1/3\ tr\left(\sigma_{ij}\right)$

σ_{ij}^d deviatoric stress tensor [MPa], $\sigma_{ij}^d = \sigma_{ij} - \sigma_0\, \delta_{ij}$

δ_{ij} Kronecker delta. Identity tensor of second rank

With $F = \hat{\sigma}^2$. Thus, Equ. (5.133) becomes Equ. (5.135).

$$\dot{\varepsilon}_{ij}^g = A e^{-\frac{Q}{RT}} \left(h_1 \sigma_0^2 + h_2 q^2\right)^{\frac{n-1}{2}} \left(\frac{1}{3} h_1\, \sigma_0\, \delta_{ij} + h_2\, \sigma_{ij}^d\right) \tag{5.135}$$

Two main invariants are derived from the above tensor of the strain rate $\dot{\varepsilon}_{ij}^g$: the rate of volumetric strain $\dot{\varepsilon}_0^g$ (Equ. (5.136) and the equivalent strain rate $\widehat{\dot{\varepsilon}^g}$ (Equ. (5.137).

$$\dot{\varepsilon}_0^g = A e^{-\frac{Q}{RT}} \left(h_1 \sigma_0^2 + h_2 q^2\right)^{\frac{n-1}{2}} h_1\, \sigma_0 \tag{5.136}$$

$$\widehat{\dot{\varepsilon}^g} = \sqrt{\frac{2}{3}} A e^{-\frac{Q}{RT}} \left(h_1 \sigma_0^2 + h_2 q^2\right)^{\frac{n-1}{2}} h_2\, q \tag{5.137}$$

$$\dot{\varepsilon}_0^g = tr\left(\dot{\varepsilon}_{ij}^g\right)$$

$$\widehat{\dot{\varepsilon}^g} = \left(2/3\, \dot{\varepsilon}_{ij}^{g\,d} : \dot{\varepsilon}_{ij}^{g\,d}\right)^{1/2}$$

$$\dot{\varepsilon}_{ij}^{g\,d} = \dot{\varepsilon}_{ij}^g - 1/3\ \dot{\varepsilon}_0^g\, \delta_{ij}$$

If the assumption from Section 5.1.2.2 holds that the hydrostatic part of the grain deformation disappears when compaction is complete, $h_1(\varphi \to 0) \to 0$, only the deviatoric part remains in this limit state: $\widehat{\dot{\varepsilon}^g} = \sqrt{\frac{2}{3}} A e^{-\frac{Q}{RT}} h_2^{\frac{n+1}{2}} q^n$. Thus, the constitutive model changes to a state as described for stationary creep of rock salt with a power law approach /HUN 98/.

There are different material functions h_1 and h_2: the original approach is given in /HEI 91/ and a modification by Korthaus in /KOR 96/ with further development in /KOR 99/. The approach of Hein /HEI 91/ is based on physical considerations and measurements of the dilatancy behaviour, short-term creep tests and further creep tests (Equ. (5.138), (Equ. (5.139).

$$h_1 = \frac{1 - a_1 \, tan^2(\phi) \, e^{a_2 \, \varphi}}{p_{max}^2} \tag{5.138}$$

$$h_2 = b_1 + b_2 \, h_1 \tag{5.139}$$

a_1, a_2 material parameter [-]

b_1 material parameter [1/MPa^2]

b_2 material parameter [-]

$\tan(\Phi)$ friction angle [-], $tan(\phi) = 0.59$

p_{max} short-term pressure to compact from φ_0 to φ [MPa], $p_{max} = \frac{c_1}{c_2}\left(\left(\frac{1-\varphi}{1-\varphi_0}\right)^{b_2} - 1 + \Delta\right)$

c_1 material parameter [MPa]

c_2 material parameter [-]

Δ numerical additive to prevent singularity in φ_0 [-]

It should be noted that $\tan(\phi)$ is not to be understood as a free parameter but has to be identified independently, otherwise there would be over-parameterization due to the mathematical equivalence of $\tan(\phi)$ and a_1.

In the state of complete compaction, a value results for h_1 which is zero only in the special case (Equ. (5.140). Thus, the aforementioned requirement in Section 5.1.2.2 of a direct transition between the behaviour of granular salt and that of rock salt is not fulfilled.

$$h_1 = \frac{1 - a_1 \, tan^2(\phi)}{\left(\frac{c_1}{c_2}\left(\left(\frac{1}{1-\varphi_0}\right)^{c_2} - 1 + \Delta\right)\right)^2} \tag{5.140}$$

Korthaus /KOR 96/ /BEC 99/ used an alternative, empirically based formulation of the porosity functions

$$h_1 = a \left(\frac{\varphi_0^c \, \varphi^c}{\varphi_0^c - \varphi^c - \Delta_1} \right)^m = \frac{a}{(\varphi^{-c} - \varphi_0^{-c} + \Delta_2)^m} \tag{5.141}$$

$$h_2 = b_1 \, h_1 + b_2 \tag{5.142}$$

a, c, m material parameter [-]
b_1, b_2 material parameter [-], $b_2 = 1$ in /KOR 96/
Δ_1, Δ_2 numerical additive to prevent singularity in φ_0 [-]

In contrast to Equ. (5.134) and Equ. (5.135), the pre-factor A of the Arrhenius function in this formulation contains almost all units [$1/(s\ MPa^n)$].

The following applies to the determination of parameters: for mathematical reasons to b: $b > 0$, and for physical reasons to parameter m: $m > 0$. Under these conditions, it can be seen for $h_1' = dh_1/d\varphi$ that its numerator tends to zero faster than the denominator. Thus, the condition of transition between granular salt and rock salt is therefore fulfilled.

In order to increase the influence of initial porosity, the approach of h_1 in Equ. (5.141) was further developed in /KOR 99/ (Equ. (5.143).

$$h_1 = a \left(\frac{\varphi_0^r \, \varphi^c}{\varphi_0^c - \varphi^c - \Delta_1} \right)^m \tag{5.143}$$

r material parameter [-]

5.2.8.4 Grain displacement

A comparable approach to grain deformation (Section 5.2.8.3) is used for the grain displacement /HEI 91/. The following aspects are taken into account, in contrast to the grain deformation approach ((5.133):

- Macaulay brackets are not used since the sign of $F - F_0$ only determines whether a dilatant or a compaction behaviour is present.
- The fluidity coefficient is a function of porosity.
- Measured intergranular cohesion can assume the function of hardening.
- The scalar function ϕ is $\phi = F$.
- An associated flow rule is used, hence, $F = G$.

Thus, there is also a generalized equivalent stress $\hat{\sigma}$ (Equ. (5.144).

$$\hat{\sigma} = n\,\sigma_0 + q \tag{5.144}$$

n material parameter [-]

The viscoplastic strain rate of grain displacement is given by Equ. (5.145), the therefore derived quantity of volumetric strain rate is given in Equ. (5.146) and that of equivalent strain rate in Equ. (5.147).

$$\dot{\varepsilon}_{ij}^{a} = g\,h_3\,(n\,\sigma_0 + q)\left(\frac{1}{3}n\,\delta_{ij} + \frac{\sigma_{ij}^{d}}{q}\right) \tag{5.145}$$

$$\dot{\varepsilon}_{0}^{a} = g\,h_3\,(n\,\sigma_0 + q)\,n \tag{5.146}$$

$$\widehat{\dot{\varepsilon}^{a}} = \sqrt{\frac{2}{3}}\,|g\,h_3\,(n\,\sigma_0 + q)| \tag{5.147}$$

h_3 porosity function [-]

5.3 Analysis of the existing constitutive model approaches

The following remarks document a systematized analysis of the constitutive models used in the project with the objective of a comparative analysis of their performance for a sufficient representation of the THM-coupled material behavior of crushed salt and the validation requirement that may still be necessary for this. The comparison serves as a basis for the planning of an experimental database required for the validation of the constitutive models. Based on the results of the constitutive model analysis, the approach of the systematized laboratory program documented in Section 6.2.3 was developed.

5.3.1 Methodological approach for comparative constitutive model analysis

The comparative analysis of constitutive models was carried out using the methodological approach developed at TUC. The methodological approach used was first elaborated within the framework of the analysis and development of damage related constitutive models for the material behaviour of rock salt and was also successfully applied several times /LUX 18/, /LUX 18a/, /LUX 19/, /DUE 19/. The main structure of the methodological approach and the scheme for the uniform structural decomposition, presentation and

subsequent comparative or evaluative analysis of the constitutive models are shown in the schematic representations in Fig. 5.13 and Fig. 5.14. The quality feature "realism" of the constitutive model, used in Fig. 5.13, essentially characterizes the validation status of the functional relationships and parameter data sets assumed in the model. From the point of view of the objective of deriving the necessary experimental investigations, which are required for a sufficient validation of the constitutive models, the analysis of constitutive models for crushed salt focuses in particular on this quality characteristic "realism", since the investigation requirements can be derived directly from it.

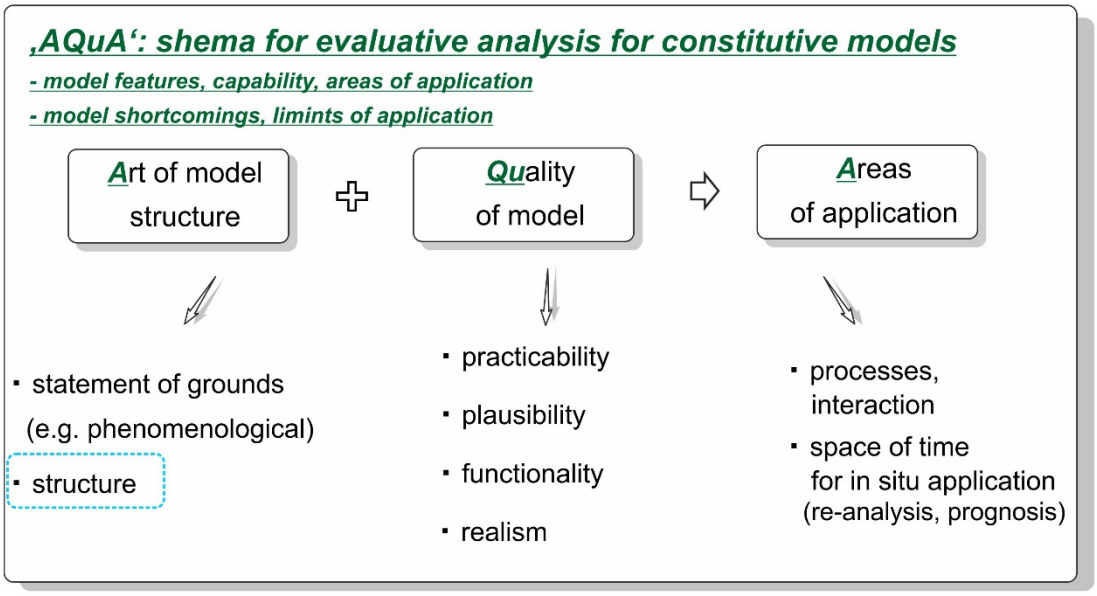

Fig. 5.13 Main structure of the methodological approach to material model analysis and material model development

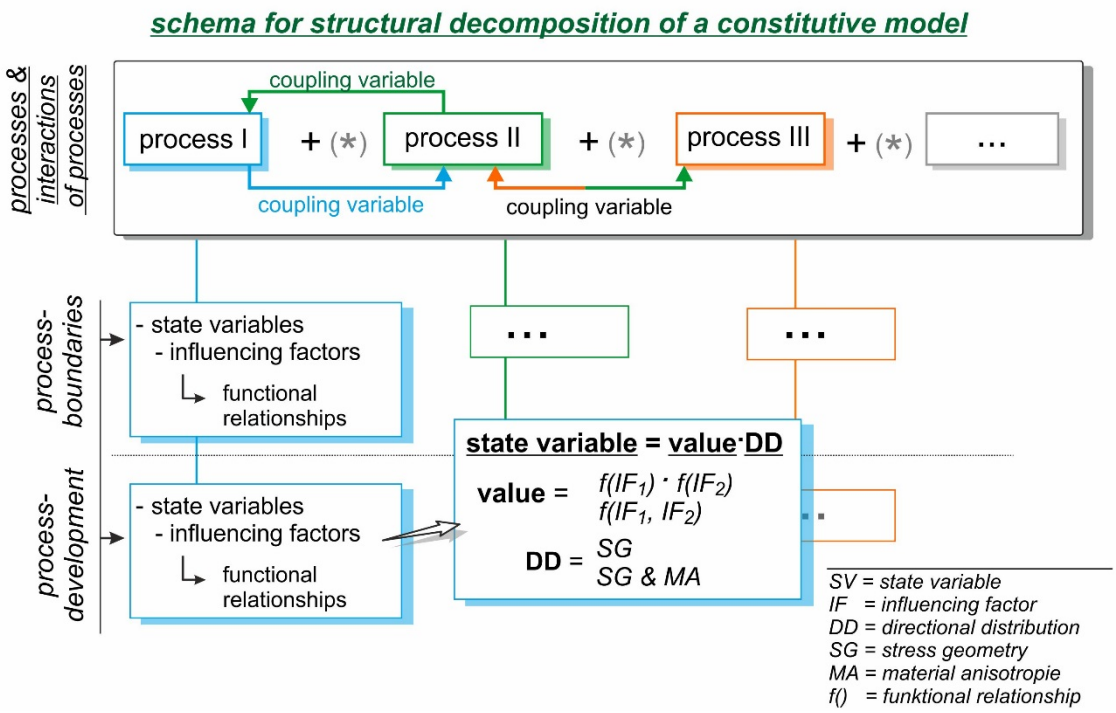

Fig. 5.14 Sketch of the structural decomposition of the constitutive model for comparative or evaluative analysis

5.3.2 Overview of the existing constitutive model approaches for crushed salt: similarities, differences and need for validation

Fig. 5.15 to Fig. 5.22 show the results of the structural decomposition of individual constitutive models for crushed salt.

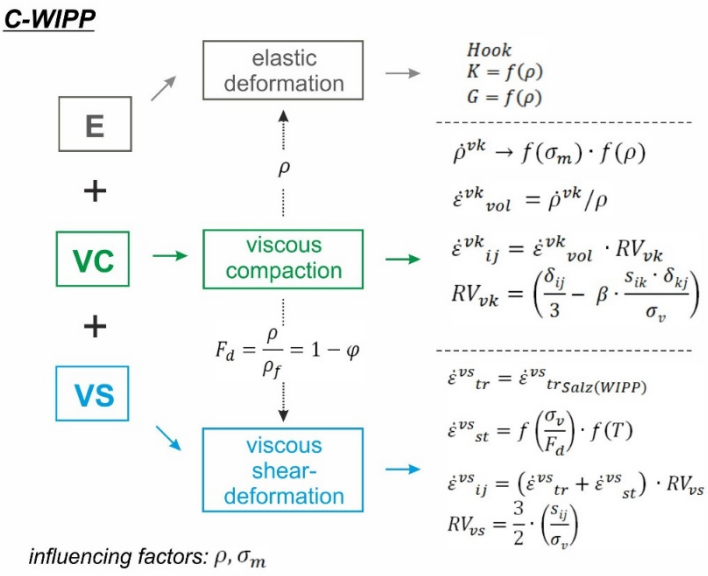

Fig. 5.15 Structural sketch for the constitutive model C-WIPP/Itasca

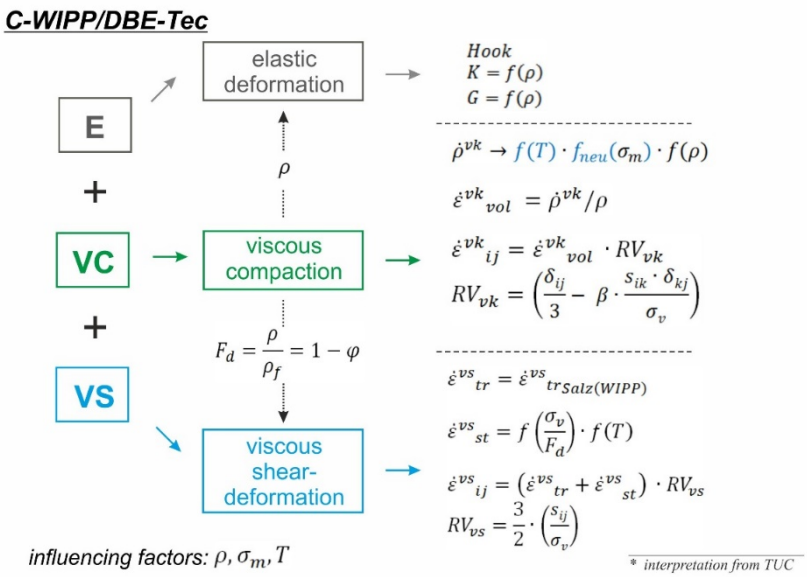

Fig. 5.16 Structural sketch for the constitutive model C-WIPP/DBE-Tec

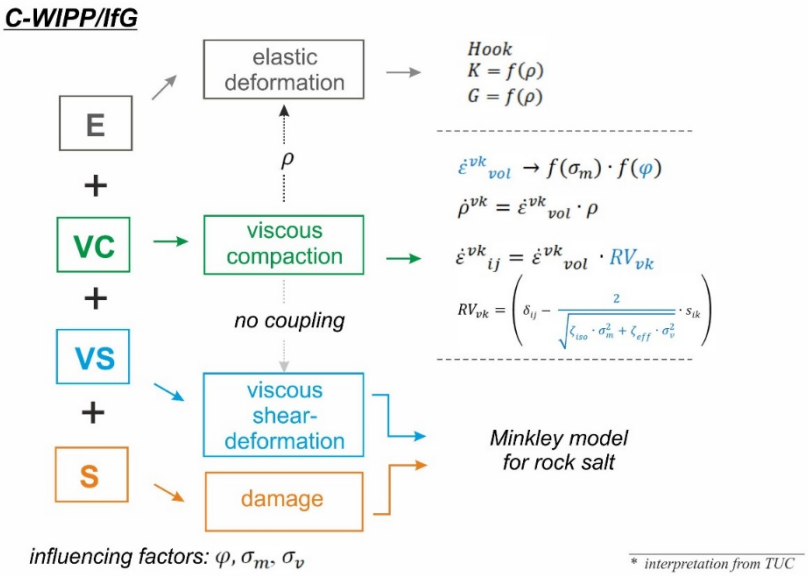

Fig. 5.17 Structural sketch for the constitutive model C-WIPP/IfG

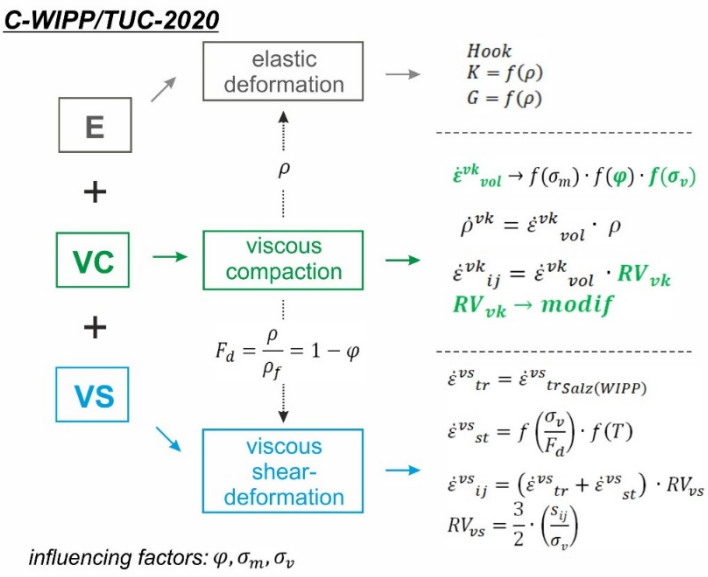

Fig. 5.18 Structural sketch for the constitutive model C-WIPP/TUC

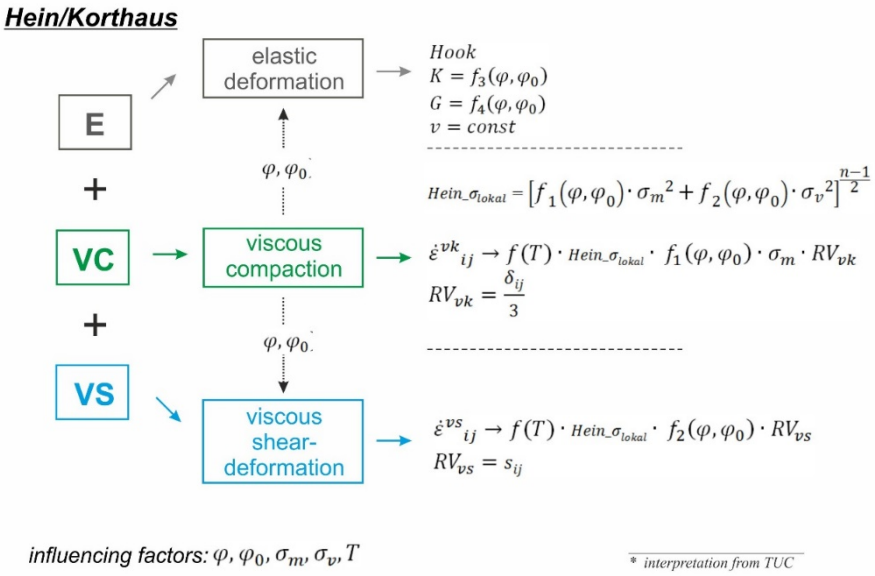

Fig. 5.19 Structural sketch for the constitutive model Hein/Korthaus

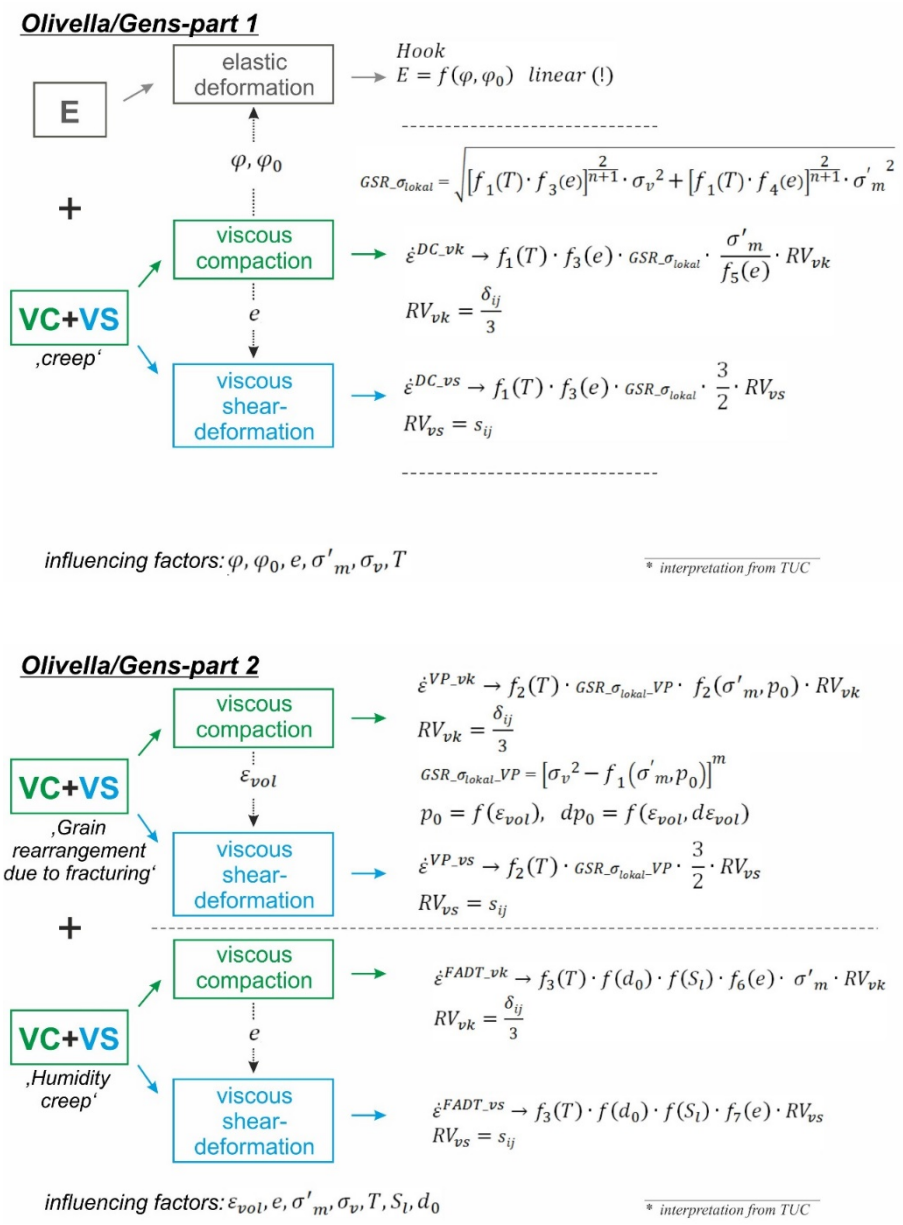

Fig. 5.20 Structural sketch for the constitutive model Olivella/Gens used from GRS

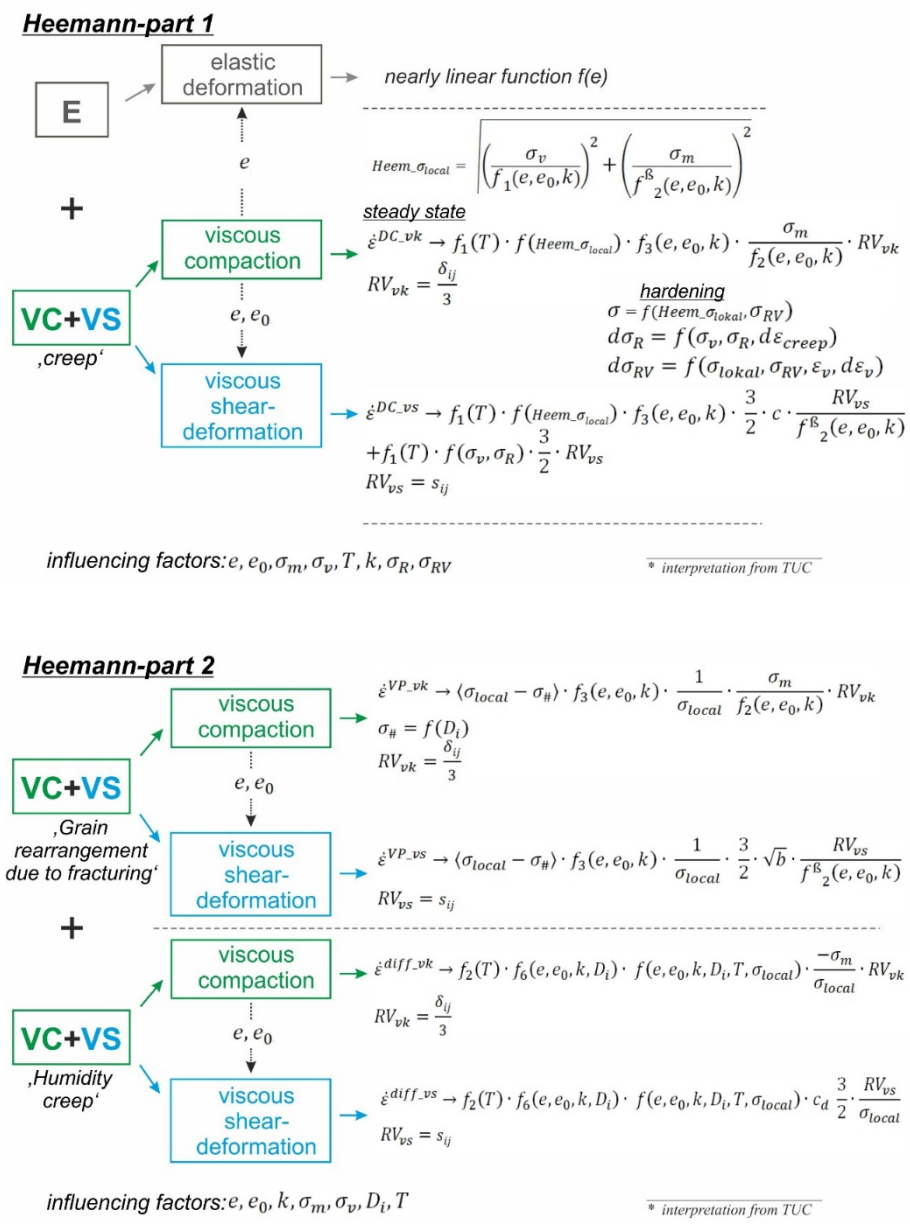

Fig. 5.21 Structural sketch for the constitutive model Heemann used from BGR

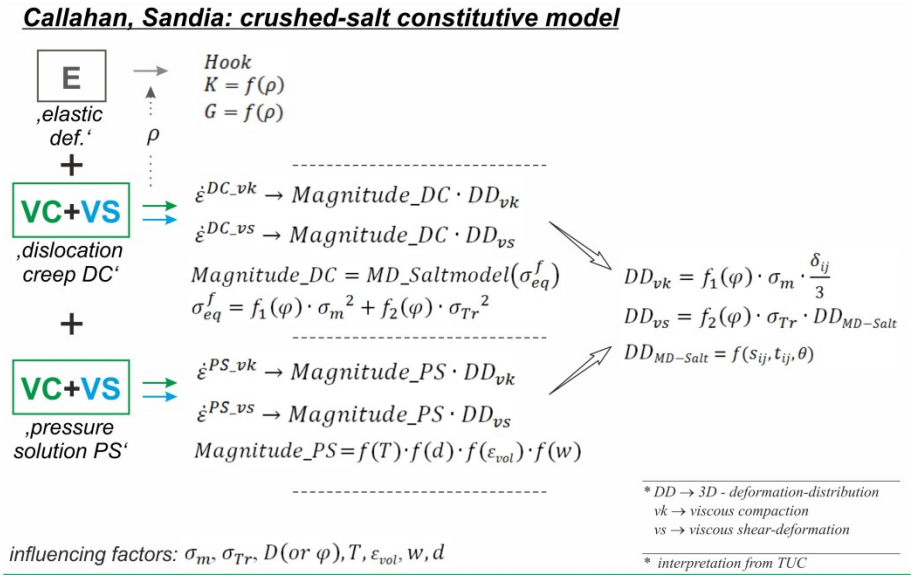

Fig. 5.22 Structural sketch for the constitutive model Callahan used from Sandia SNL

The main results of the comparative analysis for the constitutive model approaches based on this uniform structural decomposition of individual approaches will be shown in Section 6.2.5.

5.4 Benchmarking tests

The following section describes three independent triaxial experiments that aim to characterize the compaction rates of crushed salts under site-specific relevant stresses. Two tests (TK-031 and TK-033) were accomplished in 2012 and 2015 by BGR and one test was accomplished from October 2019 to March 2020 by TUC. Several modellers used the tests' outcomes independently in order to implement constitutive laws, which aim to numerically reproduce the experiments' results. Hence, the following three experiments are regarded as benchmark tests for these numerical approaches.

TUC-V2

The TUC-V2 is a multi-stage test with 5 isotropic load stages, each one including a deviatoric sub-stage.

The load history and the measurements from the TUC-V2 experiment are shown in Fig. 5.23. A detailed description of this test objectives and results was already given in Section 4.8.2.

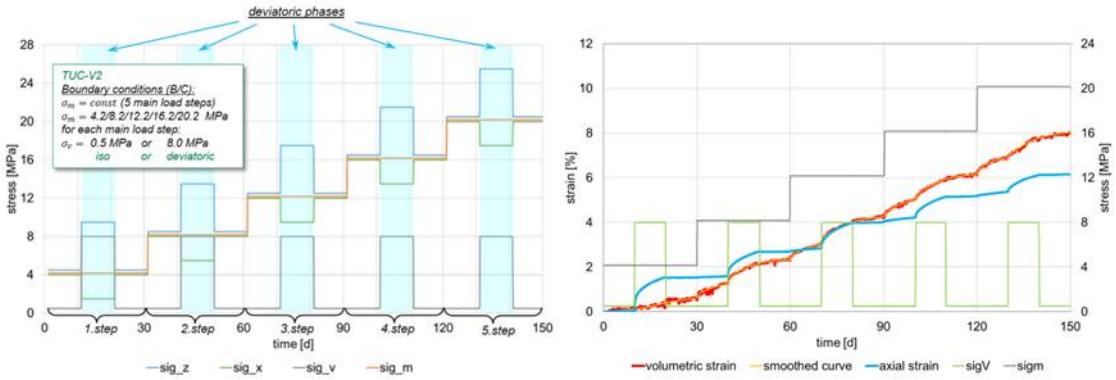

Fig. 5.23 The load history and measurement results for the multi-stage long-term test TUC-V2

5.4.1 Approaches of the individual modelling groups

5.4.1.1 BGE-TEC

Results of CWIPP

Five data sets are used for the adjustment to the three experiments (Tab. 5.4):

- KIT – Adjustment to the data set of experimental data in /KOR 96/. This data set was also used in the BAMBUS project /BEC99/ and /BEC 04/.
- TK-031, TK-033 and TUC-V2 - Individual adaptation to the respective test.
- Comm. - Joint adjustment to all three tests TK-031, TK-033, and TUC-V2.

Some parameters are unchanged in all data sets. General parameters are density $\rho = 2170$ kg/m^3 and initial porosity $\varphi_0 = 0.35$, parameters of the elastic behaviour are final Young's modulus $E_{RS} = 25$ GPa and Poisson number $\nu = 0.27$, the coefficient of thermal expansion $\alpha_{th} = 42*10^{-6}$ 1/K, and parameter of viscoplastic shear deformation are pre-factor $A_{sh} = 0.18$ 1/d, activation energy $Q_{sh} = 54$ kJ/mol, and stress exponent $n = 5$.

Tab. 5.4 Parameter data sets of CWIPP by BGE-TEC

Parameter		KIT	TK-031	TK-033	TUC-V2	Comm.
Init. Young's Modulus E_0	GPa	4.36	0.090	0.050	4.36	4.36
Viscoplastic Compaction						
Prefactor A_{co}	kg/(d*m^3)	2.3E9	9.E11	7.7E12	4.1E9	2.3E8
Activ. Energy Q_{co}	J/mol	32800	6400	831	8010	831
Parameter b_1	1/MPa	1.e-2	0.18	1.e-3	1.e-3	1.e-3
Parameter b_2	m^3/kg	-17820	-24320	-26050	-24615	-23260
Parameter b_3	1/MPa^2	5.853	4.239	8	8	5.853
Parameter b_4	-	-0.664	-1	-0.965	-0.788	-0.745

The adjustment to the test results is based on the least squares method. Thus, the result of the adjustment depends on the error function used and the weights used in it. It should be noted that some material parameters have only a low significance, which is partly caused by the experimental design, partly the model approach. As a note: The adjustment in experiment TK-031 is limited in time to 136d. Especially the creep rate shows that the following period has much higher values and is not only affected by a short-term disturbance.

Characteristic features in the behaviour of the constitutive model are shown by the strain components for TK-033 (Fig. 5.24), where compression is marked positively, and negative strain rates are not shown because of logarithmic scale:

- The part of thermal expansion does not play a role in the specific experiment.
- The elastic component only plays a subordinate role. Even though the initial value of Young's modulus was set very low, the Young's modulus value at the beginning of the tests is at least 1.3.
- Because of the wide range in the values of elastic behaviour, it can be assumed that the numerical model takes into account more than just the instantaneously reversible behaviour.
- The shear component of viscoplastic creep is negligible.
- The essential part of the total deformation is the compaction part of the viscoplastic creep.

– On average, the compaction component of viscoplastic creep meets the requirements of the tests. However, there are significant deviations in the rate distribution, which becomes clearer when considering the creep rate. The constitutive model cannot correspond to the dynamics of the creep rate with high intensity at the beginning of the individual load stage and the subsequent hardening.

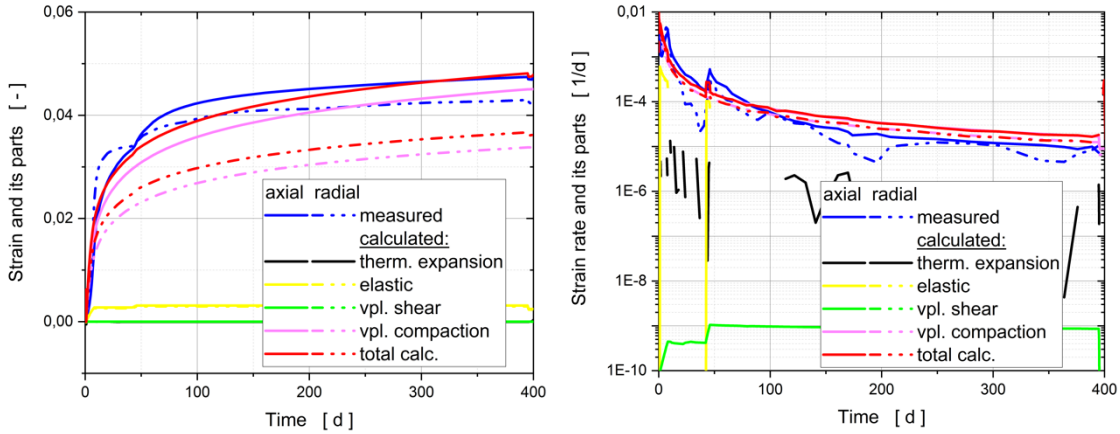

a) b)

Fig. 5.24 Measured and calculated deformation behaviour for TK-033. Calculation with parameter set TK-033: a) Components of strain in axial and radial direction. b) Components of strain rate in axial and radial direction.

The influence of the individual data sets is shown in comparison with the three experiments (Fig. 5.25). From a material point of view TK-033 shows a clearly more ductile behaviour than the two other tests, if the calculated behaviour of the individual adjustments to the individual tests (opt.) are compared to each other. The use of the parameter set KIT leads to an even more ductile material behaviour. Some of the experiments show temperature changes, however, the use of these data is only very limited for the adjustment of the activation energy as a free parameter.

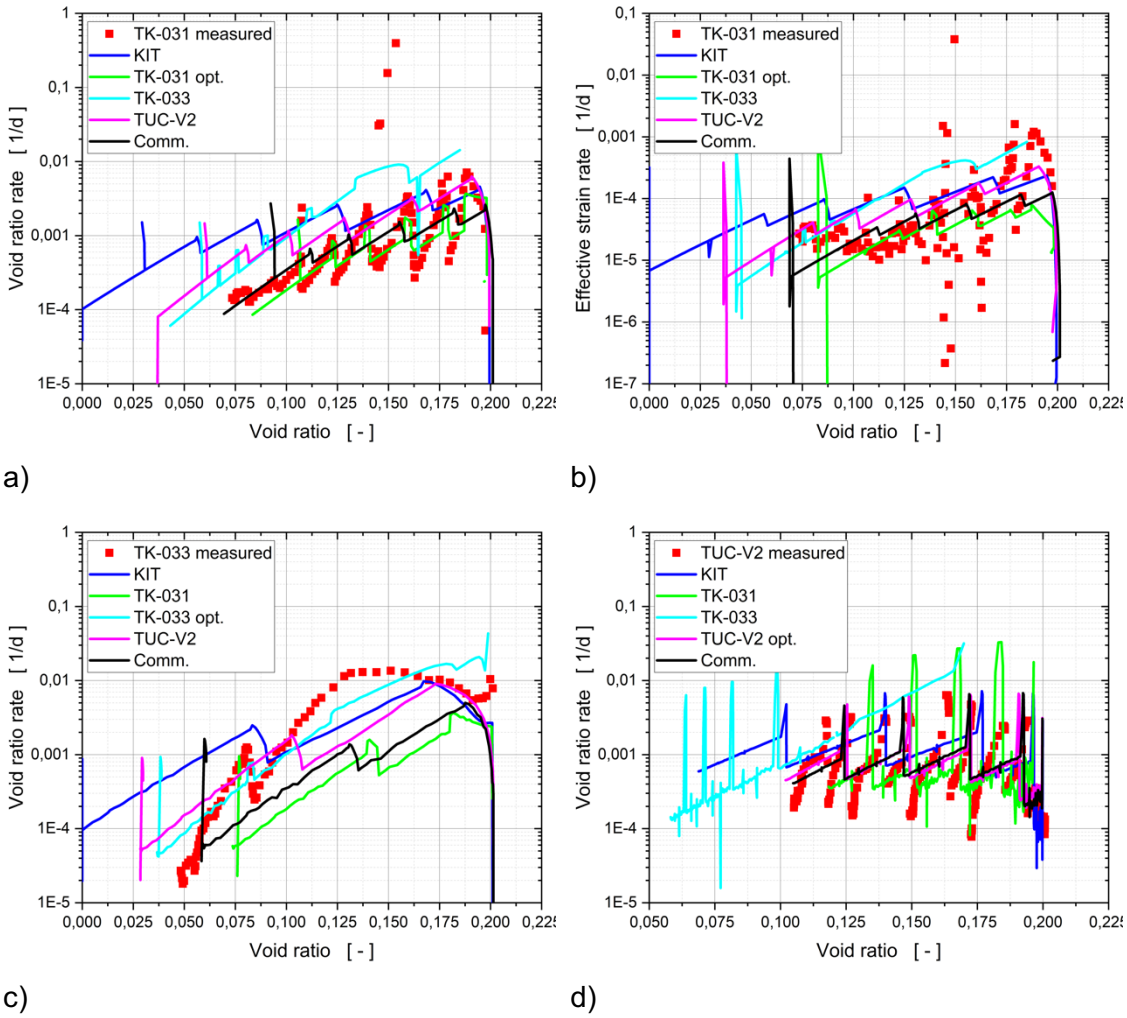

Fig. 5.25 Measured and calculated deformation behaviour; calculation with all sets of parameters: a) Rate of void ratio of TK-031. b) Rate of effective strain of TK-031. c) Rate of void ratio of TK-033. d.) Rate of void ratio of TUC-V2.

If the adjustment is evaluated against the possibilities of the constitutive model, it must be taken into account that the constitutive model shows limitations in the most different directions:

- The porosity function is taken over unchanged, accordingly the behaviour remains unchanged when compaction approaching full compaction. The derivation of the porosity function to porosity is $\frac{df_\varphi}{d\varphi} = f_\varphi \left(-B_2\, \varrho_s + \frac{1}{1-\varphi}\right)$. The value at total compaction is $\frac{df_\varphi}{d\varphi}(\varphi = 0) = (-B_2\, \varrho_s + 1)e^{B_2\, \varrho_s}$, which is finite.

- The magnitude of the compactability depends exclusively on the isotropic stress state, deviatoric stress components only have an effect in the direction of movement, but not in the magnitude of compaction, which is in contrast to the requirements (Section 5.1.2.2).
- Sub-processes that are described in Section 5.1.2.2, but not taken into account are the grain re-arrangement and damage processes in the grains.
- The influence of special field quantities such as the grain structure is missing. This influence must be covered by the functional apparatus.
- Moisture is missing as a parameter in the constitutive model; accordingly, it can only be taken into account by adjusting the parameters in sub-processes in which it has an indirect effect.
- Sub-processes of the deformation process, which are directly based on moisture, are not considered.

The conditions of the experiments investigated are such that the experimentally determined behaviour can be described with the constitutive model in its essential behaviour. The most serious disadvantage is the limited adaptation to the hardening and recovery behaviour within the viscoplastic dislocation creep. If deviatoric stresses arise, the material model lacks a corresponding approach. The other mechanisms mentioned in Section 5.1.2.2 are, as far as they are applied, not resolved separately but are included in the compaction creep.

Results of Hein

The basic idea of the constitutive model is a thermodynamic reasonable approach based on the principle of maximum dissipation rate. The constitutive model contains two viscoplastic components in addition to the instantaneous thermoelastic component and focuses on the material behaviour of a naturally dry granular salt. The viscoplastic components called grain deformation and grain displacement has to be classified as dislocation creep. Regarding the mechanism of grain deformation, Hein /HEI 91/ wrote: "This includes all mechanisms which lead to irreversible, time-dependent deformations of the grains. A characteristic feature is the absence of a "threshold" of stress. Grain deformations are possible even with the lowest loads". Grain displacement is to be interpreted as grain re-arrangement. Hein wrote about this: “This term (grain displacement) covers both the actual grain displacements, that occur after the intergranular static friction has been overcome, and the displacements of broken grain fragments. Characteristic for the grain displacements is the presence of material-typical stress states which form a

"threshold" below which no grain displacements can be detected." Both, grain deformation and grain displacement contain a coupled isotropic and a deviatoric component. Thus, they are able to generate a dilatancy or compaction even under conditions of deviatoric stress state. Currently, there is no thermodynamically consistent porosity term for the grain displacement approach. According to Hein, the part of grain displacement is considered low and is therefore neglected in the application. This argument can be accepted in view of the fact that the tests considered are tests on pre-compacted samples.

The approaches from Equ. (5.141) and Equ. (5.142) are used for the porosity functions. The original approach in Equ. (5.138) and Equ. (5.139) shows a weakness in the transition to solid rock salt and the tests examined here do not cover the requirements resulting from the modified approach in Equ. (5.143).

Six data sets are used for the adjustment to the three experiments (Tab. 5.5):

- KIT and KITimp – KIT is the given parameter set of grain deformation in /KOR 96/. KITimp is an improved adjustment of the data set of the experimental data in /KOR 96/. This experimental data set was also used in the BAMBUS project /BEC99/ and /BEC 04/.
- TK-031, TK-033 and TUC-V2 - Individual adaptation to the respective test.
- Comm. - Joint adjustment to all three tests TK-031, TK-033, and TUC-V2.

Some parameters are unchanged in all data sets. General parameters are density $\rho = 2170$ kg/m^3 and initial porosity $\varphi_0 = 0.35$, parameters of the elastic behaviour are final Young's modulus $E_{RS} = 25$ GPa and Poisson number $v = 0.27$, the coefficient of thermal expansion $\alpha_{th} = 42*10^{-6}$ 1/K, and parameter of viscoplastic deformation are activation energy $Q_{sh} = 54.2$ kJ/mol and stress exponent $n = 5$.

The identification of TK-031 is limited to the time range up to 136 d.

Tab. 5.5 Parameter data sets of Hein's model

Parameter		KITorg	KITimp	TK-031	TK-033	TUC-V2	Comm.
Init. Young's Modulus E_0	GPa	13	23.8	0.050	0.050	23.8	15
Grain deformation							
Prefactor A	1/(d*MPa^n)	0.0942	0.01136	6.74e-3	0.1469	0.4696	0.4685
Parameter a	-	0.01648	6.31e-8	1.e-4	1.e3	1.e-6	2.63e-6
Parameter c	-	0.1	0.00204	0.0634	1.79	0.019	0.014
Parameter m	-	2.25	2.974	3.892	1.548	3.578	3.122
Parameter b_1	-	0.9	0.914	0.2	0.316	1.049	1.064
Parameter b_2	-	1.	2.	1.	0.492	0.989	0.99

Characteristic features in the behaviour of the constitutive model are shown by the strain components for TK-033 (Fig. 5.26), where compression is marked positively, and negative strain rates are not shown because of logarithmic scale:

- The notes on thermal expansion, the elastic component, and the compaction part of viscoplastic creep in Section 5.4.1.1 remain valid.
- The compaction behaviour of the experiments is better described with the combined isotropic/deviational stress approach of viscoplastic creep than with a purely isotropic approach. However, deviations in the development of the rates can still be observed. The constitutive model cannot fully satisfy the dynamics of the creep rate caused by hardening and recovery.

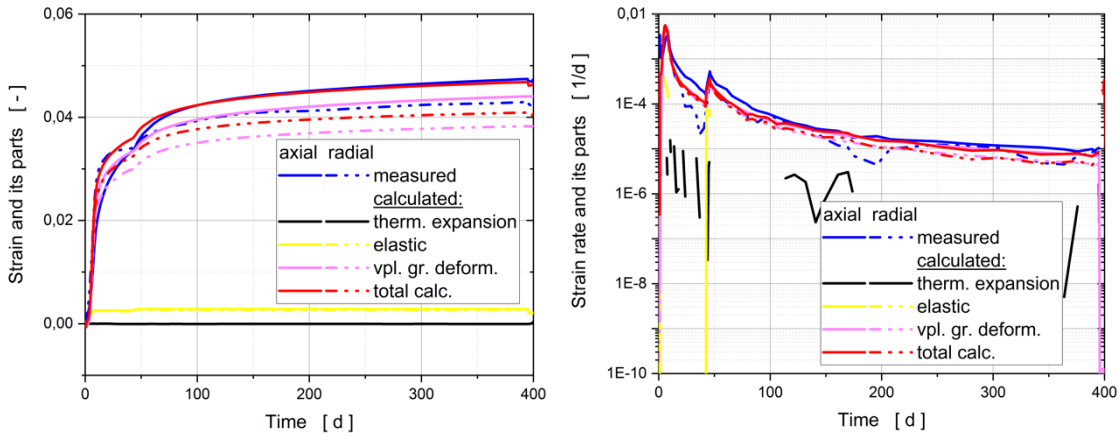

a) b)

Fig. 5.26 Measured and calculated deformation behaviour of TK-033. Calculation with parameter set TK-033: a) Components of strain in axial and radial direction. b) Components of strain rate in axial and radial direction.

The influence of the individual data sets is shown in comparison with the three experiments (Fig. 5.27).

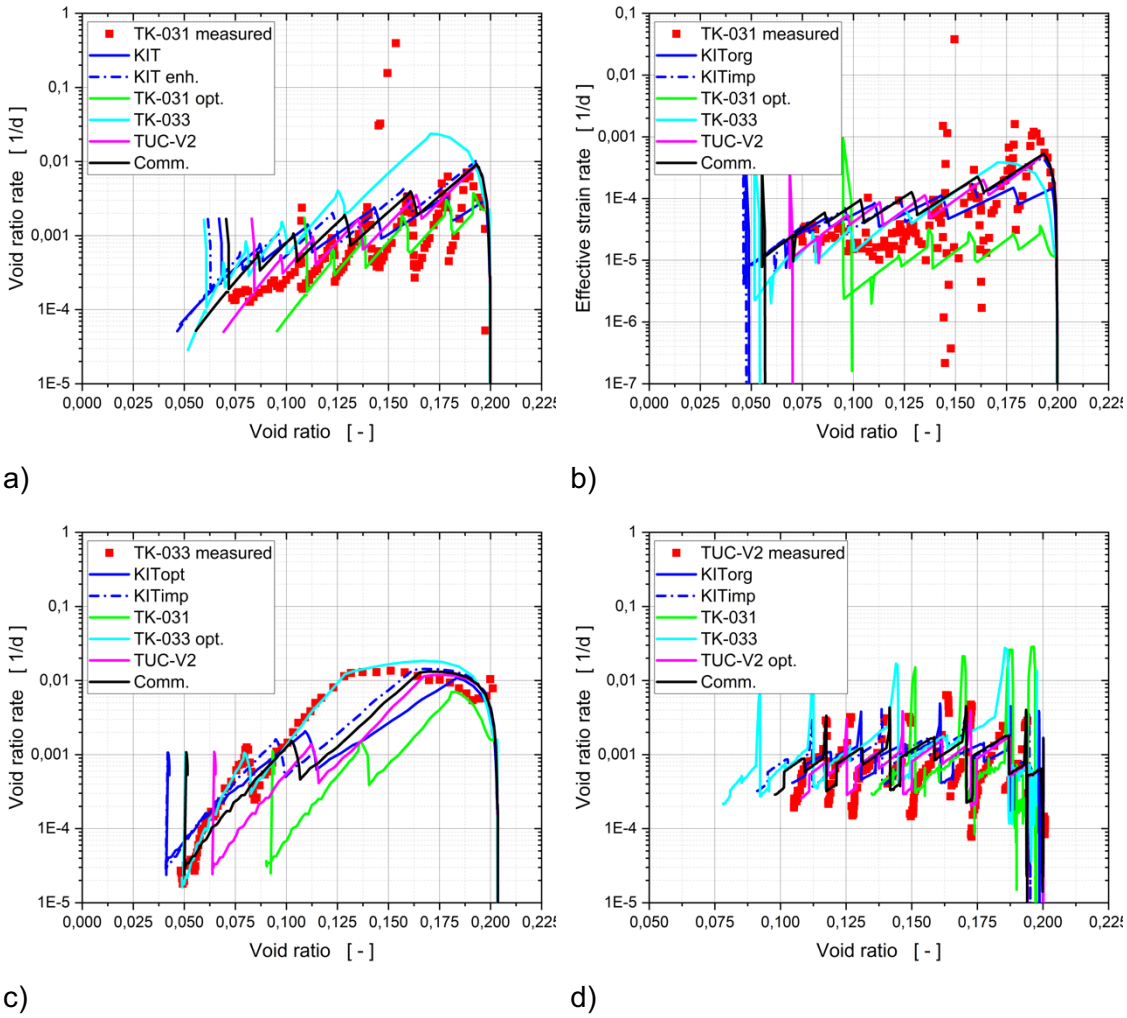

Fig. 5.27 Measured and calculated deformation behaviour; calculation with all sets of parameters: a.) Rate of void ratio of TK-031. b.) Rate of effective strain of TK-031. c.) Rate of void ratio of TK-033. d.) Rate of void ratio of TUC-V2.

TK-033 initially appears to be much more ductile with subsequent significant compaction hardening compared to the others. Although there are also differences in the behaviour calculated with the other data sets, they are more in the sense of different creep classes. Particularly noteworthy are the small differences between the results with the data sets KITimp, TUC-V2, and Comm. Thus, at least for the time being, the new crushed salt mixture composed within the framework of this project can be regarded as a component of an already existing population.

The results from all three experiments have been included in the determination of the common data set. Due to the different behaviour of TK-033, this test would have to be

classified as part of a separate population and thus excluded from common identification here. Alternatively, this experiment contains a property that is not covered by the constitutive models.

The calculated data partly match very well with the experimental data. However, there are also limitations:

- The influence of special state variables such as the grain structure and anisotropy could be included into the functional apparatus.
- Grain displacement is not taken into account in the application of the constitutive model, as no consistent formulation and experimentally validated porosity approach exist in the sense of the dissipation approach. Grain deformation (Equ. (5.135) already includes in its flow function both the influence of the mean stress and that of the deviatoric stress. However, the loading path of the two BGR tests evaluated here was nearly isotropic, only the TUC-V2 test brought the deviatory components into a certain extent. The adjustment of the deviatory part is therefore subject to greater uncertainties.
- Grain displacement is assigned to viscoplastic creep in the existing constitutive model, but from the mechanisms corresponding to Section 3.2.3 and Section 5.1.2.2 it is a plastic deformation.
- Fracture processes and the role of a failure criterion is still open.
- Moisture is not yet considered in the constitutive model.
- Furthermore, entire sub-processes in the deformation process such as pressure solution-driven processes still have to be integrated.
- An energetically consistent but also experimentally confirmed formulation of the required porosity functions does not yet exist, so that grain deformation and grain displacement can be combined with respect to the principle of maximum dissipation rate.
- There is potential for improvement in the identification process with regard to phenomena that are only weakly pronounced in the experiments, such as thermal expansion, elastic behaviour, and partly also deviatoric behaviour.

The constitutive model is already well suited to describe the compaction behaviour of dry granular salt in the porosity range covered in the tests. However, beyond adaptation to specific types of tests, it is necessary to describe the hardening and recovery behaviour in dislocation creep. In addition, the deviatoric behaviour must be improved.

5.4.1.2 GRS

This chapter describes the modelling approaches for the TK-031, TK-033 and TUC-V2 tests applied by GRS with use of the finite-element code CODE_BRIGHT. The approaches for the three tests have the same structure and differ in the initial parameter set only.

Since GRS is working in the field of crushed salt investigations for several years, parameter sets for the numerical simulation of crushed salt compaction were developed within previous projects. They are referenced to the following GRS reports:

- GRS-254: REPOPERM project phase 1 /KRÖ 09/
- GRS-288: Preliminary Safety Analysis of the Gorleben site (VSG) /MUE 12/
- GRS-450: REPOPERM project phase 2 /KRÖ 17/

TK-031

The first modelling task includes the triaxial compression test TK-031. Based on the knowledge gained in past projects, first, the three parameter sets mentioned above are used for carrying out the numerical simulation. Therefore, Fig. 5.28 shows the results for the simulation of TK-031 with the existing parameter sets.

For both, the consideration of mechanical processes only and hydraulic-mechanical (HM) coupled processes, the results show no sufficient accordance with the laboratory data. For the execution of a HM-coupled simulation, the porosity decreases rapidly with the first increase in load to a residual porosity of 0.1 %. Neglecting the hydraulic effects leads to a more realistic evolution of porosity, however, the decrease is strongly underestimated. Thus, the existing parameter sets are not suitable to simulate the compaction behaviour of TK-031 leading to a detailed investigation of parameters.

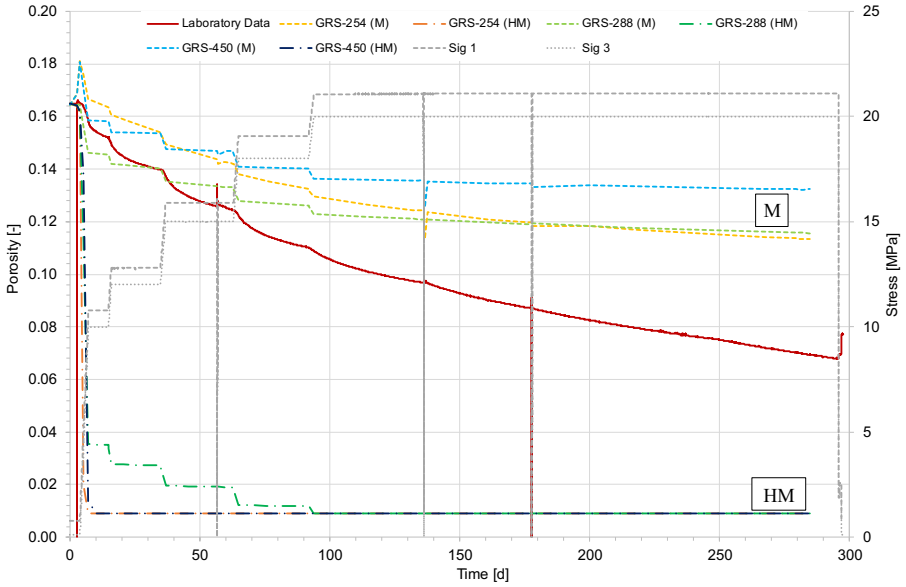

Fig. 5.28 Preliminary results of porosity evolution for the simulation of TK-031 with existing parameter sets for crushed salt in comparison with laboratory data

In CODE_BRIGHT a constitutive model for the consideration of humidity creep is included. Since already small contents of brine may induce creep effects, the modelling is executed in a hydraulic-mechanical coupled way. As basis for the further modelling work the parameter set GRS-254 was chosen.

The parameter improvement is executed in the following steps:

1) Adaption of elastic parameters including the Young's modulus and the variation of Young's modulus with porosity decrease.
2) Adaption of viscoplastic parameters including the initial value of the hardening, the hardening parameter and the fluidity.
3) Adaption of creep parameter referring the grain size in the FADT model.

The elastic behaviour of crushed salt may play only a minor role for the mechanical behaviour and its isolation is very difficult, however, it should be considered in the numerical modelling. For the simulation of the linear elastic behaviour, the generalized Hook's law is used in combination with a variation of Young's modulus with porosity (Equ. (5.67**)**.The initial value of the crushed salt specimens Young's modulus depends on the pre-compaction treatment and is determined based on the knowledge of past experimental investigations /ROT 03/.

Fig. 5.29 shows the porosity evolution of TK-031 within the first loading phase. Elastic deformations are instantaneous; thus, the porosity decrease was adjusted within the first load change. Therefore, a Young's modulus of 1,750 MPa seems appropriate.

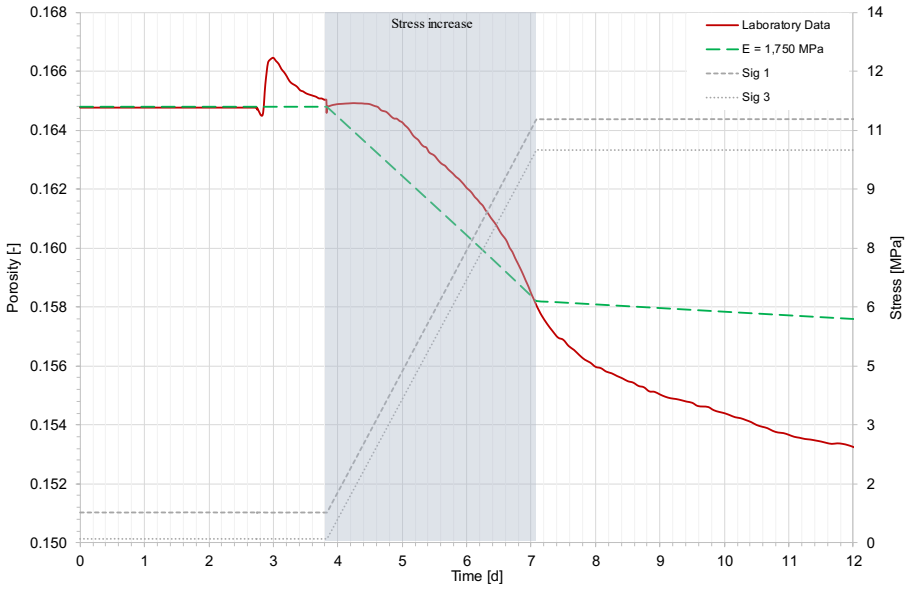

Fig. 5.29 Improvement of elastic parameter for the simulation of TK-031 with CODE_BRIGHT

Within the whole laboratory investigation, the loose crushed salt becomes a solid with ongoing compaction due to grain rearrangement, densification and bond creation. For the consideration of these phenomena a viscoplastic model is implemented in CODE_BRIGHT (Section 5.2.3).

The initial value of hardening in the hardening law depends like the Young's modulus on the pre-compaction treatment of the sample, especially on the value of stress. For a first adoption the viscoplastic parameters p_0 = 0.1 MPa, X = 0.1, Γ_0 = 0.005 $s^{-1}MPa^{-m}$ were applied. The results show a strong overestimation of porosity decrease (Fig. 5.30a, orange line). Another proof of plausibility is the evolution of hardening parameter with the mean stress. The evolution with time should follow the mean stress which is not the case for the chosen parameter set (Fig. 5.30b, orange line).

Since the initial value for hardening is chosen very low in the first approximation, it is increased in the next step to p_0 = 10 MPa. The evolutions of porosity and hardening parameter show a strong improvement in plausibility (Fig. 5.30, blue lines).

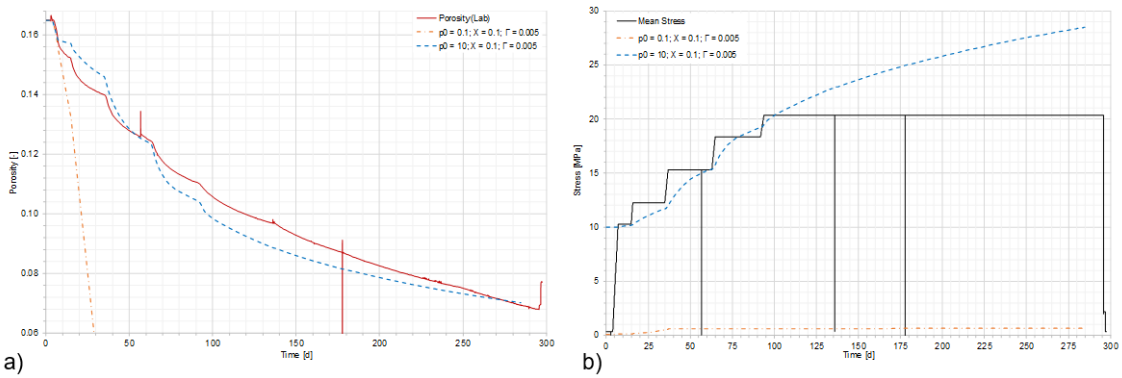

Fig. 5.30 Evolution of a) porosity and b) hardening parameter for variations of p_0

The amount of hardening increase is determined by the hardening law, especially, due to the parameter X. The functional relationship leads to an increase of hardening with decreasing X-parameter. Fig. 5.31 show the increase of hardening parameter p_0 with the decrease of X. The best improvement of hardening and porosity evolution is reached with X = 0.08.

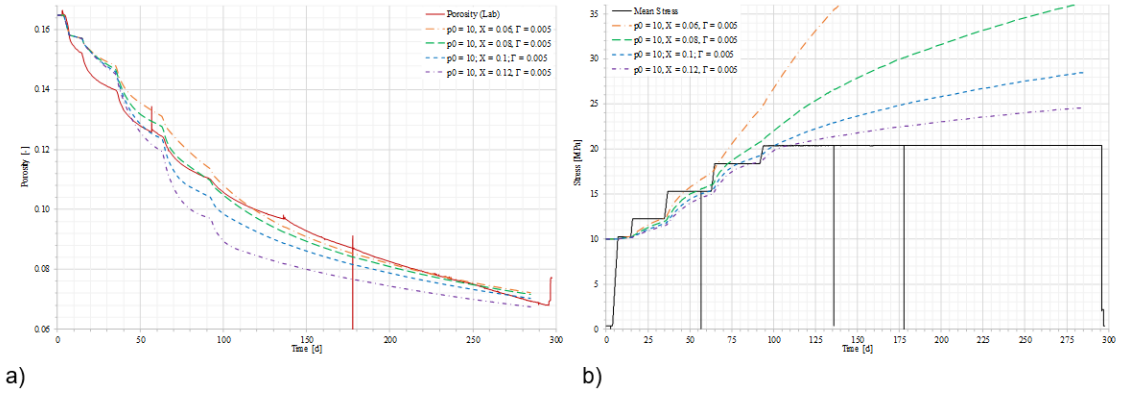

Fig. 5.31 Evolution of a) porosity and b) hardening parameter for variations of X

The viscoplastic model in Equ. (5.86) includes the fluidity acting as plastic multiplier controlling the relative strains magnitude. Fluidity is described through an Arrhenius function, however, this triaxial test was isothermal leading to no variation of fluidity with temperature. With increasing the value of fluidity, the strain increment rises which is needed for the first loading phases. With choosing $\Gamma_0 = 0.01\ s^{-1}MPa^{-m}$ and $\Gamma_0 = 0.02\ s^{-1}MPa^{-m}$ two sufficient parameter are found for building up the porosity decrease of TK-031 (Fig. 5.32).

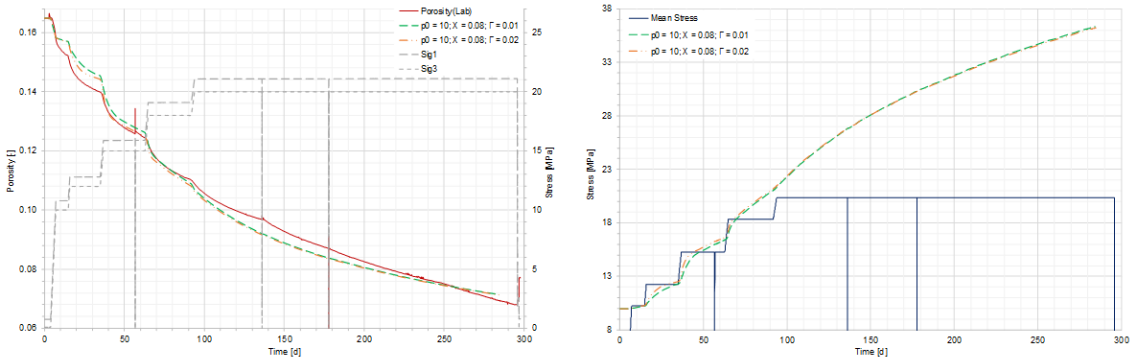

a) b)

Fig. 5.32 Evolution of a) porosity and b) hardening parameter for variations of fluidity

With the improvement of the elastic and viscoplastic part of the constitutive model a quite good approximation of porosity evolution is reached. However, creep is an important part for crushed salt compaction and should be considered, too.

The majority of creep parameter are well defined. Thus, the dislocation creep mechanism is based on the Norton creep law which parameters are well specified due to the creep classes (V = 2.08E-6), the stress exponent (n = 5) and the activation energy (Q_A = 54,000 J/mol).

For the fluid assisted transfer mechanism, the determining parameter is the grain fraction. For humidity creep the finer grain fraction plays an important role, thus its influence could be used for improvement of modelling results. Therefore, Fig. 5.33 shows the volumetric strain and its rate for the maximum, mean and minimum grain size.

No big differences can be observed by the change of maximum grain size to mean grain size, however, for the minimum value the evolution of volumetric strain becomes not plausible.

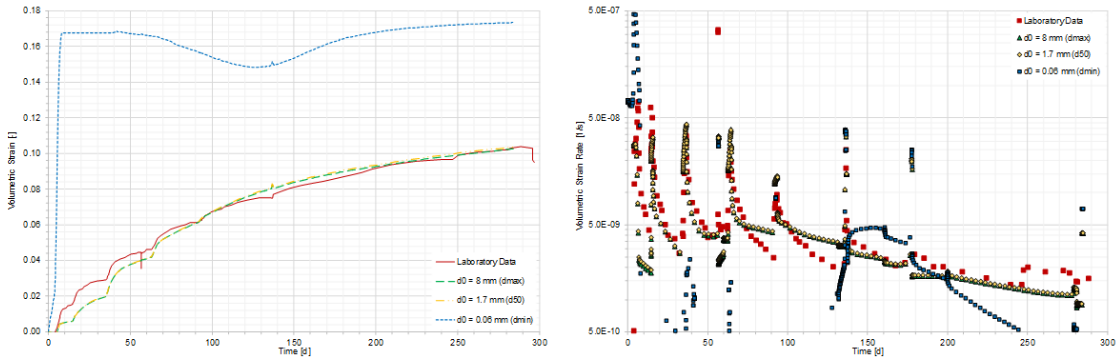

a) b)

Fig. 5.33 Evolution of a) volumetric strain and b) volumetric strain rate for variations of grain size in the FADT model

TK-033

The modelling approach for TK-033 is the same as described in the previous for TK-031, however, the initial dataset as basis for the parameter improvement is the final set of TK-031 since the crushed salt material is the same in both cases, thus they only differ in the experimental execution.

Fig. 5.34 shows the first simulation for TK-033 applying the parameter set developed for TK-031 previously. There are big deviations between the numerical results and the laboratory data, so it can be concluded that even if the same crushed salt material is used the model could not reproduce its behaviour under differing stress conditions. However, the graph shows a good reproduction of the creep behaviour in the second loading phase.

After the parameter improvement following the structure as described above, the final result shows that the whole evolution TK-033 could not be simulated sufficiently. Two parameter sets are developed, one reproducing the first load phase quite good and the other showing good accordance with the second load phase (Fig. 5.34). The difficulty within the modelling task was the strong compaction due to the high stress gradient in the beginning of the test. It could not be simulated sufficient with CODE_BRIGHT with a simultaneously good reproduction of the second phase.

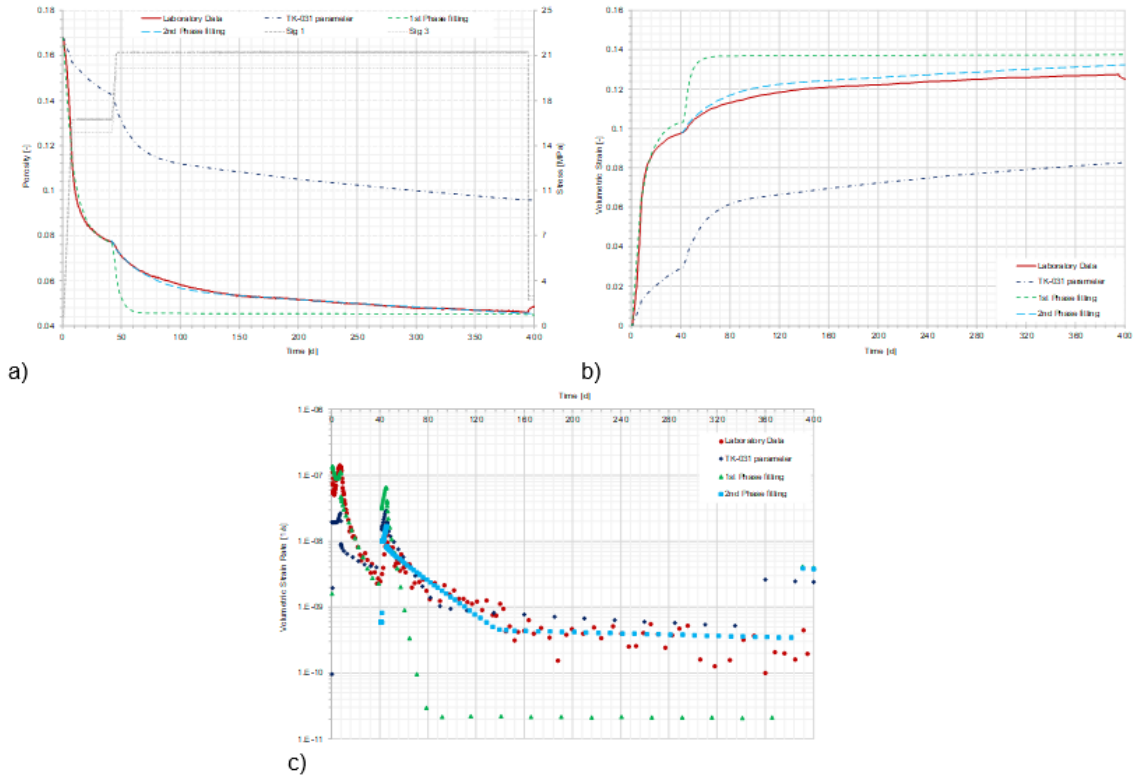

Fig. 5.34 Evolution of a) porosity, b) volumetric strain and c) strain rate for the simulation of TK-033 with the parameter set developed for TK-031 (dark blue), for the modelling of the first load phase (green) and the second load phase (light blue)

TUC-V2

The modelling procedure for the TUC-V2 test is the same as described above. As initial parameter set the TK-031 parameter are used, however, no good approximation was achieved (Fig. 5.35, orange graphs). Due to the improvement of the viscoplastic parameters an approximation of modelling results to laboratory results could be achieved for the first 70 days. A further improvement could only be achieved by changing the prefactor in the dislocation creep mechanism which corresponds to a change in creep class. In the state of knowledge rock salt is divided into different creep classes and these are adopted for crushed salt. But there are differences in the mechanical behaviour of crushed salt and rock salt and the validity of the adaption of creep classes is still an assumption and not verified yet.

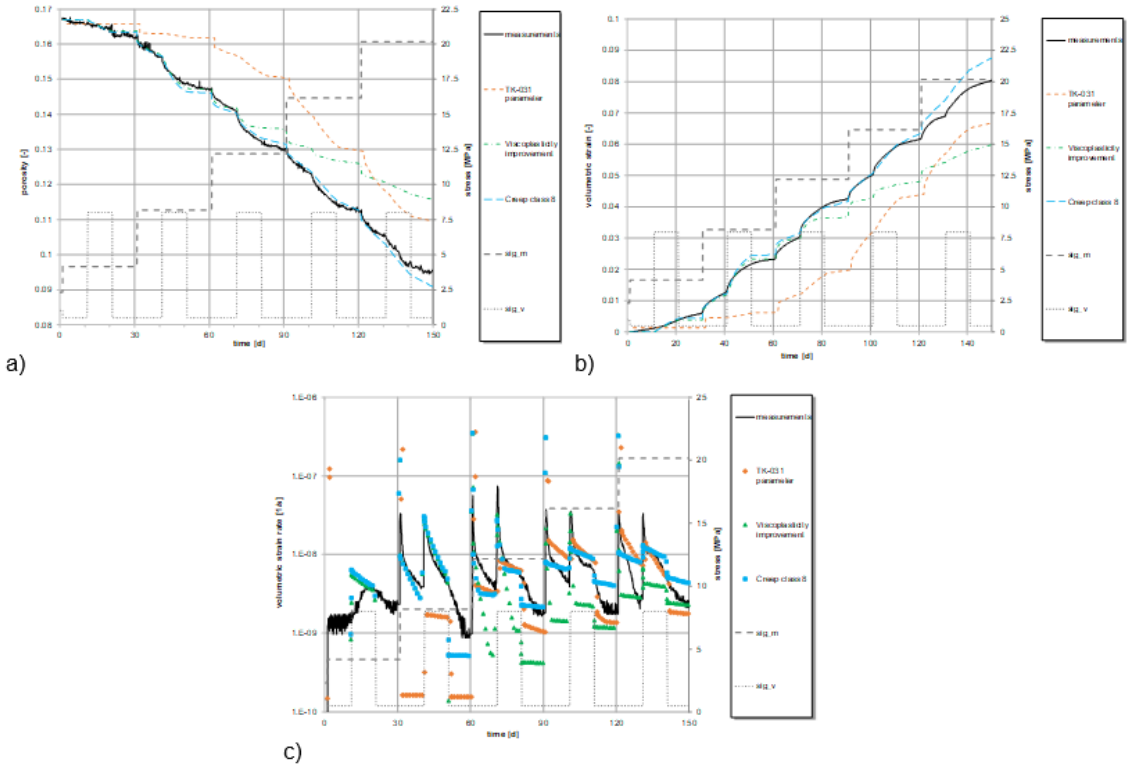

Fig. 5.35 Evolutions of a) porosity, b) volumetric strain and c) volumetric strain rate for TUC-V2 with the parameter set of TK-031, a viscoplasticity improved and a creep class improved parameter set and

5.4.1.3 IfG

To derive parameters for the benchmark tests, the IfG has employed an algorithm that focuses on the creep (i.e. constant stress) phases. It is anticipated that there is an additional “plastic” contribution to volumetric strain during the ramps that is not covered by the creep law (Equ. (5.98) and elastic compaction.

However, during the creep phases, where stress is constant and to a good approximation isotropic, the volume strain is given by the trace of Equ. (5.98). For this simple situation, the porosity as function of time can be computed analytically

$$P(t) = -\frac{1}{C_2}\ln\left[1-\left(1-e^{-C_2P_0}\right)\exp\left(-C_0\left(e^{C_1 s}-1\right)\cdot C_2\cdot(t-t_0)\right)\right] \qquad (5.148)$$

with initial value $P(t=t_0)=P_0$ and constant compressive isotropic stress $\sigma_0=-s$ (so that $s>0$).

This expression still is a nontrivial function. A set of compaction parameters is obtained in three steps:

1) Fix a value of C_2.

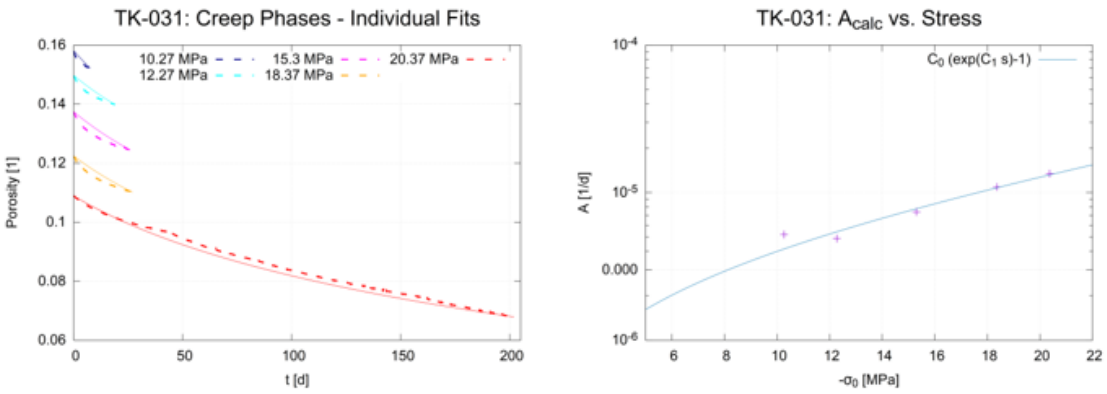

Fig. 5.36 Intermediate results for TK-031. Left panel: Analytic solution for each individual creep phase with $\boldsymbol{C_2}$ = 32.35 (dashed lines: data, solid lines: simulation). Right panel: $\boldsymbol{A_{calc}}$ (crosses) and $\boldsymbol{C_0(e^{C_1 s}-1)}$ (solid line) versus stress for $\boldsymbol{C_0}$ = 3.385*10^{-6} /d and $\boldsymbol{C_1}$ = 0.078 /MPa

2) For each creep phase, the factor $A = C_0\left(e^{C_1 S}-1\right)$ can be calculated from the duration T and initial and final porosities,
At this stage, the curves of $P(t)$ can be compared to the data, and the value of C_2 is adapted if necessary.

$$\mathrm{A_{calc}} = -\frac{1}{C_2 T}\ln\left[\frac{e^{-C_2 P_{\mathrm{final}}}-1}{e^{-C_2 P_0}-1}\right] \tag{5.149}$$

3) From a plot of $\boldsymbol{A_{calc}}$ vs s the parameters $\boldsymbol{C_0}$ and $\boldsymbol{C_1}$ can be determined

Fig. 5.36 illustrates the procedure for reference test TK-031. In the left panel, porosity evolution is plotted for the five creep phases with individually fixed values A_{calc} for a chosen value of $C_2 = 32.35$. Since the algorithm ensures that the initial and final porosities are correctly reproduced, the choice of C_2 just determines the curvature of the P-t curve. It is apparent that with the give value, the analytic solution is too flat for the first phases and slightly too curved for the last (and longest) one. The right panel plots the computed values A_{calc} and the analytic form of A; the agreement is quite reasonable.

The ramps between the creep phases can be used to determine the porosity dependence of the bulk modulus. Note that this assumes that the additional compaction during stress increases is elastic, while there plausibly is a significant plastic contribution. Hence, load-unload cycles should provide a better estimate of elastic properties. Clearly, isotropic experiments do not provide information on the shear behaviour.

To determine the bulk modulus' porosity coefficient κ, we have to separate the elastic from the creep contribution. As a simple estimate, we assume an average compaction creep rate

$$\bar{\dot{\varepsilon}} = \frac{1}{2}\left(\dot{\varepsilon}_{\mathrm{c}}(s_1, P_1) + \dot{\varepsilon}_{\mathrm{c}}(s_2, P_2)\right). \tag{5.150}$$

for a ramp from $\sigma_0 = -s_1$ to $\sigma_0 = -s_2$ with initial and final porosities P_1 and P_2 and estimate the creep compaction component. The effective bulk modulus for $P = \frac{1}{2}(P_1 + P_2)$ is then given by

$$K = \frac{\Delta s}{\Delta \varepsilon_{\mathrm{vol,elastic}}} = \frac{\Delta s}{\Delta \varepsilon_{\mathrm{vol}} - \varepsilon_{\mathrm{vol,creep}}}. \tag{5.151}$$

From a plot of K vs. P, including the bulk modulus of intact rock salt for $P = 0$, the coefficient κ can be determined.

The parameter sets derived from experiments TK-031 and TK-033 are collected in Tab. 5.6. Note that although the sample material and general test procedure are quite similar, the parameters differ significantly: The porosity dependence via C_2 is almost five times as strong for TK-033; the larger value in the exponent needs to be compensated by almost five orders of magnitude in C_0.

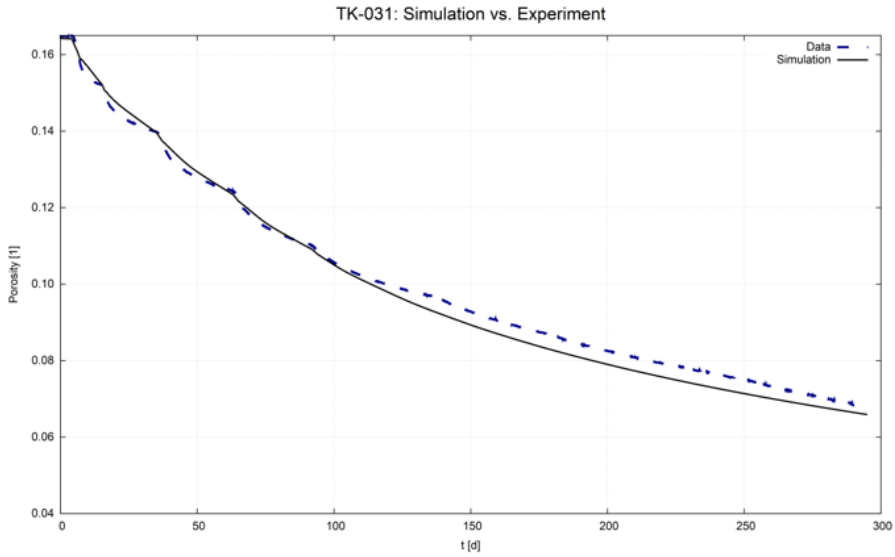

Fig. 5.37 Simulated porosity evolution vs data for TK-031

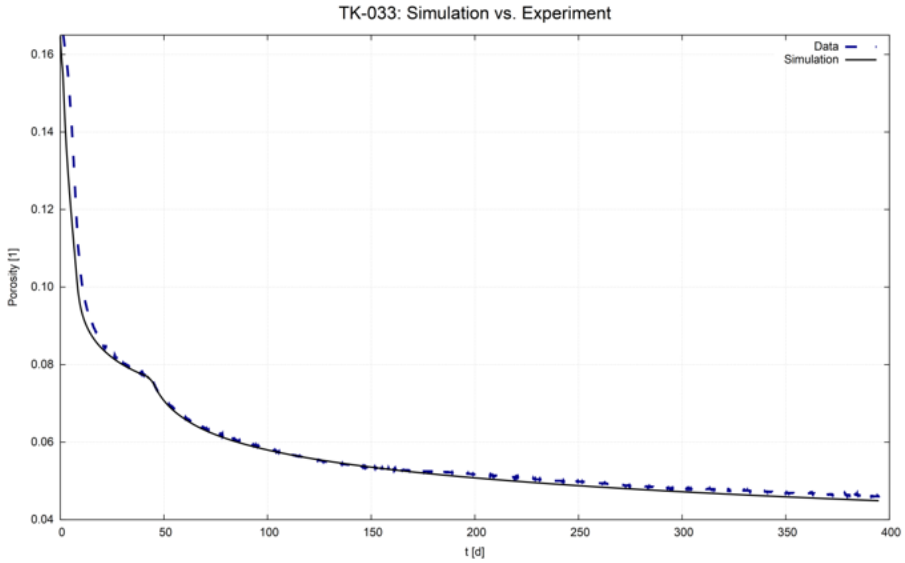

Fig. 5.38 Simulated porosity evolution vs data for TK-033

Tab. 5.6 Parameter values derived from reference tests TK-031 and TK-033

Parameter	TK-031	TK-033	TUC-V2
C_0 [1/d]	$3.385 \cdot 10^{-6}$	$1.05 \cdot 10^{-11}$	$4.05 \cdot 10^{-6}$
C_1 [1/MPa]	0.078	0.3925	0.1
C_2 [1]	32.35	140	30
κ [1]	15.8	11.8	11.8

The constitutive model has been implemented in the Itasca codes FLAC/FLAC3D and UDEC/3DEC. The experiments have been modelled with 3DEC 5.2, a distinct-element

code that allows for shear movement between blocks, such as the sample and the load platens. Porosity in the simulations is shown in Fig. 5.37 and Fig. 5.38. For both experiments, there is good agreement between data and experiment. However, it is apparent, in particular for TK-031, that at the end of the test, the simulated rates differ from the laboratory values, so that an extrapolation to lower porosities will increasingly deviate.

We now turn to the TUC-V2 test. Since the volumetric compaction creep rate does not depend on the von Mises stress, it is clear that the model will not adequately cover the results. (There is a small and indirect dependence on the stress deviator since the sample is modelled together with the load platens, so that the stress distribution in the sample is slightly inhomogeneous.)

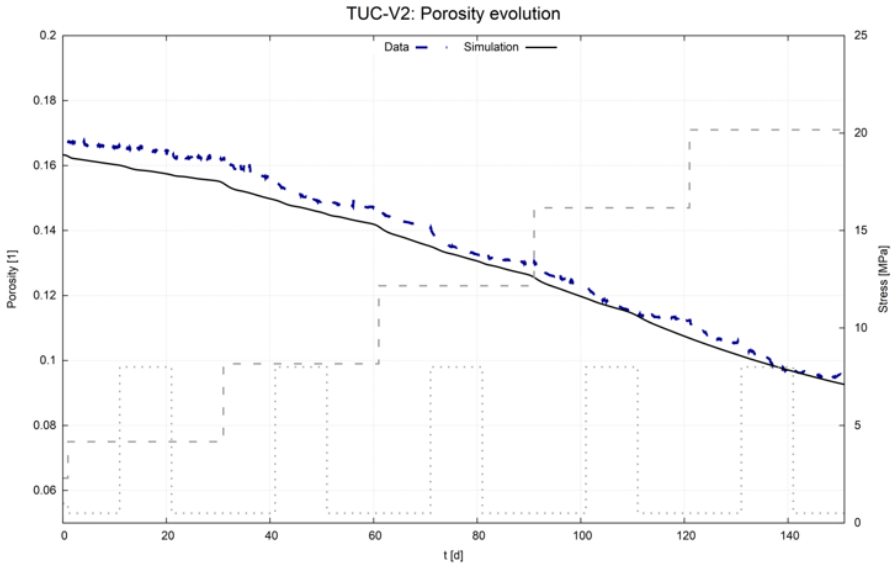

Fig. 5.39 Simulated porosity evolution vs. data for TUC-V2

Fig. 5.39 shows the porosity evolution of TUC-V2 and the simulation. While the overall trend is in reasonable agreement, the increasing compaction rates during the deviatoric phases are, as expected, not reproduced.

5.4.1.4 Sandia

The following sections describe the modelling efforts on the KOMPASS project by Sandia National Laboratories (SNL). For the KOMPASS project, we have applied the WIPP Crushed Salt Model of Callahan /CAL 99/ to simulate three triaxial compaction tests on crushed salt. The relevant equations and description of the model are provided in Section 5.2.2 of this report.

To begin, we note that unlike the other organizations involved in the modelling efforts, these results have not been optimized in any way to match the experimental data. It is clear that our results differ substantially from the test data and simply serve as a starting point from which an improved calibration of the model to the data would begin.

In this section, we describe the crushed salt tests, how the model parameters were chosen, how our numerical modelling was performed, and a comparison of the model predictions to the experimental data. Further comparison of our results and the other models results to the experimental data can be found in Section 5.4.2.

Brief overview of crushed salt tests

Two tests were performed on crushed salt from the Asse mine (Speisesalz) and the third test was performed on a synthetic mixture of crushed salts from the Sondershausen mine (Staßfurt-sequence in a bedded Zechstein salt formation). Further details on the Sondershausen synthetic mixture can be found in Section 4.2.1 and Fig. 4.3. Hereafter, we simply refer to these as Asse and Sondershausen salts. Each test was preceded by a pre-compaction phase to bring the initial sample porosity of 25 – 34 % to a porosity of approximately 16 – 17 % before the triaxial compaction phase commenced. The pre-compaction (VK) and triaxial compaction (TK) test pairs on the Asse salt were identified as VK-020/TK-031 and VK-022/TK-033. The Asse salt samples were pre-compacted in an oedometer. The third triaxial compaction test, TUC-V2, was performed the Sondershausen salt. For this case, instead of using an oedometer during the pre-compaction phase, the sample was subjected to a lateral confining stress while keeping the sample from deforming axially. This can be considered to be a case of plane strain loading. The specific details of the VK-031 and VK-033 tests are described in Section 4.6.1.2 and in Section 4.5.1 for the TUC-V2.

Material Parameter for the WIPP Crushed Salt model of Callahan

As described in Section 5.2.2, the WIPP Crushed Salt model developed by Callahan /CAL 99/ is built upon the Munson-Dawson (MD) model for dislocation induced creep of intact salt. To account for the compaction behaviour of a porous granular salt, a modified equivalent stress definition and a non-associative flow potential were introduced. The flow potential differs from the equivalent stress as long as the fractional density is less than one and defines the relative magnitude of the creep strain rate components at a given fractional density, mean stress, and equivalent stress state. An additional strain

rate term accounting for creep due to grain boundary diffusional pressure solution has been incorporated if the crushed salt is wet. According to the model formulation, as the crushed salt is consolidated, the fractional density approaches a value of one and the crushed salt behaviour evolves to that of intact salt with isochoric inelastic response.

Intact salt parameters

As part of Sandia National Laboratories (SNL) past involvement in Joint Project III /HAM 16/, the Rapid City, South Dakota, office of RESPEC was tasked with determining intact salt parameters for the MD model from laboratory testing of intact salt samples from the Asse and Sondershausen salt mines. The parameterized MD model was then used as part of a benchmarking study to evaluate the various constitutive models and computational capabilities of the Joint Project III partners /HAM 13/ /HAM 16/. The methods used and results of the MD model parameterization were documented in /DEV 11/, which can be found in Appendix C of /ARG 12/. We briefly describe the tests upon which the model was calibrated for the each of the salt types below. Unfortunately, /DEV 11/ did not specify the stress measure or strain measure used while calibrating the MD model, so the following presentation of his calibrations will simply refer to a generic "stress" $\boldsymbol{\sigma}$ and "strain" $\boldsymbol{\varepsilon}$. Even so, by using the /DEV 11/ calibrations without modification in /SIE 20/, we have implicitly assumed $\boldsymbol{\sigma}$ is the Cauchy (true) stress and $\boldsymbol{\varepsilon}$ is the logarithmic (true) strain.

Asse und Sondershausen intact salt parameterisation

The procedure used to determine the MD model parameters consisted of fitting the individual long-term creep tests and then refining the parameters to provide minimized sum-of-squares error between the measured and predicted responses to the ensemble of creep tests. Due to the limited number of tests available for analysis, some of the parameters could not be directly determined and were chosen to be the same as previously determined for Waste Isolation Pilot Plant (WIPP) salt by /MUN 89/. Note that the low stress mechanism, which is a recent addition to the MD model, was not used in this work.

<u>Asse Salt</u>

Six tests were used to determine the model parameters for intact Asse salt. Two types of creep tests were performed:

- Single stage: the axial stress σ_a and radial confining stress σ_c were held constant and
- Multi-stage: the axial stress was increased or decreased at predetermined times while the radial confining stress was held constant

The test durations varied from 20 days to over 1,000 days. The tests on Asse salt were performed at several different temperatures, but, for each individual test, the temperature T was held constant with respect to time t. Details of the tests are given in Tab. 5.7. The stress difference σ_{eff} is defined as $\sigma_{eff} = \sigma_a - \sigma_c$ the difference between the axial and radial confining stress. /DEV 11/ stated that the axial strain ε_a reported in Fig. 5.40 is the total strain minus the elastic strain. (Presumably, /DEV 11/ also subtracted the thermal strain due to raising the temperature.)

The comparison of the ε_a history from the model and the experimental data on Asse salt are generally good (Fig. 5.40), however, the model under predicts the experimental ε_a for Test #94097 data. Test #4138 and #4139 are examples of multistage tests. Note that the σ_{eff} levels are indicated in the titles for each of the test cases, and the change in the axial strain rate $\dot{\varepsilon}_a$, due to the change in σ_{eff}, is clearly identifiable in the multi-stage tests.

Sondershausen Salt

For the Sondershausen salt, four two-stage tests were used to determine the model parameters. Details of these tests are given in Tab. 5.8. These tests were performed for a duration of approximately 200 days, with the first stage being approximately 55 days in length. Again, the confining stress was held constant, but was different for each test. During stage 1, $\sigma_{eff} = 16$ MPa for all tests, while the stress difference for the second stage was different for each test. These tests were all performed at $T = 22$°C. As before, the axial strain ε_a reported in Fig. 5.8 is the total strain minus the elastic strain.

The model reasonably captures the experimental data in Fig. 5.8. During the first stage, all samples experienced the same stress difference, so the variation in the axial strain measurements is due to sample-to-sample variation and the model produces the same axial strain versus time behaviour for every sample. During the second stage loading, the typical behaviour of increased axial strain with increasing stress difference is observed. Except for test 210-04, which has the largest second stage applied stress difference, the model consistently under predicts the axial strain magnitude at later times.

Tab. 5.7 Single and multi-stage creep tests on Asse salt /DEV 11/

Test #	T [°C]	σ_{eff} [MPa]	σ_c [MPa]
04141	30	11	0
95015	22	14.1	0
04139	30	14/16	20
94097	27	20	25
04138	50	20/15/20/18/20	20
95008	30	37.2	15

Tab. 5.8 Two stage creep tests on Sondershausen salt /DEV 11/

Test #	Stage 1,2 σ_{eff} [MPa]	σ_c [MPa]
210-01	16, 19	0.5
210-02	16, 22	2.5
210-03	16, 25	5.0
210-04	16, 28	10.0

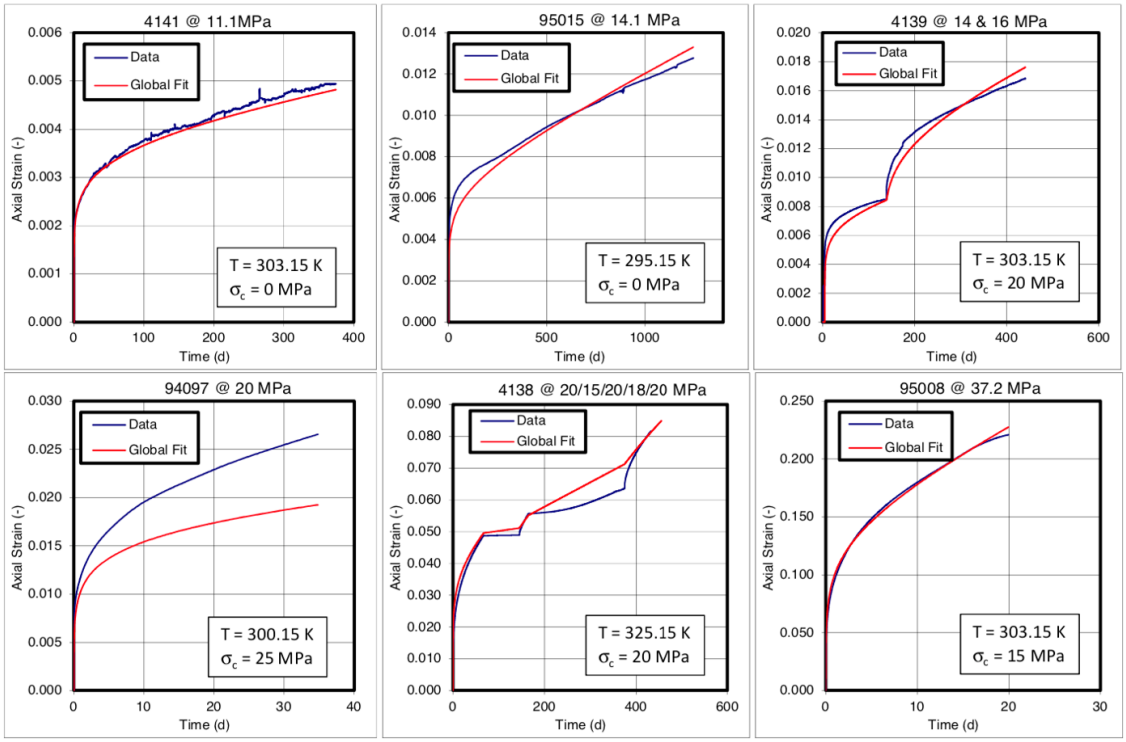

Fig. 5.40 Comparison of MD model fit and data for intact Asse salt /DEV 11/

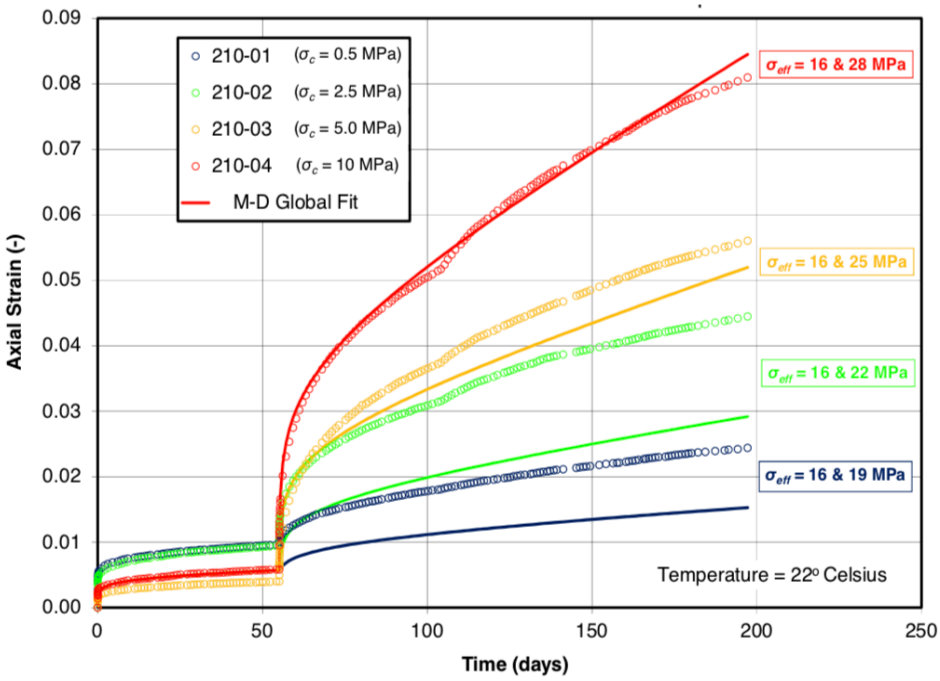

Fig. 5.41 Comparison of MD model fit and data for intact Sondershausen salt /DEV 11/

Tab. 5.9 summarizes the parameter values for the intact salt portion for the WIPP Crushed Salt model for the Asse and Sondershausen salts. Also included are the shear and bulk modulus parameters G_0, G_1, K_0 and K_1 which result in values for Young's Modulus and Poisson's ratio of 2.5×10^{10} Pa and 0.25, respectively, at an intact density of 2170 kg/m^3, as reported in /DEV 11/ and /Lux 07/.

Tab. 5.9 Model parameters for intact salt /DEV 11/

Parameter	Asse	Sondershausen	Units
ρ_{int}	2170	2160	kg/m^3
G_0	1.06×10^4	1.06×10^4	Pa
G_1	6.53×10^{-3}	6.53×10^{-3}	Pa/kg
K_0	1.76×10^4	1.76×10^4	Pa
K_1	6.53×10^{-3}	6.53×10^{-3}	Pa/kg
μ	9.85×10^9	9.85×10^9	Pa
A_0	0.0	0.0	s^{-1}
A_1	5.741×10^{21}	3.02×10^{21}	s^{-1}
A_2	2.353×10^{11}	3.48×10^{11}	s^{-1}
B_0	0.0	0.0	s^{-1}
B_1	1.180×10^5	2.23×10^9	s^{-1}
B_2	5.881×10^{-4}	9.89×10^{-4}	s^{-1}
Q_0 / R	0.0	0.0	K
Q_1 / R	12,589	12,589	K
Q_2 / R	5035.5	5035.5	K
η_0	0.0	0.0	-
η_1	5.5	5.5	-
η_2	5.0	5.0	-
q	4450	1500	-
σ_0	20.57×10^6	20.57×10^6	Pa
m_0	0.0	0.0	-
m_1	3.0	3.49	-
K_0	0.0	0.0	-
K_1	925	2.48×10^6	-
c_0	0.0	0.0	K^{-1}
c_1	2.706×10^{-2}	9.198×10^{-3}	K^{-1}
α_h	-12.93	-10.88	-
β_h	-8.518	-7.738	-
α_t	0.58	0.58	-
β_t	0.0	0.0	-

Crushed salt parametrization

There are 20 model parameters beyond those listed in Tab. 5.9 that specify the behaviour of crushed salt. Four parameters (κ_0, κ_1, n and D_t) describe the flow potential, while three parameters (η_0, η_1 and n_f) describe the equivalent stress σ_{eq}^{f}. The grain boundary diffusional pressure solution model has one parameter for the moisture dependence a, one for the grain size dependence ρ, and one for the temperature dependence Q_s / R. Four parameters (n_s, r_1, r_3 and r_4) define the pressure solution portion of the model. Two variables specify the emplaced crushed salt density ρ_* or porosity ϕ_*. Two variables specify the approximate fractional density for random dense packing of single size spheres D_0 and associated porosity ϕ_0. Note that the pair ρ_* and ϕ_* are related by $\phi_* = 1 - {\rho_*}/{\rho_{\text{int}}}$ where ρ_{int} is the density of the intact salt and the pair D_0 and ϕ_0 are related by $\phi_0 = 1 - D_0$. The moisture content w and the grain size d of crushed salt being tested complete the model parameterization.

According to /CAL 99/, these fourteen parameters were determined for WIPP salt by minimizing the weighted squared difference between the experimentally measured and model calculated strains. Similar to /DEV 11/, /CAL 99/ did not specify which stress and strain measures he used to calibrate the model, so we again assume he utilized Cauchy stress σ and logarithmic strain ε. The four flow potential parameters were determined by fitting the radial-to-axial strain rate ratio $\dot{\varepsilon}_r/\dot{\varepsilon}_a$ to measurements from 18 shear consolidation tests. These parameters are given in Tab. 5.10. While holding these 4 parameters fixed, the remaining 10 parameters, which define creep consolidation in the model, were determined by fitting the model to the experimental ε_a and ε_r data. /CAL 99/ performed two calibrations. The first used data from 18 shear consolidation tests, while the second expanded the data base to combine the 18 shear consolidation tests with 40 hydrostatic consolidation tests. For this work, we used the parameterization based on the 18 shear consolidation tests, which is shown in Tab. 5.11. This choice was somewhat arbitrary, but /CAL 99/ noted only minor differences between model responses for the two different calibrations, even though the parameter sets appear quite different.

The values used in the KOMPASS modelling were taken directly from /CAL 99/ and are listed in Tab. 5.10 and Tab. 5.11. We note that the same values are used for both salt types in this modelling work. In the future, the degree to which these parameters depend on salt type could be investigated.

Several Callahan model parameters, such as emplaced porosity, were chosen to match measurements prior to the pre-compaction and compaction tests. These test specific parameters are provided in Tab. 5.12. The value of D_0, defined as the approximate fractional density for random dense packing of single size spheres, was assumed to be 0.64 for all modelling. The corresponding porosity $\phi_0 = 1 - D_0$ is 0.36 or 36 %. The emplaced density for both VK-020 and VK-022 was ρ_* = 1432 kg/m^3. Given the intact density of Asse salt in Tab. 5.10, this corresponds to an emplaced porosity of $\phi_* = 34$ %. The water content for both of these tests was $w = 0.05$ % and the maximum salt grain diameter was $d = 8$ mm. The emplaced density for the pre-compaction phase of TUC-V2 was ρ_* = 1618 kg/m^3 and for the triaxial compaction phase was ρ_* = 1799 kg/m^3. Given the intact density of Sondershausen salt in Tab. 5.10, these emplaced correspond to emplaced porosities of $\phi_* = 25.1$ % and 16.7 %. The water content was taken to be w =0.5 %. The grain diameter, d = 10 mm, used in the model was assumed to be the largest grain size in the crushed salt sample.

The model uses both the water content and grain diameter as parameters in the pressure solution term. We chose to use the maximum value of grain diameter in our simulations though perhaps a better choice would be the mean or median grain size. We note that /CAL 99/ tabulated data for numerous tests on crushed salt and gives mean grain size each sample. The material parameter p, which appears as the exponent on the grain size parameter d in the kinetic equation for grain boundary diffusional pressure solution, was probably optimized using the mean value of grain size. The effect of this choice will be discussed when we compare our model results with the experimental data, but, for now, it is worth mentioning that smaller grain sizes lead to higher creep rates when the pressure solution term is active.

Tab. 5.10 Assumed flow potential parameters – Asse und Sondershausen salts

Parameter	Value	Units
κ_0	10.119	-
κ_1	1.005	-
n	1.331	-
D_t	0.896	-
Values taken from /CAL 99/ based on testing of WIPP salt		

Tab. 5.11 Assumed creep consolidation parameters – Asse and Sondershausen salts

Parameter	Value	Units
η_0	0.1029	-
η_1	3.9387	-
η_f	3.5122	-
a	0.3147	-
P	1.6332	-
n_s	0.5576	-
r_1	1.041×10^{-12}	$(m^p\text{-K})/(\text{Pa-s})$
r_3	15.1281	-
r_4	0.1678	-
Q_s / R	1077.46	K
Values taken from on /CAL 99/ based on shear consolidation tests on WIPP Salt		

Tab. 5.12 Test specific crushed salt model parameters

Parameter	VK-020 and VK-022 Value	TUC-V2 Value	Units
ρ_*	1432	1618 / 1799	kg/m^3
ϕ_*	0.34	0.251 / 0.167	-
D_0	0.64	0.64	-
ϕ_0	0.36	0.36	-
w	0.0005	0.005	-
d	0.008	0.01	m
Note: The two values of emplaced density ρ_* and porosity ϕ_* for TUC-V2 correspond to the pre-compaction and triaxial compaction test phases respectively.			

Numerical simulation of pre-compaction and triaxial compaction tests

The specifics of how the actual laboratory tests were performed are described in Sections 4.6.1 and 4.8.2.2. In this section, we describe how the tests were modelled.

Asse Salt Tests: VK-020 / TK-031 and VK-022 / TK-033

The WIPP Crushed Salt Model has a hardening variable, the transient strain ζ, which evolves during the pre-compaction phase so it will be non-zero when the triaxial compaction begins. Our preliminary simulations of TK-031 did not include the pre-compaction phase (VK-020) and simply assumed $\zeta = 0$ at the start of compaction. As will be shown below, these preliminary simulations over-predicted the porosity reduction at the start of the compaction phase. Our GRS colleagues fortunately observed this issue in their own simulations and suggested we simulate the pre-compaction in order to estimate the degree of hardening present at the start of the triaxial compaction phase. As suggested, we simulated the Asse salt pre-compaction and compaction phases in a single simulation, unless otherwise stated.

The process of generating crushed salt may also impart hardening upon the crushed salt grains, such that ζ may actually be non-zero prior to pre-compaction as well. To estimate the crush induced hardening, it may be useful to compare the pre-compaction response of annealed and non-annealed crushed salt. In the absence of such tests, we elected to simply assume $\zeta = 0$ prior to pre-compaction herein.

Each test sample was modelled using the 3-D finite element discretization of a cylinder similar to the one shown in Fig. 5.42. (See below for further discussion of numerical method and settings.) For the sake of efficiency, only ¼ of the cylinder was modelled. A rigid platen, though not necessary for this work, was included so that prescribed displacements during pre-compaction and applied axial loads during triaxial compaction could be applied to the top of the sample. The following boundary conditions were specified on the two symmetry planes

- No z-component of displacement on the front side plane of the sample
- No x-displacement on the left side plane of the sample

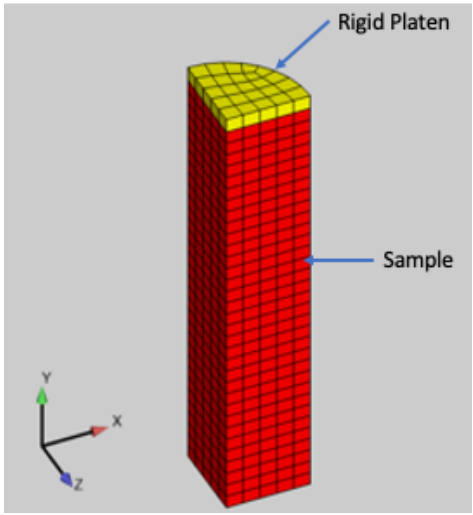

Fig. 5.42 Finite element mesh

The loading platen nodes were only allowed to move in the *y*-direction with no *x* or *z* component of displacement. This prevents any rotation of the platen-sample interface. Since the nodes on the bottom of the platen and top of the sample are the same, the same displacement constraint applies to the top of the sample. The nodes on the bottom surface of the sample were specified as no displacement in all directions. Under these conditions, the radius of the sample at the top and bottom does not change even during triaxial compaction loading, but the radius of the sample can change at other locations along the height of the model. A simpler model would be to assume frictionless contact at the platen-sample and sample-based interface. If side wall friction during the oedometric loading is ignored in this case, then the test could be modelled using a single finite element or a material point driver code, eliminating the need for a finite element code.

During the pre-compaction stage, the downward displacement (*y*-component) of the top of the platen was prescribed. To simulate the uniaxial strain loading conditions of no radial strain in the oedometer, zero displacement boundary conditions in the x and z directions on the sample's faceted cylindrical surface were enforced.

Compacting crushed salt in an oedometer produces friction forces on the exterior surface of the sample that will lead to non-homogenous states of stress and strain throughout the specimen. In the pre-compaction stage for these laboratory tests, the samples were first compressed for a period of time and then removed from the oedometer and rotated 180 degrees, reinstalled into the oedometer, and further compressed to the final target porosity. To simplify the numerical simulations, wall friction between the oedometer wall

and sample was neglected; therefore, there was no need to include the walls of the oedometer in the finite element model and the sample rotation. The total laboratory measured axial stress at the top of the sample during pre-compaction was 29 – 30 MPa, but the axial stress was not measured at the bottom of the sample; therefore, determination of the frictional contribution to the total stress was not possible.

We note a few additional details of our modelling approach of the pre-compaction stage in relation to the actual tests, which are described in Section 4.6.1.2 of this report. The height and diameter of the finite element model of the cylindrical sample was specified to be the same as the sample in the pre-compaction experiments. For VK-020 the height was 249 mm and for VK-022 the height was 244.41 mm. The modelled radius for both tests was $r_0 = 50$ mm.

A constant axial displacement rate was used to model the pre-compaction stage for each simulated test. The rate was chosen to bring the sample from the emplaced porosity at the start of the pre-compaction test to the porosity at the start of the triaxial compaction test. This assumption of constant displacement rate was true for test VK-020, which used 0.136 mm/hr for 16 days but not for test VK-022. VK-022 was loaded for a total of 33 days and used 3 different displacement rates over 3 different time periods: 0.088 mm/hr (0-12 days), 0.061 mm/hr (12-26 days) and 0.029 mm/hr (26-33 days). The constant displacement rate used in our simulation of VK-022 was the weighted average of the three different rates used in the test: 0.064 mm/hr.

Several changes were made between the pre-compaction and compaction phases. The temperature was raised to 50°C in TK-031 and to 49.5°C in TK-033. The lateral constraints on the exterior surface of the sample were replaced with a prescribed pressure boundary condition to represent the radial confining (Cauchy) stress σ_c. An axial load F was applied to the top of the rigid platen, such that the sample experienced an axial engineering (technical) stress of $\tilde{\sigma}_a = F/A_0$, where $A_0 = \pi\, r_0^2$ is the sample cross-sectional area at the start of the compaction phase.

As shown in Fig. 5.43 and Fig. 5.44, the axial and confining stresses were increased in a stepwise manner, with ramps in between each step, for both TK-031 and TK-033. The simulated and experimentally measured stresses are both plotted in order to verify that the boundary conditions were correctly applied. The simulated confining stress σ_c was taken as the xx-component of stress σ_{xx} from the element closest to the z = 0 plane at the outer edge and mid-height of the model. During TK-031, three power outages caused the three short periods of unloading and reloading shown in Fig. 5.43 and Fig. 5.44. Although they probably were not very important, these unloading and reloading periods were included in the TK-031 simulations. For those who wish to recreate the TK-031 and TK-033 simulations, the values of $\tilde{\sigma}_a$ and σ_c versus time t are listed in Tab. 5.13 and

Tab. 5.14.

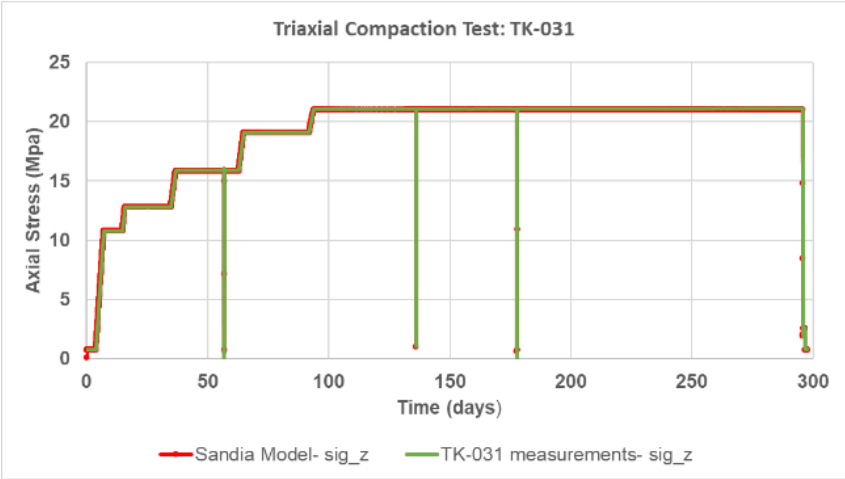

a) Axial stress $\tilde{\sigma}_a$ histories

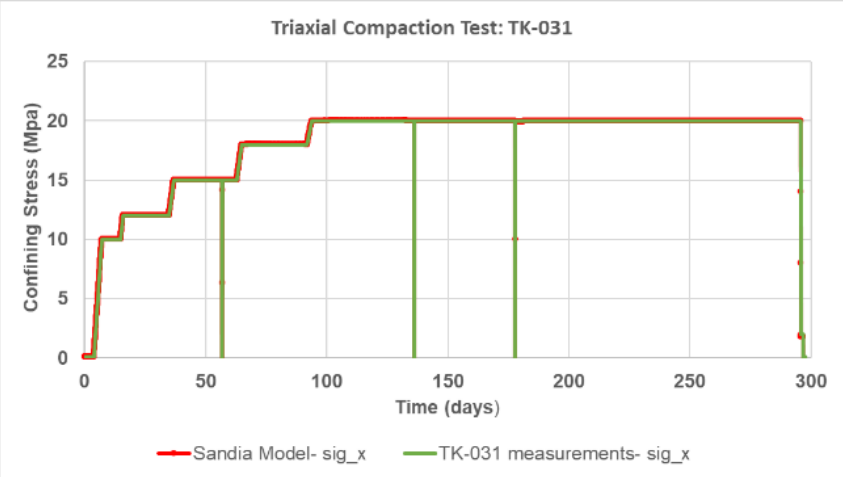

b) Confining stress σ_c histories

Fig. 5.43 Stress histories used in simulations of triaxial compaction test TK-031

Tab. 5.13 Loading history for TK-031

Load step	t [d]	$\tilde{\sigma}_a$ [MPa]	σ_c [MPa]	Load step	t [d]	$\tilde{\sigma}_a$ [MPa]	σ_c [MPa]
0	0.0000	0.77	0.10	5 (continued)	136.0951	7.40	6.33
	2.7410	0.77	0.10		136.1028	21.08	19.99
	2.8333	0.77	0.10		136.1042	21.08	20.00
	3.1667	0.77	0.10		136.1076	21.08	19.99
	3.8230	0.77	0.10		136.1111	21.08	19.99
	3.8333	0.77	0.10		136.1146	21.08	19.99
1	7.0833	10.78	10.00		136.1181	21.08	19.99
	14.7931	10.79	10.00		136.7500	21.08	19.99
	14.8278	10.79	10.00		136.7769	21.08	19.99
	14.8333	10.79	10.00		137.6667	21.08	19.99
2	15.8333	12.79	12.00		160.8333	21.09	19.99
	25.0000	12.79	12.00		177.7500	21.09	20.00
	32.0000	12.79	12.00		177.7639	12.03	11.21
	34.8333	12.79	12.00		177.7708	7.49	6.81
	36.8333	15.88	15.00		177.7847	0.68	0.03
	38.8104	15.88	15.00		177.7850	0.68	0.03
	56.7236	15.88	15.00		177.8319	0.74	0.12
	56.7340	16.02	10.00		177.8326	0.80	0.20

3	56.7353	0.01	0.19		177.8333	0.80	0.20
	56.7403	0.01	0.05		177.8336	0.81	0.21
	56.7486	0.78	0.04		177.8611	7.51	6.74
	56.7493	0.78	0.05		177.9167	21.02	19.93
	56.7521	0.79	0.10		200.0000	21.09	19.99
	56.7569	0.79	0.10		226.0000	21.10	19.99
	56.7604	1.42	0.71		226.0833	21.10	19.99
	56.8403	15.88	14.99		226.1667	21.10	19.99
	59.8625	15.89	15.00		227.5833	21.10	19.99
	59.8646	15.89	15.00		229.7500	21.10	19.99
	62.8333	15.89	15.00		229.8333	21.10	19.99
4	62.8750	15.95	15.06		246.7028	21.10	19.99
	64.8333	19.08	17.99		278.9167	21.10	20.00
	90.8354	19.09	18.00		279.0000	21.10	20.00
	91.8333	19.09	17.99		280.9847	21.10	20.00
5	91.8750	19.13	18.04		284.6667	21.11	19.99
	93.8264	21.07	19.99		284.7500	21.11	19.99
	132.0000	21.08	19.99		295.7500	21.11	19.99
	136.0708	21.08	19.99		295.7569	20.15	19.10
	136.0764	10.44	9.34		295.8764	1.89	2.00
	136.0778	7.77	6.68		296.0528	2.03	2.00
	136.0812	1.10	0.03		296.0556	2.59	2.00
	136.0819	1.08	0.00		296.7194	2.59	2.00
	136.0833	1.08	0.00		296.8403	2.59	2.00
	136.0868	1.07	0.00		296.8444	0.81	0.10
	136.0917	1.11	0.03		296.8493	0.81	0.10
	136.0924	2.07	0.99		297.7500	0.81	0.10

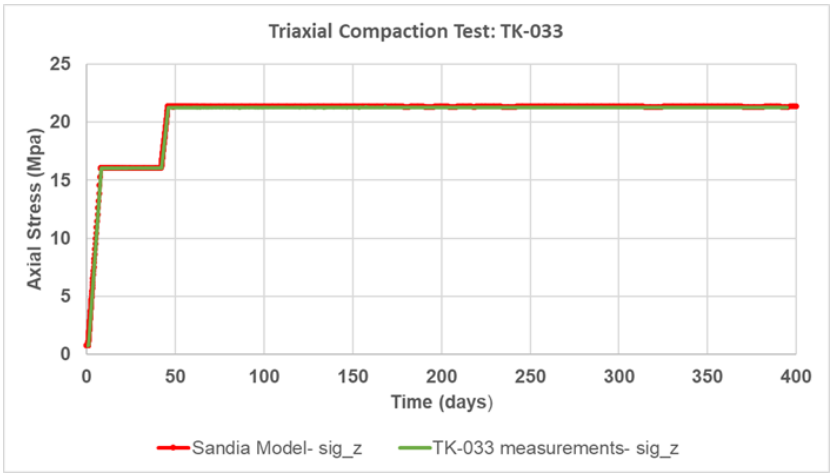

a) Axial stress $\tilde{\sigma}_a$ histories

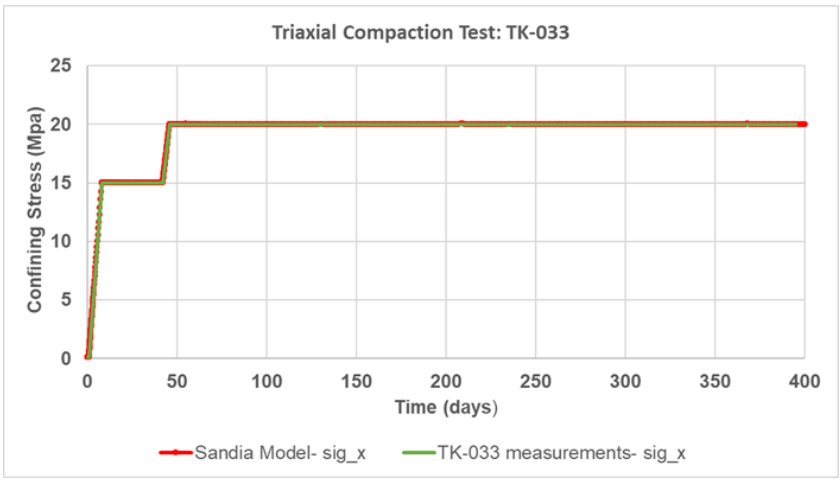

b) Confining stress σ_c histories

Fig. 5.44 Stress histories used in simulations of triaxial compaction test TK-033

Tab. 5.14 Loading history for TK-033

Load step	t [d]	$\tilde{\sigma}_a$ [MPa]	σ_c [MPa]
0	0.00	0.78	0.10
	0.96	0.78	0.10
	8.13	16.00	15.00
1	8.13	16.00	15.00
	42.13	16.00	15.00
2	45.87	21.30	20.00

	45.88	21.30	20.00
	400.00	21.30	20.00

Sondershausen Salt Test: TUC-V2

In contrast to the pre-compaction tests VK-020 and VK-022, the pre-compaction of TUC-V2 did not use an oedometer. Instead, the laboratory sample was subjected to plane strain conditions as described in Section 4.5.1. In this case, axial deformation of the sample was prevented while a constant radial confining stress of $\sigma_c = 5$ MPa was applied. The pre-compaction test lasted for a period of 2 days. After pre-compaction, the hourglass shaped test specimen was trimmed down using a lathe to a form a cylindrical test specimen of radius $r_0 = 45.05$ mm and height $h_0 = 180$ mm.

The TUC-V2 pre-compaction simulation was set up in a simple manner. The sample radius at the start of loading was 60 mm and the height was 186 mm. All components of displacement at the platen and the sample bottom were prescribed to be zero. The test confining pressure of $\sigma_c = 5$ MPa was prescribed on the outer surface of the meshed cylinder.

Attempts were made to model pre-compaction and compaction in a single simulation, but they were abandoned because we could not easily simulate the material removal by the lathe and, more importantly, the pre-compaction simulation did not sufficiently reduce the porosity. The emplaced porosity, prior to pre-compaction, was $\phi_* = 25.1$ %. After 2 days, the model predicted a volume averaged porosity of $\phi = 21.6$ %, yet the experimentally measured porosity was 16.7 %. In fact, our model parameterization indicates that it would take 33.7 days to reduce the volume averaged porosity from 25.1 % to 16.7 %. In order to simulate the triaxial compaction stage without the preceding pre-compaction phase, we simply started with a finite element discretization of the cylindrical sample with radius r_0, height h_0, a spatially uniform porosity of 16.7 %, and $\zeta = 0$. A secondary simulation also utilized a non-zero value of ζ, as will be discussed further in the results subsection.

The axial engineering stress $\tilde{\sigma}_a = F/A_0$ and confining Cauchy stress σ_c histories for the triaxial compression stage of TUC-V2 are plotted in Fig. 5.45. As before, the simulated and measured stress histories are both depicted in the plots, and the precise values of $\tilde{\sigma}_a$ and σ_c are listed in Tab. 5.15.

For this simulation, d was assumed to be 10 mm, although 8 mm may have been more appropriate for the maximum grain size, based on the discussion in Section 4.2.1. Using a grain size of 8 mm would have only slightly improved the model porosity results after 2 days.

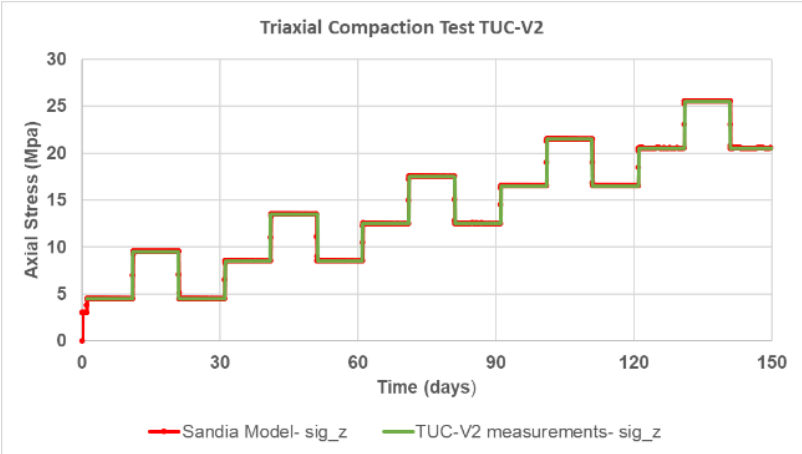

a) Axial stress $\tilde{\sigma}_a$ histories

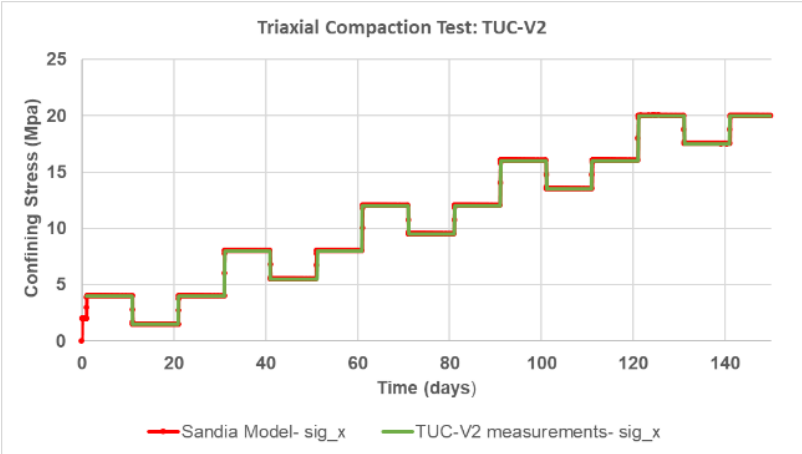

b) Confining stress σ_c histories

Fig. 5.45 Stress histories used in simulations of triaxial compaction test TUC-V2

Tab. 5.15 Loading history for TUC-V2

Load step	t [d]	$\tilde{\sigma}_a$ [MPa]	σ_c [MPa]
0	0	3	2
	1	3	2
1	1.1	4.5	4.0
	11.0	4.5	4.0
	11.1	9.5	1.5
	21.0	9.5	1.5
	21.1	4.5	4.0

	31.0	4.5	4.0
2	31.1	8.5	8.0
	41.0	8.5	8.0
	41.1	13.5	5.5
	51.0	13.5	5.5
	51.1	8.5	8.0
	61.0	8.5	8.0
3	61.1	12.5	12.0
	71.0	12.5	12.0
	71.1	17.5	9.5
	81.0	17.5	9.5
	81.1	12.5	12.0
	91.0	12.5	12.0
4	91.1	16.5	16.0
	101.0	16.5	16.0
	101.1	21.5	13.5
	111.0	21.5	13.5
	111.1	16.5	16.0
	121.0	16.5	16.0
5	121.1	20.5	20.0
	131.0	20.5	20.0
	131.1	25.5	17.5
	141.0	25.5	17.5
	141.1	20.5	20.0
	151.0	20.5	20

Numerical Method and Settings

For this work, the SNL developed code Sierra/Solid Mechanics /SIE 20/ was used. The domain was discretized using eight-node hexahedral finite elements with selective deviatoric integration. The sample had either 5 or 6 elements across the radius and 28 to 33 elements along the length, depending on the sample dimensions.

The equilibrium equations, without inertia terms, were solved iteratively at each time step using a non-linear pre-conditioned conjugate gradient technique. Solution convergence

was evaluated by monitoring the relative residual $\hat{R} = \|\boldsymbol{R}\|_2/\|\boldsymbol{F}\|_2$, where $\boldsymbol{R}$ is the discretized equilibrium residual vector, $\boldsymbol{F}$ is the boundary condition reaction force vector, and $\|*\|_2$ is the discretized L_2 norm of a quantity. A solution was considered converged when $\hat{R}$ was below 5 x 10^{-4}. Initial runs indicated that specifying a tighter relative residual tolerance of 1 x 10^{-5} did not change the results.

At the beginning of the pre-compaction phase, an initial time step of 1 x 10^{-4} s was used. Experience has shown that a small initial time step is often needed when the loose crushed salt is first being loaded. In our numerical simulations, the time step was allowed to increase by as much as 5 % for each subsequent step. During the triaxial compaction phase, an initial time step of 1,000 s was used during each step change in axial load. As before, the time step was allowed to increase by as much as 5 %.

While formal element size, residual tolerance, and time step convergence studies were not performed, we believe the quantities of interest are sufficiently close to converged values.

Post-processing of Simulation Results

Before continuing to the discussion of the comparison of our model results with the experimental data, we need to discuss how we obtained the relevant variables from the finite element results. Note, that the results are presented using the convention that compressive stresses and strains are positive. In the evaluation of model results, the mean stress σ_{m} and stress difference σ_{v} are of mixed character since the axial stress is evaluated as an engineering stress while the radial confining stress is a Cauchy stress.

- The mean stress was computed as $\sigma_{\mathrm{m}} = (\tilde{\sigma}_{\mathrm{a}} + 2\sigma_{\mathrm{c}})/3$
- The stress difference was calculated as $\sigma_{\mathrm{v}} = \tilde{\sigma}_{\mathrm{a}} - \sigma_{\mathrm{c}}$
- The axial strain was computed as $\varepsilon_{\mathrm{a}} = \frac{h_0 - h}{h_0}$, where h_0 is the height of the sample at the beginning of the triaxial compaction test and h is the height at time t.
- The average radial strain was calculated as $\varepsilon_{\mathrm{r}} = \frac{d_0 - d}{d_0}$ with $d = \sqrt{\frac{4\,V}{\pi\,h}}$, V is the volume. V is computed by summing up all the salt element volumes in the finite element mesh, which will be slightly less than the volume of a true cylinder due to the faceting of the cylindrical surface in the finite element model.

- Average volume strain was computed as $\varepsilon_{\mathrm{v}} = \frac{V_0 - V}{V_0}$ where V_0 is the total volume of the salt elements at the beginning of the triaxial compaction test.
- The volume averaged porosity ϕ was calculated using the total volume of solid material V_{s} and $V.$, $\phi = (V - V_{\mathrm{s}})/V$ with $V_{\mathrm{s}} = V_0\left(1 - \hat{\phi}\right)$. $\hat{\phi}$ is the porosity at the beginning of the triaxial compaction test. We assumed the solid volume of the salt was constant for all time.
- All rate quantities were approximated using finite difference expressions. For example, the volumetric strain rate $\dot{\varepsilon}_{\mathrm{v}}$ was approximated using $\dot{\varepsilon}_{\mathrm{v}} = \frac{\varepsilon_{\mathrm{v},i} - \varepsilon_{\mathrm{v},i-1}}{\Delta t}$, where Δt is the time increment and $\varepsilon_{\mathrm{v},i}$ is the volume strain at time increment i

Comparison of Model and Experimental Data

This section covers the results of the numerical model simulations applied to the three triaxial compaction tests: TK-031, TK-033, and TUC-V2. As noted earlier, the pre-compaction phase was included before the compaction phase in TK-031 and TK-033, but not in TUC-V2. It is also worth repeating that these model results have not been optimized in any way to match the experimental data. In most of the figures, the mean stress σ_{m} and the stress difference σ_{v} are plotted using the secondary *y*-axis of the figure to give an indication of the loading history.

Asse Salt Test- TK-031

In this test, the mean stress was increased, held constant for a period of time and then increased again. This pattern occurred five times. The mean stress increase was achieved by increasing both the axial stress and radial confining stresses while keeping the stress difference relatively low.

Fig. 5.46a, b and c compare the axial and radial strain predictions with the experimental measurements. Fig. 5.46a and b show that the model over predicts the axial strain recorded in the laboratory test for the entire time period while the predicted and experimental radial strain are closer. Fig. 5.46c plots the ratio of radial to axial strain $\varepsilon_{\mathrm{r}}/\varepsilon_{\mathrm{a}}$. While the model shows a near constant ratio of 0.7 for the entire test, the experimental data initially shows the radial strain to be significantly higher than the axial strain before levelling off at around 100 days. This result is unexpected given that the axial stress is always higher than the radial confining stress and the overall applied stress conditions are nearly isotropic.

The porosity histories are depicted in Fig. 5.46d. The predicted porosity reduction is greater than the measured values early in the experiment, when $\sigma_{\mathrm{m}} < 17$ MPa, but the predicted porosity reduction rate is smaller than the measured rate for $\sigma_{\mathrm{m}} > 17$ MPa later in the experiment. If the test had been carried out for a longer period, then it appears the predicted and measured curves would cross.

The impact of simulating the pre-compaction prior to compaction is shown in Fig. 5.47a. Including the hardening which occurs during pre-compaction reduces the initial porosity decrease that occurs when the triaxial compaction loads are first applied. The overall effect diminishes with time as the model porosity for the two cases are similar at the end.

Fig. 5.47a also shows the effect of top and bottom sample end constraint on the porosity. The simulations which allow the top and bottom surfaces of the sample to slip freely (frictionless) were performed with a single finite element. The frictionless simulations show slightly greater porosity reduction than the no slip simulations. From a practical standpoint it should be sufficient to do future simulations using the simpler and more efficient single-element model for laboratory and model comparisons.

One other aspect to consider is our use of $d = 8$ mm rather than some other perhaps more representative value. Choosing a smaller grain size increases the overall compaction predicted by the model. When 4 mm grain size is used, for example, the model predicts even greater porosity reduction, but does not significantly change the porosity reduction rate at the end of the test, as illustrated in Fig. 5.47b.

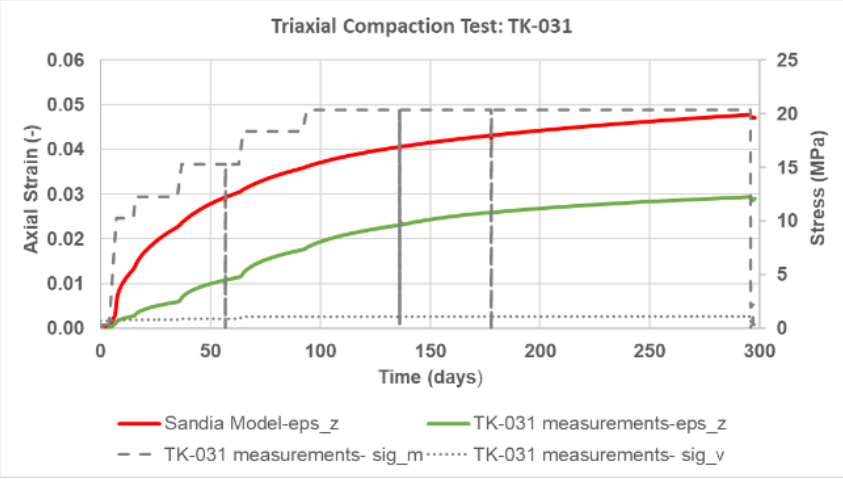

a) Axial strain histories

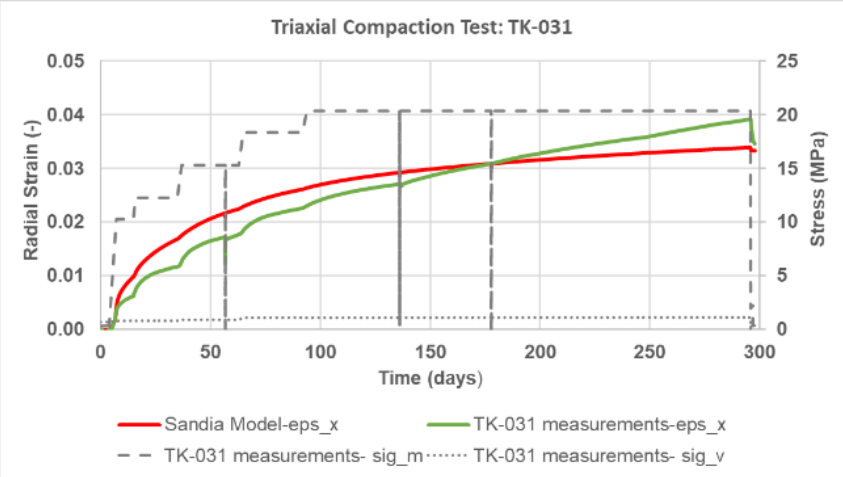

b) Radial strain histories

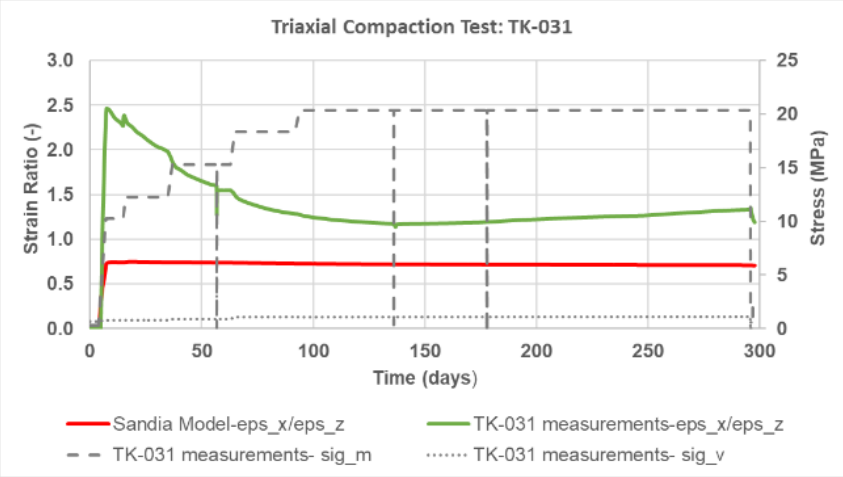

c) Strain ratio $\varepsilon_r/\varepsilon_a$ histories

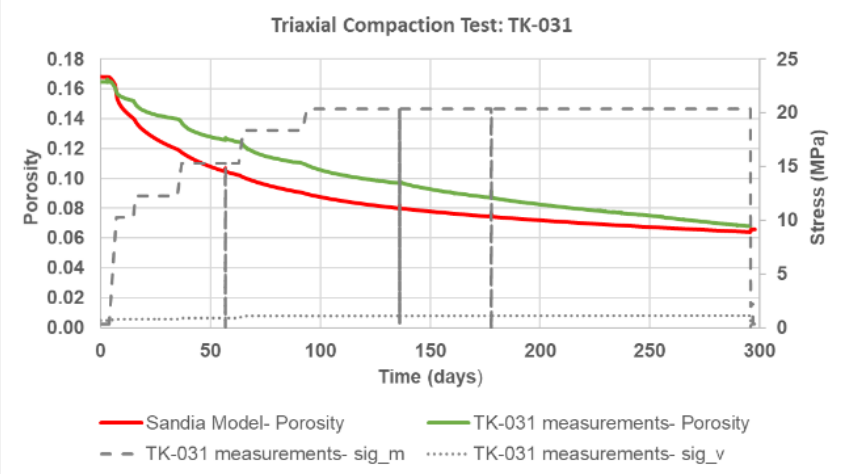

d) Porosity histories

Fig. 5.46 Comparison of predictions and measurements for TK-031

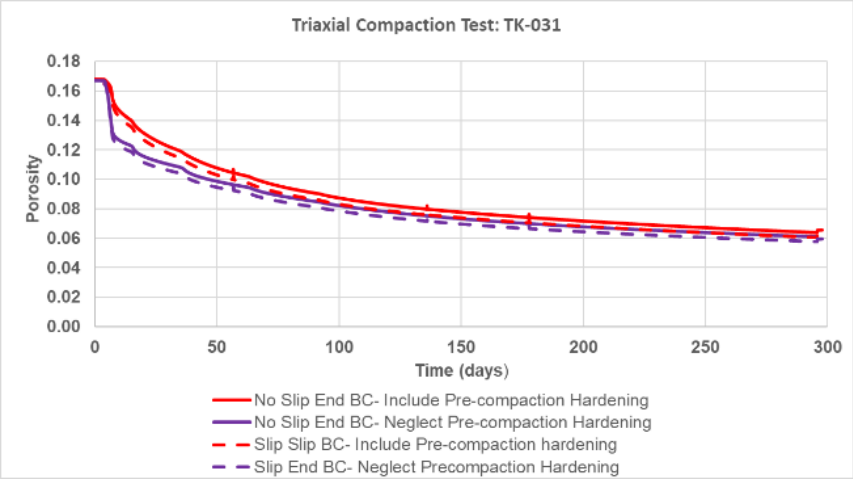

a) Effect of pre-compaction and sample end restraint

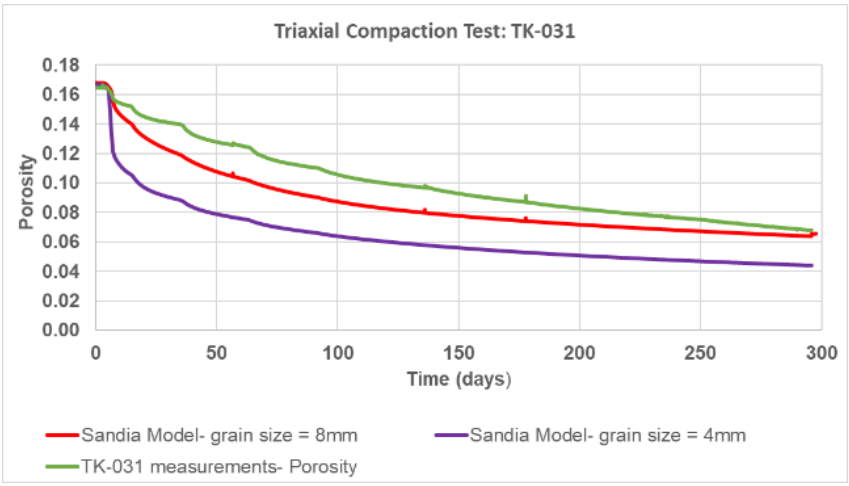

b) Effect of grain size

Fig. 5.47 Effect of various factors on porosity predictions for triaxial compaction test TK-031

Asse Salt Test- TK-033

In this test, only two loading stages were used, but as in TK-031, the axial stress and radial confining stress were both increased at the same time resulting in an increased mean stress while still keeping the stress difference small.

The axial and radial strains are compared against the measurements in Fig. 5.48a, b, and c. In contrast to the results described for test TK-031, the predicted and experimental axial strain histories for TK-033, shown in Fig. 5.48a, would be considered quite satisfactory. The model, however, under predicts the experimental radial strains, as shown in Fig. 5.48b. The main deviation in the radial strain histories occurs during the first 10 days of the first loading stage. In this case, the experimental radial strain is initially higher, but

the overall character of the model and experimental radial strain histories are quite similar. Fig. 5.48c compares the strain ratio. As in the TK-031 simulation results, the predicted TK-033 ratio is 0.7. In this case, however, the experimental strain ratio levels off to a value of 0.84, which is substantially closer to the predictions than in TK-031.

Fig. 5.48d compares the predicted and measured porosity. In this test, the model under predicts the decrease in porosity, which is expected, given the differences in the radial strain results. As in TK-031, if the test had been carried out for a longer period then it appears that the simulation and experimental curves would cross. In this case, the rate of porosity change in the model is higher at later times when compared to the experiment.

The impact of including the hardening during the pre-compaction stage is shown in Fig. 5.49a. The effect is the same as seen in TK-031: greater porosity decreases when pre-compaction hardening is ignored.

The effect of grain size on the predicted porosity is shown in Fig. 5.49b. Unlike TK-031, reducing the maximum grain size to d = 4 mm brings the predicted porosity closer to the test value at the end of the test. Similar to TK-031, however, reducing the maximum grain size does not improve the porosity reduction rate at the end of the test.

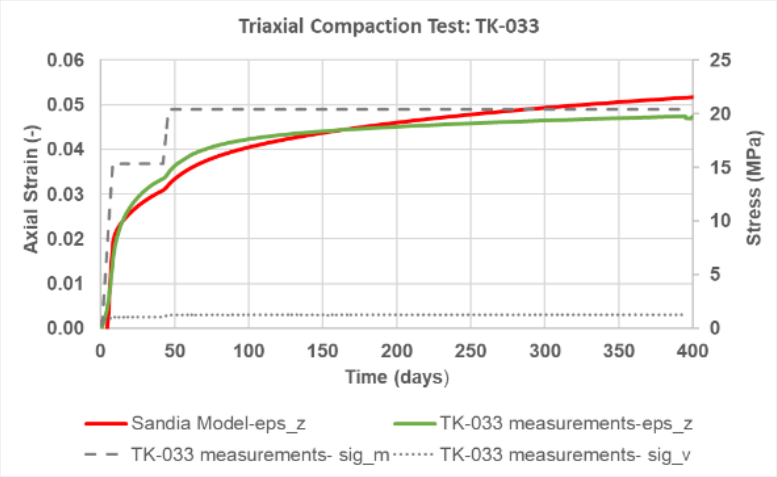

a) Axial strain histories

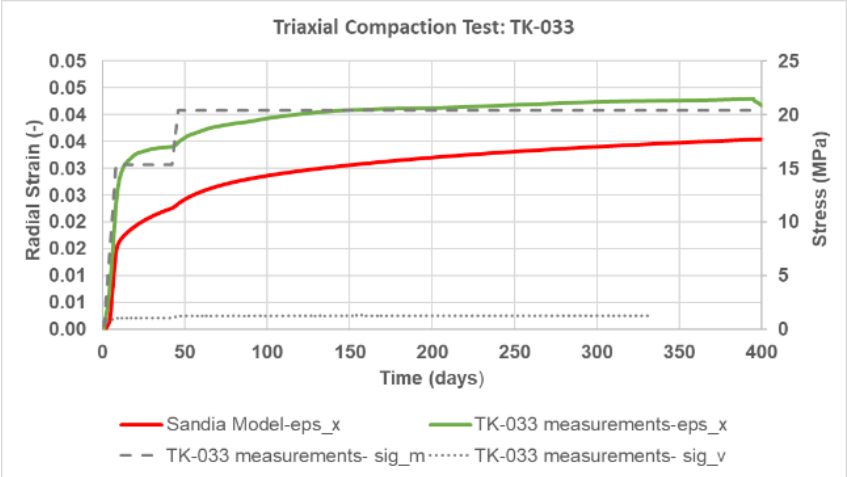

b) Radial strain histories

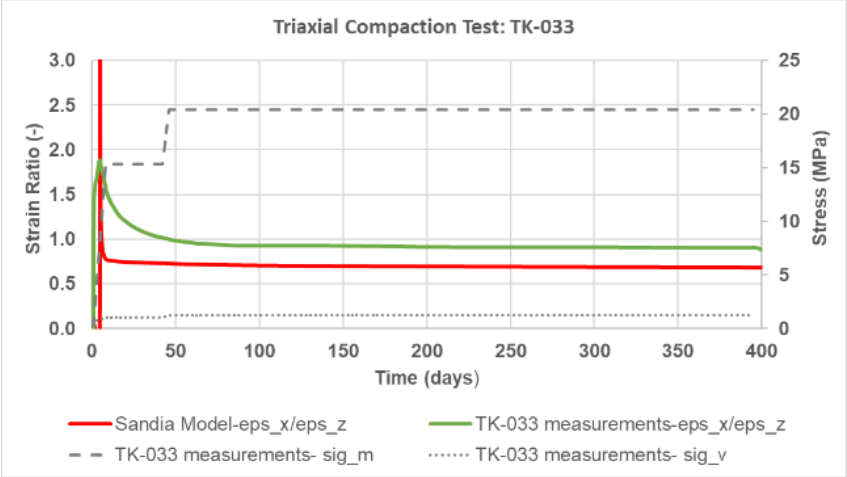

c) Strain ratio $\varepsilon_r/\varepsilon_a$ histories

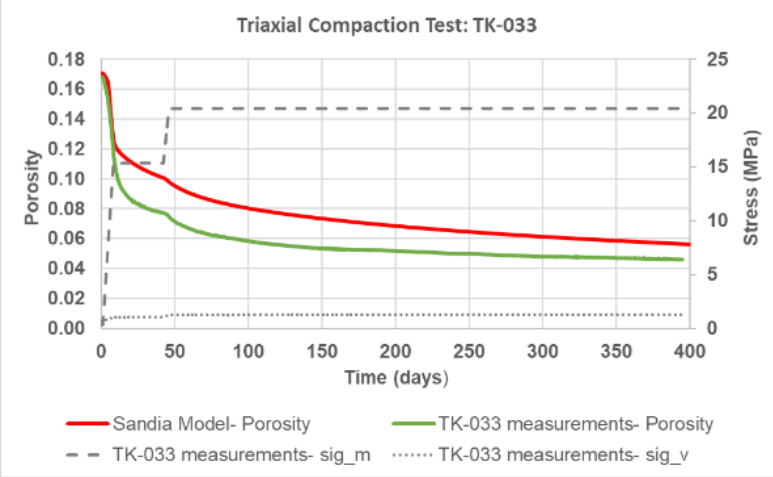

d) Porosity histories

Fig. 5.48 Comparison of predictions and measurements for TK-033

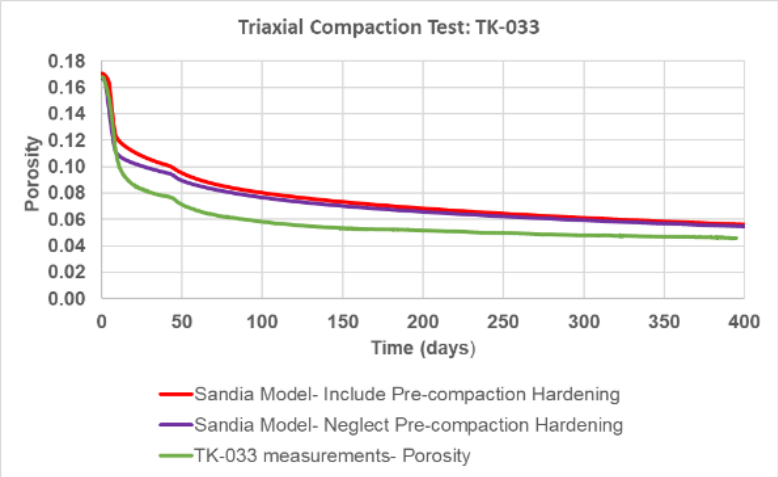

a) Effect of pre-compaction and sample end restraint

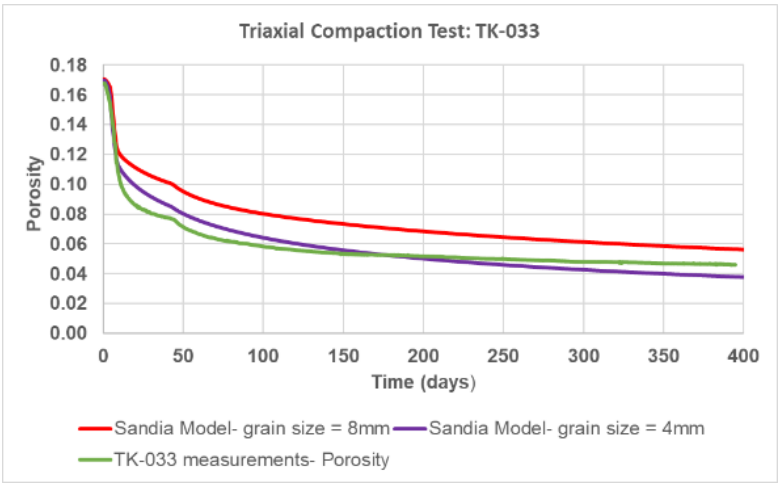

b) Effect of grain size

Fig. 5.49 Effect of various factors on porosity predictions for triaxial compaction test TK-033

Sondershausen Salt Test TUC-V2

The objective of this test was to determine the effect of deviatoric stresses on viscous volumetric deformations. The loading history is described in Section 4.8.2.2 as 5 load stages each lasting a period of 30 days. The mean stress was increased at each subsequent stage. Within each constant mean stress stage, the stress difference starts out approximately 0.5 MPa for 10 days, followed by a 10 day period at 8.0 MPa, and another 10 day period of 0.5 MPa. In contrast to the previous tests, where the stress difference was kept relatively low throughout the entire test, the stress difference in TUC-V2 alternates between 0.5 MPa and 8.0 MPa.

The predicted and experimental axial strain histories for TUC-V2 are shown in Fig. 5.50a. Overall, the predicted axial strains are somewhat larger than the measured over the 150 day time period. During periods when the mean stress is low, the model predicted substantially greater axial compaction than the test.

In Fig. 5.50b, the radial strains are compared. During the first 10 days, the radial strains from the test are very low even though the mean stress is 4.2 MPa. Presumably this is because the experimental sample was pre-compacted with a radial confining stress of 5 MPa before the triaxial compaction test commenced. In contrast, the model does predict radial compaction during the first 10 days of the TUC-V2 test. At 10 days, the axial stress increases and the confining stress decreases, resulting in a radial strain decrease, i.e. a radial expansion. The model qualitatively captures this decrease in radial strain, but grossly under predicts the magnitude. From a visual standpoint, the major difference between the predicted and measured radial strain occurs during the first 20 days.

Similarly, the discrepancy between the predicted and measured strain ratio in Fig. 5.50c is primarily due to the differences that developed in the first 20 days. In comparison to the Asse Salt tests, the model for the TUC-V2 test gives a strain ratio of approximately 0.3. The lower strain ratio could be due to differences in the two crushed salt types, the pre-compaction procedure, and/or the larger stress differences in TUC-V2.

Fig. 5.50d and e show the porosity and volumetric rate strain histories. The model predicts a greater decrease in porosity and therefore larger volumetric strain than seen in the experimental test data. Again, had we used a smaller maximum grain size than 10 mm, the model would have produced a greater porosity reduction. During the time periods where the stress difference is 0.5 MPa the model produces a volumetric strain rate significantly larger than recorded in the experiment. On the other hand, when the stress difference is raised to 8 MPa, at t =10, 40, 70, 100, and 130 days the measured and predicted volumetric strain rates are remarkably similar in magnitude until the stress difference is returned to 0.5 MPa 10 days later. The measurements and predictions both show increased volumetric strain rate when the mean stress is increased.

The impact of including hardening during the pre-compaction stage is shown in Fig. 5.51. In this secondary model of TUC-V2, the effect of pre-compaction was introduced by specifying the maximum value of the transient strain parameter ζ = 0.0248 as an initial condition. This value was extracted from the pre-compaction simulation at t = 33.7 days which was when the porosity was computed to be 0.167, the starting porosity of the TUC-

V2 test. The resulting trend is the same as seen in TK-031 and TK-033: slightly less porosity reduction when pre-compaction hardening is modelled.

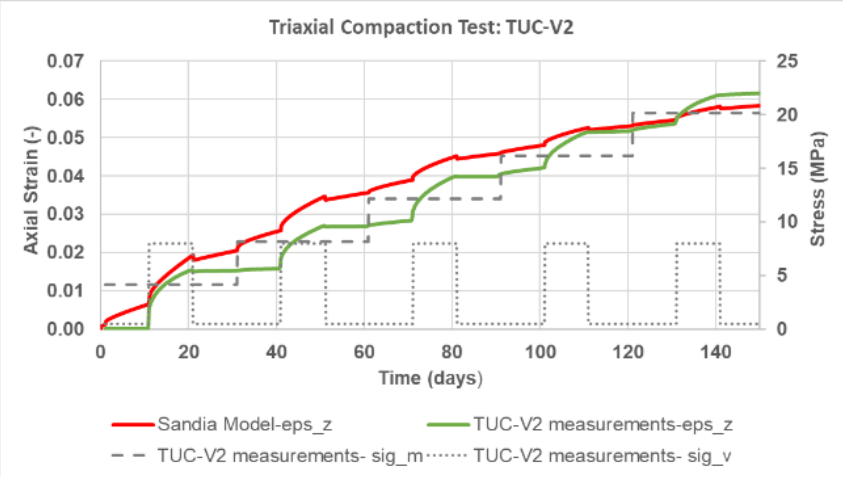

a) Axial strain histories

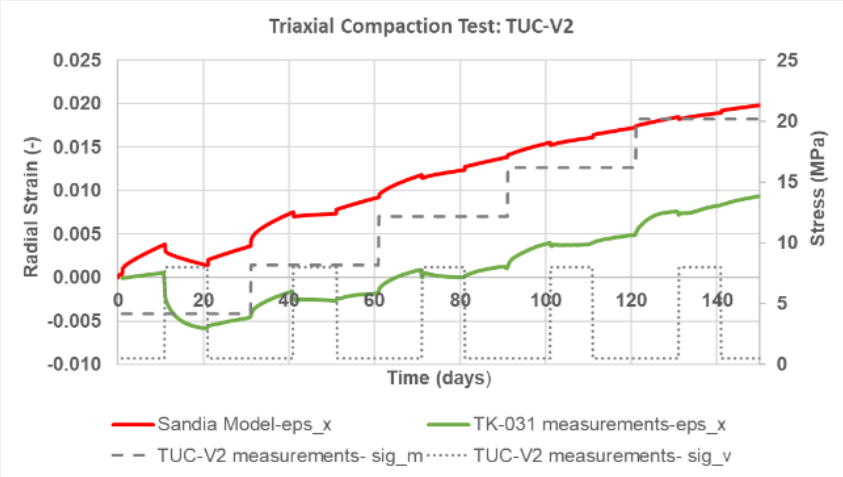

b) Radial strain history

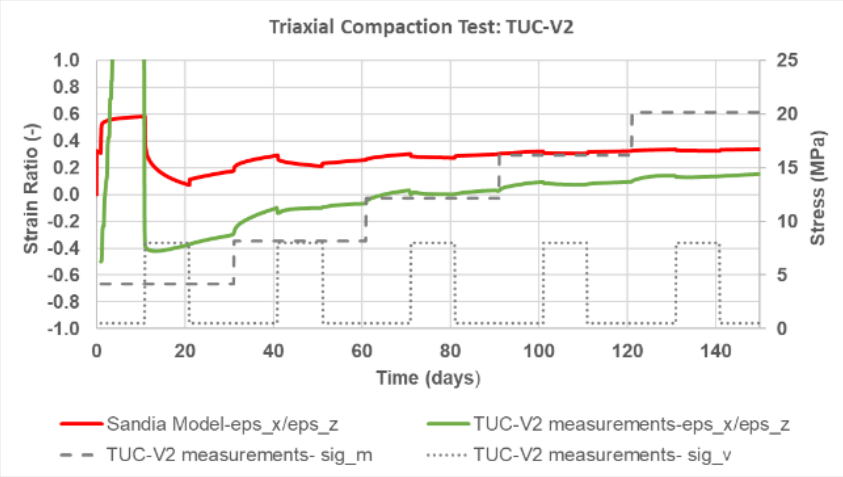

c) Strain ratio $\varepsilon_r/\varepsilon_a$ histories

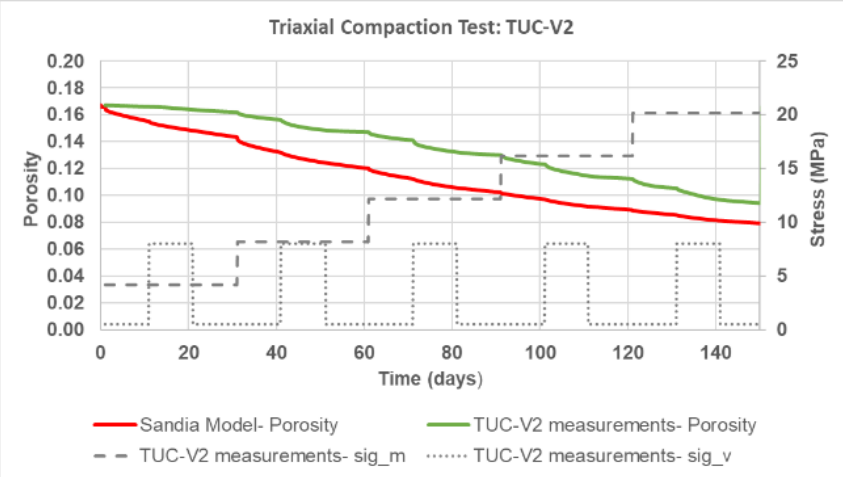

d) Porosity histories

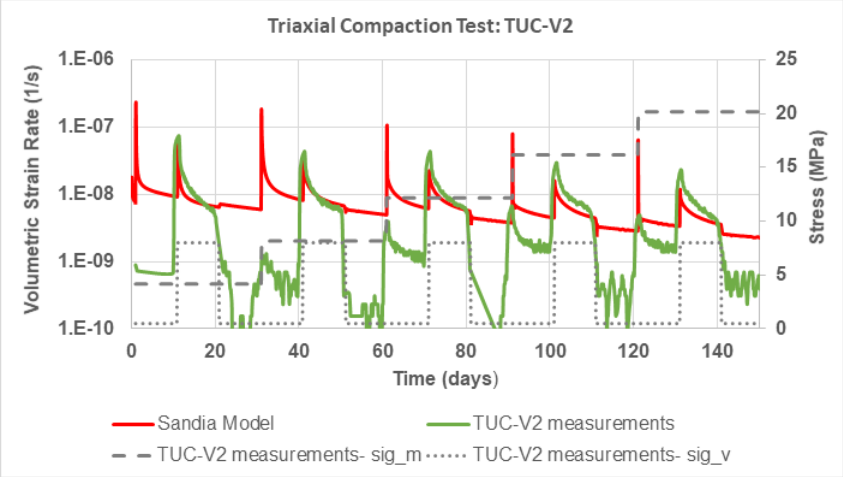

e) Volumetric strain rate histories

Fig. 5.50 Comparison of predictions and measurements for triaxial compaction test TUC-V2

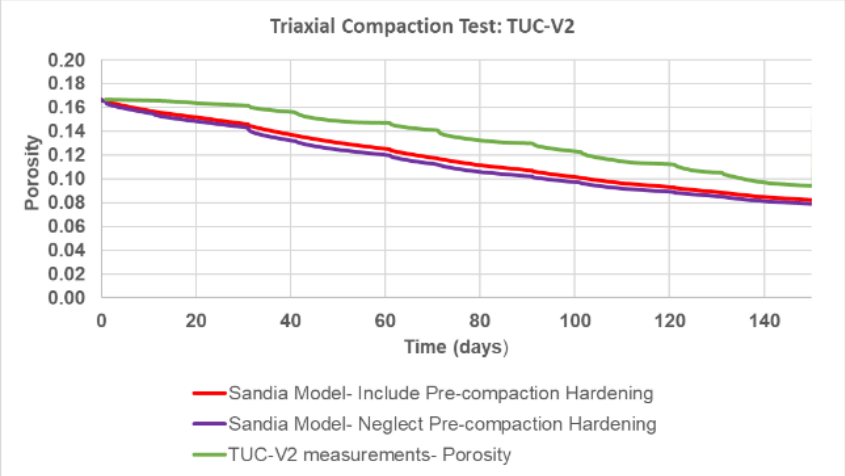

Fig. 5.51 Effect of pre-compaction hardening on porosity predictions for triaxial compaction test TUC-V2

Summary

We used the constitutive model developed by /CAL 99/ and our in-house finite element code Sierra/Solid Mechanics /SIE 20/ to numerically simulate three triaxial compaction tests on crushed salt. Our results were obtained using model calibrations for intact Asse and Sondershausen salt performed by /DEV 11/ and crushed WIPP salt /CAL 99/. The model results were directly compared to the experimental data without recalibration to match the test data.

We modelled the pre-compaction tests in order to account for hardening that the salt would undergo due to loading prior to the triaxial compaction test. We showed some modelling results where the pre-compaction stage was not included to illustrate the impact of pre-compaction hardening on the comparison of model porosity with the data from the tests. We also showed the effect of our choice for the grain size parameter on the model results, as well as choice of sample end restraint on porosity.

Future work could include a calibration of the Callahan model parameters to improve the model comparison with the tests, and closer examination of where the Callahan model itself could be improved.

5.4.1.5 TUC

Recently developed procedure for parameter determination for the constitutive model C WIPP on the basis of a multistage long-term test with isotropic load (test TK-031 by BGR)

The constitutive model C-WIPP/Itasca contains only two functional terms to record the influencing factors porosity and mean stress on the compact behaviour. An optimally suited test to determine the parameters for these two function terms is the test type V1, shown in Fig. 6.8. On the one hand, it contains comparatively long test duration in order to be able to consider the widest possible range of experimentally proven porosity values within the framework of parameter determination without the need of extrapolation for experimentally unproven porosities. On the other hand, a minimum of about 4-5 load steps with different levels of isotropic stress are estimated to be suitable in order to determine the dependence of the compaction on the mean stress as precisely as possible, both with regard to the suitability of the functional dependence and with regard to the determination of parameters. The TK-031 test by BGR fulfils both requirements outlined above, since it covers a porosity range between a maximum of about 17% and a minimum of about 7% with a test time of about 300d in total and, in addition, takes into account 5 load steps with mean stresses of about 10.3 MPa in minimum and about 20.5 MPa in maximum.

The methodology of the parameter determination developed and applied within the framework of the research project is schematically outlined in Fig. 5.52. Afterwards, the parameter determination is carried out in 6 steps as follows:

1) Derivation of the volumetric strain rates from the measured volume change of the test specimen (usually connected with the necessity of a mathematical smoothing of the test values). The derivation of the volumetric strain rates is necessary because these values correspond directly to the constitutive model formulation and are subsequently used for a direct comparison between calculated and measured values.
2) Normalization of the measurement curve of the volumetric strain rates obtained in step 1 to one load level by levelling all jumps in the volumetric strain rate caused by a loading change using multiplicative factors.
3) Displaying of the normalized volumetric strain rate as a function of porosity.

4) Comparison of this normalized volume change rate with the volume change rate calculated for the constitutive model (→ C-WIPP/Itasca uses an exponential function, C-WIPP/TUC uses a multiplicative superposition of an exponential and a power function). Derivation of constitutive model parameters that generate the best possible agreement between the measured values and the calculated values.
5) Use of the normalization factors defined in step (2) (volume change rate at load change) for the determination of the parameters for the dependence of the compaction rate on the mean stress. Analogous to work step (3), the displaying of the measuring points not versus time, but versus the mean stress is necessary.
6) Derivation of the parameters for the elastic compaction from the measured values recorded during the load change: by the using difference between the metrologically determined values for the total compaction rate and the calculated values for the viscous compaction rate. It must be taken into account that the order of magnitude of the elastic compaction is significantly smaller than for the viscous compaction, so that the elastic strain rates are localized in the order of magnitude of the inaccuracies in the determination of the parameters for the viscous compaction rates and can therefore only be derived comparatively roughly by the above procedure. For a clearly more precise determination of the elastic compaction rate, specific experiments for more precise determination of the elastic compaction were therefore designed and integrated into the laboratory test program proposed for a more detailed analysis of the compaction behaviour of crushed salt, as described in chapter 6.2.3.

With regard to the schematic sketch of the parameter determination method documented in Fig. 5.52, it should be noted that the viscous shear deformations (marked with a red cross) cannot be determined by the TK-031 test due to the lack of deviatoric load steps. With regard to the evaluation of test TK-031 it should be noted that only the measurement data of the first 140 test days up to the power failure were taken into account, since the measurement values determined after the power failure are considered to be less plausible, since a significant change in the time-dependent course of the state variables is observed without any change in the load.

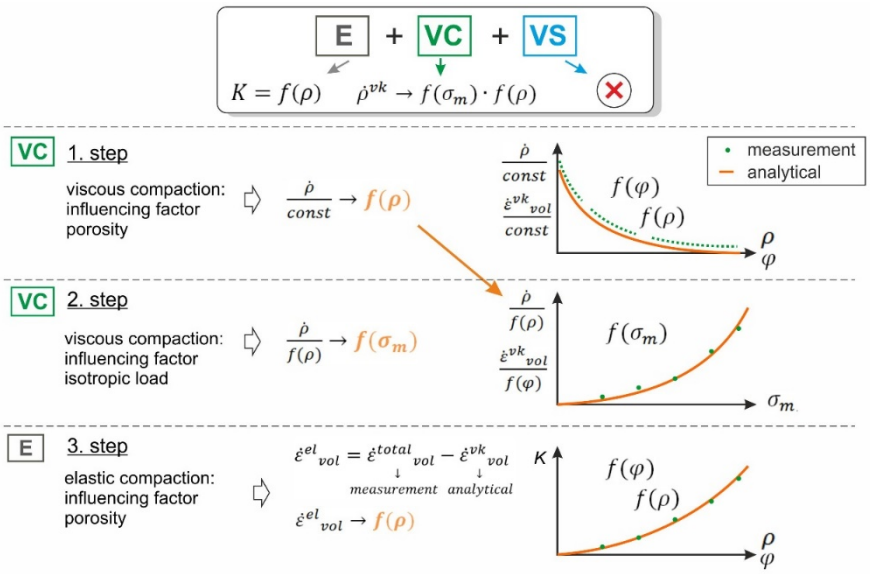

Fig. 5.52 Schematic sketch of the methodology of the parameter determination for the computational part of the constitutive model C-WIPP/TUC using a multi-stage triaxial long-term test with isotropic load

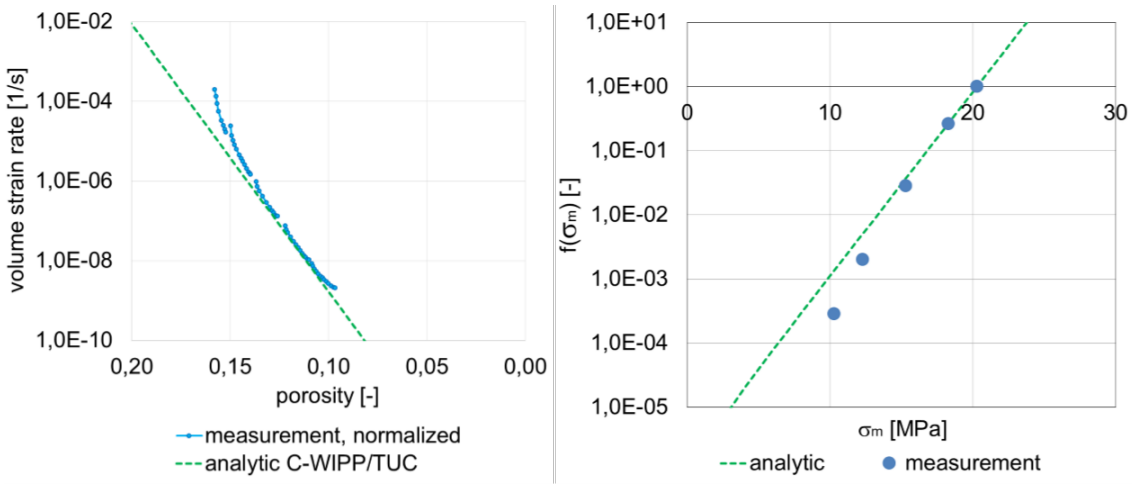

Fig. 5.53 Parameter determination for the model C-WIPP/TUC using the experiment TK-031

Fig. 5.54 shows the back analysis of test TK-031, which was carried out after the constitutive model parameters had been defined, and shows a very good agreement between the calculated and the measured volumetric strains and thus the change in porosity. Consequently the functionality of the methodology used for parameter determination can be assessed as verified. Furthermore, it can be assumed, at least implicitly, that the constitutive model C-WIPP/TUC has an obviously sufficient functionality for the realized stress conditions. However, the recalculation of individual strain components has not yet been finally validated. Fig. 5.55 shows a comparative back analysis with the material

models C-WIPP/Itasca and C-WIPP/TUC for the volumetric strain and for the individual strain components. The inadequate consideration of the directional distribution in the C-WIPP/Itasca model and the tendency of correct consideration of the directional distribution in the C-WIPP/TUC model is made clear by the comparative application: while the C-WIPP/Itasca model calculates almost completely missing x-strains and, in return, significantly overestimated z-strains, the strains calculated with the C-WIPP/TUC model show a physically meaningful order of magnitude for both strain components. With reference to the above statement, however, it must be expressly pointed out that a quantitative comparison between the measured and calculated values for strain components was not possible on the basis of experiment TK-031, since the measured values show a physically implausible relationship between the horizontal and vertical strain components (expected $\varepsilon_z > \varepsilon_x$, measured $\varepsilon_z < \varepsilon_x$).

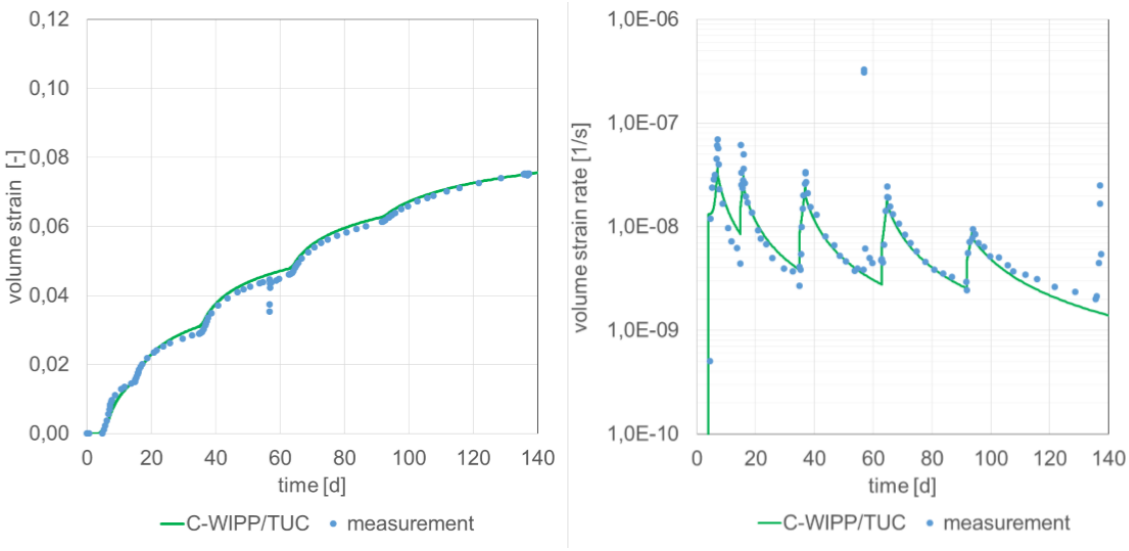

Fig. 5.54 Recalculation of the volumetric strain in test TK-031 with the constitutive model C-WIPP/TUC

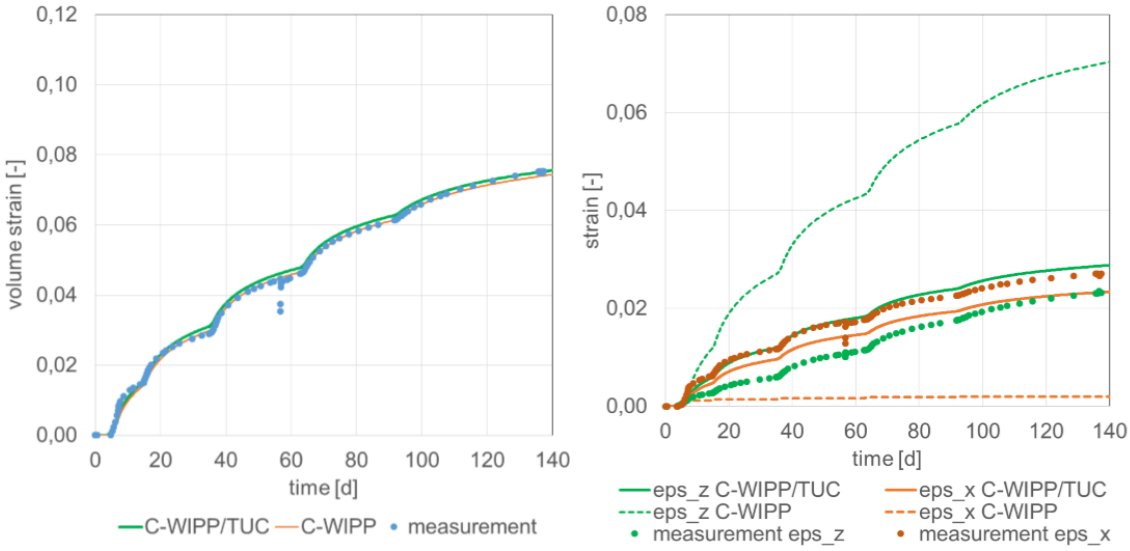

Fig. 5.55 Recalculation of the volumetric strain and the individual strain components in the TK-031 experiment with the constitutive model C-WIPP/Itasca and with the constitutive model C-WIPP/TUC in comparison

Methodology for comparative systematized analysis of several tests (tests TK-031 and TK-033 of BGR and TUC-V2 of TUC)

The objective of the development of the methodology for the comparative systematized analysis of different experiments was to make possible a comparative analysis that is largely independent of the formulation of the constitutive laws.

The results obtained within the framework of the research project are limited to a methodology for the comparative analysis of the dependence of the crushed salt compaction on the porosity. However, it is expected that the methodological approach can be extended to other functional dependencies.

Analogous to the methodical procedure for the parameter determination for a single test according to the above explanations here also

- the volume change rates are derived from the measured values of the volume change,
- the volume change rates are displayed versus the porosity,
- a normalization of these values to one stress level was carried out.

As an additional requirement, in contrast to the analysis of a single test, a normalization of all tests to one and the same stress level must be considered in principle. This is not

always possible, since different tests do not necessarily involve one load step with the same load level. In this case, the normalization is performed to a load level that is as similar as possible for all tests that are to be compared and analyzed.

In the following, the tests TK-031 and TK-033 from BGR and TUC-V2 from TUC are analyzed. The load histories of the tests are compared in Fig. 5.56. Fig. 5.57 shows a comparative presentation of the measured porosities.

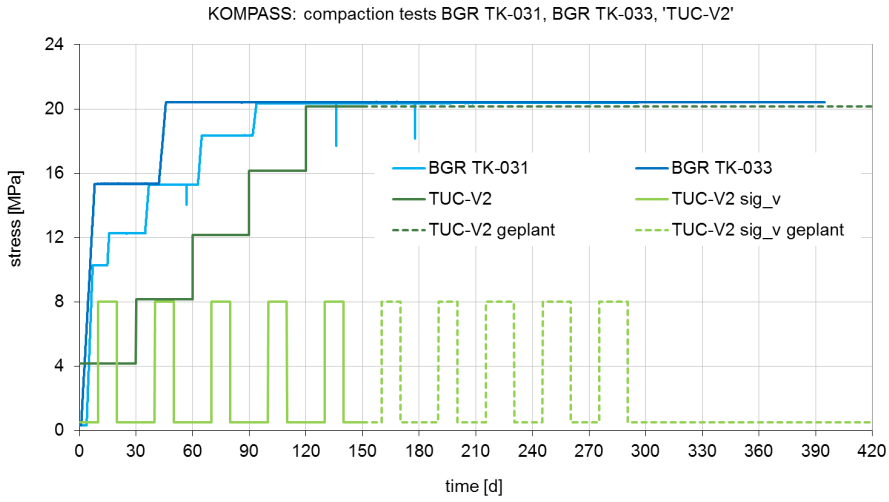

Fig. 5.56 Load histories of tests TK-031, TK-033 of BGR and TUC-V2 in comparison

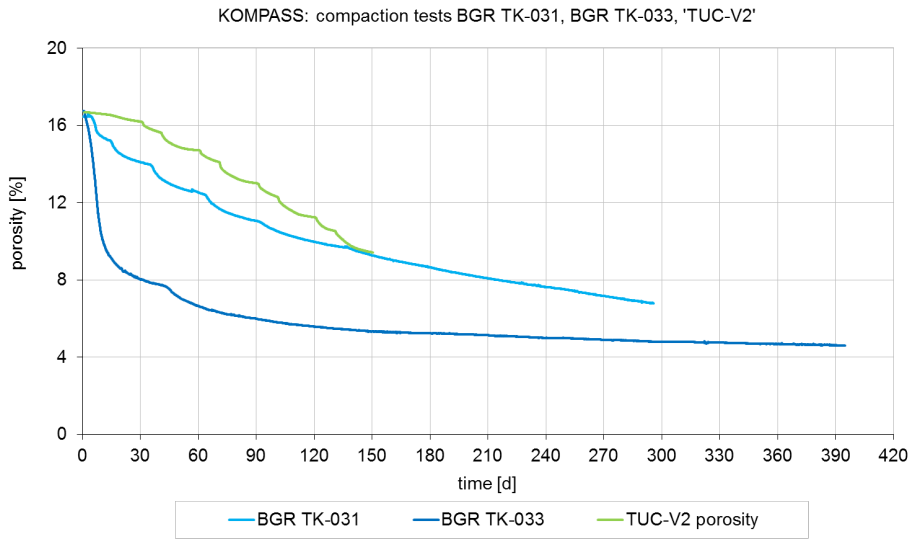

Fig. 5.57 Measurement results of tests TK-031, TK-033 of BGR and TUC-V2 in comparison (in terms of porosity change)

For the selected tests TK-031, TK-033 and TUC-V2 a normalization of the volumetric strain rates to a uniform load level was possible, since the last load level in all three tests was approximately σ_m =20MPa.

Fig. 5.58 shows the normalized volume strain rates of the tests in analogy to Fig. 5.53 in comparison. The following findings can be derived from the analysis of these normalized curves:

- All three tests show the same inclination. This means that all three test specimens show a similar and comparable dependency between volume strain rate and porosity. As a result, it is to be expected that all three tests can be recalculated with a uniform parameter data set in the part of the functional relationship for the influencing factor porosity, independent of the selected constitutive model.
- Furthermore, it can be seen that for the TK-031 and TUC-V2 tests not only an equal inclination for relation between volume strain rate and porosity is given, but also that the absolute numerical values of volume strain rate for the both tests are largely identical. This means that the multiplicative/pre-factor parameter, which controls the magnitude of the volumetric rates in the model, can also be selected uniformly for both experiments. This finding is not self-evident, but rather surprising, since samples of different materials were used for the two experiments, which were carried out with different moisture contents (0.1% versus 0.5%), at different temperatures (50°C versus 30°C) and in different laboratories with different test equipment.
- Although the TK-031 and TK-033 tests document the same inclinations for volume strain rate, there are clearly different orders of magnitude of the values. This observation is also surprising considering the fact that both tests were carried out with the same material, at the same temperature, with the same moisture content and in the same laboratory. As a consequence, it is to be expected that the recalculation of these two tests with one parameter set (at least based on the functional dependencies in the material model C-WIPP) will not be possible.
- Finally, it should be noted that the measurement results of experiment TK-031 after the power failure at t ≈ 140 days show a conspicuously changed inclination of the curve and are consequently not or only subordinately taken into account in the interpretation and analysis.

All three tests show the same gradient. This means that all three test specimens show a similar and comparable dependency between volume strain rate and porosity. As a result, it is to be expected that all three tests can be recalculated with a uniform parameter data set, irrespective of the selected constitutive model.

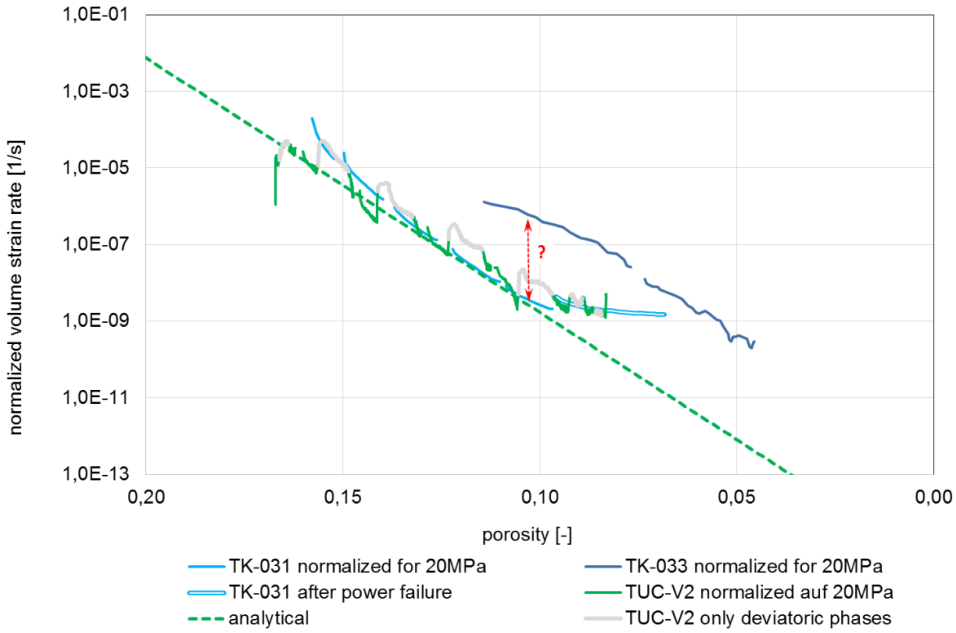

Fig. 5.58 Normalized measurement results of tests TK-031, TK-033 of BGR and TUC-V2 in comparison (as volumetric strain rates)

This comparative analysis of the tests provides at the same time the parameter sets for the functional relationships for dependency on porosity.

Following this comparative analysis, the parameter determination for the test TUC-V2 was realized in the way previously described in Fig. 5.31. Surprisingly, this set showed agreements with the parameters determined for the test TK-031 experiment. The main diagrams for parameter determination using the TUC-V2 test are shown in Fig. 5.38. For the test TK-33, no individual determination of the parameters for the stress dependence was carried out, since only two loading levels were realized in the test, i.e. a sufficiently reliable correlation between load level and compaction cannot be determined.

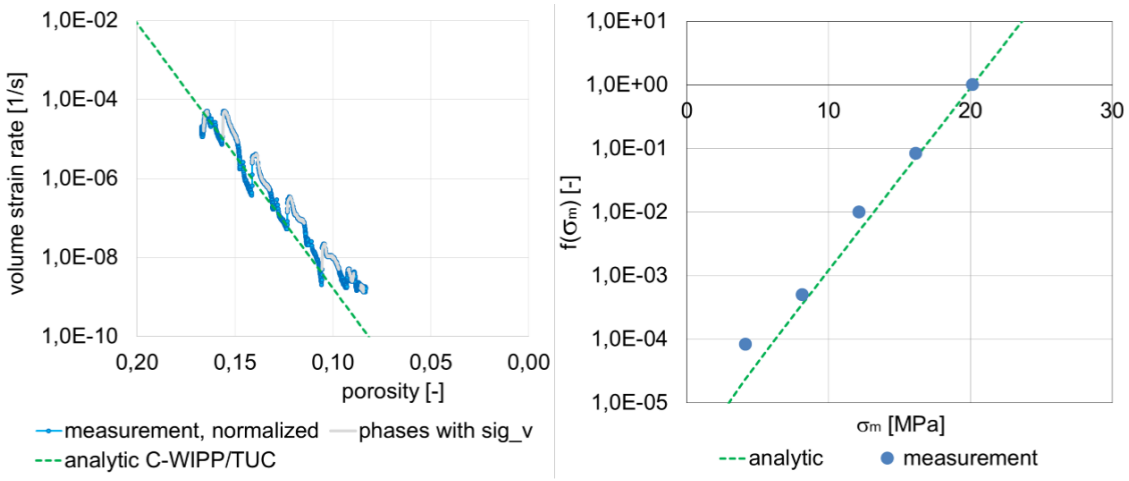

Fig. 5.59 Parameter determination for the TUC-V2 experiment

Recalculation of TK-031 and TK-033 conducted by BGR and TUC-V2

Based on the comparative systematic analysis of the tests TK-031, TK-033 and TUC-V2 and the individual analysis of these tests documented in the previous chapter with determination of the constitutive model parameters, a computational back analysis of the three tests was carried out.

The results of the recalculation were fully confirmed with the findings of the analysis already documented in the previous chapter. This means that the tests TK-031 and TUC-V2 can be recalculated with an identical parameter data set and good agreement between measured and calculated values. In contrast, the recalculation of the TK-033 test with this parameter set shows an unsatisfactory agreement or can only be significantly improved by using the multiplicative factor to F = 350 in parameter C_0 (Fig. 5.60).

Fig. 5.61 and Fig. 5.62 document the results of the recalculation for the test TUC-V2 in detail. Both volumetric and axial strains as well as the rate of volumetric strain are plotted. The physically correct effect of the modification realized in the constitutive model C-WIPP/TUC by introducing a functional dependence on the deviatoric stress is confirmed by a very good accordance between the measured and calculated values. The achieved improvement of the functionality of the constitutive model becomes even more obvious by the comparative presentation of the results of the back calculations with the constitutive model C-WIPP/TUC and with the constitutive model C-WIPP/Itasca.

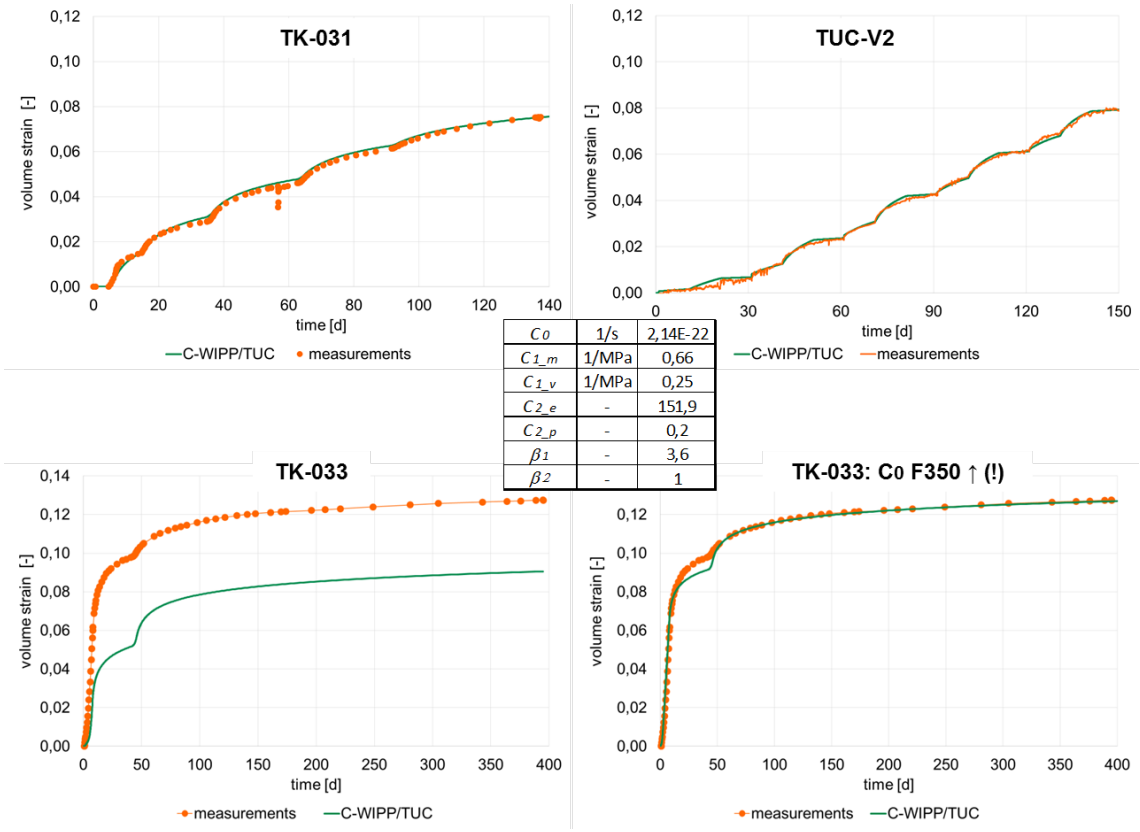

C_0	1/s	2,14E-22
C_{1_m}	1/MPa	0,66
C_{1_v}	1/MPa	0,25
C_{2_e}	-	151,9
C_{2_p}	-	0,2
β_1	-	3,6
β_2	-	1

Fig. 5.60 Recalculation of the tests TK-031, TK-033 and TUC-V2 with C-WIPP/TUC with a uniform parameter set and recalculation of TK-33 with a pre-factor C0 increased by a factor of 350

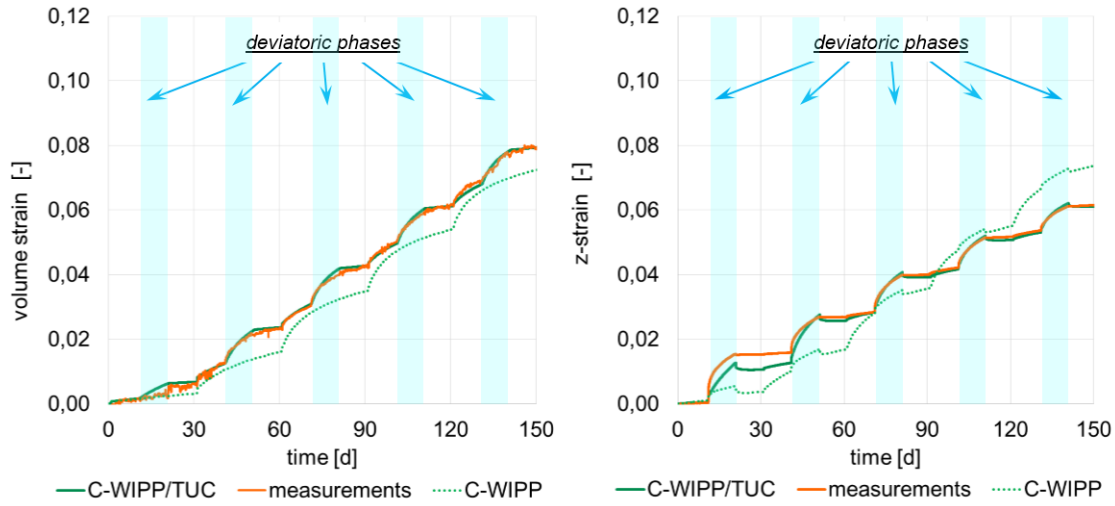

Fig. 5.61 Recalculation of the experiment TUC-V2 with C-WIPP/TUC and with C-WIPP/Itasca in comparison: volumetric and axial strain

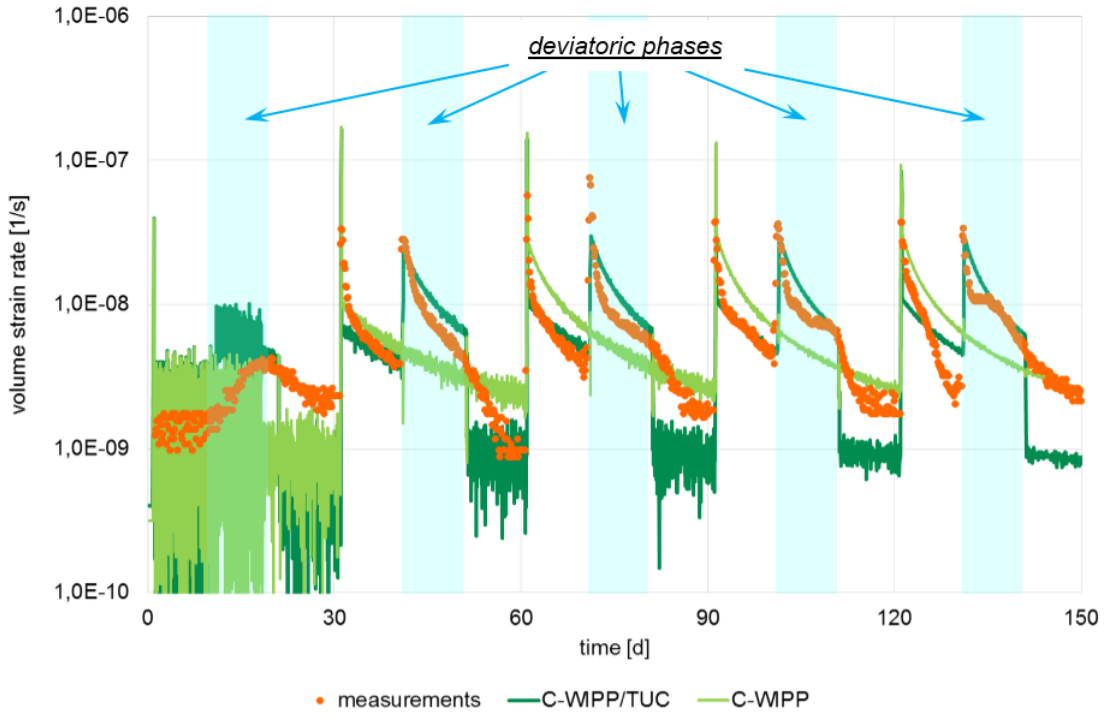

Fig. 5.62 Recalculation of the TUC-V2 experiment with C-WIPP/TUC and with C-WIPP/Itasca in comparison: volumetric strain rates

The results of the above analysis can be summarised as follows:

- The suitability and effectiveness of the methodology for the comparative systematized analysis of several experiments was confirmed by the recalculations of the experiments.
- The two tests TK-31 and TUC-V2 were recalculated accurately in quantity and quality with the modified model variant C-WIPP/TUC using a uniform parameter data set. This result is a first indicator regarding the functionality of the constitutive model and also a first indicator for the comparability and reliability of the laboratory measurement values.
- The results of the TK-033 test, on the other hand, showed a different behaviour compared to the TK-031 and TUC-V2 tests, both with regard to the measured values and consequently also in the recalculation, which can only be reproduced comparatively well by varying the multiplicative pre-factor C_0 in the constitutive model C-WIPP/TUC.

As a result, both the methodology developed for test evaluation and parameter determination and the functionality of the modifications made to the constitutive model are proven to be suitable.

5.4.2 Evaluation of modelling results

The objective of the benchmark was to gain experience in the validation of the constitutive model approaches due to use of the triaxial long-term tests with good isolation of the individual influencing factors.

The three tests TK-031, TK-033 and TUC-V2 address only few following influencing factors: isotropic load, deviatoric load and porosity. The comparability of the tests (a) is given for the tests TK-031 and TK-033 due to the same load type (isotropic multistage), the same material, the same water content and even the same lab; (b) is not given for the tests TK-031 and TK-033 versus TUC-V2 due to different materials and water contents. So, the requirement to recalculate these three tests with the same parameter set can first be made only for the two tests TK-031 and TK-033. However the methodological pre-analysis of these test data due to normalization of the volumetric strain rates (Fig. 5.58) showed the low comparability between the tests TK-031 and TK-033 due to significant differences in the compaction rates even for the same load levels and the same porosity areas. So, one of these two tests have to be seen as a runaway /not representative test. Thus, even for these two tests the requirement to recalculate the test data with the same parameter set cannot be made. Therefore, these three different tests, despite some similarity in the loads, do not form a systematic coherent system of data. Consequently, no uniform set of parameters can be required for the recalculation of these three tests, regardless of the quality of the individual material model approaches.

In order to evaluate the quality and capabilities of the constitutive model approaches using this small exemplary validation study, three main criteria/quality levels for the validation can be used:

1) The model takes into account the influencing factors addressed in the test, and the assumed functional relationships for these factors are suitable to satisfactorily recalculate the test.
2) The model takes into account the influencing factors addressed in the test, but the assumed functional relationships for these factors are not suitable to satisfactorily recalculate the test.
3) The model does not take the influencing factors addressed in the test into account at all.

If the level 3 of validation quality is identified by the recalculation, then the validation was not successful, and the model approach must be extended with the missing influencing factors. If level 2 of validation quality is identified by the recalculation, then the validation

was not successful and the functional relationship in the model approach must be modified/optimized for the respective influencing factor. If the level 1 is identified by the recalculation, then the validation was successful and the functionality of the model particularly regarding the investigated influencing factor is proven.

Fig. 5.63 to Fig. 5.65 show the summary of the recalculation results for all project partners for these three tests.

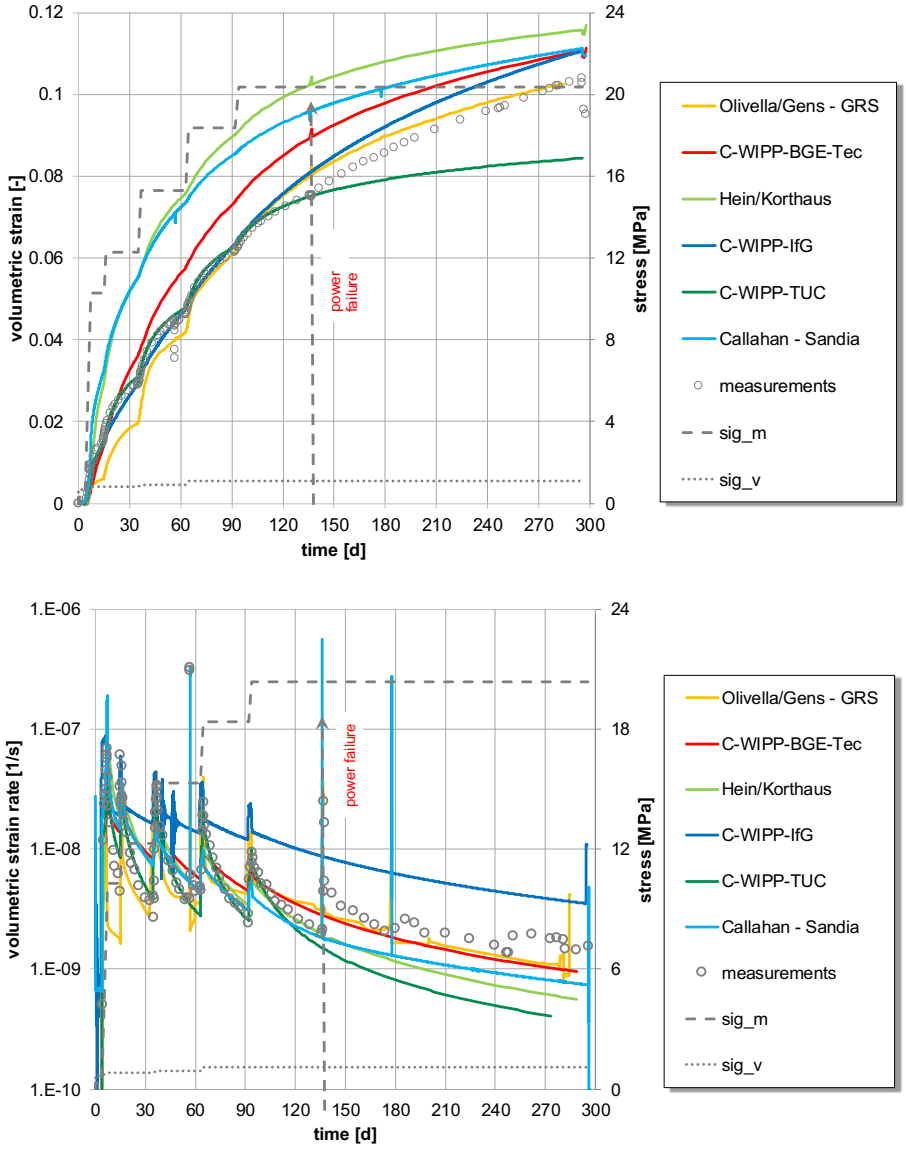

Fig. 5.63 Recalculation results for the long-term multistage test TK-031 (BGR)

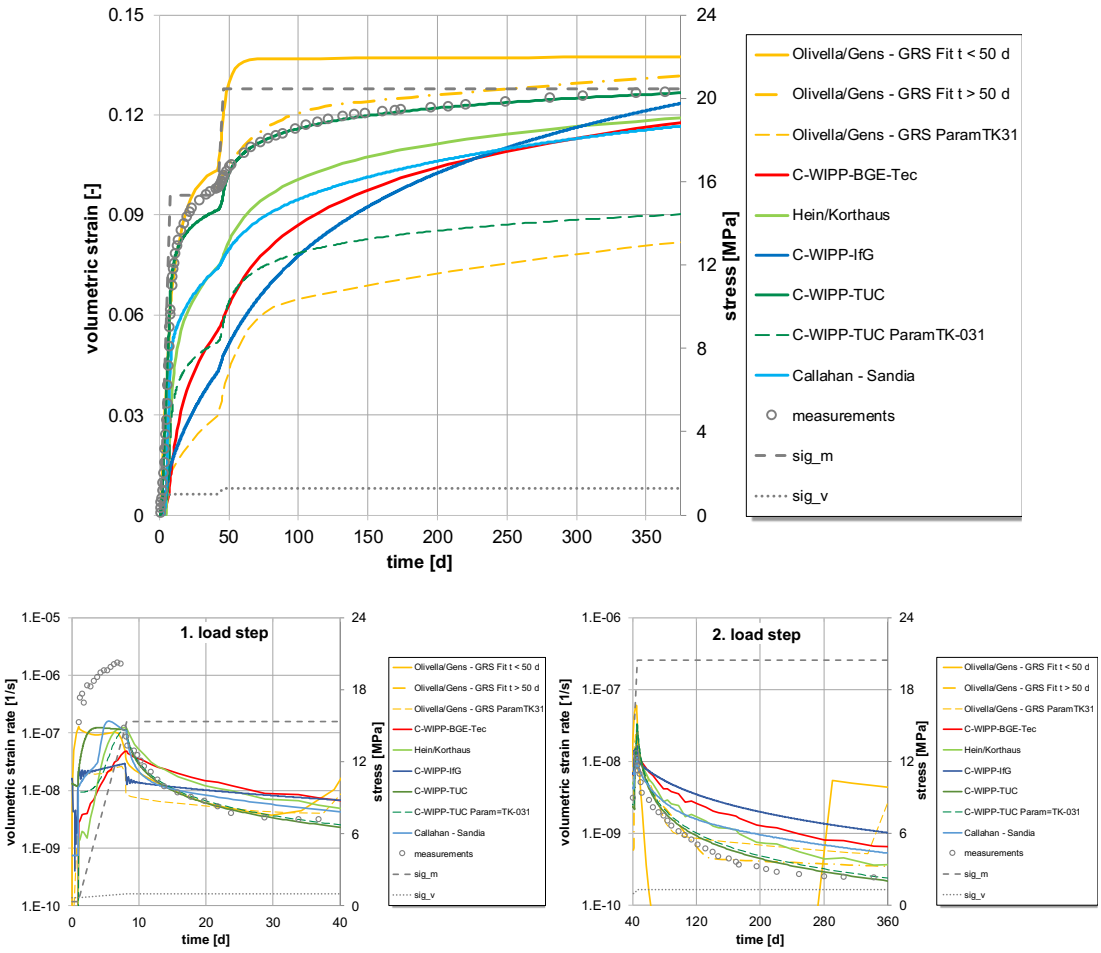

Fig. 5.64 Recalculation results for the long-term multistage test TK-033 (BGR)

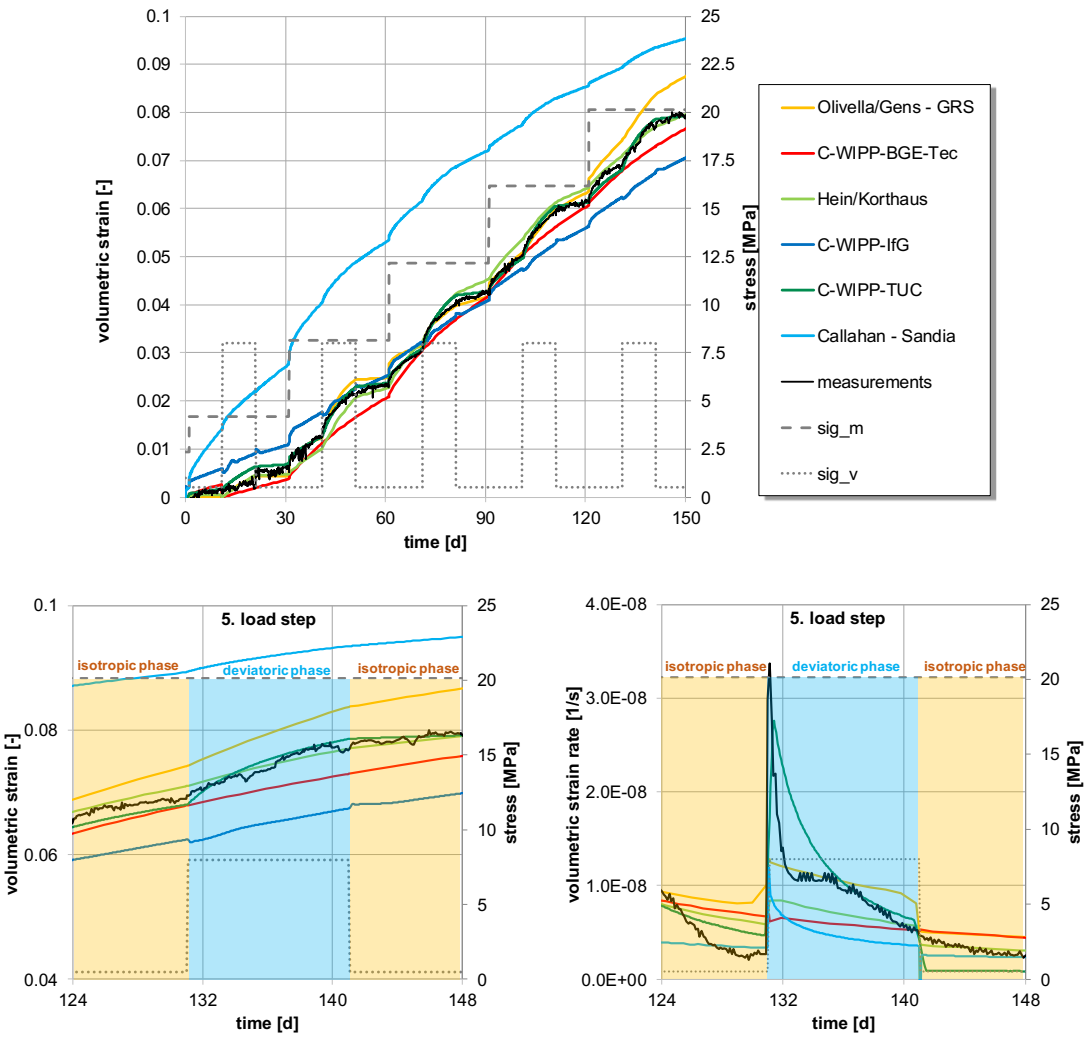

Fig. 5.65 Recalculation results for the long-term multistage test TUC-V2

Following can be seen from these comparative results:

1) The test with isotropic load TK-031 is suitable to be built up for all model approaches that were used here due to the incorporation of both main influencing factors – mean stress and porosity – in all of them.
2) The try to recalculate the two tests TK-031 and TK-033 with a uniform set of parameters was not successful for all model approaches. The main difficulties can be seen in the recalculation of the first load stage, alternatively an individual set of parameters have to be used for this test (Fig. 5.64). Therefore, the expectations are met which results in this case not due to the shortcomings in the model

approaches but confirms the previous model-independent analysis which identify a surprisingly different behaviour of the test samples TK-031 and TK-033.

3) The test with deviatoric load phases (TUC-V2) causes difficulties in the recalculation for those model approaches that do not take into account the influence of deviatoric stress on volumetric strain development. For example, it is not present in the C-WIPP/Itasca formulation resulting in an unsatisfactory recalculation of the deviatoric phases in the TUC-V2 test. The model approaches with explicit consideration of this influence show more or less appropriate reactions in these phases (Fig. 5.64).

6 Conclusion and future recommendations

6.1 Summary

The objective of the project KOMPASS was the development of methods and strategies for the reduction of deficits in the prediction of crushed salt compaction leading to an improvement of the prognosis quality in order to assess barrier function. It includes the development of experimental methods for determining crushed salt properties in the range of low porosities, the enhancement of process understanding and the investigation and development of existing numerical models.

First, an easily available and permanently producible synthetic crushed salt material was chosen which could operate as a reference material for generic investigations also beyond this project. Preferred was a Staßfurt formation in a bedded salt formation. The Staßfurt-formation is to be found one of the most promising host rocks for the disposal of heat-emitting radioactive waste. Finally, a crushed salt material with optimized grain size distribution was chosen from a salt mine carried out by the “Glückauf Sondershausen Entwicklungs- und Sicherungsgesellschaft mbH”.

Since most of the previous research work on crushed salt was focused on domal salt formations, horizontally bedded salt samples from Teutschenthal were characterised by oedometer test in this project. The material shows a similar compaction pattern to domal salt deposits, however, exposes a wider range in load resistance development. An important aspect in the comparison of domal and horizontally bedded salt is the natural humidity content of the crushed salt. In general, horizontal bedded salt has a higher value of humidity and a general tendency for water uptake from humid air. Thus, the humidity creep may play a more important role for horizontally bedded salt.

A new approach regarding the laboratory investigation on the THM behaviour of crushed salt was pursued. The objective was to produce a pre-compacted specimen with low porosity and natural grain structure corresponding to in-situ compacted material which can be used in further investigations of THM behaviour at low porosities (≈ 1 % – 5 %). Within this project different techniques have been developed and successfully executed. An important outcome of this project is the possibility to produce pre-compacted samples in short-term for further use in laboratory experiments.

Within the project, IfG used their pre-compacted specimen for isostatic long-term creep tests under varying stress, temperature and humidity conditions to determine creep properties. The test results show the suitability of long-term creep tests to derive reliable information on the time- and stress dependent compaction behaviour and the possibility of extrapolating the different datasets to longer time scales than the limited test duration. Additionally, a new compaction cell for a multi-parameter monitoring of various parameters during compaction tests was designed by IfG. Up to date, pre-tests on dry samples with measurement of gas permeability were executed successfully and further test are under execution.

Since crushed salt's compaction behaviour is not conclusively known yet and a validation of numerical models for all assumed influencing factors and functional relationships is still missing, TUC developed an approach for a laboratory program to gain a systematically structure database on the THM-coupled compaction behaviour. In the course of this new approach, two pilot tests were executed with a successful verification of the technical feasibility for the isolated consideration of individual functional dependencies. A further discussion is given in Section 4.8.

An important basis of the experimental investigations in KOMPASS is the comparability of grain structure of pre-compacted samples with in-situ compacted crushed salt. This can be ensured due to microstructural investigations. Within this project the development of methods for the microstructural investigation are advanced so far that a verification is possible in a further project phase. Individual investigations on the microstructure of the loose crushed salt, pre-compacted specimen and long-term compacted specimen are done.

For numerical investigations various existing models for the description of crushed salt compaction are characterized and benchmarking simulations on three individual triaxial tests are done. Some constitutive models show good accordance with the experimental results for all three benchmarking, however, the magnitude of influencing factors is very small and further validation work has to be done. A discussion about this could be found in Section 6.2.4.

6.2 Future recommendations

6.2.1 Microstructure investigations

Samples of three different types (uncompacted, pre-compacted and compacted crushed salt) were investigated within the KOMPASS-project. The observed microstructures (Section 3.3.2) were associated with three deformation mechanisms: cataclasis (1), diffusive mass transfer (2) and intracrystalline plasticity (3). Intragranular (Fig. 4.8, Fig. 4.50), en-échelon (Fig. 4.4, Fig. 4.5, Fig. 4.51), transgranular (Fig. 4.7, Fig. 4.52) fractures and fluid inclusions (Fig. 4.5, Fig. 4.6, Fig. 4.7, Fig. 4.53, Fig. 4.54, Fig. 4.55) were present in all investigated samples. Grain boundary diffusion (Fig. 4.56, Fig. 6.1), bended unbroken grains and bended grain boundaries (Fig. 4.58) were present in pre-compacted (Section 4.7.1) and compacted (Section 4.7.2) material only. Fig. 6.1 compares the abundance of microstructural deformation indicators in uncompacted, pre-compacted and compacted samples. Note that the given quantity is based on our subjective impression only. In total, about 16 thin sections were examined.

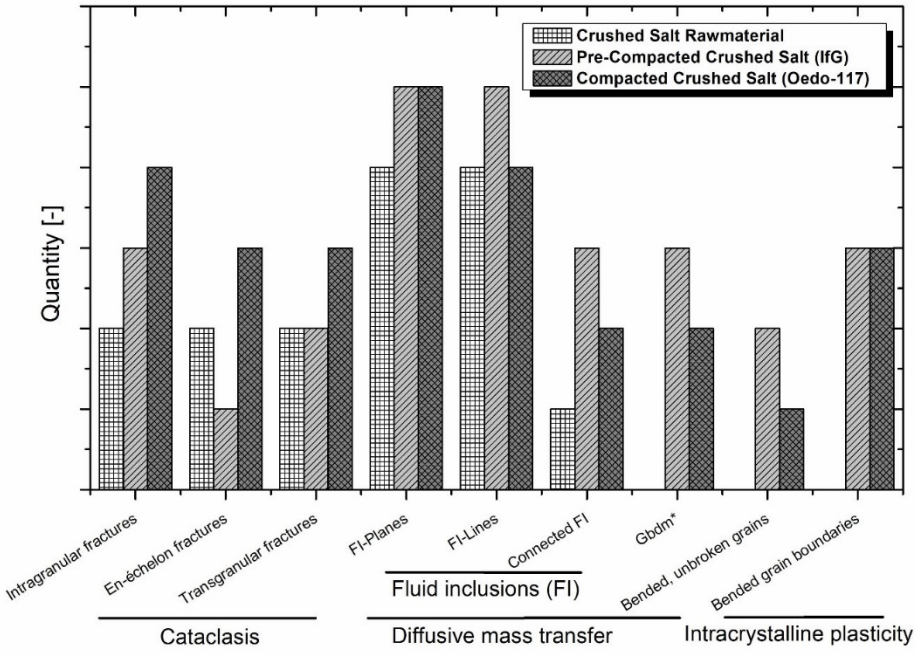

Fig. 6.1 Observed microstructures in loose crushed salt (two sections) compared to pre-compacted crushed salt (eight sections) and compacted crushed salt (six sections). Quantity is just a exclusively value relative to each other. *Gbdm stands for an indicator of grain boundary diffusion, namely rounded grain edges with even grain contact /HAN 14/

In Section 3.2.3, pressure-solution creep was outlined as a fundamental deformation mechanism characterized by dissolution and precipitation processes. Within the project, indicators for the occurrence of grain boundary diffusional pressure mechanisms could be established on thin sections of compacted crushed salt samples (Fig. 6.2).

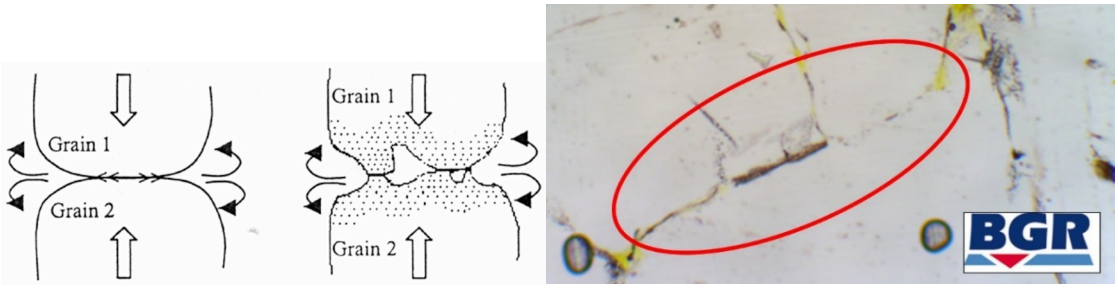

Fig. 6.2 Visualization of grain boundary diffusion. Left: Schematic representation of pressure solution /HAN 14/. Right: Microstructural indicators for grain boundary diffusion in a compacted crushed salt sample.

All observed microstructures show indicators for several mechanisms and hence state a complex interplay of cataclasis, diffuse mass transfer and (for compacted samples) intracrystalline plasticity. Future work will address the topics subgrain investigations and subgrain piezometry /SCH 05/, /SCH 07/. Although subgrain analysis requires careful etching techniques or irradiation, the investigations of subgrain orientation, shapes, and sizes along with dislocation densities will aide in the determination of dominant mechanisms and sample stress states to further enhance consolidation methods. Therefore, future investigations shall also include a series of samples with variated grades of compaction, as well as various moisture conditions. These grades might correlate to the abundance of the different mechanism-indicators, thus improving the understanding of micromechanical processes to produce more complete constitutive models.

6.2.2 Laboratory plans for the next project phase: plane strain pre-compaction by TUC

Within the scope of the project, a new method for pre-compaction in fast motion under in-situ similar loading conditions (TE-stress, plane strain state) in compression bearing cells was developed and tested by TUC. Within the scope of the test series, the pre-compaction cells were continuously optimized in terms of design so that the sensitive connection between rubber sleeve and pressure piece was designed to be both tight against the ingress of jacket pressure oil and axially movable to prevent a tensile crack

in the rubber sleeve induced by the compaction-induced constriction. Within the framework of the test specimen production it could be successfully demonstrated that specimens made of pre-compacted crushed salt can be machined on a lathe to cylindrical test specimens with plane-parallel end faces and smooth lateral surface even with a residual porosity of up to 18%. Even if the investigations into the suitability of time-lapse tests for the production of in-situ equivalent crushed salt test specimens of defined initial porosity could not yet be completed within the framework of the research project, it can be stated that the influence of the stress level is significantly less than originally estimated, i.e. even with smaller stresses at a level of 3 – 5 MPa within comparatively short stressing times of a few days, a significant compaction results; that an increasing moisture content of the crushed salt intensifies the compaction process and that it appears possible on the basis of systematic serial investigations to generate clearly reproducible and predictable relations between final porosity, stress level, stress duration and crushed salt moisture.

Within the framework of the research project, a total of 23 compaction tests were carried out on classified crushed salt with variation of the test duration, the moisture content of the samples and the stress level. As a result of the pre-compaction tests and the test specimen production by means of a lathe, a total of 8 crushed salt test specimens with varied moisture and porosity were produced for further mechanical and structural investigations.

Two of these test specimens were sent to the composite partners Sandia and BGR for microscopic examinations. Two further test specimens were used for mechanical investigations on the compaction behaviour for the tests designated TUC-V2 and TUC-V3.

Based on the fundamentally positive experiences with the pre-compaction technique developed in the research project, further systematic test series were planned for a continuation of the project with the aim of establishing reproducible and predictable correlations between stress level, stress duration, crushed salt moisture and the respective target porosity. Fig. 6.3 shows a summary of the investigations on pre-compaction carried out in this respect and planned for the next project phases.

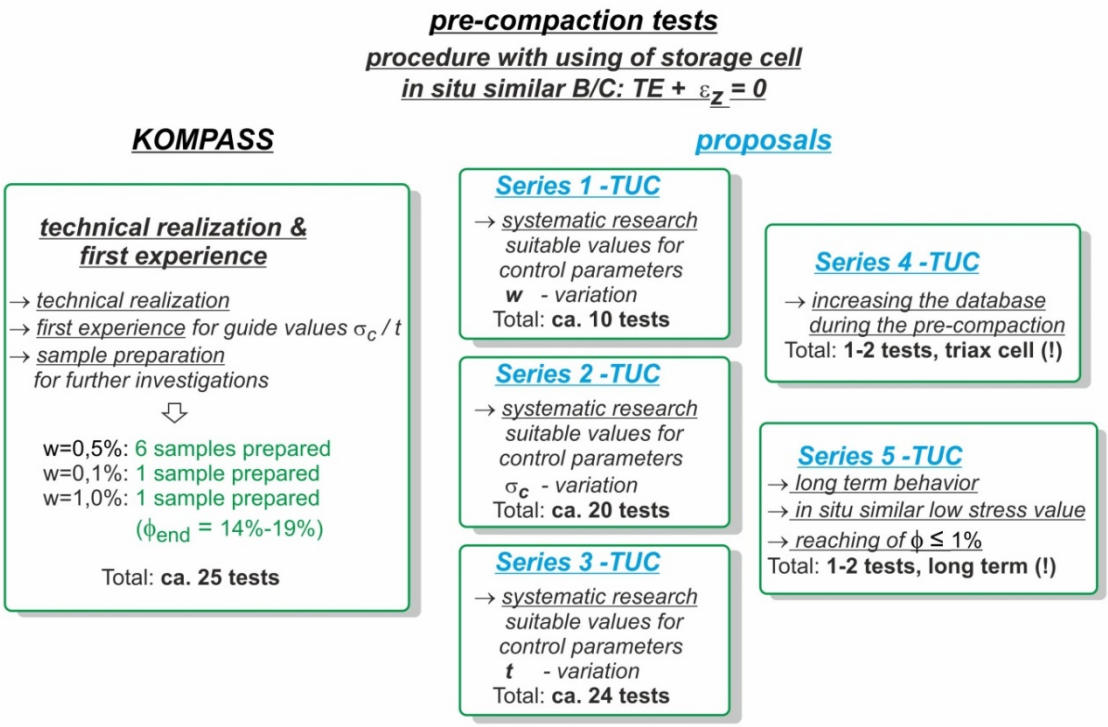

Fig. 6.3 Overview of the performed and planned investigations on the pre-compaction of crushed salt under in-situ similar stress conditions in fast motion

6.2.3 Laboratory plans for the next project phase: long-term compaction behaviour

6.2.3.1 Procedure for the design of experiments

As mentioned previously, the compression behaviour of crushed salt in space and time, depending on the load history and the material properties, is not yet conclusively known. I.e. available constitutive models have neither been adequately validated for all assumed influencing factors and functional relationships, nor do comprehensive systematic experimental databases exist, which would allow an extensive complete validation.

With the objective of preparing a conceptual design of a systematized laboratory program corresponding to the above-mentioned requirements, the following steps were taken (Fig. 6.4):

1. Overview and analysis of currently available experimental investigations.

2. Determination and summary of new requirements and objectives with regard to the capabilities, realism, functionality and reliability of the statements of the constitutive

models for the description of the material behavior of crushed salt as well as formulation of resulting new requirements for the laboratory database needed for the (further) development and validation of the constitutive models.

3. Formulation of guidelines and principles for planning of laboratory program.

4. Creation of a test system with coordinated correlated tests and creation of individual specific operating modes and boundary conditions for each individual test of the laboratory program. The operating modes and boundary conditions have to be optimized for the respective influencing factor, the respective process or the respective state variables.

5. Structuring of the laboratory program with respect to priority setting and effort estimation. The prioritization is essentially carried out according to the following criteria:

    a. How significant is the influence of the factor in relevant in-situ situations?
    b. How extensive, reliable and precise has this influence factor been investigated in the laboratory to date?
    c. How complex and technically feasible is the planned investigation with regard to the influencing factor?

6. Cyclical continuous revision, addition or modification of the laboratory program as a result of new findings from the new experiments already carried out in the program or as a result of technical discussions with the project partners.

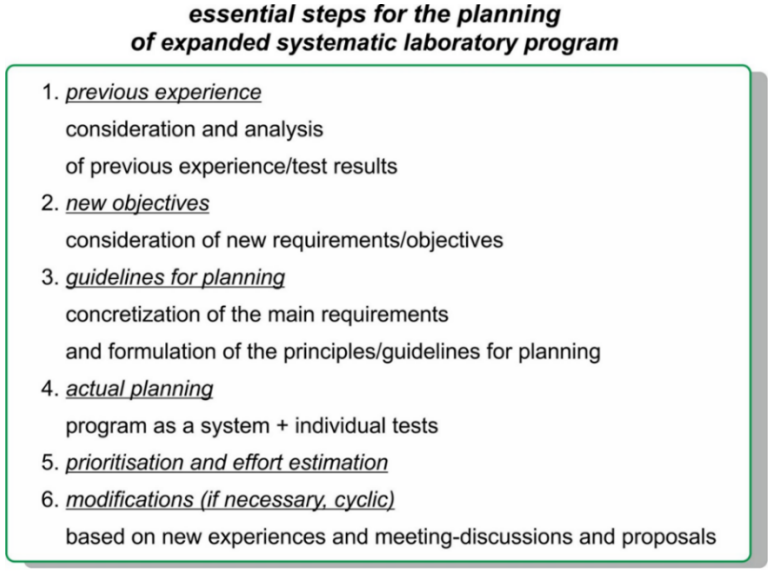

Fig. 6.4 Essential steps in the planning of a comprehensive laboratory program belonging to a systematic investigation of the material behaviour of crushed salt

6.2.3.2 Overview and analysis of existing experimental database

Overview and analysis of existing available experimental data was carried out under the objective of evaluating their uniformity in terms of comparability of experimental results, completeness of data basis, reliability and degree of precision of measurements.

Because laboratory investigations on crushed salt compaction carried out in the past years have been extensively documented in the literature and also described in summary form, it is refrained from repeating this presentation with reference to selected literature /KRÖ 09/, /WIE 17/, /KOR 96/, /CAL 99/, /BEC 99/, /BEC 04/, /KRÖ 17/, /LAM 18/. With respect to Section 4.8.1 the evaluations within the scope of the present research report are rather limited to those aspects, which were of particular importance in the subsequently documented planning of the demanded laboratory test program. That is, overview and analysis of existing database within the current research project is restricted by a schematic sketch of the historical sequence of research projects regarding crushed salt (Fig. 4.1) and a detailed analysis of two triaxial compaction tests on crushed salt (TK-031; TK-033) conducted in the past by BGR and one triaxial compaction test on crushed salt (TUC-V2) conducted in frame of this project.

6.2.3.3 New requirements and current research needs

The extended requirements on the material properties of crushed salt (sufficiently low permeability and porosity) resulting from the paradigm change in the safety case on the one hand and the necessity of a long-term qualified prognosis of the load-bearing and sealing behaviour of crushed salt in space and time on the other hand, necessitate new requirements on the experimental database, which must be available for the (further) development and validation of the material models. Essential requirements on an experimental database for the further development and validation of material models for the THM coupled simulation of backfill made by crushed salt are:

- The comparability of the data, i.e. the experiments must be carried out on a material that is similar with regard to salt type, grain size and mineral composition.
- Systematically coordinated tests in such a way that the effects of each individual influencing factor on the THM behaviour of crushed salt (e.g. water content, mean stress, deviatoric stress, stress geometry, load rate, time, temperature, porosity, etc.) can be proven and validated by clearly interpretable and reproducible correlations.

- Accurate and reliable measurements of low porosity (< 1 % – 5 %) and low permeability ($K < 10^{-19}$ m^2) as well as related stress conditions. To date, both properties are subject to uncertainties: permeability due to limitations of flowmeters and pressure gauges and porosity foremost due to the error span in solid matter density. The porosity of highly compacted crushed salt, for instance, is lower than the error span of the porosity evaluation itself. As such highly compacted, low-porosity materials have come more into focus of nuclear waste storage, it is desirable to consider these errors and uncertainties in an upcoming sensitivity analysis across all the methods used.

In order to ensure the completeness of the planned systematic test series for the investigation of the material behaviour of crushed salt, functional relationships must be recorded for all in-situ relevant influencing factors as far as possible. To ensure the transferability of the material behaviour of crushed salt determined by the planned systematic test series, functional relationships have to be recorded for the in-situ relevant value ranges of the influencing factors.

A schematized representation of the main influencing factors characterizing the THM behaviour of crushed salt with associated special technical test features, which were considered within the scope of the work for the establishment of a comprehensive test program, is shown in Fig. 6.5. The need for investigation outlined in Fig. 6.5 is based on an analysis of the currently available measurement data on crushed salt and an initial analysis of the currently available constitutive model approaches for crushed salt.

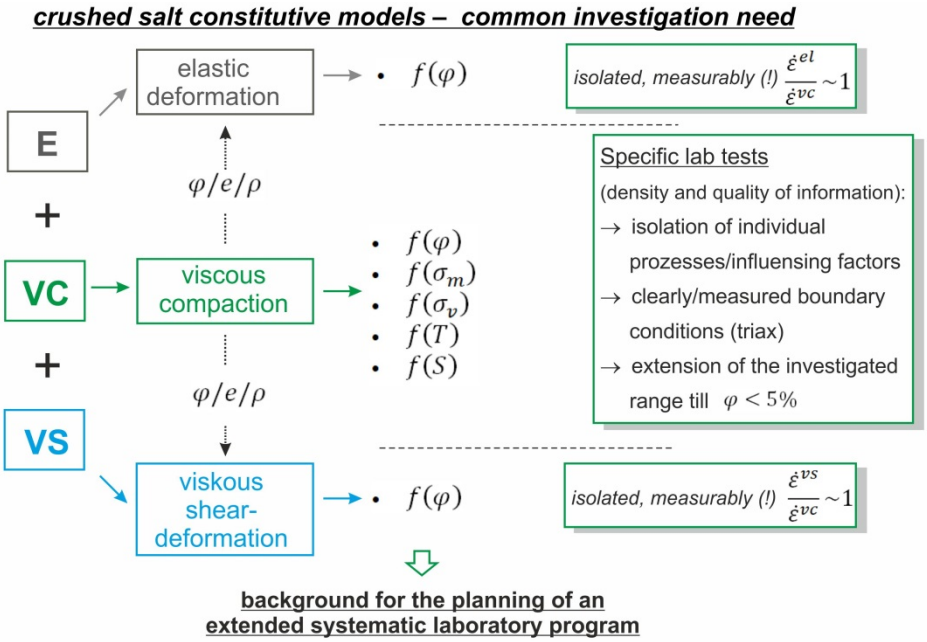

Fig. 6.5 Schematic representation of the main factors characterizing the THM behaviour of crushed salt

6.2.3.4 Approach for a substantial systematic experimental laboratory program

In accordance with the procedure described in Fig. 6.3 for the systematized planning of a laboratory test program characterizing the THM material properties of crushed salt in space and time, the iterative planning process (steps 4, 5 and 6 in Fig. 6.4) is documented below.

Fig. 6.6 shows the first iterative planning step. It is recorded which influencing factors are investigated by which test types. Accordingly, the following factors are to be investigated:

- Influence of porosity (of the current compaction status) on (a) the viscous compaction behaviour, (b) the elastic compaction behaviour, (c) the viscous creep behaviour;
- Influence of isotropic stress (characterized in constitutive models by the mean stress or by the first stress invariant) on the compaction behaviour;
- Influence of the deviatoric stress (characterized in constitutive models by the equivalent stress of Mises or the second stress invariant) on the compaction behaviour;
- Influence of moisture content on compaction behaviour;

- Influence of the stress geometry on the compaction behaviour (compaction under isotropic conditions, under TC/UC conditions or TE/UE conditions), especially with respect to the directional distribution of individual strain components;
- Influence of the type of stress on the compaction behaviour (strain controlled with constant strain rate versus stress controlled with constant stress);
- Influence of the pre-compaction (of the pre-compaction method) on the further compaction behaviour caused by the changed material structure and possibly by material anisotropy.

The designation 'V' or 'S' in Fig. 6.6 defines the type of investigation as follows:

V – multi-stage test with variation of the value of the respective influence factor from load stage to load stage;

S – a series of single-stage tests in which the variation of the influence factor is not carried out within a single test but through a series of individual tests.

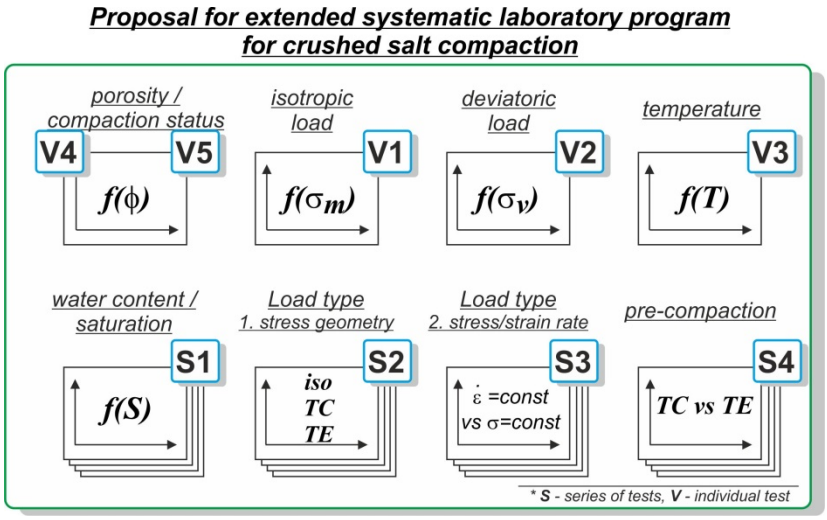

Fig. 6.6 First iteration step for planning the laboratory test program

In the second iteration step of the planning, the planned experiments were specified in more detail by determining for each type of experiment or series of experiments which parameters must be kept constant and in which areas the respective influencing factor should be varied (criterion: in-situ relevant and/or technically feasible). The keeping of all other parameters/factors constant when varying a single factor ensures that the respective influence or process is isolated or isolatable. Furthermore, the derivation and definition of globally valid values of those parameters which are kept constant in each

case (e.g. for T = const a numerical value of T = 30°C is defined for all tests in which the variation of the temperature is not provided for), increases the uniformity and comparability of individual tests among themselves and consequently generates a qualified system of correlating measurement data in contrast to the currently only available compilation of measurement results of individual tests. The result of this second iteration stage is schematically sketched in Fig. 6.7. For clarification, some of the currently available triaxial tests are entered in Fig. 6.7 in order to show their allocation or affiliation in the sense of the system outlined above.

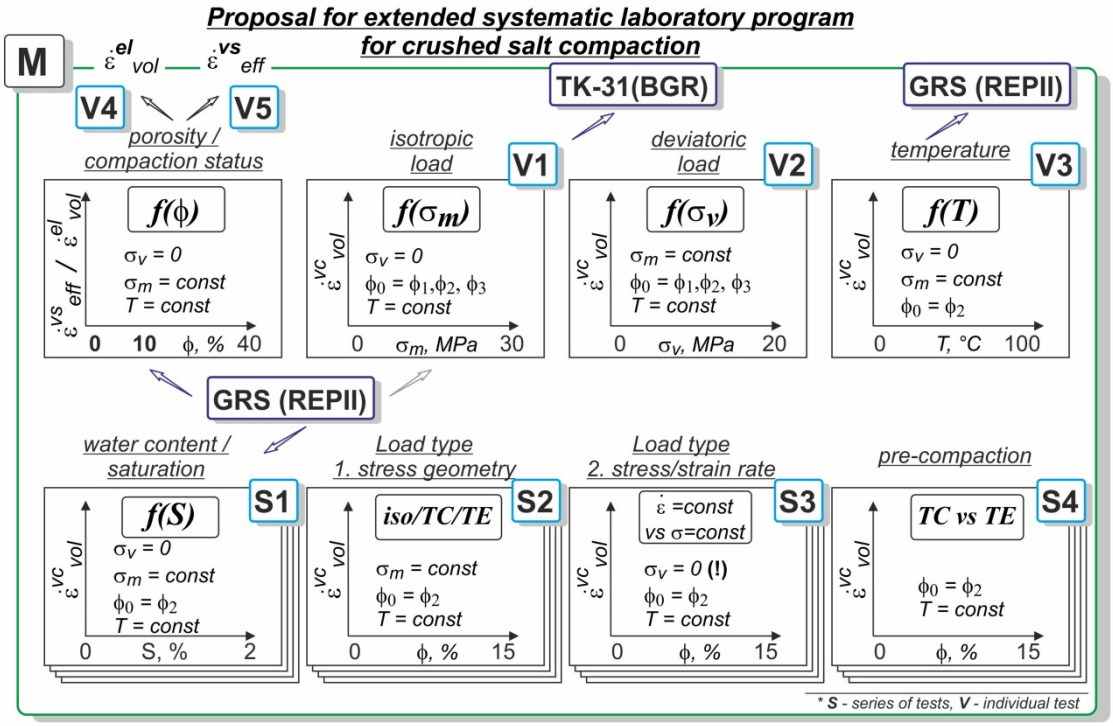

Fig. 6.7 Second iteration step for planning the laboratory test program

In the third iteration step, a final concretization was carried out, in that for each individual experiment of the program, a mode of operation (load history) was developed which was considered to be optimally suited and in part also new. Figures 6.7 to 6.16 show the operating modes of the multi-stage tests (V-tests) and the test series (S-tests) together with the expected results as follows:

V1 in Fig. 6.8:

Multi-stage isotropic load test with at least 4 – 5 load stages for the analysis of the functional dependence on crushed salt compaction on porosity and mean stress. The load history is analogous to the mode of operation selected by BGR in the TK-031 test.

V2 in Fig. 6.9:

Multi-stage deviatoric load test maintaining the isotropic load level constant with variation of the deviatoric load for the analysis of the functional dependence of the crushed salt compaction on porosity and on the magnitude of the deviatoric load.

V3 in Fig. 6.10:

Multi-stage isotropic load test maintaining the isotropic load level constant with variation of the temperature for the analysis of the functional dependence of the crushed salt compaction on porosity and on the temperature.

V4 in Fig. 6.11:

Multi-stage isotropic load test to analyze the functional relationship between elastic volume strain and porosity. The elastic volume strains are also generated in the transition phase between two load stages in test type V1 but are relatively small compared to the viscous compact strains additionally generated in test type V1 and consequently can only be quantified to a limited extent of precision by measurement. The objective of test type 4 is therefore to specify the operation mode in such a way that elastic strains reach a larger or comparable order of magnitude to the viscous strains. In order to guarantee this, it is planned in accordance with Fig. 6.11 for test type V4 to realize the most intensive possible change in the isotropic load in each of five equidistant load stages. The viscous compaction phases between the individual elastic load changes should generate such a significant change in porosity that a quantitative isolation or separation of elastic and viscous volume strain components can be determined for the largest possible range of porosity.

V5a in Fig. 6.12:

Multi-stage deviatoric load test for the analysis of the functional dependence between viscose-induced shear deformations and porosity. In a total of five load stages, deviatoric stress is cyclically increased to a respective equal stress level and subsequently reduced again, so that the functional dependence between the viscous shear deformations and the magnitude of the porosity at constant deviatoric load can be analysed. The existence of this relationship is assumed in almost all available constitutive models of the material behaviour of crushed salt. However, the quantitative differences in the approaches of these constitutive models are enormous (under otherwise identical boundary conditions, differences of up to ten orders of magnitude are predicted depending on the selected constitutive model). Evidence for the above statement is documented, for example, in

/KRÖ 17/ by the comparative presentation of the results of analytical benchmark calculations. As a consequence, the differences shown in /KRÖ 17/ point to a markedly insufficiently validated functional correlation or to a fundamental deficit in the process of understanding the crushed salt reaction, which can only be eliminated on the basis of suitable experimental investigations. Regardless of the general focus on the material behaviour of crushed salt in the low porosity range, it is recommended that the range of relevant porosities starting at ≤ 25 – 30 % also be investigated, so that this functional relationship, which has been insufficient investigated to date, can be characterized experimentally as precisely and generally validly as possible.

V5b in Fig. 6.13:

This operation mode is a slight modification of test type V5a. Based on the experiences from the pilot test TUC-V2 (detailed description in the chapter 4.8.2), the duration of the first deviatoric load stage was extended from 10 days to 40 days in order to reduce transient creep deformations and to induce predominant stationary creep deformations in the following 4 load stages.

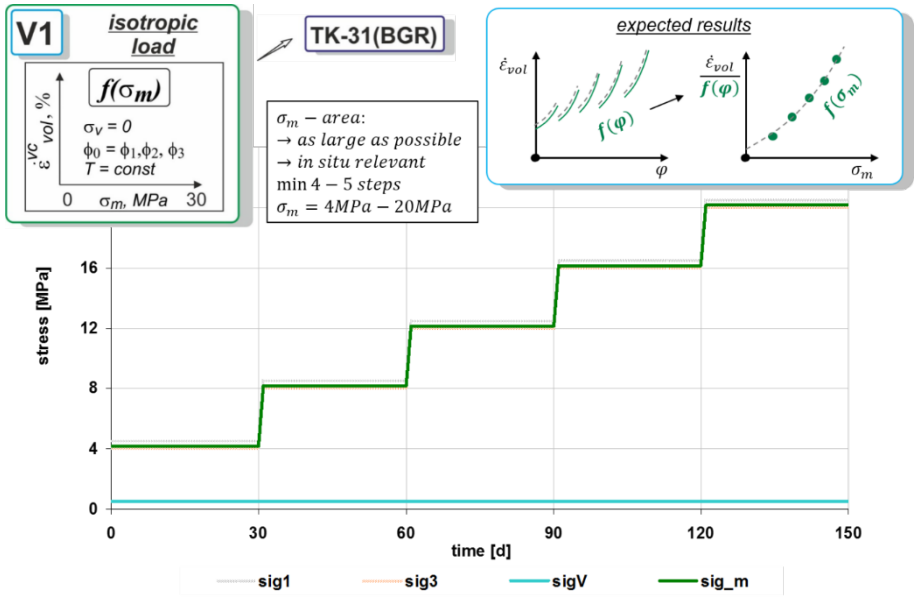

Fig. 6.8 Loading history of test type V1

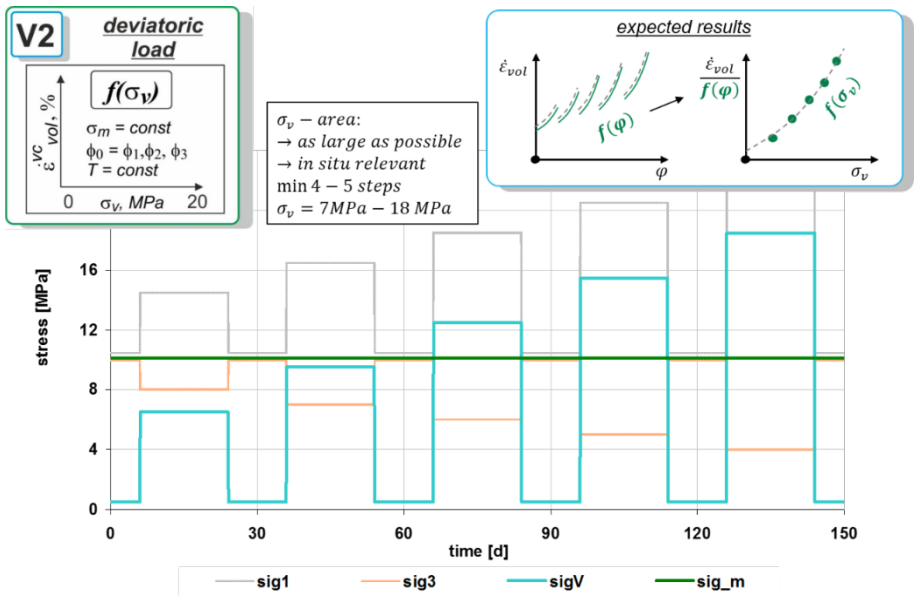

Fig. 6.9 Loading history of test type V2

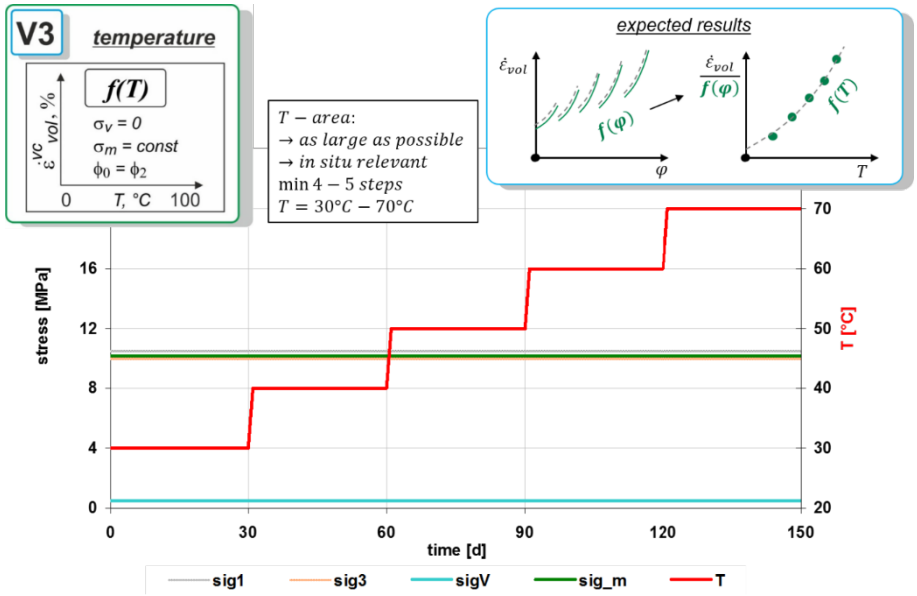

Fig. 6.10 Loading history of test type V3

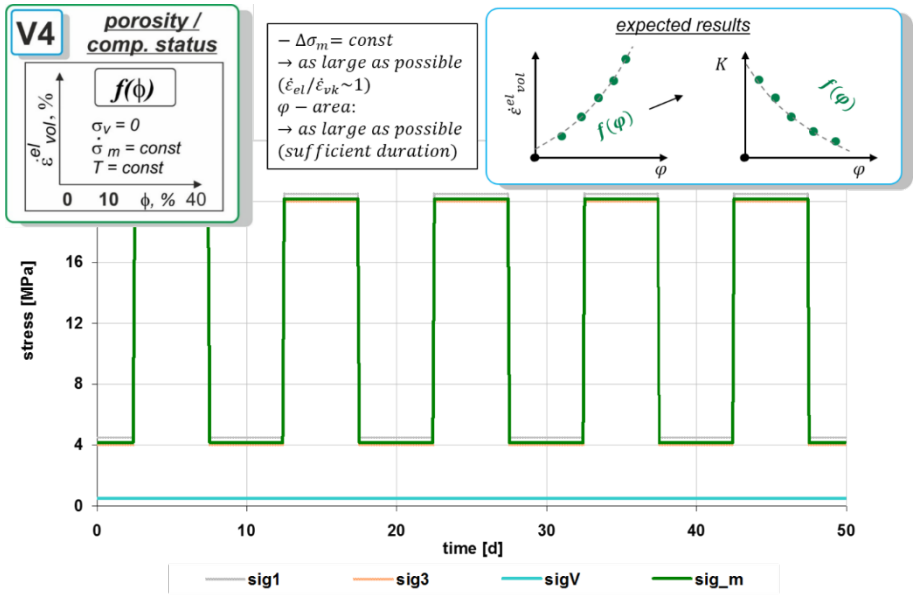

Fig. 6.11 Loading history of test type V4

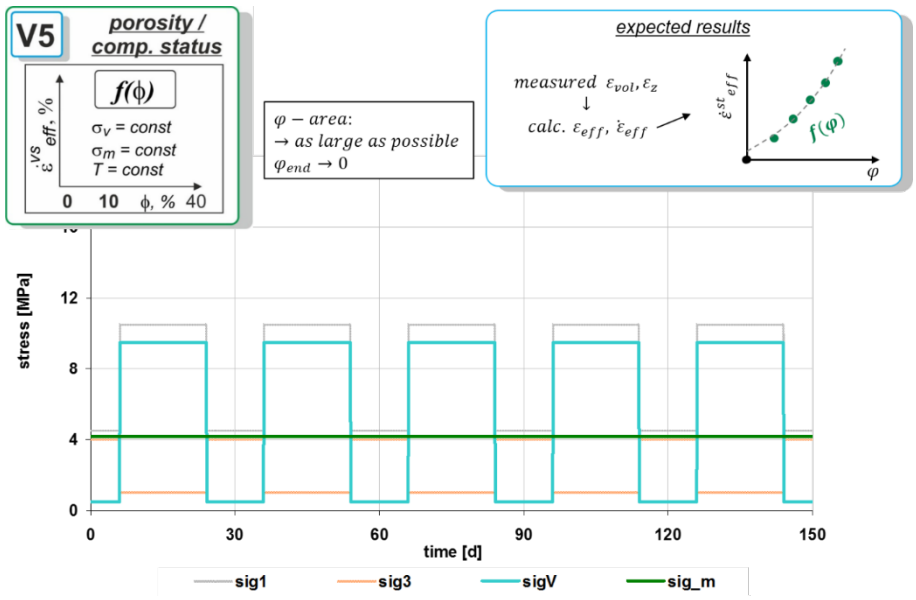

Fig. 6.12 Loading history of test type V5a

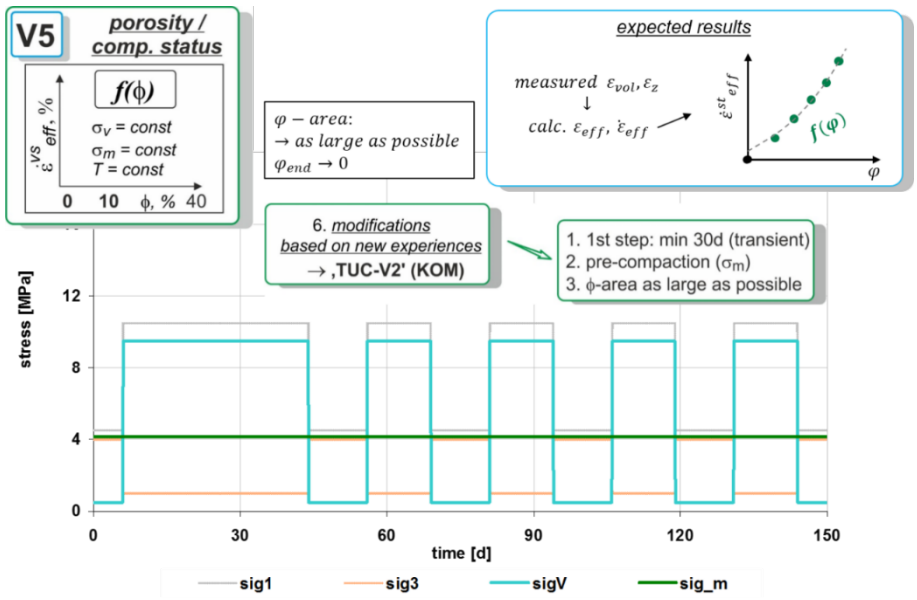

Fig. 6.13 Loading history of test type V5b, modified

S1 in Fig. 6.14:

Test series with isotropic maintenance of the mean stress (deviatoric stress = 0 MPa) at the same level and variation of the saline moisture content for the investigation of the functional dependence between moisture content and compaction. These tests are designed analogue to GRS tests, documented in /KRÖ 17/, but without load change, in order to avoid change in compaction components from the dependence between stress level and compaction behaviour). A further difference to the tests documented in /KRÖ 17/ about the influence of salt moisture on the compaction behaviour results from the planned higher number of individual tests in test series S1, which, as planned, results in a finer resolution of the functional dependency. The functional correlation expected in the result of test series S1 is on the one hand essential for the representation of relevant in-situ situations, but on the other hand has not been sufficiently investigated so far. The above statement is confirmed by the finding that it is currently not proven whether the influence of the moisture content on the compaction behaviour of crushed salt is working similar to a switching function, i.e. from a quantitatively defined initial value of the moisture content and must be considered accordingly in the constitutive models, or whether there is a dependency between the moisture content and the intensity of crushed salt compaction which increases continuously with the quantity of the moisture content.

S2 in Fig. 6.15:

Test series S2 is characterized by three individual tests with constant mean stress over the test period and varied load geometry. Besides the scalar magnitude of the volumetric

strain, the individual components of the deformations are the main measurement objective. The volumetric and axial deformation components are measured, the horizontal deformation component can be derived by calculation. An optional, more precise metrological determination of the horizontal deformation component by strain gauges (constructive limited to small deformations in the order of ≈ 1%) or a circumferential measurement (Cantilever bridge / measuring chain) remains unaffected by this. The directional dependency of the deformations induced by the stress geometry has not been validated very much so far and is not for example with the material model C-WIPP/Itasca only not realistically represented in the result of mathematical analyses, but is also demonstrably implausible (Section 0.5).

S3 in Fig. 6.16:

The objective of the tests planned within the framework of the S3 test series is to generate a data basis with which a validation of the constitutive models can be checked regarding their suitability for back analysis of varied and combined load types with a uniform parameter data set. The tests planned with test series S3 are thus intended to demonstrate the performance and prediction quality of the constitutive models developed on the basis of test types V1 to V5 and test series S1 and S2. The tests planned for test series 3, with reference to the introductory remarks, are necessary against the background of the knowledge that comparative calculations for the back analysis of oedometer and triaxial tests with currently available constitutive models have shown, that a sufficient agreement between the state variables measured in the test and those calculated using the available constitutive models is only possible, even when using the same type of crushed salt mixtures, if the constitutive model parameters are determined in relation to the test. Vice versa, it is not possible to back-calculate compaction tests on similar crushed salt material when varying the loading history with a uniform parameter data set. The reason for this is, due to the oedometer test technique mainly used in the past, deficits in the process understanding (constructional caused missing or not completely known and/or controllable load boundary conditions in the oedometer test). In order to eliminate the existing deficits, triaxial tests with a new type of operation mode are proposed, in which, in addition to the experimental specification of a strain-controlled load, an isotropic load is at the same time ensured in contrast to oedometer tests. Due to the experimental realisation of isotropic load conditions, the number of simultaneously effective processes and influencing factors is reduced and consequently the interpretability of the measurement results is increased.

S4 in Fig. 6.17:

In contrast to the tests described above with V1 – V5 and S1 to S3 for the analysis and qualification of the THM-coupled compaction behaviour of crushed salt, the tests planned under test series S4 are intended to show whether, to what extent and, if applicable with which test techniques a pre-compaction of crushed salt can be realized which is temporally shortened in comparison to the in-situ conditions (time-lapse tests), without thereby inadmissibly changing the material properties of the crushed salt material pre-compacted by time-lapse tests in comparison to the material properties of a crushed salt material pre-compacted long-term under in-situ loading conditions. This means, that it has to be shown that not only an artificially pre-compacted crushed salt (briquette) is generated as a result of the time-lapse tests, but also that the THM material properties of the pre-compacted crushed salt material taken from time-lapse tests are comparable with those of a crushed salt material pre-compacted under in-situ loading conditions. For this purpose, both comparative microstructural investigations of artificially and under in-situ conditions pre-compacted crushed salt test specimens and triaxial tests for the comparative analysis of the THM properties of artificially and under in-situ conditions pre-compacted crushed salt test specimens are planned and required.

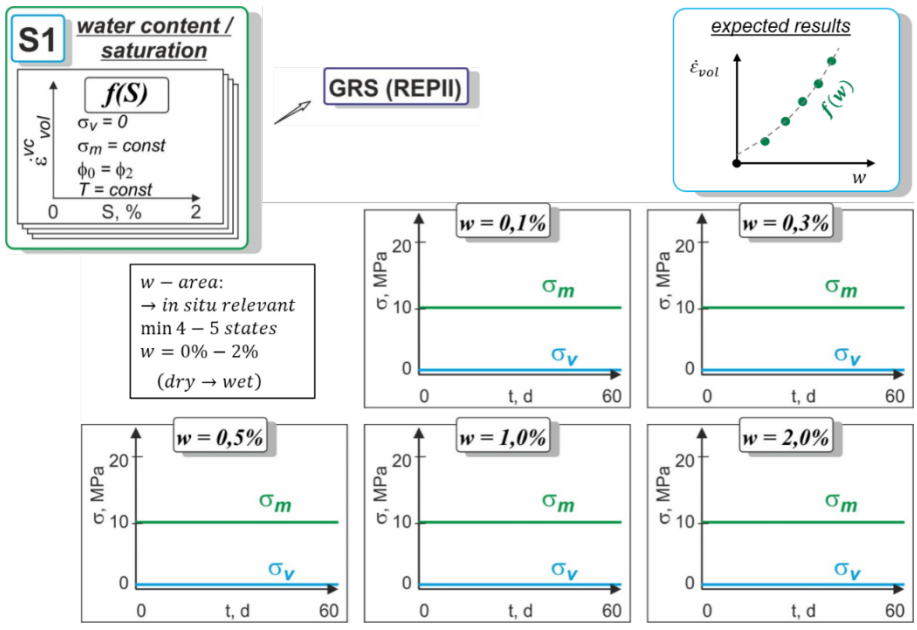

Fig. 6.14 Loading history of test series S1

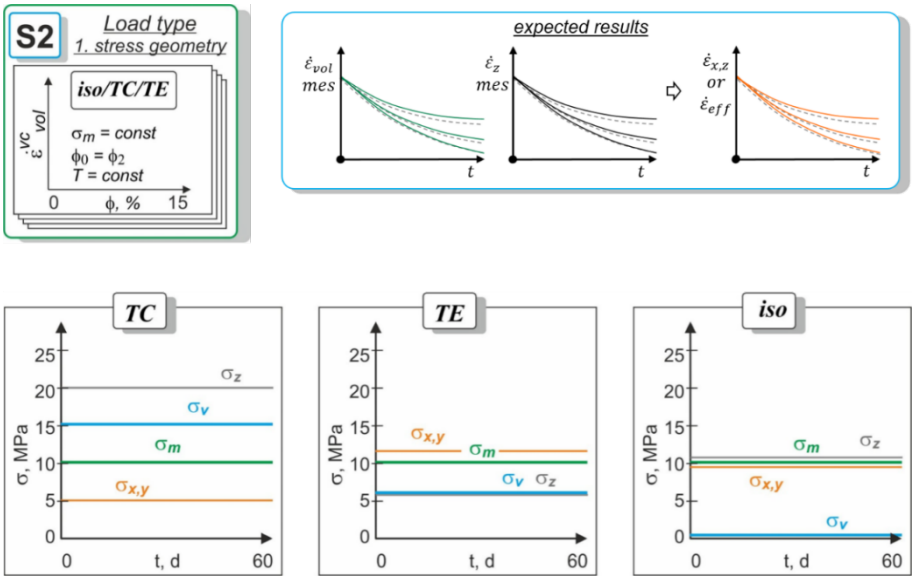

Fig. 6.15 Loading history of test series S2

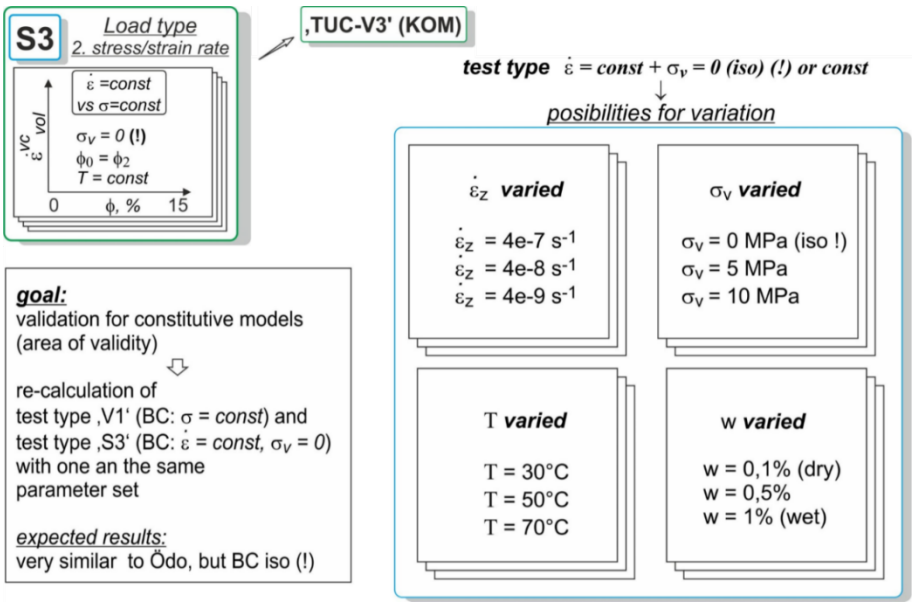

Fig. 6.16 Loading history of test series S3

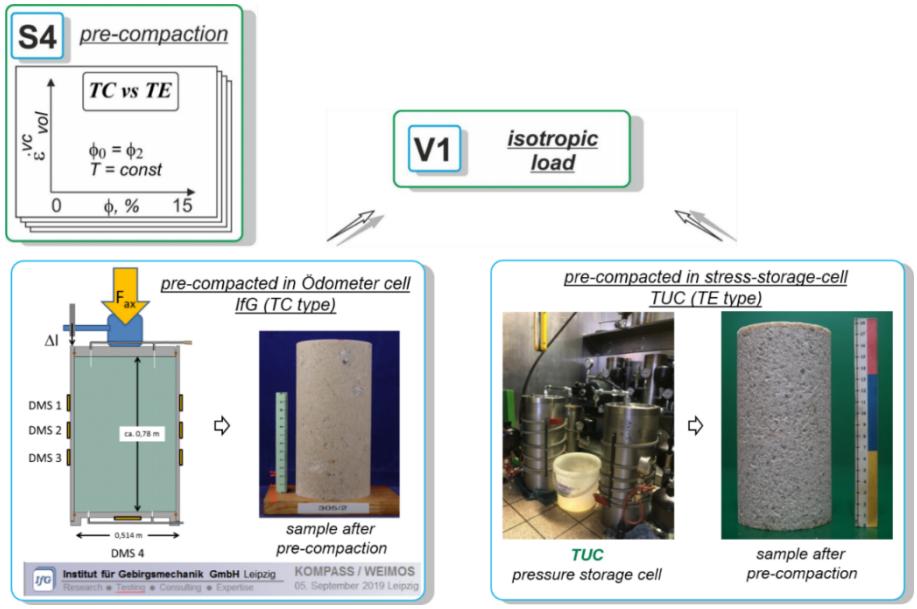

Fig. 6.17 Test series S4 for the qualification test of pre-compaction techniques

Fig. 6.18 shows the coordinated draft of the planned laboratory test program as a result of the technical talks and discussions between the project partners GRS, TUC, Sandia, BGR, IfG and BGE-TEC within the framework of the joint research project. Compared to the planning draft shown in Fig. 6.7, the following modifications were incorporated into the laboratory test program:

- The laboratory test program is divided into three main blocks as follows: The first experimental block, designated Part 1, contains the experiments for the systematic development of an experimental database, with which a comprehensive validation and, if necessary, also qualification and (further) development of the constitutive models for crushed salt compaction can be carried out. The second experimental block, designated Part 2, contains investigations on long-term crushed salt compaction down to the range of small porosities of less than 1 %. For this purpose, both type V1 (isotropic single stage) and type V4 (isotropic multi-stage) tests from test block Part 1 can be used if the small porosities envisaged are achieved by the specified duration of the tests. Finally, the third test block (Part 3) contains the necessary investigations on the dependence of the permeability on the porosity, if necessary, on the minimal principle stress, as well as investigations on the dependence of the compaction process on the pore pressure.
- Investigations on the influence of temperature on crushed salt compaction originally planned within the framework of a multi-stage experiment were replaced by

a series of individual experiments, as they are easier to carry out from an experimental point of view. The associated disadvantage of a scattering of the test results induced by the material behaviour (tests on different test specimens) is estimated as altogether small and acceptable in view of the general homogeneity of crushed salt mixtures.

- For investigations on the influence of the loading geometry on the compaction behaviour, a test with plain strain load geometry (plane strain conditions) was supplemented.

In view of the scope of the overall tests required according to Fig. 6.18 and the test time required for realization, red marker in Fig. 6.19 was used to prioritize the planned tests so that the experimental investigations primarily required for the purpose of test accompanying constitutive model development and validation are carried out at an early stage and the material characteristics required for the purpose of quantitative verification are subsequently determined. Additionally, the allocation of the TUC-V2 test in frame of this program was indicated.

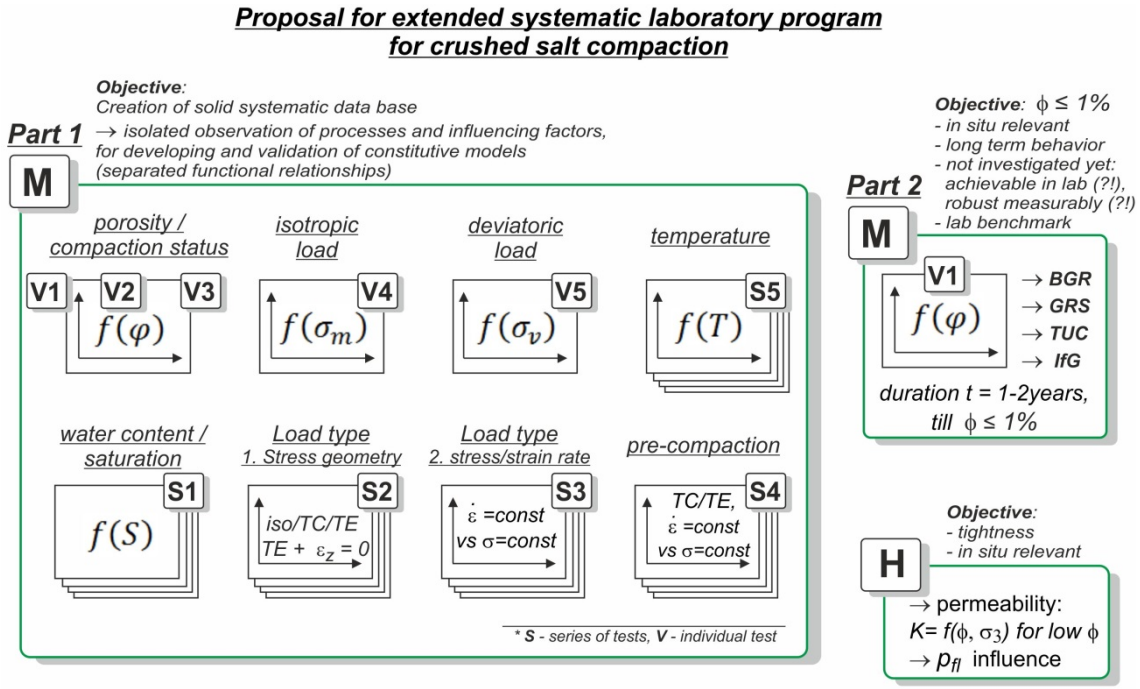

Fig. 6.18 Test program for the systematically analysis of the THM-coupled behaviour of crushed salt

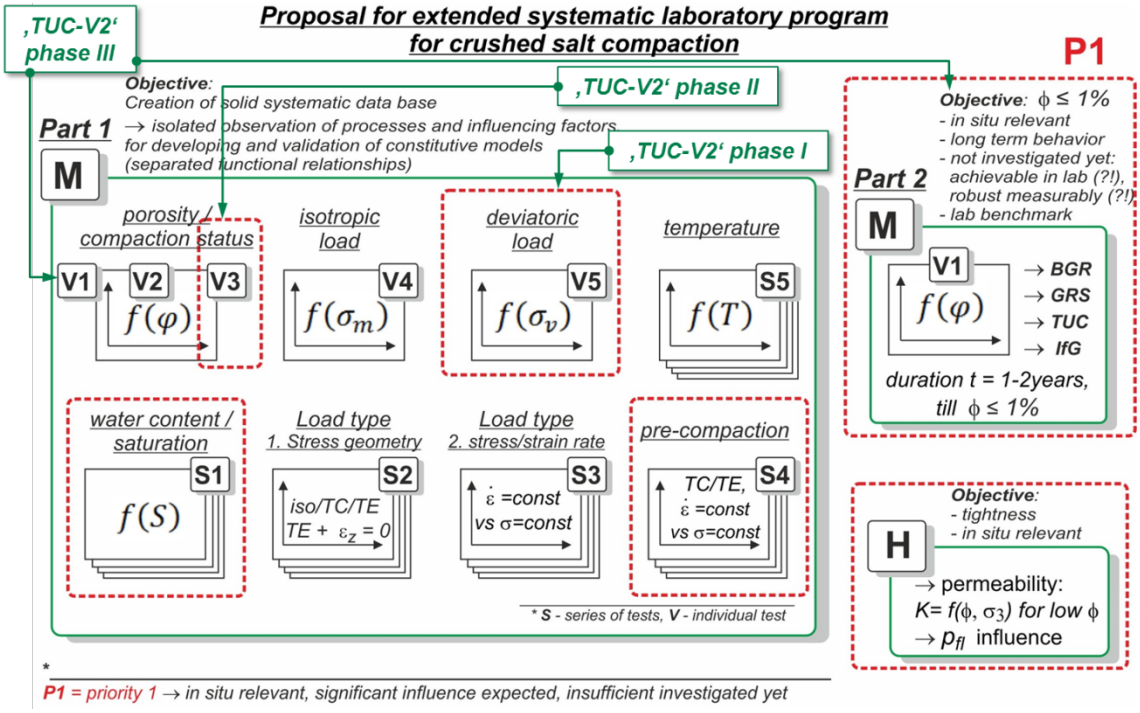

Fig. 6.19 Final version of the approach for a comprehensive systematically laboratory program with prioritization and allocation of the TUC-V2 test

6.2.3.5 Summary

The experimental investigations carried out within the framework of the research project on the compaction behaviour of crushed salt are characterized by

- a systematic analysis of the new requirements that will be placed on a prognosis of the THM-coupled material behaviour of crushed salt after the introduction of the containment rock zone concept (paradigm change),
- a systematic derivation of the need for investigations resulting from the new requirements to ensure a sufficiently proven and qualified experimental database for the analysis of the functional dependencies between crushed salt compaction and external load on the one hand and for the (further) development and validation of the crushed salt models on the other hand.

Based on the knowledge gained from the above-mentioned investigations, a laboratory programme consisting of coordinated individual tests and test series was developed, with which the functional dependencies between different influencing factors (mean stress, deviatoric stress, porosity, moisture content, etc.) and the compaction behaviour can be analysed in each case in isolation.

To test the technical feasibility of novel test operational modes and to obtain experimental data for the as yet insufficient investigated influencing factor of deviatoric stress, two pilot tests on pre-compacted crushed salt were realized. Fig. 6.20 documents the load histories of these two triaxial tests.

Furthermore, it should be analysed whether the fluid pressure criterion is valid for highly compacted crushed salt in order to demonstrate the transition to slightly damaged rock salt (Fig. 2.2) as the demonstration of barrier function is the final goal.

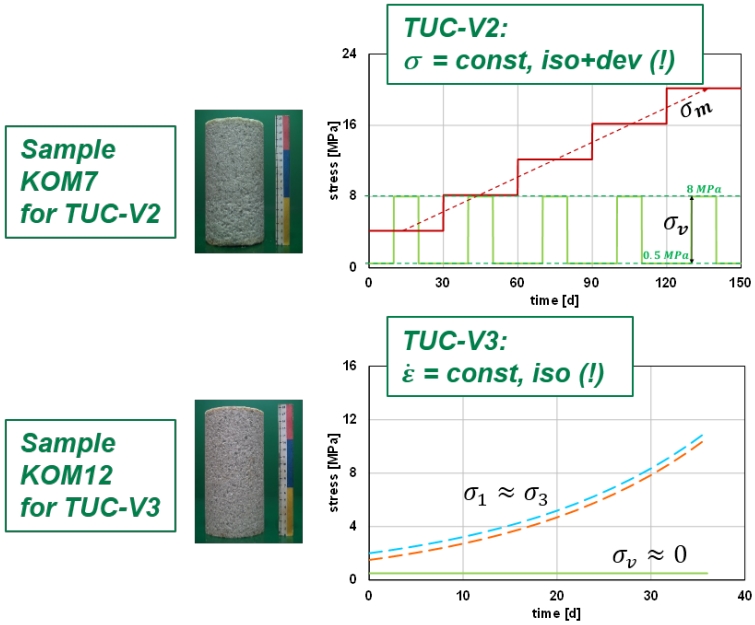

Fig. 6.20 Pilot tests on compaction behaviour with novel test operation modes conducted within the frame-work of the research project

Since the two tests with novel operational modes were not only successfully realized, but the results of their evaluation also showed that the functional dependence between the viscous compaction of crushed salt and the deviatoric stress can be clearly quantified by the new experimental technique, it is planned for a continuation of the research work: to investigate within a second testing phase of again 150 days test time the dependence between the viscous shear deformation and the porosity and finally in a third test phase the compaction behaviour under isotropic loading conditions in the range of small porosities of approx. 5 % to 1 %. Fig. 6.21 shows the load curve for the first load stage already realized within the framework of the research project and additionally the two test phases intended for a planned continuation of the research work. Fig. 6.19 shows the assignment of the three test phases to the planned laboratory test program.

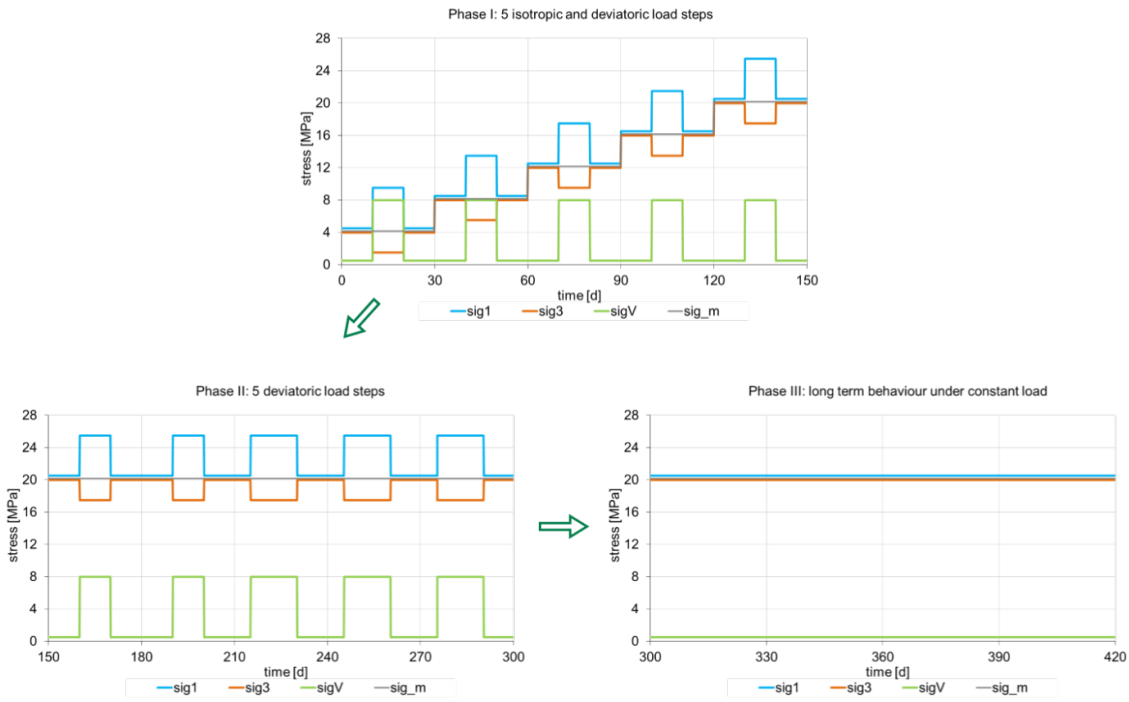

Fig. 6.21 Experimental Phase I of the TUC-V2 pilot test realized in the research project and, if the research work continues, planned experimental phases II and III

6.2.4 Numerical modelling

6.2.4.1 Overview of the existing constitutive model approaches for crushed salt: similarities, differences in structure and need for validation

Based on the currently established main focused applications for constitutive model approaches in order to build up relevant in situ situations, first the requirements with reference to functionality, quality and area of validity for the approaches was defined, so called ‘target-state’. In the second step ‘as-is-state’ (current given available functionality) for the model approaches was comparative analyzed and evaluated. From the results of these two steps the need for further developments for the model approaches, for the validation of these approaches and for the building of one systematic experimental data base, which serves the ability of the complete comprehensive validation, was derived. After the definition of the investigation needs, the next step of concretization was realized due to the planning of the model developments and the design of the lab program for the long-term compaction behavior was developed.

Following a short summary will be given to the two last concretization steps, which define further investigations directions and areas:

1) Comparative evaluation of the model approaches to define the need in the development, validation and experimental data base,
2) Design of lab program to produce the needed experimental data base.

Based on the by TUC developed methodology for the comparative analysis of the constitutive model approaches (shown in Fig. 5.13 and Fig. 5.14) the uniform structural decomposition of individual model approaches was done (shown in Section 5.3). In the next step the comparative analysis in order to find the differences, similarities and the common investigation need was realized. In order to give a short view to the results of this analysis Fig. 6.22 shows a schematic compilation of the constitutive models, so that the basic structures and the main considered influencing factors can be identified by comparison. Additional, Fig. 6.23 shows a formalized collection structure of the common features of the different constitutive models. Further, Fig. 6.24 shows the identified need in the experimental data base to serve the sufficiently validation.

On the basis of these analysis results the approach for laboratory program for the study of functional relationships and for the validation of the constitutive model approaches was developed. This program was described in the previous Section.

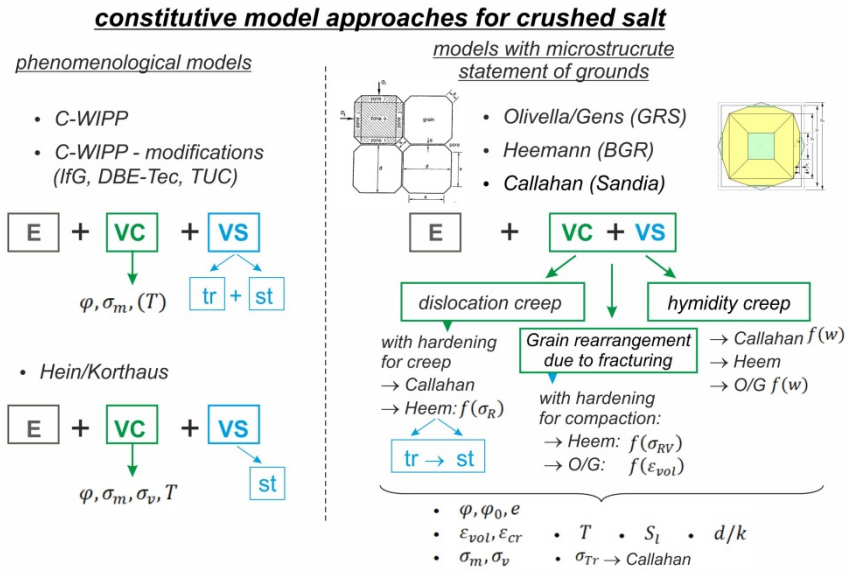

Fig. 6.22 Schematic compilation of the material models for crushed salt: basic structure and considered main influencing factors in comparison

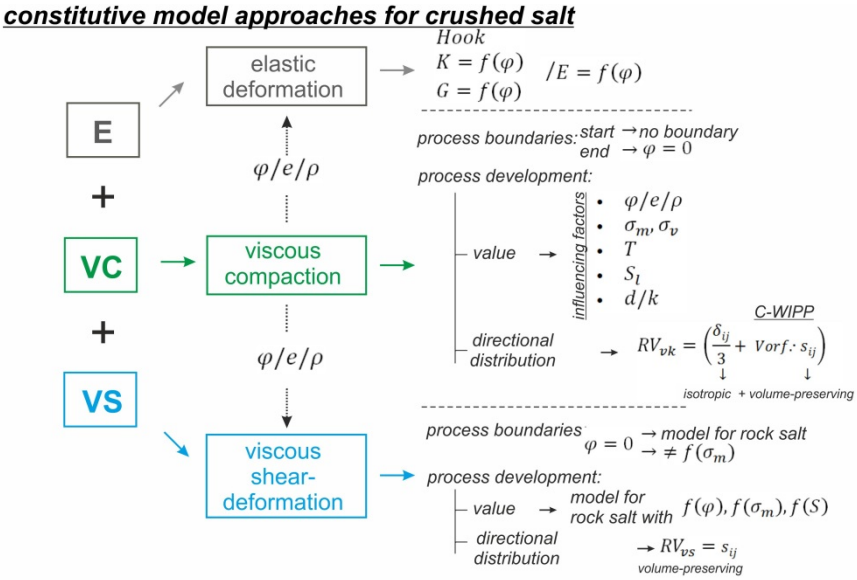

Fig. 6.23 Formalized collection structure of the constitutive models for crushed salt: common features of the constitutive models, common need for validation and need for experimental investigations

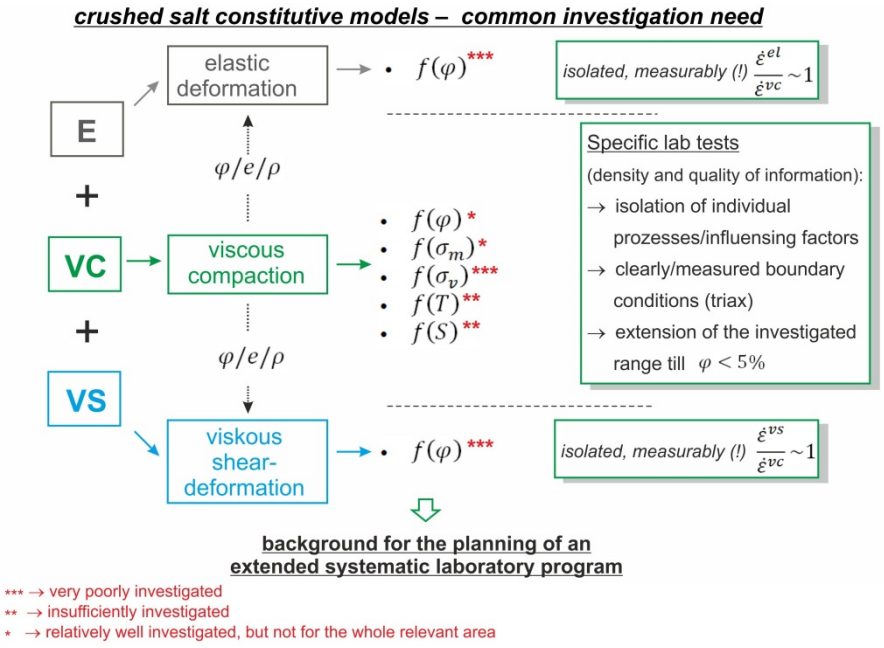

Fig. 6.24 Schematic representation of the main factors characterizing the THM behaviour of crushed salt and the need of the validation of accordingly functional relationships in the constitutive model approaches

Finally, Fig. 6.25 demonstrates schematically previous described in frame of this project realized main working steps.

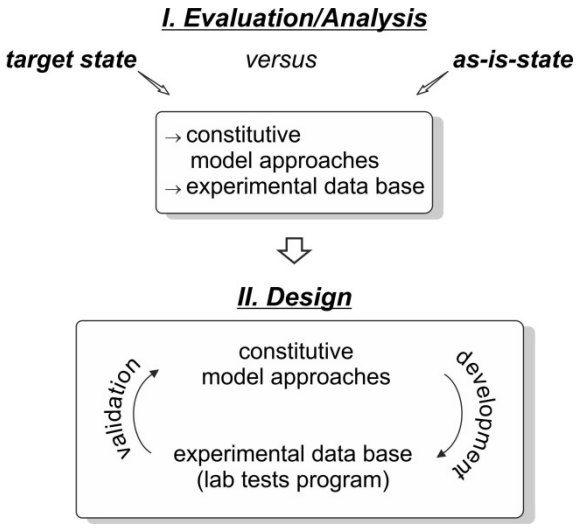

Fig. 6.25 Main working steps in frame of this project: definition of 'as-is-state' and 'target-state' in the constitutive modelling for crushed salt, derivation of need for further developments and design of laboratory program to serve this need.

6.2.4.2 Current findings and further need for validation

In summary, the following finding and insights from the benchmark results can be stated:

1. Some model approaches are capable of reproducing all three benchmarking tests, but it should not be forgotten that even in this optimal case, this is only the first step for validation, because

    a. only the three factors addressed in the experiments are validated,

    b. the validation only refers to the range of orders of magnitude of the influencing factors represented in the tests and

    c. the three tests form only a very small and non-systematised group of experiments.

2. Some model approaches are not able to represent all effects in these tests correctly. Depending on the constitutive model approach the reason for this is either

    a. due to a complete missing of consideration of the influencing factor or

    b. due to a functional relationship for this influencing factor which has not been chosen in an entirely optimal way.

These main results of the benchmark finally show that:

1. The most constitutive model approaches require further development and optimization in their formulations;

2. The models require a well-founded, systematized, comprehensive laboratory database for the validation of their current or future modified formulations/assumptions.

In correlation with the laboratory plans presented in Section 6.2.3 a systematic model validation of a wide range of influencing factors is possible and can present the basis for further model improvements.

References

/ALK 08/ Alkan, H., Müller, W.: Numerical Modelling of Dilatancy induced Percolative Permeation in Rock Salt. ISTec. ISTec-A-1319. Garching. 2008

/ARG 12/ Argüello, J.G., Holland, J.F., Bean, J.E.: International Benchmark Calculations of Field Experiments at the Asse Salt Mine, SAND2012-8193, Sandia National Laboratories, Albuquerque, NM, 2012.

/AST 16/ ASTM C457 / C457M-16, Standard Test Method for Microscopical Determination of Parameters of the Air-Void System in Hardened Concrete, ASTM International, West Conshohocken, PA, 2016, www.astm.org

/AUB 98/ Aubertin, M., Hardy, H.R. Jr. (eds.): Ecole Polytechnique (Montreal, Canada): 4th Conference Mechanical behavior of salt : Ecole Polytechnique (Montreal, Canada 17. and 18. 06.1996). TTP Trans Tech Publications. Clausthal-Zellerfeld. 1998.

/BEC 99/ Bechthold.W., Rothfuchs, T., Poley, A., Ghoreychi, M.,Heusermann, S., Gens, A. &Olivella, S.: Backfilling and Sealing of Underground Repositories for Radioactive Waste in Salt (BAMBUS Project). Final Report. - European Commission, nuclear science and technology, EUR 19124 EN, Luxembourg, 1999

/BEC 04/ Bechthold, W. Smailos, E., Heusermann, S., Bolllngerfehr, W., BazarganSabet, B., Rothfuchs, T.,Kamlot, P.,Grupa, J., Olivella, S. & Hansen, F.D.: Backfilling and sealing of underground Repositories for radioactive waste in salt (BAMBUS II Project). Final report. - European Commission, nuclear science and tech-nology, EUR 20621 EN, Luxembourg, 2004.

/BER 19/ Bérest, P., Gharbi, H., Brouard, B., Brückner, D., DeVries, K., Hévin, G., Hofer, G., Spiers, C., Urai, J.: Very slow creep tests on salt samples. Rock Mechanics and Rock Engineering 52, pp. 2917 – 2934. Doi: 10.1007/s00603-019-01778-9, 2019

/BIR 40/ Birch, F., Clark, H.: The Thermal Conductivity of Rocks and its Dependence upon Temperature and Composition – Part I. Am. J. Sci., 238. pp. 529 – 558. 1940

/BLE 02/ Blenkinsop, T.: Deformation Microstructures and Mechanisms in Minerals and Rocks. Kluwer Academic Publishers, ISBN 0-412-73480-X, 2002.

/BMU 17/ Bundesministerium für Umwelt, Naturschutz und nukleare Sicherheit (BMU): Standortauswahlgesetz (StandAG) vom 5. Mai 2017 (BGBl. I S. 1074), das zuletzt durch Artikel 247 der Verordnung vom 19. Juni 2020 (BGBl. I S. 1328) geändert worden ist.

/BMU 20/ Bundesministerium für Umwelt, Naturschutz und nukleare Sicherheit (BMU): Verordnung über Sicherheitsanforderungen und vorläufige Sicherheitsuntersuchungen für die Endlagerung hochradioaktiver Abfälle - Vorläufiger Entwurf. Stand 06.04.2020. Abgerufen am 13.07.2020 von https://www.bmu.de/gesetz/verordnung-ueber-sicherheitsanforderungen-und-vorlaeufige-sicherheitsuntersuchungen-fuer-die-endlagerun/).

/BOL 12/ Bollingerfehr, W., Filbert, W., Dörr, S., Herold, H., Lerch, C., Burgwinkel, P., Charlier, F., Thomauske, B., Bracke G., Kilger, R.: Endlagerauslegung und -optimierung. Bericht zum Arbeitspaket 6 – Vorläufige Sicherheitsanalyse für den Standort Gorleben. Köln: GRS – 281. 2012

/BOL 18/ Bollingerfehr, W., Bertrams, N., Buhmann, D., Eickemeier, R., Fahland, S., Filbert, W., Hammer, J., Kindlein, J., Knauth, M., Liu, W., Minkley, W., Mönig, J., Popp, T., Prignitz, S., Reinhold, K., Simo, E., Thiemeyer, T., Völkner, E., Wolf, J.: KOSINA – Concept developments for a generic repository for heat-generating waste in bedded salt formations in Germany. BGE Technology, Peine. BGE TEC 2018-13. 2018.

/BRA 08/ Brasser, Th.; Bletz, B.; Noseck, U.; Schmidt, G.: Die Rolle Natürlicher Analoga bei der Sicherheitsbewertung von Endlagern - Anhang „Natürliche Analoga“. - in: Brasser, T. Droste, J., Müller-Lyda, O, Neles, J., Sailer, M., Schmidt, G., Steinhoff, M..: Endlagerung wärmeentwickelnder radioaktiver Abfälle in Deutschland. - Gesellschaft für Anlagen- und Reaktorsicherheit (GRS) mbH, GRS-247, 96 S. + 22 Anhänge auf CD, Köln, 2008.

/BRE 99/ Brenner, J., Feddersen, H.-K., Gies, H. Wehe , R. , Rotfuchs., T., Storck, R.: Untersuchung von Altversatz als Analogon zur Konvergenz und Kompaktierung versetzter untertägiger Hohlräume im Salz über lange Zeiträume - Phase I. Gesellschaft für Anlagen- und Reaktorsicherheit (GRS) mbH, GRS-147, Köln, 1999.

/CAL 91/ Callahan, G.D., DeVries, K.L.: Analysis of Backfilled Transuranic Waste Storage Rooms. SAND91-7052. RE/SPEC, Inc. Report to Sandia National Laboratories. Sandia National Laboratories, Albuquerque, NM, USA. 1991.

/CAL 99/ Callahan, G.D.: Crushed Salt Constitutive Model, SAND98-2680, prepared by RESPEC, Rapid City, SD, for Sandia National Laboratories, Albuquerque, NM, 1999.

/CAS 89/ Casas, E., Lowenstein. T.K., Diagenesis of Saline Pan Halite: Comparison of Pétrographie Features of Modern, Quaternary and Permian Halites. Journal of Sedimentary Petrology, Vol. 59, 1989.

/COS 93/ Cosenza, P., Ghoreychi, M.: Coupling between mechanical behavior and transfer phenomena in salt. In /GHO 96/.

/CRI 02/ Cristescu, N. D., Hardy Jr., H. R. and Simionescu, R. O. (ed.); University of Bucharest (Bucharest, ROM) and University of Florida (Gainesville, FL, US): Basic and Applied Salt Mechanics - Proceedings of the Fifth Conference on Mechanical Behaviour of Salt (Bucharest, ROM 9. – 11.08.1999). Abingdon: Balkema, 2002.

/DAE 16/ Deutsche Arbeitsgemeinschaft Endlagerforschung (DAEF): Short statement referring the publication of „Deformation-assisted fluid percolation in rock salt“ (published in Science on 30.11.2015), April 2016

/DAV 96/ Davidson, B., Dusseault, M.: Granular Halite Backfill as a Structural and Disposal Medium. In /AUB 98/.

/DES 13/ Desbois, G., Urai, J.L., Pérez-Willard, F., Radi, Z., Offerns, S., Burkart, I., Kukla, P.A., Wollenberg, U.: Argon broad ion beam tomography in a crygenic scanning electron microscope: a novel tool for the investigation of representative microstructures in sedimentary rocks containing pore fluid. Journal of Microscopy – 249, Pt 3, pp. 215-235, 2013.

/DEV 11/ DeVries, K.L.: Munson-Dawson Model Parameter Estimation of Sondershausen and Asse Salt. RESPEC Memo to Tom Pfeifle Sandia National Laboratories, January 25, 2011.

/DUE 15/ Düserloh, U., Herchen, K., Lux, K.-H., Salzer, K., Günther, R.-M., Minkley, W., Hampel, A., Argüello Jr, J.G., Hansen, F.D.: Joint Project III on the comparison of constitutive models for the thermomechanical behavior of rock salt. III. Extensive laboratory test program with argillaceous salt from WIPP and comparison of test results. In: /ROB 15/, pp. 13–21.

/DUE 19/ Düsterloh, U.; Stahl, U.; Lerche, S.; Dyogtyev, O.; Zhao, J.: 1. Zwischenbericht - Prüfungsphase D, im Rahmen der Prüfung der Unterlagen zum Planfeststellungsverfahren zur Stilllegung des Endlagers für radioaktive Abfälle Morsleben (ERAM) - Prüfkomplex 6 "Schachtverschlusssystem der Schächte Bartensleben und Marie" - Prüfungsphase (D) -Rechnerische Prüfung Unterlage P 500, 2019

/ENG 12/ Engelhardt, H.-J.; Stradinger, A.; von Borstel, L.E.: Bestimmung der Oberflächenfeuchte von Steinsalzgrus aus den Erkundungsbergwerk Gorleben (Arbeitspaket 9.1.2) Vorläufige Sicherheitsanalyse Gorleben, 2012

/EZE 14/ Ezersky, M., Goretsky, I.: Velocity–resistivity versus porosity–permeability inter-relations in Dead Sea salt samples, Engineering Geology, Vol 183, 2014, pp. 96-115.

/FAH 18/ Fahland, S., Hammer, J, Hansen, F.D., Heusermann, S., Lux, K.-H., Minkley W. (eds.): The mechanical behaviour of salt IX – Proceedings of the 9th Conference. Federal Institute for Geosciences and Natural Resources (BGR). Hannover, 12. – 14.09.2018.

/GLA 16/ Glaubach, U., Hofmann, M.: Schachtverschlüsse für Endlager für hochradioaktive Abfälle - ELSA-Phase 2: Konzeptentwicklung für Schachtverschlüsse und Test von Funktionselementen von Schachtverschlüssen; Teilbericht zum Arbeitspaket 3: Laborversuche zu den Arbeitsschritten 2.1 bis 2.6. Vorhaben ELSA – Phase 2 02E11193A, TU-BA Freiberg, 2016.

/GHO 96/ Ghoreychi, M. (ed.): Mechanical behavior of salt – Proceedings of the Third Conference. Ecole Polytechnique (Palaiseau, France 14. – 16. 09.1993). Cleveland: TTP Trans Tech Publications, 1996.

/HAM 13/ Hampel, A., Argüello, J.G., Hansen, F.D., Salzer, K., Minkley, W., Lux, K.-H., Herchen, K., Pudewills, A., Yildirim, S., Staudtmeister, K., Rokahr, R., Gährken, A., Missal, C., Stahlmann, J.: *Benchmark Calculations of the Thermo-Mechanical Behavior of Rock Salt--Results from a US-German Joint Project,* 47th US Rock Mechanics/Geomechanics Symposium, ARMA 13-456. 2013.

/HAM 16/ Hampel, A., Herchen, K., Lux, K.-H., Günther, R.M., Salzer, K., Minkley, W., Pudewills, A., Yildirim, S., Rokahr, R., Missal, C., Gährken, A., Stahlmann, J.: Vergleich aktueller Stoffgesetze anhand von Modellberechnungen zum thermo-mechanischen Verhalten und zur Verheilung. Projektträger Karlsruhe, Wassertechnologie und Entsorgung (PTKA-WTE), Karlsruher Institut für Technologie (KIT), BMBF-FKZ 02E10810, DOI: 10.2314/GBV:87169817X, 2016..

/HAN 97/ Hansen, F.D.: Reconsolidated Salt: Compaction, Constitutive Modeling, and Physical Processes. Int. J. Rock Mech. & Min. Sci. – 34:3-4, Paper No. 119, 1997.

/HAN 14/ Hansen, F.D., Popp, T., Wieczorek, K., Stührenberg, D.: Granular Salt Summary: Reconsolidation Principles and Applications. Fuel Cycle Research & Development, FCRD-UFD-2014-000590. SAND2014-16141R, 2014.

/HAN 16/ Hansen, F.D., Gadbury, C.: Reconsolidated Salt as a Geotechnical Barrier. WM2016 Conference, Phoenix, Arizona, SAND2015-9936C, 2016.

/HEE 01/ Heemann, U., Heusermann, S.: Theoretical and Experimental Investigation on Stresses and Permeability in the BAMBUS Project. In Jakusz, S. (ed): Disposal Technologies and Concepts. Proceedings of the DisTec-Conference, Kontec GmbH, Hamburg. 2004.

/HEE 19/ Heemann, U.: private information. Federal institutie for Geosciences and Natural Resources (BGR). Hannover. 2019

/HEI 91/ Hein, H.-J.: Ein Stoffgesetz zur Beschreibung des thermomechanischen Verhaltens von Salzgranulat – Ein Beitrag zur Endlagerung wärmefreisetzender radioaktiver Abfälle. Fakultät für Maschinenwesen der RWTH Aachen, Aachen, 1991.

/HUN 94/ Hunsche, U., Schulze, O.: Das Kriechverhalten von Steinsalz.- Kali und Steinsalz, 11 (8/9), 238-255. 1994

/HUN 98/ Hunsche, U., Plischke, I, Schulze, O.: ERA Morsleben – Gebirgsmechanische und geotechnische Untersuchungen im Labor und in-situ – Abschlussbericht zum Arbeitspaket 9M 213 100 15 – Ingenieurgeologische Erkundung von Homogenbereichen. Hannover: BGR, 1998 (Archiv-Nr. 117 213, Tgb.-Nr. 10 683/98).

/IFG 06/ Institut für Gebirgsmechanik GmbH, Leipzig: Investigation of the Mechanical Behaviour of Precompacted Crushed Salt in Contact to the Host Rock. NF-PRO RTDC3. WP 3.5 (Crushed Salt Engineered Barrier Behaviour). (D3.5.5) Report on long-term creep tests and gas injection tests on moistened salt bricks during compaction. February, 2006.

/IFG 20/ Institut für Gebirgsmechanik GmbH, Leipzig: Überprüfung des perkolationsgetriebenen Transports von Fluiden im Wirtsgestein Steinsalz unter relevanten Bedingungen für ein Endlager. Project PeTroS. Final repor. FKZ 4717E03250. Leipzig, 2020.

/ITA 12/ Itasca Consulting Group Inc.: FLAC3D Fast Lagrangian Analysis of Continua in 3 Dimensions – Creep Material Models. Minneapolis (MN): 2012.

/JOB 15/ Jobmann, M., Müller, C., Schirmer, S., 2015. Remaining porosity and permeability of compacted crushed rock salt backfill in a HLW repository, DBE TECHNOLOGY contribution. Peine, 2015.

/KAK 93/ Kakihana, H., Hardy, H.R. Jr., Hoshi, T., Toyokura, K. (eds.): Seventh Symposium on Salt – Symposium held at the Kyoto International Conference Hall. 6. – 9.4.1992. Elsevier, Amsterdam. 1993.

/KOR 91/ Korthaus, E.: Thermische und thermomechanische Prognoserechnungen zum TSS-Versuch (Thermische Simulation der Streckenlagerung) Primärbericht (Nr. 19.03.03.P.04 A). FZK. Karlsruhe. 1991

/KOR 96/ Korthaus, E.: Consolidation and deviatoric deformation behaviour of dry crushed salt at temperatures up to 150 °C. In /AUB 98/. Montreal, 1996

/KOR 99/ Korthaus, E.: Consolidation behaviour of dry crushed salt: Triaxial tests, benchmark exercise, and in-situ validation. In /CRI 02/.

/KRÖ 09/ Kröhn, K.-P., Stührenberg, D., Herklotz, M, Heemann, U., Lerch, Ch., Xie, M.: Restporosität und -permeabilität von kompaktierenden Salzgrus-Versatz, Repoperm – Phase 1. GRS – 254, ISBN 978-3-939355-29-8, Gesellschaft für Anlagen- und Reaktorsicherheit (GRS) gGmbH, September 2009.

/KRÖ 17/ Kröhn, K.-P., Stührenberg, D., Jobmann, M, Heemann, U., Czaikowski, O., Wieczoerk, K., Müller, C., Zhang, C.L., Moog, H., Schirmer, S., Friedenberg, L.: Mechanical and hydraulic behaviour of compacting crushed salt backfill at low porosities, Repoperm – Phase 2. GRS – 450, ISBN 978-3-946607-32-8, Gesellschaft für Anlagen- und Reaktorsicherheit (GRS) gGmbH, Februar 2017.

/KUH 14/ Kuhlmann, K.L.: Summary Results for Brine Migration Modelling Performed by LANL, LBNL and SNL for the Used Fuel Disposition Program. Sandia National Laboratories (SNL). Alberquerque, NM. 2014.

/LAM 18/ Lampe, B.C., Stormont, J.C., Lynn, T.D., Bauer, S.J.: Experimental investigation of the influence of pore pressure and porosity on the deformation of granular salt, International Journal of Rock Mechanics and Mining Sciences, 2018

/LÜD 14/ Lüdeling, Ch., Minkley, W.: A Crushed–Salt Model with Creep, Compaction and Strain Softening, and Application to Tailings Heaps. In: J. Labuz et al. (eds.), Proceedings of the 48th US Rock Mechanics/Geomechanics Symposium,1-4 June 2014, Minneapolis, Minnesota, USA, Minneapolis, MN, USA. 2014.

/LUX 07/ Lux, K.-H., Eberth, S.: Fundamental and First Application of a New Healing Model for Rock Salt. In: /WAL 07/, pp. 129-138.

/LUX 18/ Lux, K.-H.; Lerche, S.; Dyogtyev, O: Pysikalische Modellierung und numerische Simulation intensiver Schädigungsprozesse im Salinargebirge, Teil1: Laborative Untersuchungen und Stoffmodellentwick-lung für die Abbildung von Schädigungsprozessen im Salinargebirge, Teil2: Validierung und exemplarische Anwendungen im Kavernenbau, Erdöl Erdgas Kohle, Heft 1-2, 2018

/LUX 18a/ Lux, K.-H.; Lerche, S.; Dyogtyev, O: Intense damage processes in salt rocks – a new approach for laboratory investigations, physical modelling and numerical simulation. In: /FAH 18/.

/LUX 19/ Lux, K.-H., Lerche, S., Dyogtyev, O: Процессы умеренного и интенсивного разрушения и деформации в соляных породах: новый подход в лабораторных исследованиях, теоретическом модели-ровании и численных расчетах, Подземное хранение газа, Газовая промышленность, GASPROM, № 11, 2019

/MAC 15/ Barry-Macaulay, D., Bouazza, A., Wang, B., Singh, R.M.: Evaluation of thermal conductivity of models. Can. Geotech. J., 52. pp. 1892 – 1900. 2015.

/MIL 18/ Mills, M.M., Stormont, J.C., Bauer, S.J.: Micromechanical processes in consolidated granular salt. Engineering Geology – 239, pp. 206-213, 2018.

/MIN 07/ Minkley, W., Mühlbauer, J.: Constitutive models to describe the mechanical behaviour of salt rocks and the imbedded weakness planes. In: The Mechanical Behaviour of Salt – Understanding of THMC Processes in Salt, eds.M. Wallner et al., pp. 119-129. London: Taylor & Francis. 2007.

MLY 99/ Müller-Lyda, I.: Eigenschaften von Salzgrus als Versatzmaterial im Wirtsgestein Salz – Bericht über den Workshop des Bundesamtes für Strahlenschutz und des Projektträgers Entsorgung vom 18 und 19. Mai 1999, GRS-143

/MÖN 20/ Mönig, J., Bertrams, N., Bollingerfehr, W., Fahland, S., Frenzel, B., Maßmann, J., Mayer, K.-M., Müller-Hoeppe, N., Reinhold, K., Rübel, A., Schubarth-Engelschall, N., Simo, E., Thiedau, J., Weber, J.R., Wolf, J.: Empfehlungen zur sicherheitsgerichteten Anwendung der geowissenschaftlichen Abwägungskriterien des StandAG Synthese aus dem Vorhaben RESUS. Gesellschaft für Anlagen- und Reaktorsicherheit (GRS) gGmbH. GRS-567. Braunschweig. 2020.

/MUE 12/ Müller-Hoeppe, N., Breustedt, M., Wolf, J., Czaikowski, O., Wieczorek, K.: Integrität geotechnischer Barrieren, Teil 2, Vertiefte Nachweisführung. Bericht zum Arbeitspaket 9.2, Vorläufige Sicherheitsanalyse für den Standort Gorleben. Oktober 2012

/MUE 14/ Müller-Hoeppe, N., Schmidt, H., Polster, M.: Construction engineering: concept to describe the permeability of the excavation damaged zone as a function of pressure, Z. Dt. Ges. Geowiss. (German J. Geosci.). 165(1). Schweizerbart'sche Verlagsbuchhandlung, Stuttgart, Germany. pp. 107 – 114, 2014

/MUN 79/ Munson, D.E., Dawson, P.R.: Constitutive Model for the Low Temperature Creep of Salt (With Application to WIPP). SAND-79-1853, Sandia National Laboratories, Albuquerque, NM, 1979.

/MUN 89/ Munson, D.E., Fossum, A.F., Senseny, P.E.: Advances in Resolution of Discrepancies Between Predicted and Measured In-Situ WIPP Room Closures, SAND88-2948, Sandia National Laboratories, Albuquerque, NM, 1989.

/OLI 02/ Olivella, S., Gens, A.: A constitutive model for crushed salt. Int. J. Numer. Anal. Meth. Geomech.;26:719-746 (DOI:10.1002/nag.220). 2002

/PEN 07/ Pennock, G.M., Zhang, X., Peach, C.J., Spiers, C.J.: Microstructural study of reconsolidated salt. In: /WAL 07/.

/POP 98/ Popp, T., Kern, H.: Ultrasonic Wave Velocities, Gas Permeability and Porosity in Natural and Granular Rock Salt, Phys. Chem. Earth, Vol. 23, No.3, pp. 373-378, 1998.

/POP 06/ Popp, T., Böhnel, H., Salzer,: Investigation of the Mechanical Behaviour of Precompacted Crushed Salt in Contact to the Host Rock. NF-PRO RTDC3. WP 3.5 (Crushed Salt Engineered Barrier Behaviour). Report on long-term creep tests and gas injection tests on moistened salt bricks during compaction (Deliverable 3.5.5). Institut für Gebirgsmechanik GmbH, Leipzig, 28. February, 2006.

/POP 07/ Popp, T., Wiedemann, M., Böhnel, H., Minkley, W.: Untersuchungen zur Barriereintegrität im Himblick auf das Ein-Endlager-Konzept. Abschlussbericht zum Forschungsvorhaben SR 2470, Institut für Gebirgsmechanik GmbH, Leipzig, 2007.

/POP 18/ Popp, T., Minkley, W., Fillinger, E. & Boettge, V.: Closure of the Teutschenthal backfill mine - About the challenge to elaborate a geomechanical safety concept in salt formations. In: /FAH 18/, pp. 385-402.

/REE 16/ Reedlunn, B.: Reinvestigation into Closure Predictions of Room D at the Waste Isolation Pilot Plant. SAND2016-9961, Sandia National Laboratories, Albuquerque, NM, 2016

/REE 18/ Reedlunn, B.: Enhancements to the Munson-Dawson Model for Rock Salt. Sandia National Laboratories, Albuquerque, NM, 2018

/ROB 15/ Roberts, L., Mellegard, K.D., Hansen, F.D. (eds.): Proc. 8th Conference on the Mechanical Behaviour of Salt. South Dakota School of Mines and Technology (Rapid City, USA, 26. – 28.05.2015). London: Taylor & Francis, 2015.

/ROT 03/ Rothfuchs, T., Dittrich, J., Droste, J., Müller, J. Zhang, C.-L.: Final Evaluation of the Project “Thermal Simulation of Drift Emplacement” (TSDE-Project). Final report. GRS-194, Gesellschaft für Anlagen- und Reaktorsicherheit (GRS) gGmbH, 2003

/SAL 15/ Salzer, K., Günther, R.-M., Minkley, W., Naumann, D., Popp, T., Hampel, A., Lux, K.-H., Herchen, K., Düsterloh, U., Argüello Jr, J.G., Hansen, F.D.: Joint Project III on the comparison of constitutive models for the thermomechanical behavior of rock salt. III. Extensive laboratory test program with clean salt from WIPP. In: /ROB 15/

/SAN 88/ Sander, W.: Quantitative Beschreibung der Lösungsmetamorphose beim Einbringen von Wasser in ein Bergwerk im Zechsteinsalinar.- Kali und Steinsalz, Band 10, Heft 2, S. 54 – 61, 1988.

/SCH 04/ Schenk, O., Urai, J.L.: Microstructural evolution and grain boundary structure during static recrystallization in synthetic polycrystals of Sodium Chloride containing saturated brine. Contrib. Mineral Petrol. – 146: 671-682, 2004.

/SCH 05/ Schléder, Z., Urai, J.L.: Microstructural evolution of deformation-modified primary halite from the Middle Triassic Röt Formation at Hengelo, The Netherlands. International Journal of Earth Science – 94. 941 – 955, 2005.

/SCH 07/ Schléder, Z., Urai, J.L.: Deformation and recrystallization mechanisms in mylonitic shear zones in naturally deformed extrusive Eocene-Oligocene rocksalt from Eyvanekey plateau and Garmsar hills (central Iran). Journal of Structural Geology – 29,2. pp. 241 – 255, 2007.

/SER 93/ Serata, S., Fuenkajorn, K.: Formulation of a constitutive equation for salt. In /KAK 93/.

/SIE 20/ Sierra/Solid Mechanics: Sierra/Solid Mechanics User's Guide 4.56.2, SAND2020-5362, Sandia National Laboratories, Albuquerque, NM and Livermore, CA. 2020.

/SJA 87/ Sjaardema, G.D., Krieg, R.D.: A Constitutive Model for the Consolidation of WIPP Crushed Salt and Its Use in Analyses of Backfilled Shaft and Drift Configurations, SAND87-1977, Sandia National Laboratories, Albuquerque, NM, 1987.

/SPI 93/ Spiers, C.J., Brzesowsky, R.H.: Densification Behaviour of Wet Granular Salt: Theory vs. Experiment. In /KAK 93/, pp. 83-92.

/STE 85/ Stelte, N.: Analytische Approximation der Konvergenzrate salz-grusversetzter und unter hydraulischem Druck stehender Hohlräume im Salzgestein. Abschlußbericht. Fachband 15 zum Projekt Sicherheitsstudien Entsorgung: Einzeluntersuchungen zur Radionuklidfreisetzung aus einem Modellsalzstock; Berlin, 1985.

/STO 17/ Stormont, J., Lampe, B., Mills, M., Panery, L., Lynn, T., Piya, A.: Improving the understanding of the coupled thermal- mechanical – hydrologic behavior of consolidating granular salt, Final report, NEUP13-4384, 2017

/STÜ 98/ Projekt Gorleben: Kompaktion und Permeabilität von Salzgrus. BGR-Abschlussbericht zum BfS-Arbeitspaket 9G 21382100 (Berichtszeitraum 1995 – 1997), Archiv-Nr. 116 992. Hannover, 1998.

/STÜ 02/ Stührenberg, D.: Salzgrus., Projekt Gorleben: Kompaktion und Permeabilität von Salzgrus. BGR-Abschlussbericht zum BfS-Arbeitspaket 9G 21382100 1998 – 2001. Hannover.

/STÜ 13/ Stührenberg, D.: R+D Radioactive Waste Repository – THM Geotechnical Barriers – Triaxial Compaction Test TK-031, Evaluation Report, 9Y3214100000, Bundesanstalt für Geowissenschaften und Rohstoffe, Hannover, 2013.

/STÜ 17/ Stührenberg, D.: Methodenbericht Oedometerversuch – Bestimmung des Versatzwiderstands von Salzgrus im weggeregelten Oedometerversuch. Dokumentation zum Qualitätsmanagement. BGR B3.5/B500011-01/2017-0002/001, Hannover, 2017.

/THI 16/ Thiemeyer, N., Zulauf, G., Mertineit, M., Linckens, J., Pusch, M., Hammer, J.: Microfabrics and 3D grain shape of Gorleben rock salt: Constraints on deformation mechanisms and paleodifferential stress. Tectonophysics – 676, 1-19, 2016.

/UPC 20/ Universitat Politècnica de Catalunya (UPC): CODE_BRIGHT User's Guide; Department of Civil and Environmental Engineering, Barcelona, 2020.

/WAL 07/ Wallner, M., Lux, K.H., Minkley, W., Hardy, H.R. Jr. (eds.): The Mechanical Behaviour of Salt – Understanding of THMC Processes in Salt. Proceedings of the 6th Conference. Federal Institute for Geosciences and Natural Resources (BGR). Hannover, 22. – 25.05.2007. London: Taylor & Francis, 2007.

/WAR 06/ Warren, J.K.: Evaporites: Sediments, Resources and Hydrocarbons. Springer, Berlin, 1036p., 2006.

/WIE 12/ Wieczorek, K., Lerch, C., Müller-Hoeppe, N., Czaikowski, O., Navarro, M.: Zusammenstellung von Stoffparametern für Salzgrus Technischer Bericht im Vorhaben „Vorläufige Sicherheitsanalyse für den Standort Gorleben“. Braunschweig: GRS, unveröffentlichtes Manuskript. 2012.

/WIE 17/ Wieczorek, K., Düsterloh, U., Heemann, U., Lerch, Ch., Lüdeling, Ch., Müller-Hoeppe, N., Popp, T., Stührenberg, D., Wolters, R.: Reconsolidation of crushed salt backfill - review of existing experimental database and constitutive models and need for future R&D work. DAEF Stellungnahme, 2017.

List of figures

List of tables

Gesellschaft für Anlagen- und Reaktorsicherheit (GRS) gGmbH

Schwertnergasse 1
50667 Köln
Telefon +49 221 2068-0
Telefax +49 221 2068-888

Boltzmannstraße 14
85748 Garching b. München
Telefon +49 89 32004-0
Telefax +49 89 32004-300

Kurfürstendamm 200
10719 Berlin
Telefon +49 30 88589-0
Telefax +49 30 88589-111

Theodor-Heuss-Straße 4
38122 Braunschweig
Telefon +49 531 8012-0
Telefax +49 531 8012-200

www.grs.de

ISBN 978-3-947685-94-3